Comprehensive Studies of Nearby Core-Collapse Supernovae with Neutrinos in Super-Kamiokande

March, 2026

Fumi NAKANISHI

Graduate School of
Environmental, Life, Natural Science and Technology
(Doctor's Course)
OKAYAMA UNIVERSITY

Abstract

A core-collapse supernova explosion is a phenomenon that occurs at the end of a star's life if it is 8 or more solar masses, whereas more massive stars may collapse directly into black holes without producing a successful explosion. Since over 99% of the energy emitted during a supernova explosion is carried away by neutrinos, observing supernova neutrinos is critical for understanding the explosion mechanism. In recent years, theoretical models of supernova explosions using various stellar masses and equation of state (EOS) have been developed. In the Super-Kamiokande (SK) experiment, preparations are ongoing to observe neutrinos from the next nearby Galactic supernova. I integrate theoretical and observational approaches to investigate supernova explosions.

In this study, I developed a simulation code to quantitatively estimate the expected supernova neutrino signals in SK. This code is applied to two complementary studies: a theoretical study and an observational study.

On the theoretical side, I developed an analytical method to identify supernova models using this simulation code. Neutrinos from supernovae, particularly those emitted during the late phase of core collapse, provide a unique probe of the final stages of massive star evolution. Understanding these neutrinos is essential for revealing the physical processes that govern the collapse of the stellar core and the subsequent formation of compact remnants. While previous studies demonstrated the potential of various techniques to extract essential physical information, their practical application was limited by the lack of realistic treatment of experimental backgrounds. In this work, I address this limitation by incorporating both signal and background events into our analysis framework, thereby optimizing it to reflect realistic observational conditions at SK. Using this framework, I study several long-duration supernova models, simulating late-phase neutrino observations with particular emphasis on the timing information. I further explore the possibility of discriminating among models based on the timing information from this last event, highlighting the sensitivity of such approaches to different supernova mechanisms and equations of state.

On the observational side, a failed supernova (failed SN) candidate, M31-2014-DS1, was reported in 2024 in the Andromeda galaxy (M31), located at a distance of approximately 770 kpc. Motivated by this discovery, I conduct a dedicated search for neutrinos from this event using SK data. Based on the estimated time of black hole formation inferred from optical and infrared observations, I define a search window for candidate neutrino events and apply a cluster search utilizing both timing and energy information. No significant neutrino excess is observed within the defined search region. Consequently, I place a 90% confidence level upper limit on the electron antineutrino luminosity from M31-2014-DS1. Despite adopting an 18 MeV energy threshold to suppress backgrounds, the search provides meaningful constraints on the Shen-TM1 EOS, yielding an upper limit of 1.76×10^{53} erg, slightly above the expected value of 1.35×10^{53} erg. These results not only demonstrate the sensitivity of SK to failed SNe but also provide the first experimental constraints on failed SN models by limiting their predicted neutrino emission.

Furthermore, I evaluate the future sensitivity to failed SN observation in the SK-Gd experiment, which introduces gadolinium with a large thermal neutron capture cross section, as well as in Hyper-Kamiokande (HK), the next-generation detector of SK. In the SK-Gd experiment, background events can be significantly reduced by using delayed gamma-ray signals associated with neutron capture. By applying the analysis framework established in this work, I demonstrate that neutrino searches can be extended to lower energy regions. On the other hand, HK has an effective volume approximately an order of magnitude larger than that of SK, providing high detection sensitivity to supernovae at greater distances. Our estimates show that a detection efficiency of nearly 100% can be achieved for failed SNe occurring within a distance of 1 Mpc. Furthermore, when combined with the failed SN rate inferred from past optical observations, I find that approximately one failed SN is expected to be observed over a five-year observation period. These results indicate that the probability of observing supernova neutrinos, including those of failed SNe, is significantly enhanced in SK-Gd and HK experiments.

Acknowledgements

I would like to express my gratitude to the many people who have supported me throughout my time in the laboratory, not only during the writing of this doctoral thesis but also throughout my research activities.

First, I would like to thank my supervisor, Prof. Yusuke Koshio, for his patient guidance in research direction and analysis techniques. When I first joined the laboratory, I had little knowledge of the field, but he kindly and carefully guided me throughout my studies. He gave me the opportunity to pursue research on supernovae after joining the laboratory, and as I gained more knowledge, my interest in the field continued to grow. He also provided me with many opportunities to present my research at conferences and meetings. On each occasion, he generously offered thoughtful advice on both the preparation of presentation slides and the delivery of my presentations.

I would also like to thank the members of the Particle Physics Laboratory at Okayama University. In particular, I am grateful to Dr. Yota Hino, who supported me. Whenever I had questions, he always took the time to answer them patiently and clearly. I would also like to thank Dr. Masayuki Harada, who taught me many important aspects of research. From the basics of programming to how to communicate with collaborators, Harada-san kindly guided me in many areas, Whenever I encountered difficulties in my research, Harada-san always provided thoughtful and insightful advice. I would also like to express my appreciation to Dr. Seiya Sakai. Sakai-san approaches everything with great care, which I have always respected. Sakai-san kindly reviewed my slides, which often contained small mistakes, and provided helpful comments. I am also grateful to Hussain Kitagawa, Tomohiro Tano, Yuki Shiraishi, Tomoaki Tada, Koyo Takeya, Sikaras Mahasawin, Kouki Hamaguchi, Akinori Higashi, Mei Homma, Ayana Asai, Yuto Asano, Shotaro Oshita, Yasumaro Hanakawa, Nozomu Meguro, and Rio Hatanaka. Finally, I would like to thank the office manager, Rie Yamamoto, for her assistance with many procedures and for her support in various aspects of laboratory life.

I am also grateful to the members of the nuLC collaboration. From the time I first joined the laboratory, they generously guided me on which papers to read and how to study the field. In particular, I would like to thank Prof. Yudai Suwa, Prof. Ken'ichiro Nakazato, Prof. Kohsuke Sumiyoshi, Dr. Akira Harada, Prof. Roger Wendell, Dr. Masamitsu Mori, Dr. Masamichi Zaizen, and Dr. Ryuichiro Akaho. Through monthly meetings and comments on my manuscripts, they always provided insightful advice that guided my research.

I would also like to thank the members of the Super-Kamiokande supernova research group. Dr. Masayuki Nakahata, Prof. Motoyasu Ikeda, Prof. Hiroyuki Sekiya, Dr. Yosuke Ashida, and Dr. Guillaume Pronost provided valuable comments that helped me advance my research.

Finally, I would like to express my deepest gratitude to my family for their constant support and encouragement.

Contents

List of Figures

List of Tables

Chapter 1

Introduction

1.1 Supernova

A supernova is the final stage in the life of a massive star. The observation of supernova neutrinos emitted during this explosion plays a crucial role in understanding the explosion mechanism.

1.1.1 Stellar evolution

Before describing the supernova itself, I briefly outline the life cycle of massive stars.

A star is a self-gravitating ball of gas that shines due to nuclear fusion reactions in its core. Since the Coulomb barrier is smallest for hydrogen, nuclear burning begins with hydrogen fusion at the stellar center. After hydrogen is exhausted, a helium core forms and contracts until helium burning begins. This process continues with the successive burning of heavier elements such as carbon, oxygen, neon, and silicon, forming progressively heavier cores. Eventually, an iron core is produced—the most stable nucleus—surrounded by onion-like shells of lighter elements (silicon, oxygen, carbon, helium, hydrogen). For stars more massive than about $12M_{\odot}$, the evolution proceeds to form a substantial iron core. Figure 1.1 schematically illustrates this stellar evolution.

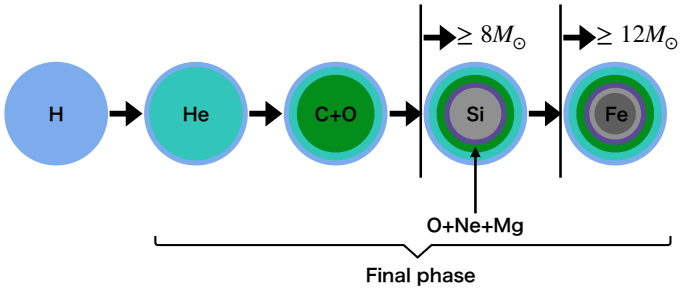

FIGURE 1.1: Schematic illustration of stellar evolution, showing that stars with initial mass above $8M_{\odot}$ develop a silicon core, while those more massive than $12M_{\odot}$ subsequently from an ironcore.

1.1.2 Types of suprernovae

There are various mechanisms that can lead to supernova explosions, and they are classified by combining the characteristics of their optical spectra and light curves. In the classification scheme of supernova explosions shown in Figure 1.2, the first step is to check whether hydrogen is present in the spectrum. If hydrogen lines are observed, the event is defined as a Type II supernova. If no hydrogen is present, the spectrum

is then examined for the presence of silicon. If silicon is detected, the supernova is classified as Type Ia; if not, the presence of helium is checked. If helium is found, it is classified as Type Ib, and if helium is absent, it is classified as Type Ic.

In this classification, the uppercase Roman numerals (I or II) indicate features of the light curve, while the lowercase letters (a, b, c) denote spectral features. Type Ia supernovae are categorized as thermonuclear (nuclear burning) supernovae, while all other types are categorized as core-collapse supernovae. In addition, unlike other types of supernovae that occur only in young, star-forming galaxies, Type Ia supernovae are also observed in old elliptical galaxies without ongoing star formation. This suggests that Type Ia supernovae originate from long-lived stellar systems. It is currently thought that they occur when gas accretes from an evolved giant companion star onto a primary white dwarf[1], when two white dwarfs merge, and the mass exceeds the Chandrasekhar limit (Eq. 1.4), leading to an explosion.

When a star with a mass on the order of the solar mass undergoes a supernova explosion, the kinetic energy released reaches 10^{51} erg. There are two possible energy sources for such explosions. One is nuclear fusion energy: if rapid nuclear burning occurs and all carbon atoms of a star with mass M are converted into iron, the energy released can be expressed as

$$E_{\rm nuc} = \left(m_C - \frac{12}{56}m_{\rm Fe}\right)c^2 \times \left(\frac{M}{m_C}\right) = 2\times10^{51}\ {\rm erg}\left(\frac{\rm M}{\rm M_\odot}\right), \tag{1.1}$$

where m_C and $m_{\rm Fe}$ are the masses of a carbon and an iron nucleus, respectively, c is the speed of light, and $M_\odot$ is the solar mass.

The other candidate is gravitational energy. If a star of roughly solar mass undergoes rapid gravitational collapse, the gravitational energy released can be estimated as

$$E_g = \left(-\frac{GM^2}{R_i}\right) - \left(-\frac{GM^2}{R_f}\right) \sim \left(\frac{GM^2}{R_f}\right) = 3\times10^{53}\ {\rm erg}\left(\frac{\rm M}{\rm M_\odot}\right)^2\left(\frac{\rm R_f}{10\ {\rm km}}\right)^{-1}, \tag{1.2}$$

where R_i and R_f are the stellar radii before and after collapse, respectively. Here it is assumed that the star rapidly contracts to the size of a neutron star (about 10 km) and that $R_i \gg R_f$. G denotes the gravitational constant.

At present, these two scenarios are understood such that Type Ia supernovae are explosions powered by nuclear fusion energy, while the other types are powered by gravitational energy release. In this paper, I focus on core-collapse supernovae, which release a large number of neutrinos during the explosion.

1.1.3 Core collapse supernovae

Figure 1.3 illustrates the time evolution of a core-collapse supernova explosion. First, the iron core can no longer support its own gravity and begins to collapse (1). During this collapse, electrons are captured by protons, producing electron neutrinos. At the very early stage, these neutrinos can escape freely, but once the core density reaches 10^{11} g cm^{-3}, neutrinos become trapped inside the core. This stage (2) is called "neutrino trapping." Neutrinos trapped in the core undergo multiple scatterings with matter and gradually diffuse outward, eventually escaping beyond the core. The

[1]The final evolutionary stage of a star with a mass below $8M_\odot$. After the red giant phase and helium burning, the hydrogen-rich outer layers are lost through mass ejection, leaving behind a degenerate core supported by electron degeneracy pressure.

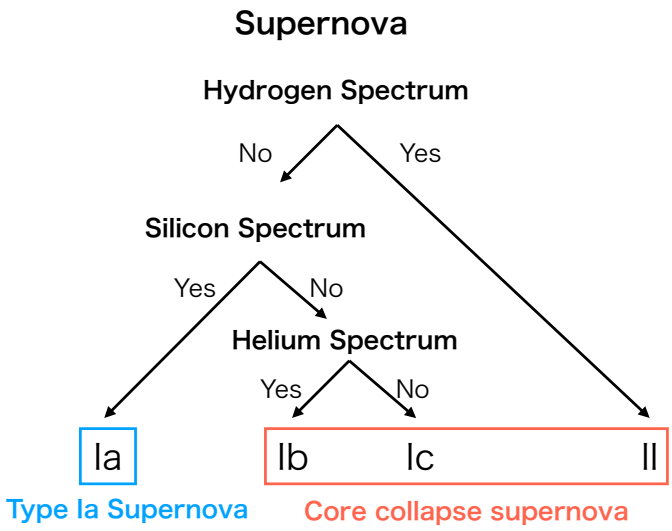

FIGURE 1.2: Classification of supernova explosions

boundary between the inner region where neutrinos cannot escape, and the outer region where they can is referred to as the "neutrinosphere." In general, the average energy of supernova neutrinos reflects the temperature at the neutrinosphere.

As the collapse proceeds and the core density reaches $\sim 10^{14}$ g cm^{-3}, the core suddenly stiffens due to the repulsive component of the nuclear force. Although the inner core becomes incompressible, matter from the outer layers continues to accrete onto it, causing a bounce at the boundary and generating a shock wave (3). Immediately after the bounce, the central region forms a hot and lepton-rich proto-neutron star (PNS), which serves as the inner core during the early post-bounce phase. The newly formed PNS has a central density exceeding nuclear saturation density and consists of high-temperature, high-density nuclear matter, with temperatures reaching above 10 MeV. This shock wave propagates outward, dissociating nuclei along the way. Electron capture reactions occur more readily on free nucleons than on nuclei. Inside the neutrinosphere, the mean free path of neutrinos is shorter than the diameter of the PNS, so neutrinos produced by electron capture cannot escape. While neutrinos produced by electron capture are trapped inside the neutrinosphere, they are suddenly released once the shock wave reaches its surface. In this phase, the luminosity of electron neutrinos can reach 10^{53} erg within several hundred milliseconds, a process known as the "neutronization burst" (4).

The shock wave continues to propagate, but since matter continues to fall toward the center (5), the shock loses energy due to nuclear dissociation and eventually stalls (6). If the stalled shock is revived by heating from neutrinos emitted by the PNS and by hydrodynamical effects such as convection (7), it propagates outward again, and the star successfully explodes. If the revival fails, the star collapses under its own gravity and forms a black hole. Even after a shock revival, a large amount of energy remains in the PNS. Approximately half of the total energy emitted in neutrinos during the supernova comes from the cooling of the PNS. This process, called the "PNS cooling phase" (8), lasts for tens of seconds, during which neutrinos carry away the remaining energy and the PNS gradually cools into a stable neutron star. Ultimately, depending on the progenitor mass, the remnant of the supernova will be either a neutron star (9) or a black hole. The process by which a black hole forms is known as a "failed supernova" (failed SN), and the details are described in Section 1.1.4.

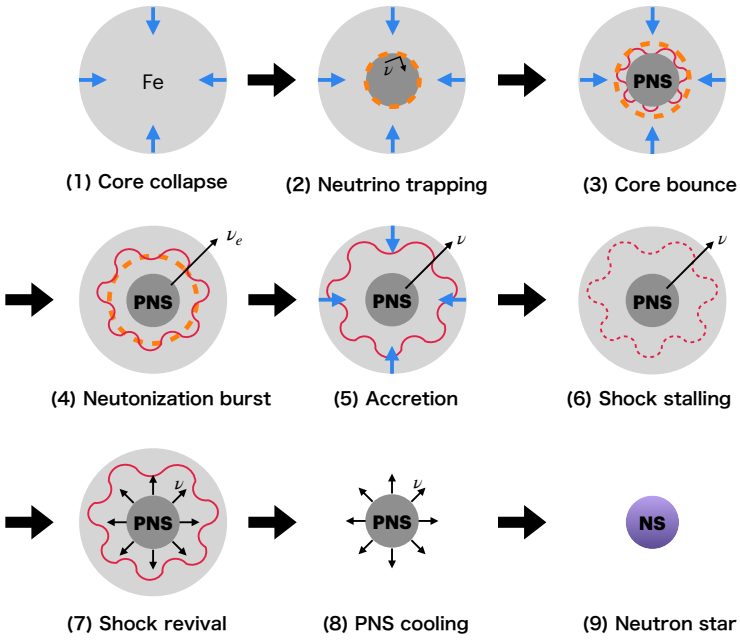

FIGURE 1.3: Schematic illustration of the core-collapse supernova explosion

As gravitational collapse proceeds, the central core becomes divided into two regions: an inner core that contracts subsonically (i.e., at speeds lower than the sound speed) and an outer core that undergoes supersonic free fall. As the density approaches the nuclear saturation density, the core matter transforms into high-temperature and high-density nuclear matter composed of protons and neutrons. When the density exceeds the nuclear density and reaches $\sim 10^{14}$ g cm^{-3}, the repulsive component of the nuclear force causes a rapid stiffening of the equation of state (EOS), halting the contraction. The inner core material then decelerates successively from the center outward, and the rebound of the halted material generates pressure perturbations that propagate outward as sound waves. Meanwhile, the outer core material continues to infall supersonically from above, and a shock wave forms at the interface between the infalling outer core and the decelerating inner core.

The inner core typically has a radius of $R \sim 10$ km and a mass of $M = 0.6$–$0.8\ M_\odot$. If the entire gravitational binding energy of the inner core were converted into the shock, the energy of the shock at its formation would be approximately

$$E_{\rm shock} = \frac{3}{5}\frac{GM^2}{R} \sim \mathcal{O}(10^{53})\ \text{erg}. \tag{1.3}$$

The time evolution of the core during the collapse and the formation of the shock wave is illustrated in Figure 1.4.

After the core bounce, a PNS is formed at the center of the collapsing star (Figure 1.3(3)). During the collapse phase, electron capture reactions on protons proceed efficiently, resulting in matter that is rich in neutrons. Nevertheless, a considerable fraction of protons and electrons still remains within the core.

The onset of collapse is governed by specific microphysical processes in the iron core, which are summarized below. The properties of the iron core are a key factor determining whether a massive star undergoes a successful explosion or collapses into a compact object. During the final stages of stellar evolution, iron is synthesized, and

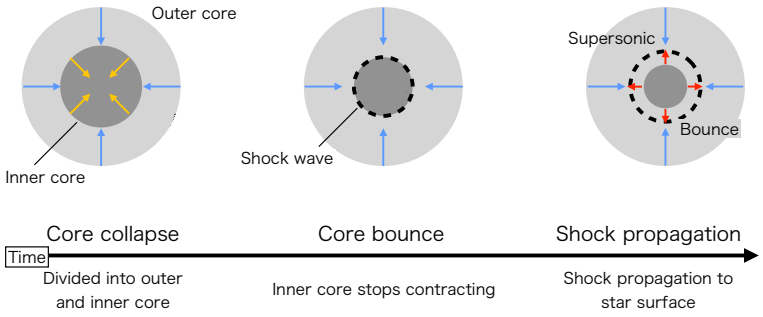

FIGURE 1.4: Example of the time evolution of the supernova core [1].

the core mass gradually increases. Although the final iron-core mass depends on the progenitor's evolution and on the adopted stellar-evolution model, it is typically on the order of $\sim 1.4 M_\odot$. The structure of the iron core is supported by the pressure of highly degenerate electrons, which results from the extremely high density. In the relativistic limit, the EOS of a degenerate electron gas yields a pressure proportional to the density to the power of 4/3. Solving the stellar structure under this EOS leads to the Chandrasekhar mass limit,

$$M_{\rm ch} = 1.457 \left(\frac{Y_e}{0.5} \right)^2 M_\odot, \tag{1.4}$$

where Y_e is the number of electrons per nucleon. In the case of ^{56}Fe, this ratio is $Z/A = 0.46$.

As the iron core approaches its limiting mass, various nuclear reactions occur in the interior. Among these, two processes accelerate rapidly and destabilize the core, triggering gravitational collapse: electron capture on nuclei and photodisintegration. The former occurs because the average energy of degenerate electrons increases with density, enabling weak-interaction reactions that convert nuclei into more neutron-rich species. For example,

$$\mathrm{e}^- + {}^{56}\mathrm{Fe} \rightarrow \nu_e + {}^{56}\mathrm{Mn}, \tag{1.5}$$

where an electron is absorbed and a neutrino escapes from the core. As a result, the number of electrons—which provide the electron degeneracy pressure supporting the star—decreases. The reduction in pressure leads to further compression, raising the electron Fermi energy and accelerating additional electron-capture reactions. This feedback process reduces the electron degeneracy pressure further and accelerates the collapse.

The second trigger of iron-core collapse is the photodisintegration of iron and other nuclei. At temperatures exceeding 0.5 MeV, the iron core does not consist of a single nuclear species such as ^{56}Fe; instead, it reaches nuclear statistical equilibrium (NSE), in which various nuclear species are populated according to chemical equilibrium conditions. Because weak and electromagnetic interaction timescales are sufficiently short, equilibrium is maintained among the relevant nuclear reactions. One example is the reaction in which iron is photodisintegrated into helium nuclei and neutrons:

$$\gamma + {}^{56}\mathrm{Fe} \rightarrow 13\,{}^4\mathrm{He} + 4\mathrm{n} - 125\ \mathrm{MeV}. \tag{1.6}$$

Forming iron from nucleons and α particles releases binding energy, whereas the reverse reaction is endothermic. Comparing the total rest masses on both sides shows

that the right-hand side exceeds the left by 125 MeV, indicating that the reaction requires energy input. During collapse, as the core compresses, part of the available energy is consumed by nuclear photodisintegration. Because this energy is diverted into breaking up heavy nuclei, the pressure does not increase sufficiently to halt contraction. Consequently, gravitational collapse continues to accelerate.

1.1.4 Failed supernovae

While Section 1.1.3 discussed the general picture of successful core-collapse supernovae (CCSNe) leading to neutron star formation, not all massive star collapses result in such explosions.

A failed SN refers to a stellar collapse that does not result in a successful explosion, but instead leads directly to the formation of a black hole. In such cases, the outgoing shock wave launched at core bounce fails to overcome the pressure of the infalling stellar envelope, and thus stalls before reaching the stellar surface. As a result, no bright optical transient is expected, and the entire star collapses almost silently into a black hole.

Theoretical studies have predicted that failed supernovae are accompanied by intense but short-lived neutrino emission lasting several seconds before the event horizon formation [e.g., 30, 3]. The total neutrino energy release is comparable to that of a successful CCSN ($\sim 10^{53}$ erg), but the emission timescale is shorter, and the spectrum tends to be hotter because of the rapid contraction of the PNS. Therefore, neutrinos provide the only observable signature of such events, making detectors like Super-Kamiokande (SK) uniquely suited to probe their occurrence in nearby galaxies. Identifying or constraining failed SN neutrino signals is also important for understanding the black hole formation rate and the fate of massive stars at the upper end of the initial mass function.

Massive stars with ZAMS mass[2] above approximately $9M_\odot$ show significant diversity in their pre-supernova structure. In particular, key properties such as the iron-core mass, envelope binding energy, and density profile are not determined by the ZAMS mass. As a result, the explodability of massive stars exhibits a non-monotonic dependence on the ZAMS mass.

Previous study [55] demonstrated that the core-collapse outcome is not uniquely determined by the progenitor mass; stars with similar masses can result in either successful explosions or direct black hole formation, depending on their internal structure. The compactness parameter,

$$\xi_{\mathrm{M}} = \frac{M/M_\odot}{R(M)/1000\ \mathrm{km}}, \tag{1.7}$$

has been widely used to quantify the pre-collapse density structure and to characterize the tendency for black hole formation. Core-collapse simulations reported in [55] indicate that progenitors with a compactness parameter of $\xi_{2.5} < 0.15$ lead exclusively to successful explosions, whereas models with $0.15 \leq \xi_{2.5} \leq 0.35$ can result in either explosions or black hole formation. Progenitors with $\xi_{2.5} > 0.35$ are predicted to collapse directly into black holes. Analysis by [56] suggests that a critical compactness threshold of $\xi_{2.5} \gtrsim 0.2$ is consistent with both the observed absence of red supergiant SN II progenitors above $\sim 16\ M_\odot$ [57] and the excess of the cosmic star formation rate relative to the observed CCSN rate [58]. However, while a general correlation

[2]ZAMS mass refers to the initial mass of a star at the onset of hydrogen burning in its core, marking the beginning of its main-sequence evolution.

exists—high compactness favors collapse into a black hole—the compactness alone cannot fully predict the explosion outcome. To address this limitation, Ertl et al. [59] proposed a two-parameter criterion that more reliably distinguishes between exploding and non-exploding progenitors. These parameters are defined at the mass coordinate where the dimensionless entropy per baryon $s = 4$:

$$M_4 \equiv \frac{m(s=4)}{M_\odot}, \tag{1.8}$$

$$\mu_4 \equiv \left.\frac{dm/M_\odot}{dr/1000\ \mathrm{km}}\right|_{s=4}. \tag{1.9}$$

Both quantities are derived directly from the pre-supernova density and entropy profiles. This (M_4, μ_4) criterion can successfully reproduce the explosion behavior in more than 97% of the investigated progenitor models, showing a closer connection to the physical conditions governing the neutrino-driven explosion mechanism than the compactness parameter alone. Figure 1.5 shows the remnant mass as a function of the progenitor's ZAMS mass, calculated by [2] using a neutrino-driven explosion model. This figure illustrates the non-monotonic behavior of explodability, with certain mass ranges leading to successful supernova explosions that form neutron stars (red lines), and others resulting in failed SN (black lines).

1.1.5 Fallback supernovae

A fallback supernova (fallback SN) represents an intermediate case between a successful explosion and a failed SN [60]. In this scenario, the core-collapse initiates a shock wave that successfully ejects part of the stellar envelope, but the explosion energy is insufficient to unbind all of the material. As a result, a fraction of the ejecta loses outward momentum and falls back onto the central compact remnant. If the accretion rate is large enough, the PNS can subsequently collapse into a black hole several seconds to minutes after the initial explosion.

This delayed black hole formation scenario—often referred to as a "fallback-induced" collapse—produces a distinct neutrino signal compared to both ordinary and failed SNe. The early phase resembles that of a successful explosion with a gradual decline in neutrino luminosity, followed by a sudden termination of the signal at the moment of black hole formation, as discussed in [61]. Such time evolution provides a characteristic signature that could be used to distinguish fallback events if detected in real time. Because of their intermediate nature, fallback supernovae play a key role in connecting ordinary core-collapse explosions with failed ones, and may contribute significantly to the population of black holes formed from relatively low-mass progenitors.

1.2 Supernova Neutrinos

1.2.1 Neutrino Emission from CCSNe

Neutrino emission characteristics

In the CCSN process, various types of neutrinos are emitted. An example of the time evolution of the neutrino emission and average energies is shown in Figure 1.6. Here, the electron neutrino is denoted by ν_e, the electron antineutrino by $\bar{\nu}_e$, and the muon

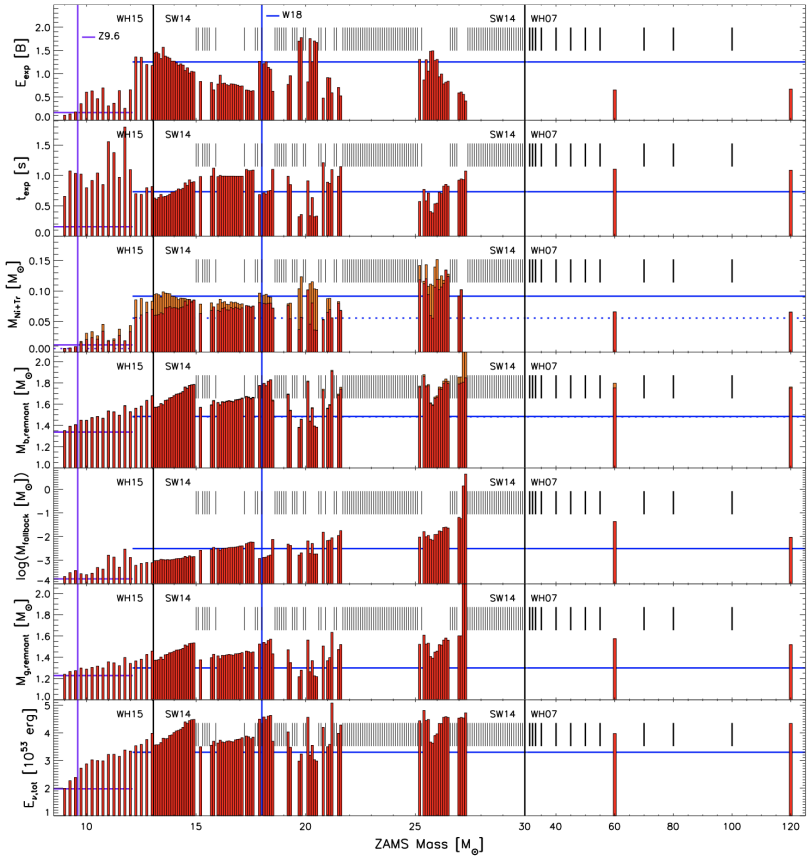

FIGURE 1.5: Summary of explosion and remnant properties obtained from all progenitor models calibrated from SN1987A observational data [2]. From top to bottom, the panels present: the final explosion energy E, in units of 10^{51} erg, the explosion onset time $t_{\rm exp}$, the ejected masses of ^{56}Ni (red) and tracer elements (orange), the baryonic mass of the compact remmnant with fallback mass indicated in orange, the fallback mass itself, the gravitational mass of the compact remnant, and the total radiated neutrino energy $E_{\nu,\rm tot}$. Vertical black lines separate the different progenitor groups included in the model set. Blue vertical lines mark the calibration models, with corresponding results shown as horizontal solid or dashed blue lines, representing Crab-like and SN 1987A-like progenitor properties, respectively.

and tau neutrinos collectively by ν_x[3]. The horizontal axis represents time with the origin defined at core bounce.

As shown, at $t \sim 0.03$ s, the neutronization burst (Figure 1.3(4)) appears as a peak in the electron neutrino luminosity curve. This arises from enhanced electron capture reactions as the shock propagates and dissociates nuclei, liberating protons that capture electrons. The phase from $t = 0.1$–0.3 s is referred to as the accretion phase, during which matter continues to fall onto the shock. In this stage, neutrinos of all flavors are emitted through processes such as positron capture on neutrons and e^-e^+ pair annihilation, resulting in neutrino luminosity curves that are nearly identical in shape. Subsequently, in the cooling phase of the PNS ($t \sim 20$ s), the neutrino luminosities decrease over time as the PNS cools. The following sections focus

[3]In the case of supernova neutrinos, ν_μ and ν_τ behave almost identically in their interactions; thus, they are commonly grouped together and denoted as ν_x.

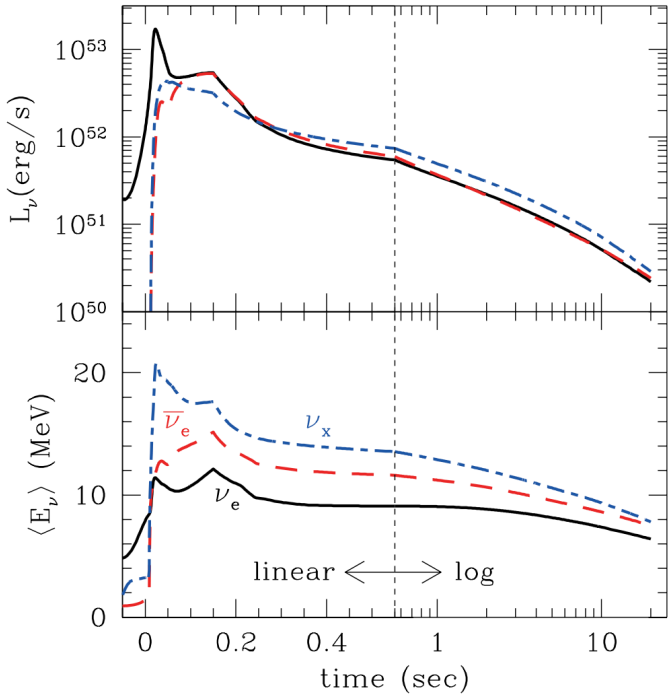

FIGURE 1.6: Time evolution of the luminosity (top) and average energy (bottom) of supernova neutrinos [3]. The horizontal axis represents the time measured from the core bounce. The black, red, and blue lines correspond to ν_e, $\bar{\nu}_e$, and ν_x, respectively.

specifically on the detailed characteristics of the neutrino emission that accompanies the explosion.

After the core bounce, the shock wave initially propagates outward while mass accretion onto the central region continues. During this accretion phase, the inner core with a radius of order 100 km contracts as it forms the central object. About one second after the bounce, the shock reaches the stellar surface and triggers the explosion, terminating further accretion and fixing the mass of the remnant. By this time, a PNS in quasi-hydrostatic equilibrium has been established (Figure 1.6). Inside this newly formed PNS, neutrinos are trapped within the dense and hot nuclear matter. They undergo frequent scattering, absorption, and emission processes, which exchange energy between matter and neutrinos and regulate the heating and cooling of the surrounding layers (Figure 1.7). These interactions maintain thermal coupling between neutrinos and matter until the local density decreases sufficiently for neutrinos to decouple at the neutrinosphere. Once decoupled, neutrinos gradually diffuse outward and escape the PNS. This diffusive emission continues for roughly 20 s (Figure 1.6). Over this cooling phase, the temperature of the entire PNS decreases, its density increases, and the star contracts into a compact neutron star with a radius of about 10 km. The time evolution of the neutrino luminosity and average energy directly reflects this thermal contraction and cooling of the PNS. During this phase, charged-current interactions,

$$\nu_e + n \to e^- + p, \tag{1.10}$$

$$\bar{\nu}_e + p \to e^+ + n, \tag{1.11}$$

transfer the neutrino energy, typically several tens of MeV, to nucleons and nuclei,

reflecting their thermal production in the hot and dense interior of the PNS. When these reactions occur, electrons or positrons are produced, and the transferred neutrino energy heats the material. This process is known as *neutrino heating*.

Conversely, when electrons or positrons are captured by nucleons,

$$e^- + p \rightarrow \nu_e + n, \tag{1.12}$$

$$e^+ + n \rightarrow \bar{\nu}_e + p, \tag{1.13}$$

A fraction of the matter energy is carried away by the emitted neutrinos. If these neutrinos escape from the star, the matter loses energy, and this process is called *neutrino cooling*. When heating and cooling are balanced, the local temperature of the material remains steady. As shown in Figure 1.7, neutrino emission dominates near the PNS surface, forming a cooling region. In contrast, outside this region, where neutrino absorption dominates, the matter is heated, its internal energy increases, and pressure rises. This *heating region*, located beneath the stalled or expanding shock wave, plays a key role in reviving the shock and driving the explosion. The mechanism in which trapped neutrinos heat the surrounding matter to power the explosion is known as the *neutrino-driven explosion mechanism*. Efficient absorption of neutrinos emitted from the cooling region into the heating region sustains high heating rates over several seconds, enhancing the likelihood of a successful explosion. These neutrinos are simultaneously responsible for the thermal evolution of the PNS, which cools into a neutron star, and the emitted flux constitutes the observable supernova neutrino signal.

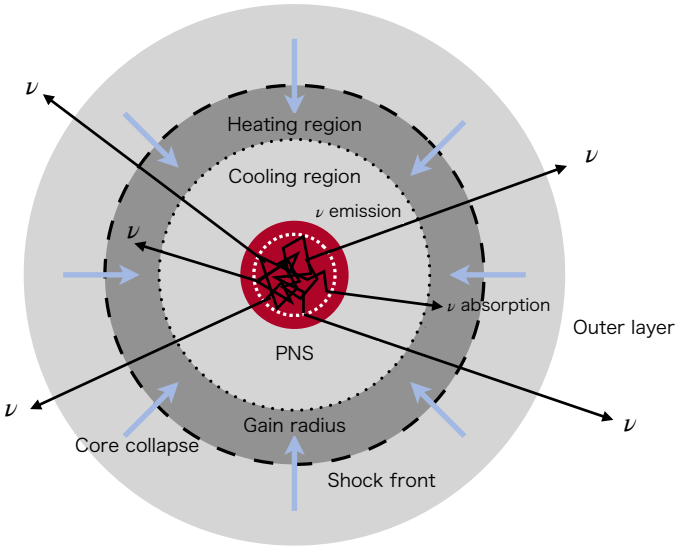

FIGURE 1.7: Schematic illustration of neutrino emission and absorption inside a core-collapse supernova [1]. While the outer core continues gravitational collapse, a PNS forms at the center. Neutrinos are trapped inside the PNS, where they undergo frequent scattering and absorption reactions. Near the surface of the PNS, neutrino emission dominates (cooling region), whereas in the layer between the surface and the shock front, neutrino absorption dominates (heating region). The boundary between these regions is called the gain radius.

As shown in Figure 1.6, during the cooling phase after ~ 1 s, both the neutrino luminosity and average energy decrease monotonically, reflecting the gradual cooling

of the PNS. Compared with the short-duration burst at core bounce, this phase lasts for over 10 s and dominates the total energy and number of emitted neutrinos. The events observed from SN 1987A, spread over $\sim$ 10 s, are interpreted as originating mainly from this cooling phase. The characteristics of the emitted neutrino spectra are determined by the detailed neutrino interaction processes involved.

The average neutrino energy depends on flavor, decreasing in the order of ν_x, $\bar{\nu}_e$, and ν_e (Figure 1.6). This hierarchy arises because the dominant interaction channels and reaction depths differ among flavors. For instance, ν_e are produced mainly through reactions involving electrons (Eq. (1.12)), which occur in relatively low-density outer regions, leading to lower average energies. In contrast, $\bar{\nu}_e$ originates from reactions involving positrons (Eq. (1.13)), which occur in hotter, denser inner layers, resulting in higher average energies. The ν_x interact only via neutral-current reactions, which take place in even deeper regions, thus yielding the highest average energies. Consequently, the radius of the neutrinosphere differs by flavor, with R_{ν_e} being the largest and R_{ν_x} the smallest (Figure 1.8). This energy hierarchy among neutrino species is an essential feature of supernova neutrino emission.

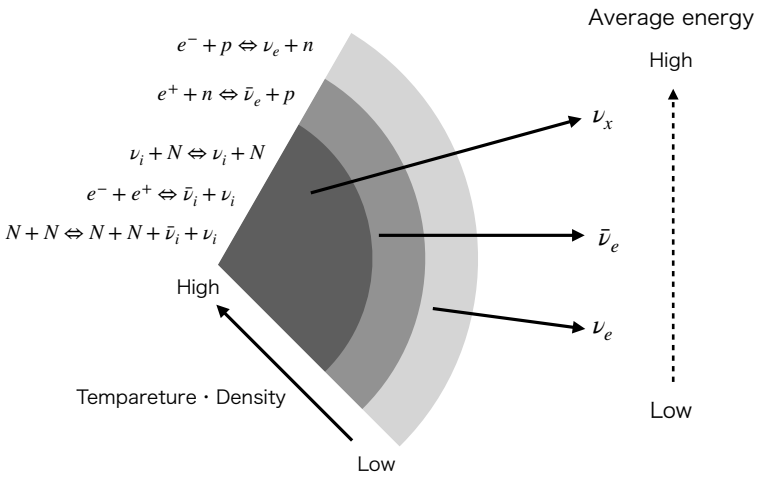

FIGURE 1.8: Flavor hierarchy of supernova neutrino energies [1]. Because the dominant reactions differ by flavor, their average energies vary accordingly. Here, N denotes a nucleus and ν_i represents any neutrino species.

As the cooling phase progresses, the difference in average energy between neutrino flavors gradually diminishes. This occurs because the PNS structure becomes simpler as it cools and contracts, reducing the separation of neutrino decoupling layers. In the late cooling phase, as density increases, the EOS of dense nuclear matter significantly affects the structure of the core (Section 1.4). Therefore, observation of supernova neutrinos, which carry information about these conditions, provides a crucial probe of the supernova core and the EOS of nuclear matter.

1.2.2 Neutrino Emission from Failed SNe

In this section, the characteristics of neutrino emission from failed SNe are described. The overview and physical picture of the failed SN are described in Section 1.1.4.

The neutrino emission from the failed SNe exhibits distinct temporal and spectral features. The luminosity and average energy increase steadily due to the continuous accretion of matter onto the PNS until the sudden cutoff at the time of black hole

formation. The emission duration is typically shorter than that of successful explosions, and the average neutrino energies are significantly higher. Figure 1.9 presents the time evolution of the neutrino luminosity and the rms energy, which characterizes the typical energy scale of the emitted neutrinos, for both an ordinary CCSN model ($13M_{\odot}$) and a failed supernova model ($40M_{\odot}$) [4]. In the ordinary SN case, the luminosity gradually declines as the accretion rate decreases and the core continues to deleptonize. In contrast, the luminosity in the failed SN model keeps rising up to the moment of black hole formation, reflecting the increasing mass accretion onto the PNS and the corresponding compression of the neutrino-emitting region. The luminosities of electron neutrinos and electron antineutrinos become nearly identical. This is because the electron degeneracy is largely lifted in most regions of the cooling layer, resulting in electrons and positrons being captured with similar chemical potentials. In the early phase after core bounce, the emission of electron-type neutrinos is dominated by rapid electron capture processes. As the collapse proceeds toward black hole formation, muon and tau neutrinos decouple from deeper and hotter regions of the PNS. As a result, the neutrino luminosity spectrum of muon and tau neutrinos is shifted toward higher than in the early phase.

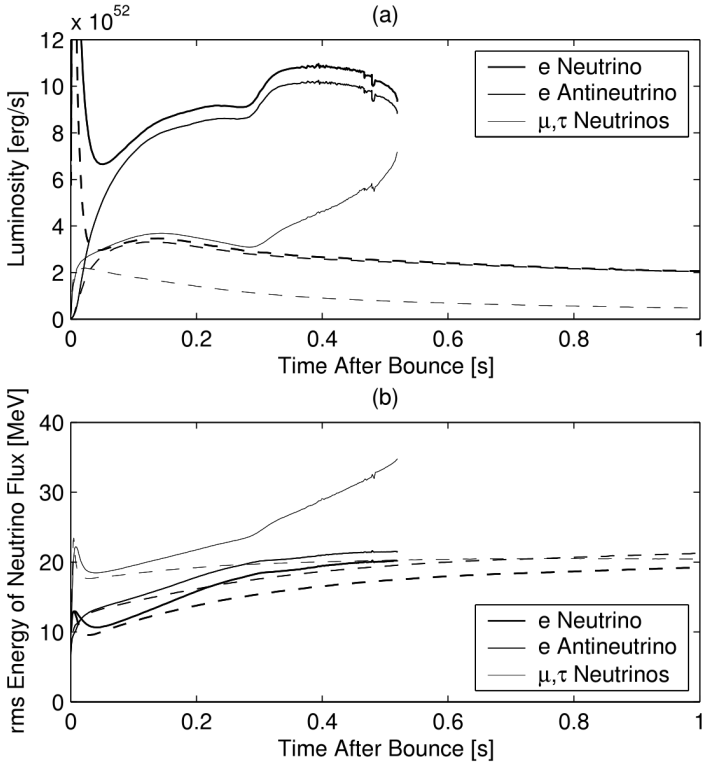

FIGURE 1.9: The time evolution of luminosity and rms energy [4]. The dashed line and thin like represent $13M_{\odot}$ ordinary SN model and $40M_{\odot}$ failed SN model, respectively.

1.2.3 Ordinary SN Neutrino Observation

Overall supernova neutrino observation

Figure 1.10 illustrates the distance scale relevant to supernova neutrino observations and the corresponding expected event rates. In the case of a galactic supernova

occurring within a few kpc, such as Betelgeuse at $\sim$ 200 pc or a typical event at $\sim$ 10 kpc, a large number of neutrino events are expected to be detected in current neutrino observatories such as SK. Such detections would provide crucial insights into the explosion mechanism, progenitor properties, and constraints on the nuclear EOS, as well as offering opportunities for multi-messenger observations with gravitational waves and electromagnetic signals. The details of nuclear EOS discrimination are described in Section 4.

For supernovae occurring in nearby galaxies such as the Large Magellanic Cloud ($\sim$ 50 kpc) or Andromeda Galaxy ($\sim$ 800 kpc), only a few neutrino events are expected per burst. Although the statistics are limited, such events can still provide information on possible diversity in explosion mechanisms and neutrino emission characteristics among different progenitor systems.

At extragalactic distances of the order of Mpc, individual supernovae become undetectable in neutrinos; however, the cumulative emission from all past CCSN events forms the diffuse supernova neutrino background (DSNB). The DSNB carries integrated information about the cosmic core-collapse rate, the neutrino spectra, and the population of supernova progenitors across cosmic history. This DSNB search in SK is described in Appendix B.1.

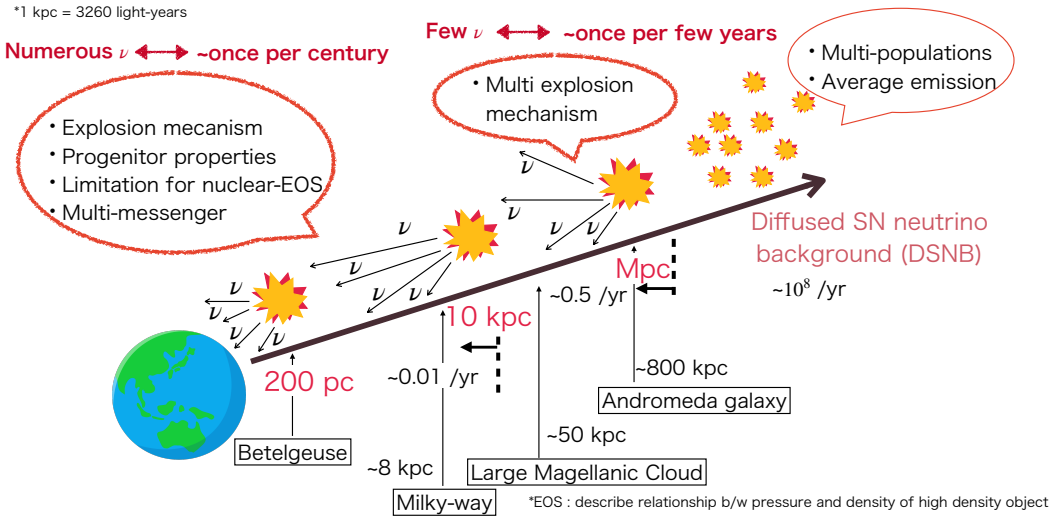

FIGURE 1.10: Distance scale relevant to supernova neutrino detection. Nearby Galactic events (within ~10 kpc) produce numerous neutrinos, enabling detailed studies of explosion mechanisms and nuclear EOS. At distances up to several hundred kiloparsecs, only a few events are expected, while beyond ~1 Mpc the cumulative emission forms the diffuse supernova neutrino background (DSNB).

Supernova neutrino observation from SN1987A

So far, the only supernova neutrinos ever observed are those from SN 1987A, which exploded in the Large Magellanic Cloud on February 23, 1987. At that time, three underground detectors–Kamiokande II in Japan [62], IMB in the United States [63], and Baksan in Russia [64]–successfully detected neutrino signals from the event. Figure 1.11 shows the distributions of the detected neutrino events in energy and time for the Kamiokande II and IMB detectors [5]. These observations were in good agreement

with the basic theoretical picture of CCSNe, and the total released energy was consistent with the expectation from gravitational binding energy (Eq. 1.2). However, due to the limited number of detected events, it was not possible to distinguish among different explosion models. Since then, many neutrino observatories, including SK as described in Chapter 2, have been preparing for the next galactic supernova explosion in order to further understand the explosion mechanism of CCSNe.

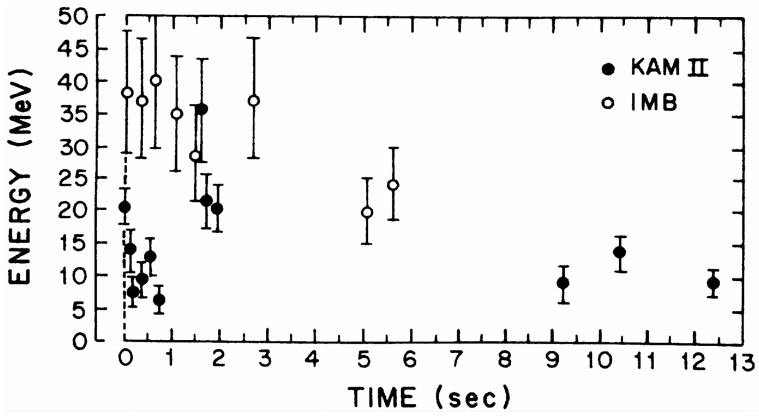

FIGURE 1.11: Time and energy distributions of neutrino events detected from SN 1987A by the Kamiokande II and IMB detectors [5].

1.3 Neutrino Oscillation inside Stellar Core

1.3.1 Neutrino oscillation in vacuum

In this section, I consider the case of two neutrino flavors, ν_e and ν_μ. These represent the flavor eigenstates of the neutrino, while the corresponding mass eigenstates, ν_1 and ν_2, can be expressed as orthogonal linear combinations of the flavor states as follows:

$$\begin{aligned} |\nu_1\rangle &= \cos\theta\,|\nu_\mu\rangle - \sin\theta\,|\nu_e\rangle\,, \\ |\nu_2\rangle &= \sin\theta\,|\nu_\mu\rangle + \cos\theta\,|\nu_e\rangle\,. \end{aligned} \tag{1.14}$$

According to the Schrödinger equation, each mass eigenstate evolves in time with a simple phase factor:

$$\begin{aligned} \nu_1(t) &= \nu_1(0)\,e^{-iE_1t/\hbar}, \\ \nu_2(t) &= \nu_2(0)\,e^{-iE_2t/\hbar}. \end{aligned} \tag{1.15}$$

As can be seen from these expressions, neutrino oscillation occurs as a result of the interference between the two eigenstates, in a manner analogous to coupled oscillators. A neutrino produced as ν_e can transform into ν_μ as it propagates, and the transition probability is given by

$$P_{\nu_e\to\nu_\mu} = \sin^2(2\theta)\,\sin^2\left[\frac{(m_2^2 - m_1^2)c^3t}{4\hbar E}\right], \tag{1.16}$$

as described in [65].

From this expression, it is evident that two parameters are necessary for neutrino oscillation to occur: a mixing angle (θ) and a nonzero mass difference between the

eigenstates. This is why the observation of neutrino oscillation implies that neutrinos must have nonzero mass. However, neutrino oscillation experiments are only sensitive to the mass-squared differences (Δm^2) between the eigenstates, and the absolute neutrino masses remain unknown. While the above discussion considers two neutrino flavors, there are in fact three neutrino flavors in nature. The two independent mass-squared differences are defined as

$$\begin{aligned} \Delta m^2_{21} &= m^2_2 - m^2_1, \\ \Delta m^2_{32} &= m^2_3 - m^2_2, \\ \Delta m^2_{31} &= m^2_3 - m^2_1. \end{aligned} \tag{1.17}$$

Experimental results indicate that one of these mass splittings is relatively small, while the other is comparatively large. The two close mass states are denoted as ν_1 and ν_2 ($m_2 > m_1$), and the third, more separated state is referred to as ν_3. Depending on the ordering of these masses, two possible hierarchies are considered: the *normal ordering*, in which ν_3 is heavier than ν_1 and ν_2, and the *inverted ordering*, in which ν_3 is lighter than the other two. At present, it is not yet experimentally established which of these two scenarios is realized in nature (see Figure 1.12).

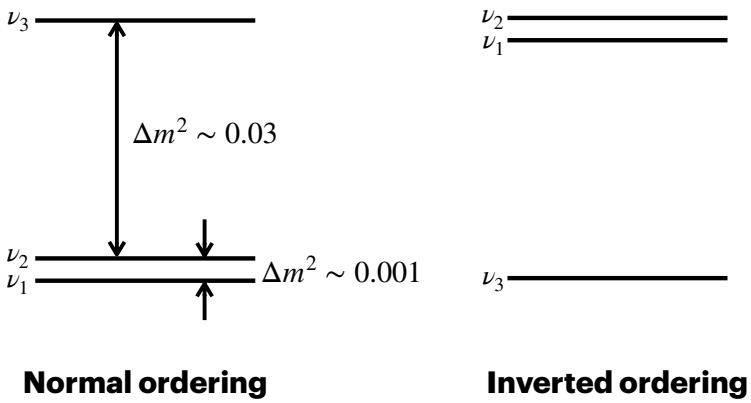

FIGURE 1.12: Schematic illustration of the neutrino mass spectra for the normal and inverted mass orderings.

Within the framework of the Standard Model, neutrinos are treated as massless particles. The observation of neutrino oscillations, however, has provided compelling evidence that neutrinos have a finite but extremely small mass. Neutrino oscillation is a quantum mechanical phenomenon in which a neutrino changes its flavor state while propagating through space.

1.3.2 Neutrino oscillation in matter

It is well known that neutrino oscillations in matter differ from those in vacuum. When neutrinos propagate through dense matter such as the interior of a star, the potential induced by electrons in the medium modifies the oscillation behavior. In particular, when this potential satisfies a resonance condition, the oscillation probability is dramatically enhanced, a phenomenon known as the Mikheyev–Smirnov–Wolfenstein (MSW) effect.

In matter, the transition primarily occurs at the resonance layer, where the density is approximately given by $(\rho_{\text{res}} - \Delta\rho_{\text{res}})/(\rho_{\text{res}} + \Delta\rho_{\text{res}})$. The resonance density ρ_{res} is

expressed as

$$\rho_{\rm res} \approx \frac{1}{2\sqrt{2}G_{\rm F}} \frac{\Delta m^2}{E} \frac{m_N}{Y_e} \cos 2\theta, \tag{1.18}$$

where $G_{\rm F}$ is the Fermi constant, m_N the nucleon mass, E the neutrino energy, and Y_e the electron fraction per baryon. For small vacuum mixing angles, the width of the resonance layer is approximately

$$2\Delta\rho_{\rm res} \approx 2\rho_{\rm res} \tan 2\theta. \tag{1.19}$$

Using Eq. (1.18), the resonance density can be estimated as

$$\rho_{\rm res} \sim 1.4 \times 10^{16}\ {\rm g\ cm^{-3}} \left(\frac{\Delta m^2}{1\ {\rm eV}^2}\right) \left(\frac{10\ {\rm MeV}}{E}\right) \left(\frac{0.5}{Y_e}\right) \cos 2\theta. \tag{1.20}$$

Figure 1.13 illustrates the level-crossing diagram for the case of two neutrino flavors. In a medium such as the solar interior, a single resonance layer exists as described by Eq. (1.18). An electron neutrino produced in the high-density region undergoes a flavor transition when passing through this resonance layer, reaching the surface at $\rho = 0$ [66].

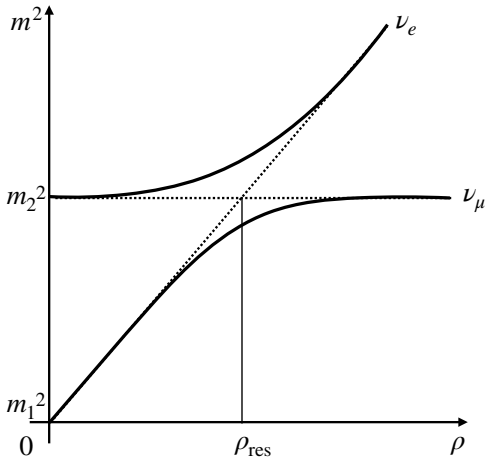

FIGURE 1.13: Schematic level-crossing diagram for two-flavor neutrino oscillations. The horizontal axis represents the electron density in matter, where $\rho = 0$ corresponds to the stellar surface.

The probability P_f that a neutrino initially in the ν_2 mass eigenstate transitions to the ν_1 eigenstate at the resonance layer can be expressed as a function of energy:

$$P_f = \exp\left[-\left(\frac{E_{\rm na}}{E}\right)^{2/3}\right], \tag{1.21}$$

where the characteristic energy including the matter effect, $E_{\rm na}$, is given by

$$E_{\rm na} = \left(\frac{\pi}{12}\right)^{3/2} \frac{\Delta m^2 \sin^3 2\theta}{\cos^2 2\theta} \left(\frac{2\sqrt{2}G_{\rm F}Y_e}{m_N}A\right)^{1/2}. \tag{1.22}$$

In Figure 1.13, P_f represents the probability that a ν_e transitions to the $|\nu_1>$ mass eigenstate at $\rho_{\rm res}$. If the transition is fully adiabatic, $P_f \sim 0$, and all ν_e convert into

ν_μ. Conversely, if the transition is non-adiabatic, $P_f \sim 1$, and no conversion occurs.

Observations of solar neutrinos have shown that the transition is nearly adiabatic, indicating that P_f is primarily determined by the vacuum mixing angle θ_{12}. Although the value of θ_{12} is periodically updated through solar neutrino measurements, I adopt $\sin^2\theta_{12} = 0.28$ in this study.

1.3.3 Neutrino oscillations in CCSNe

Once the neutrino masses and flavor mixings are understood, the role of neutrinos in the explosion mechanism of CCSNe can be clarified. In this section, I describe the effects of neutrino oscillations due to matter effects, as discussed in the previous section, on supernova neutrinos.

Because the interior of a supernova is extremely dense, there exist two resonance layers where the matter-induced oscillation effect occurs. The lower-density resonance, ${n_e}^L$, is determined by the mixing angle θ_{12}, while the higher-density resonance, ${n_e}^H$, is determined by θ_{13}. Neutrinos are initially produced in the deep core where $n_e \gg {n_e}^H$. At the time of production, the relationship between flavor and mass eigenstates is given by

$$\nu_{m_3} = \nu_e, \quad \nu_{m_2} = \nu_\tau, \quad \nu_{m_1} = \nu_\mu. \tag{1.23}$$

Accordingly, the initial neutrino fluxes are expressed as

$$\begin{aligned} N^{\rm gen}_{\nu_1} &= N^{\rm gen}_{\nu_x}, \\ N^{\rm gen}_{\nu_2} &= N^{\rm gen}_{\nu_x}, \\ N^{\rm gen}_{\nu_3} &= N^{\rm gen}_{\nu_e}, \end{aligned} \tag{1.24}$$

where ν_x denotes ν_μ or ν_τ.

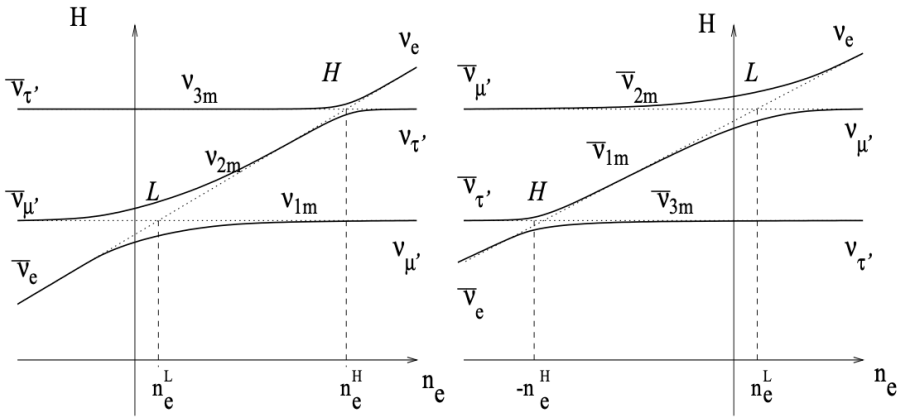

FIGURE 1.14: Schematic illustration of neutrino level crossing in a supernova [6]. The left (right) panel shows the case of Normal (Inverted) ordering. The solid curves represent the eigenvalues of the Hamiltonian H as a function of the electron number density, and the dashed lines correspond to the energies of ν_e, ν'_μ, and ν'_τ. The region $n_e < 0$ corresponds to antineutrinos.

Figure 1.14 illustrates the level-crossing diagrams for neutrinos inside a supernova. Neutrinos (or antineutrinos) are produced in the high-density region of the supernova core and propagate outward through matter with a gradually decreasing density. For neutrinos, the stellar interior corresponds to $n_e > 0$, while for antineutrinos, it corresponds to $n_e < 0$.

In the case of Normal ordering (left panel of Figure 1.14), neutrinos pass through two resonance layers before reaching the stellar surface and are affected by oscillations in both regions. Antineutrinos, however, experience only the lower resonance ${n_e}^L$ and are unaffected by the higher resonance ${n_e}^H$. In contrast, for Inverted ordering (right panel of Figure 1.14), antineutrinos experience both ${n_e}^L$ and ${n_e}^H$ resonances, whereas neutrinos experience oscillations only at ${n_e}^L$.

Let P_H denote the transition probability of $\nu_3 \to \nu_2$ at ${n_e}^H$, and P_L that of $\nu_2 \to \nu_1$ at ${n_e}^L$. Then, the flux of ν_e produced at the core that becomes ν_1 at the stellar surface is $P_H P_L N^{\rm gen}_{\nu_e}$. Similarly, the fluxes of ν_μ and ν_τ that become ν_1 at the surface are $(1-P_L)N^{\rm gen}_{\nu_x}$ and $P_L(1-P_H)N^{\rm gen}_{\nu_x}$, respectively. Thus, the total ν_1 flux at the surface is

$$N^{\rm sur}_{\nu_1} = P_H P_L N^{\rm gen}_{\nu_e} + (1 - P_H P_L) N^{\rm gen}_{\nu_x}. \tag{1.25}$$

By applying the same argument to ν_2 and ν_3, the surface fluxes are

$$\begin{aligned} N^{\rm sur}_{\nu_2} &= (P_H - P_H P_L) N^{\rm gen}_{\nu_e} + (1 - P_H + P_H P_L) N^{\rm gen}_{\nu_x}, \\ N^{\rm sur}_{\nu_3} &= (1 - P_H) N^{\rm gen}_{\nu_e} + P_H N^{\rm gen}_{\nu_x}. \end{aligned} \tag{1.26}$$

Equations (1.25) and (1.26) can be written in a unified form as

$$N^{\rm sur}_{\nu_i} = a_i N^{\rm gen}_{\nu_e} + (1 - a_i) N^{\rm gen}_{\nu_x}, \tag{1.27}$$

where

$$a_1 = P_H P_L, \quad a_2 = P_H(1 - P_L), \quad a_3 = 1 - P_H. \tag{1.28}$$

Using Eq. (1.27), the ν_e flux at the stellar surface is expressed as

$$N^{\rm sur}_{\nu_e} = \sum_i |U_{1i}|^2 N^{\rm sur}_{\nu_i} = N^{\rm gen}_{\nu_e} \sum_i |U_{1i}|^2 a_i + N^{\rm gen}_{\nu_x} \Big(1 - \sum_i |U_{1i}|^2 a_i\Big), \tag{1.29}$$

where U_{ij} denotes the elements of the neutrino mixing matrix. The coefficient

$$\begin{aligned} p &\equiv \sum_i |U_{1i}|^2 a_i \\ &= |U_{11}|^2 P_H P_L + |U_{12}|^2 (P_H - P_H P_L) + |U_{13}|^2 (1 - P_H) \end{aligned} \tag{1.30}$$

represents the survival probability that a ν_e produced at the core remains ν_e at the surface. The total generated flux of ν_e, ν_μ, and ν_τ is $N^{\rm gen}_{\nu_e} + 2N^{\rm gen}_{\nu_x}$, and the combined flux of ν_μ and ν_τ at the surface is therefore

$$N^{\rm sur}_{\nu_\mu} + N^{\rm sur}_{\nu_\tau} = (1 - p) N^{\rm gen}_{\nu_e} + (1 + p) N^{\rm gen}_{\nu_x}. \tag{1.31}$$

The transition probabilities at ${n_e}^H$ and ${n_e}^L$ are determined by the mixing angles θ_{13} and θ_{12}, respectively. As described above, θ_{12} is constrained by solar neutrino observations, whereas θ_{13} is sufficiently large that the transition at ρ_H is adiabatic, allowing the approximation $P_H \sim 0$.

Taking these into account, the neutrino fluxes at the supernova surface used in this study are expressed as follows. For the Normal ordering case:

$$\begin{aligned} N^{\rm sur}_{\nu_e} &= N^{\rm gen}_{\nu_x}, \\ N^{\rm sur}_{\nu_x} &= N^{\rm gen}_{\nu_e} + N^{\rm gen}_{\nu_x}, \\ N^{\rm sur}_{\bar{\nu}_e} &= N^{\rm gen}_{\bar{\nu}_e} \cos^2\theta_{12} + N^{\rm gen}_{\bar{\nu}_x} \sin^2\theta_{12}, \\ N^{\rm sur}_{\bar{\nu}_x} &= N^{\rm gen}_{\bar{\nu}_e} \sin^2\theta_{12} + N^{\rm gen}_{\bar{\nu}_x} (1 + \cos^2\theta_{12}). \end{aligned} \tag{1.32}$$

For the Inverted ordering case:

$$\begin{aligned} N_{\nu_e}^{\rm sur} &= N_{\nu_e}^{\rm gen}\sin^2\theta_{12} + N_{\nu_x}^{\rm gen}\cos^2\theta_{12}, \\ N_{\nu_x}^{\rm sur} &= N_{\nu_e}^{\rm gen}\cos^2\theta_{12} + N_{\nu_x}^{\rm gen}(1+\sin^2\theta_{12}), \\ N_{\bar{\nu}_e}^{\rm sur} &= N_{\bar{\nu}_x}^{\rm gen}, \\ N_{\bar{\nu}_x}^{\rm sur} &= N_{\bar{\nu}_e}^{\rm gen} + N_{\bar{\nu}_x}^{\rm gen}. \end{aligned} \tag{1.33}$$

The difference is that, in the Normal ordering case, all ν_e produced in the core convert to ν_x at the stellar surface, while in the Inverted ordering case, all $\bar{\nu}_e$ convert to $\bar{\nu}_x$.

1.4 Equation of State of Nuclear Matter in Supernova Cores

Neutron stars are compact objects with mean densities exceeding nuclear saturation density. To understand matter in such extreme conditions, it is necessary to investigate the EOS of dense nuclear matter. The structure of high-density nuclear matter can be probed through observational data of neutron stars. Among the fundamental quantities obtained from such observations is the relation between the mass and radius (M–R relation) of a neutron star. This structure can be derived by solving the Tolman–Oppenheimer–Volkoff (TOV) equation, which follows from Einstein's field equations of general relativity for a spherically symmetric distribution of matter:

$$\frac{dP(r)}{dr} = -\frac{G\rho(r)M(r)}{r^2}\left\{1+\frac{P(r)}{\rho(r)c^2}\right\}\left\{1+\frac{4\pi P(r)r^3}{M(r)c^2}\right\}\left\{1-\frac{2GM(r)}{rc^2}\right\}^{-1}, \tag{1.34}$$

where $P(r)$ is the pressure, $\rho(r)$ is the density, and $M(r)$ is the enclosed mass at radius r. G denotes the gravitational constant and c the speed of light. The terms in the curly brackets on the right-hand side represent general relativistic corrections, which account for the contribution of pressure to the total energy (mass) and the curvature of spacetime that enhances the gravitational potential.

To solve this equation, one must determine the three variables $P(r)$, $\rho(r)$, and $M(r)$. Here, $M(r)$, often referred to as the mass coordinate, expresses the enclosed mass as a function of radius and is defined as

$$M(r) = \int_0^r 4\pi r'^2 \rho(r')\, dr'. \tag{1.35}$$

For a star with radius R, $M(R)$ corresponds to its total mass. By combining Eq. (1.34) with the EOS that relates $P(r)$ and $\rho(r)$, the internal structure of the neutron star can be obtained [7].

Figure 1.15 shows the mass–radius (M–R) relation of neutron stars. In actual calculations of neutron star structure, the central density n_c is first set at $r = 0$. Using the EOS, the corresponding pressure P and density ρ for the given n_c are obtained. With these initial conditions and the EOS $P(\rho)$, Eqs. (1.34) and (1.35) are numerically integrated outward until the pressure drops to zero. The point where the pressure becomes $P(r = R) = 0$ defines the stellar radius R, and the neutron star mass is then given by $M(r = R)$.

Repeating this procedure for various values of center density (n_c) yields the M–R curve. The M–R relation corresponds uniquely to a given EOS, meaning that, in principle, the EOS of dense matter can be directly constrained from observations.

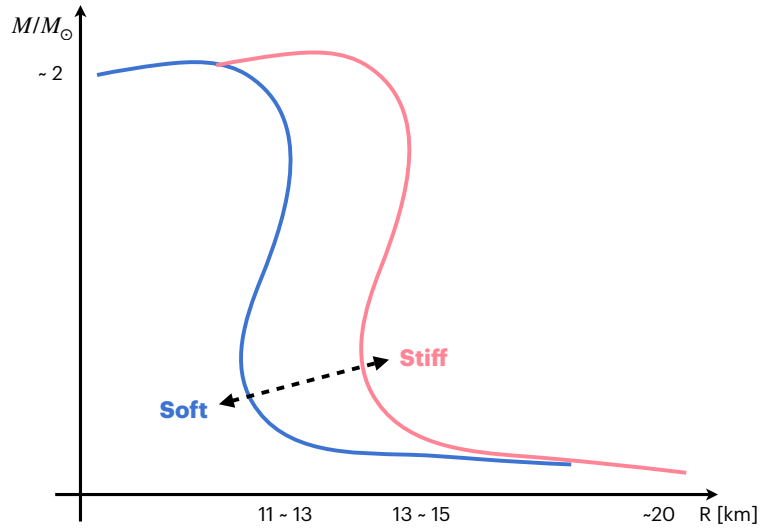

FIGURE 1.15: Schematic illustration of the mass–radius (M–R) relation for neutron stars. For small M, neutron stars consist of relatively loosely bound matter and therefore have large radii. When the central density reaches $n_c = 1$–$2n_0$, dilute matter becomes highly compressed. The rising part of the curve indicates that the contraction of matter halts once the radius R decreases below a certain value.

The difference in radius for the same stellar mass reflects the stiffness of the matter composing the neutron star: a larger radius implies a stiffer EOS, while a smaller radius corresponds to a softer EOS. Accordingly, EOSs that predict smaller (larger) radii for a given mass are referred to as soft (stiff) equations of state.

The EOS characterizes nuclear matter through the relation between pressure and density. It is often illustrated by the energy per nucleon as a function of the baryon number density for symmetric nuclear matter and pure neutron matter. At the same density, neutron matter has a higher energy than symmetric nuclear matter. The density at which symmetric nuclear matter reaches the minimum energy per nucleon is referred to as the nuclear saturation density, n_0. The energy difference between neutron matter and symmetric nuclear matter defines the symmetry energy, whose value at n_0 is denoted by S_0. The curvature of the energy around n_0 is characterized by the incompressibility parameter K. The general example of the EOS describing the relation between $P(r)$ and $\rho(r)$ discussed above is shown in Figure 1.16. This figure shows the relation between the energy per nucleon and the baryon number density for nuclear matter composed solely of neutrons (neutron matter) and for nuclear matter containing equal numbers of protons and neutrons (symmetric nuclear matter). Neutron matter has a higher energy than symmetric nuclear matter at the same density. The density at which symmetric nuclear matter exhibits a minimum in the energy per nucleon is called the nuclear saturation density, n_0. The energy difference between neutron matter and symmetric nuclear matter is called the symmetry energy. In particular, the symmetry energy at n_0, denoted as S_0, and the curvature of symmetric nuclear matter near n_0, represented by the incompressibility K, are important parameters that characterize the EOS.

To understand the internal structure of dense astrophysical objects, such as the cores of CCSNe, and to clarify the explosion mechanism, various theoretical calculations have been carried out to construct different EOS models. By determining the neutron star structure from these EOSs and comparing the results with observational

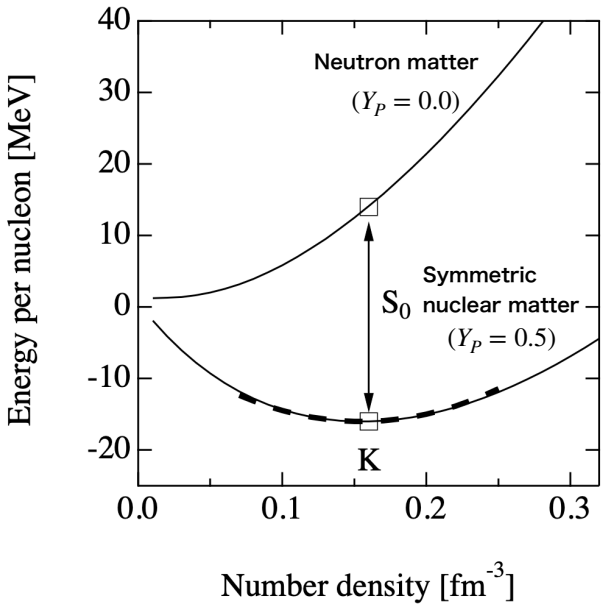

FIGURE 1.16: Examples of equations of state for symmetric nuclear matter and pure neutron matter [7, 1]. The energy per nucleon is plotted as a function of the baryon number density.

constraints, I can gain insights into the properties of dense matter and the mechanisms of supernova explosions. Since the neutrino light curves from supernovae also depend on the EOS, observations of supernova neutrinos can provide additional constraints on the EOS.

The stiffness and composition of an EOS are reflected in the predicted mass and radius of a neutron star. Therefore, precise observational data can strongly constrain viable EOS models. In particular, the maximum observed mass of neutron stars provides a stringent lower limit on the stiffness of the EOS. Recent observations of massive neutron stars, with measured masses of $1.97 \pm 0.04\, M_\odot$ [67] and $2.01 \pm 0.04\, M_\odot$ [68], indicate that a realistic EOS must be able to support at least a $2\, M_\odot$ neutron star. This requirement has led to the development of EOS models that satisfy these constraints and can be applied to supernova simulations.

Among the most representative models are the Shen EOS [69, 70] and the Lattimer & Swesty EOS [71]. Although these models do not necessarily reproduce all the latest observational constraints, they have been widely used in core-collapse simulations and exhibit clear differences in their treatment of symmetry energy. A more recent model, the Togashi EOS [72], has also been developed to better match observational data while maintaining consistency with nuclear physics experiments. The major differences among the EOS models arise from how they describe **uniform nuclear matter**. Uniform nuclear matter refers to the high-temperature and high-density region in the core of a PNS, where nucleons are uniformly distributed at densities exceeding the nuclear saturation density. In constructing an EOS, each model first assumes a theoretical framework to describe the thermodynamic behavior of such uniform nuclear matter. The properties of **non-uniform nuclear matter**, which appears in the outer region of the PNS where both free nucleons and nuclei are present, are then derived by applying suitable approximations based on the underlying model of uniform nuclear matter. The main characteristics of the four representative EOS models are summarized below.

- **Shen EOS:** based on relativistic mean-field (RMF) theory.
- **Lattimer & Swesty EOS:** a liquid-drop model improved with realistic nuclear interactions.
- **Togashi EOS:** a more recent model consistent with nuclear experiments and astrophysical observations.
- **Furusawa-Togashi EOS:** a extend version of Togashi EOS.

1.4.1 Shen EOS

In the Shen EOS model, uniform nuclear matter is described based on the *relativistic mean-field* (RMF) theory. This theory treats the Lagrangian composed of nucleons and meson fields, where the meson fields are replaced by their mean-field values determined by the baryon density. The energy states of nucleons are then obtained by solving the Dirac equation that includes the contribution of these mean-field potentials.

In the RMF framework, the nucleons in stationary nuclei or nuclear matter are described by spinor fields Φ_i that satisfy the Dirac equation for relativistic fermions:

$$[-i\boldsymbol{\alpha}\cdot\nabla+\beta M^*+U_V]\Phi_i=\epsilon_i\Phi_i, \tag{1.36}$$

where $\boldsymbol{\alpha}$ and β are Dirac matrices. The nucleon mass M is modified by the scalar potential U_s, leading to the effective mass

$$M^*=M+U_s=M+g_\sigma\sigma, \tag{1.37}$$

and the nucleons move under the vector potential

$$U_V=g_\omega\omega+g_\rho\tau_3\rho. \tag{1.38}$$

Here, g_ω and g_ρ represent the coupling constants between nucleons and the ω and ρ mesons. In the description of nuclei, an additional electromagnetic field representing the Coulomb interaction is included. However, since the current discussion focuses on nuclear matter, the electromagnetic contribution is neglected.

For *non-uniform nuclear matter*, which consists of nuclei and surrounding nucleon gas, the density distribution is assumed using the *Thomas–Fermi approximation*, varying parameters such as the central density and nuclear radius. The corresponding energy is calculated from the uniform matter described by the RMF theory, and the parameters (e.g., central density and radius) are determined by minimizing the total energy.

1.4.2 Lattimer & Swesty EOS

The Lattimer & Swesty (LS) EOS describes uniform nuclear matter using a more realistic formulation of the simplified model. The free energy density is expressed as

$$f_H(n,T,Y_p)=\varepsilon(n,T,Y_p)-Ts(n,T,Y_p), \tag{1.39}$$

where, in addition to the number density n and temperature T, the proton fraction per baryon $Y_p(=1-Y_n)$ is treated as an independent variable. The internal energy

density ε and entropy density s are given by

$$\varepsilon(n,T,Y_p) = \sum_t \frac{\tau_t}{2m_t^*} + [c_1 + 4c_2 Y_p(1-Y_p)]n^2 + c_3 n^{1+d} - Y_p n\Delta, \tag{1.40}$$

$$s(n,T,Y_p) = \sum_t \left(\frac{5}{3}\frac{\tau_t}{2m_t^*} - n_t\eta_t\right), \tag{1.41}$$

where t denotes the nucleon species (proton or neutron). The quantity m_t^* represents the *effective mass*, and $\tau_t/2m_t^*$ corresponds to the kinetic energy density of nucleon t. The term $\Delta = m_n - m_p$ denotes the neutron–proton mass difference, and η_t is defined as $\eta_t = (\mu_t - U_t)/k_B T$, with μ_t the chemical potential and $U_t \equiv \delta_\varepsilon/\delta_{n_t}$ the potential energy. The parameters c_1, c_2, c_3, and d are constants determined such that the model reproduces, as accurately as possible, the experimentally known properties of *symmetric nuclear matter* ($Y_p = 0.5$) at zero temperature, including the *saturation density*, *binding energy*, *incompressibility*, and *symmetry energy*. For *non-uniform nuclear matter*, a *liquid-drop model* is adopted. Similar to the Shen EOS, the model parameters are optimized to minimize the free energy (Eq. 1.40), and the thermodynamic quantities are then computed. Publicly available LS EOS tables correspond to incompressibility parameters $K = 375$, 220, and 180 MeV. In this study, the model with $K = 220$ MeV, referred to as LS220 EOS, is employed.

1.4.3 Togashi EOS

The Togashi EOS describes uniform nuclear matter based on a microscopic many-body theory of nucleons derived from realistic nucleon–nucleon interactions constrained by nucleon scattering data. At zero temperature, the Hamiltonian H of uniform nuclear matter is expressed as the sum of two-body and three-body interaction terms, H_2 and H_3, respectively:

$$\begin{aligned} H &= H_2 + H_3 \\ &= -\sum_{i=1}^{N} \frac{\hbar^2}{2m}\nabla_i^2 + \sum_{i<j}^{N} V_{ij} + \sum_{i<j<k}^{N} V_{ijk}, \end{aligned} \tag{1.42}$$

where m denotes the neutron rest mass, while V_{ij} and V_{ijk} represent the two-body and three-body potential energies, respectively. The term V_{ij} corresponds to the potential energy between the nucleon pair (i,j). Using this Hamiltonian, the EOS for uniform nuclear matter is determined by extending the variational method originally proposed by *Schmidt* and *Pandharipande* to finite temperature [24].

For *non-uniform nuclear matter*, the model adopts the *Thomas–Fermi approximation*, similar to the Shen EOS, to describe nuclei embedded in a nucleon gas. Although the same approximation method is used, the underlying nuclear interaction model differs; therefore, the types of nuclei that form in non-uniform matter vary between the Togashi and Shen EOS models.

Figure 1.17 compares the EOS for the Shen, Lattimer & Swesty, and Togashi models. Among the three models, the Shen EOS exhibits the steepest increase in energy with nucleon density for neutron matter, while the Togashi EOS shows the weakest dependence. The symmetry energy at the saturation density n_0 for the Shen, LS220, and Togashi EOSs is $S_0 = 36.9$ MeV, 29.3 MeV, and 29.1 MeV, respectively. The properties of nuclei formed in non-uniform nuclear matter mainly depend on the symmetry energy at low densities. A larger symmetry energy leads to a higher

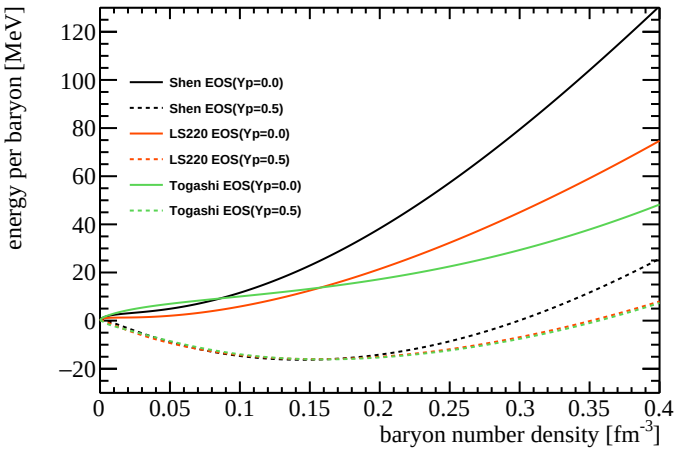

FIGURE 1.17: Comparison of the three EOS models. Black, red, and green lines represent the Shen EOS, Lattimer & Swesty EOS, and Togashi EOS, respectively. Solid lines correspond to neutron matter, while dashed lines correspond to symmetric nuclear matter. The Lattimer & Swesty EOS with incompressibility $K = 220$ MeV is denoted as LS220 EOS.

proton fraction, which enhances the formation of heavy nuclei. Because the Togashi EOS predicts relatively large symmetry energy at low densities, it tends to produce a greater abundance of heavy nuclei near the surface region of the PNS.

1.4.4 Furusawa-Togashi EOS

The Furusawa-Togashi EOS is an extended version of the Togashi EOS. The phase diagram of nuclear matter is broadly divided into a uniform phase and a non-uniform phase. While uniform nuclear matter consists mainly of free nucleons and electrons, with some light nuclei potentially included, non-uniform nuclear matter is characterized by the formation of heavy nuclei at lower densities and temperatures. The Furusawa-Togashi EOS directly utilizes the uniform matter by [72], as in the Togashi EOS. However, they differ in their descriptions of non-uniform matter. In the Togashi EOS, the Thomas-Fermi approximation is adopted to describe the structure of non-uniform nuclear matter, assuming a single representative species of nuclei. In contrast, the Furusawa-Togashi EOS models non-uniform matter as a mixture of multiple nuclear species, assuming nuclear statistical equilibrium.

The difference between the Togashi EOS and the Furusawa-Togashi EOS and its impacts on the PNS cooling have already been investigated in [73]. That result indicates the heavy nuclei of the Furusawa-Togashi EOS smaller mass numbers and represent a smaller fraction of the matter than those of the Togashi EOS in the surface region of the PNS. Since heavy nuclei have a large cross section for coherent scattering with neutrinos, which is proportional to the square of the mass number, the neutrino opacity is larger and the outer layer of PNS gets hotter for an EOS with larger mass number nuclei [74]. Therefore, PNS cooling with the Furusawa-Togashi EOS leads to neutrino emission with a lower average energy and a shorter duration compared to the Togashi EOS.

In this paper, PNS cooling with the Furusawa-Togashi EOS is computed for the same PNS mass models in [20]. For this purpose, the initial conditions are set identical to those of the Togashi EOS models with the same M_b and $M_{\rm ZAMS}$. This is justified by the fact that initially the PNS is composed of uniform nuclear matter, for which the Furusawa-Togashi EOS is identical to the Togashi EOS [73]. The $\bar{\nu}_e$ luminosity and average energy of the PNS cooling models is shown in Figure 1.18. The left panel focuses on the dependence on the EOS and $M_{\rm ZAMS}$ for models with $M_b = 1.62 M_\odot$. When models with $M_{\rm ZAMS} = 15 M_\odot$ and $40 M_\odot$ are compared, the difference in the initial condition is found to have only a minor impact on the neutrino signal, as reported in [21]. As for the EOS dependence, PNS models with the Shen EOS have a shorter timescale than those with other EOSs. This is because the Shen EOS results in a larger neutron star radius, and less compact PNS configurations lead to more rapid cooling. Since the Togashi EOS and the Furusawa-Togashi EOS share the high-density region, which primarily determines the neutron star radius, their PNS models exhibit a similar neutrino light curve during the Kelvin-Helmholtz cooling phase [75, 76], which corresponds to the period until the $\bar{\nu}_e$ luminosity drops to approximately 10^{50} erg s^{-1}.

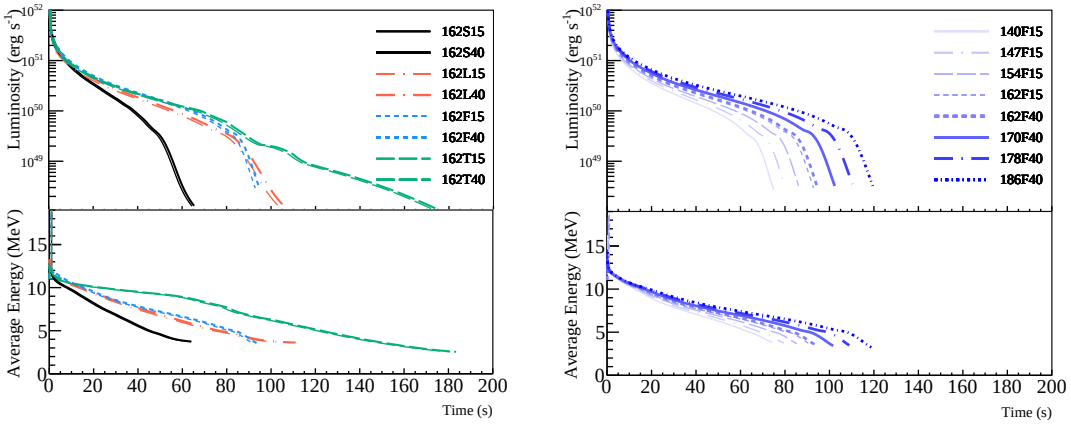

FIGURE 1.18: Luminosity (upper) and average energy (lower) of $\bar{\nu}_e$ emitted during proto-neutron-star (PNS) cooling as a function of time after the bounce. The left panel shows PNS models with a baryon mass of $M_b = 1.62 M_\odot$, where thin and thick lines correspond to models with $M_{\rm ZAMS} = 15 M_\odot$ and $40 M_\odot$, respectively, and solid (black), dashed (green), dotted-dashed (red), and dotted (blue) lines correspond to models with the Shen EOS, the Togashi EOS, the LS220 EOS, and the Furusawa–Togashi EOS, respectively. The right panel shows models with the Furusawa–Togashi EOS, where the lines correspond, from bottom to top, to $(M_b, M_{\rm ZAMS}) = (1.40 M_\odot, 15 M_\odot)$, $(1.47 M_\odot, 15 M_\odot)$, $(1.54 M_\odot, 15 M_\odot)$, $(1.62 M_\odot, 15 M_\odot)$, $(1.62 M_\odot, 40 M_\odot)$, $(1.70 M_\odot, 40 M_\odot)$, $(1.78 M_\odot, 40 M_\odot)$, and $(1.86 M_\odot, 40 M_\odot)$.

1.5 Supernova Survey with Telescopes

1.5.1 Supernova observations with optical telescopes

Supernova observations play a crucial role in astrophysics for several reasons. Type Ia supernovae serve as distance indicators for cosmology. CCSNe provide crucial insights not only into the explosion mechanisms of massive stars but also into the synthesis and

dispersal of heavy elements that enrich the interstellar medium and influence galactic chemical evolution. Optical and near-infrared observations are particularly important for tracing the light curves and spectra of supernovae, enabling the determination of explosion parameters such as energy, ejecta mass, and ^{56}Ni production.

1.5.2 Survey strategies and observational parameters

Modern supernova surveys employ wide-field telescopes that repeatedly scan large areas of the sky in a time-domain approach known as cadence observation. This strategy enables the detection of transient events such as supernovae shortly after explosion, allowing detailed follow-up observations. Key observational parameters include:

- **Survey area:** The choice of sky coverage and revisit frequency depends on the scientific goals, such as early discovery or volume completeness.
- **Photometric bands and exposure time:** Surveys typically employ multiple optical bands and optimized exposure times to balance depth and coverage.
- **Limiting magnitude and detection depth:** The limiting magnitude m_V (apparent magnitude in the V band) determines the volume of the survey and the distance up to which supernovae can be detected. For example, a limit of $m_V \sim 18$ corresponds to nearby events ($\lesssim 100$ Mpc), while deeper surveys ($m_V > 22$) can probe cosmological distances.

Detected candidates are typically identified via image subtraction techniques and then confirmed through spectroscopic or photometric classification.

1.5.3 Major optical and near-infrared surveys

Several wide-field time-domain surveys have been conducted or are currently in operation. Representative optical and near-infrared projects are summarized below.

ASAS-SN (All-Sky Automated Survey for SuperNovae): ASAS-SN monitors the entire sky on a nightly basis with a limiting magnitude of $m_V \sim 18$ mag, efficiently detecting bright, nearby supernovae within $\lesssim 100$ Mpc. It provides an unbiased census of bright transients and serves as an early alert system for follow-up campaigns [77].

Zwicky Transient Facility (ZTF): ZTF operates on the 48-inch Samuel Oschin Schmidt Telescope at Palomar Observatory with a field of view of 47 deg^2. It surveys the sky every 2–3 days, enabling large-scale statistical studies of Type Ia supernovae and the discovery of rare or fast-evolving transients [78].

ATLAS (Asteroid Terrestrial-impact Last Alert System): Although primarily designed for asteroid detection, ATLAS has discovered a large number of supernovae and other optical transients. Its rapid cadence allows near-real-time detection of nearby explosions. [79]

Near-infrared Surveys: Near-infrared searches play an essential role in detecting supernovae obscured by dust, particularly in star-forming regions and galactic nuclei. Examples include the UKIRT Hemisphere Survey and the VISTA Variables in the Via Lactea (VVV) survey, both of which have expanded the known population of highly reddened or embedded transients.

1.6 Structure of This Thesis

This thesis provides a comprehensive study of neutrino observations from nearby CC-SNe. The overall flow of the thesis is summarized in Figure 1.19. Chapter 1 provides a general introduction and the scientific motivation for the study of neutrinos from stellar core collapse. In Chapter 2, the SK detector is described, including its detection principles and detector sensitivity for supernova neutrino events. Chapter 3 introduces the supernova neutrino event generator and explains the simulation framework.

Based on this simulation framework, Chapter 4 and 5 present two independent analyses. Chapter 4 presents a study of neutrinos associated with stellar core collapse, focusing on the characteristics of late-phase neutrino emission. This chapter demonstrates that the time distribution of late-phase neutrino events, in particular the last observed event time, is sensitive to differences in the EOS. Chapter 5 focuses on a search for neutrinos from a failed SN candidate, M31-2014-DS1, in the Andromeda galaxy. A cluster search using time information is performed using SK data. Chapter 6 provides a discussion of the physical considerations derived from the results obtained in this study and the prospects for observing failed SN neutrinos in future experiments. The sensitivity improvements expected from the gadolinium-loaded SK experiment, as described in Section 2.1.3, and from the next-generation detector Hyper-Kamiokande are evaluated.

Finally, Chapter 7 summarizes the main results of this thesis and discusses their implications for future supernova neutrino observations.

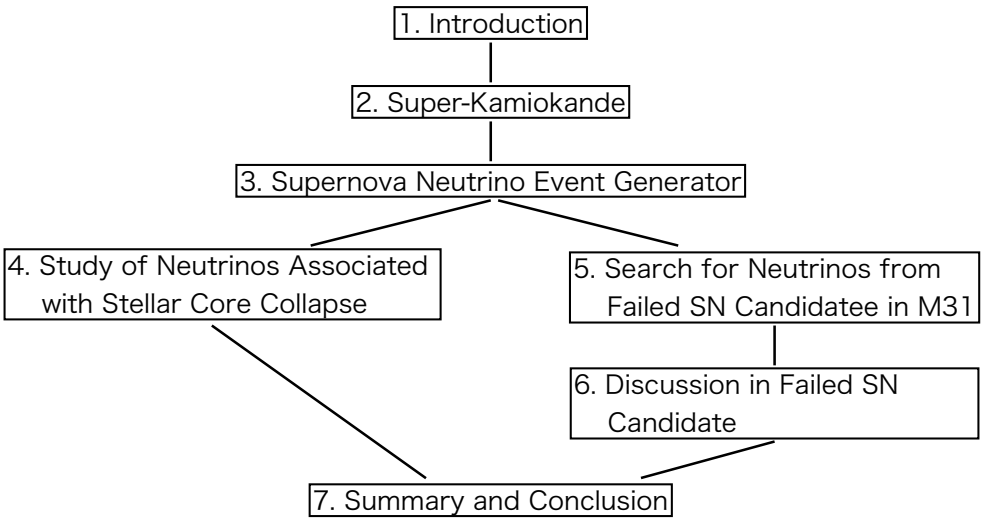

FIGURE 1.19: Schematic illustration of the structure of this thesis.

Chapter 2

Super-Kamiokande Experiment

In the following section, the SK detector used in this study is described, with a focus on its capability to detect supernova neutrinos from both nearby Galactic events and extragalactic sources out to 1 Mpc.

2.1 Detector Overview

SK is a large water Cherenkov detector located 1000 m underground (equivalent to 2700 m water depth) in the Kamioka mine, Gifu, Japan [8]. The detector consists of a cylindrical stainless-steel tank with a diameter of 39.3 m and a height of 41.4 m, containing 50 kton of ultra-pure water. An overview of the SK detector is shown in Figure 2.1. At this depth, only cosmic-ray muons with energies above approximately 1.3 TeV can reach the detector, resulting in a muon rate of about 2 Hz. As discussed in Chapter 5.4, these cosmic-ray muons constitute one of the main background sources in the supernova neutrino analysis; therefore, the reduced muon flux at this depth is advantageous for the study.

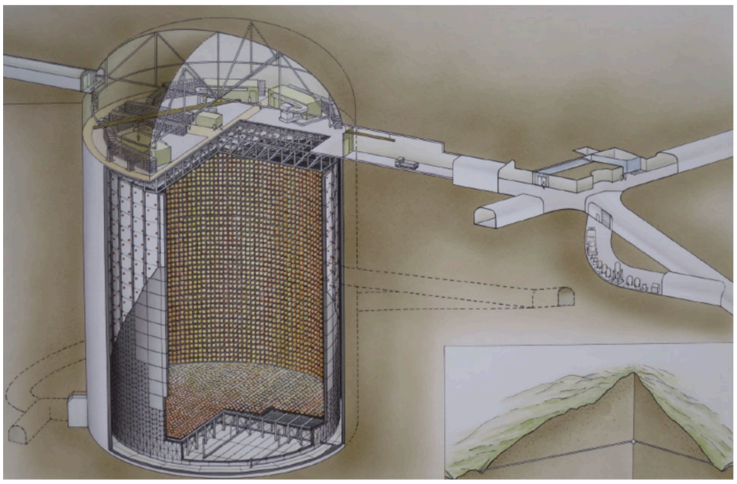

FIGURE 2.1: Schematic view of the Super-Kamiokande detector [8].

The SK detector is optically divided into two regions: the inner detector (ID) and the outer detector (OD). The ID is equipped with 20-inch photomultiplier tubes (PMTs) to detect Cherenkov light emitted by charged particles traversing the water volume, while the OD is instrumented with 8-inch PMTs to tag entering and exiting particles. The main physics objectives of SK include the search for proton decay, studies of neutrino oscillations using solar, atmospheric, and accelerator neutrinos,

searches for dark matter, and astrophysical observations such as solar and supernova neutrinos.

SK began operation in April 1996 and has since undergone eight distinct operational periods, referred to as SK-I through SK-VIII. During SK-I (1996–2001), the detector operated with 40% photocathode coverage in the ID. Following a maintenance shutdown, an accident in 2001 caused a chain-reaction implosion that destroyed about half of the ID PMTs. In response, SK-II (2002–2005) operated with 20% coverage, with each PMT enclosed in protective acrylic and fiberglass shells. After restoration of the PMTs, SK-III (2006–2008) resumed operation with full 40% coverage. A major electronics upgrade in SK-IV (2008–2018) replaced the front-end electronics, enabling deadtime-free data acquisition with reduced electronic noise. This upgrade lowered the energy threshold and allowed detection of neutron captures on hydrogen. In 2019, following an eight-month maintenance period aimed at preventing water leakage, SK-V began operation. In July 2020, SK entered the SK-VI phase with the addition of gadolinium sulfate ($Gd_2(SO_4)_3$) to the ultra-pure water, marking the beginning of the SK-Gd project to enhance neutron detection efficiency. Initially, the gadolinium concentration was 0.01% by mass, which was increased to 0.03% in June 2022, initiating the SK-VII period. The SK-VII phase did not continue uninterrupted. In October 2023, the magnetic compensation coils, which are used to correct the geomagnetic field inside the tank and to guide electrons efficiently toward the PMT photocathodes, malfunctioned and brought this operational period to an end. After repair work conducted between July and August 2024, the detector resumed stable operation and has been operating as SK-VIII since then.

2.1.1 Detection principle

Cherenkov radiation

Cherenkov radiation is a phenomenon in which a charged particle emits light when its velocity in a medium exceeds the speed of light in that medium. In SK, Cherenkov photons produced by this process are detected. A schematic illustration of Cherenkov radiation is shown in Figure 2.2. The momentum threshold for detecting Cherenkov photons depends on the particle species: for example, 0.57 MeV/c for electrons, 118 MeV/c for charged pions, and 1151 MeV/c for protons.

As illustrated in Figure 2.2, a charged particle moving at velocity v travels a distance $vt = \beta ct$ during time t, where $\beta = v/c$. In the same interval, Cherenkov photons propagate a distance of $(c/n)t$, where n is the refractive index of the medium. Therefore, the Cherenkov angle θ_c is given by

$$\cos\theta_c = \frac{(c/n)t}{\beta ct} = \frac{1}{n\beta}. \tag{2.1}$$

Here, θ_c is the angle between the particle trajectory and the direction of Cherenkov photons. In the case of water ($n \sim 1.34$), the condition $\cos\theta_c \leq 1$ requires $\beta \geq 1/n \sim 0.746$. Thus, Cherenkov radiation is emitted when the particle velocity exceeds approximately 74.6% of the speed of light in vacuum. Furthermore, substituting $n \sim 1.34$ and $\beta \sim 1$ into Eq. 2.1, the maximum Cherenkov angle in water is obtained as $\theta_c \sim 42°$.

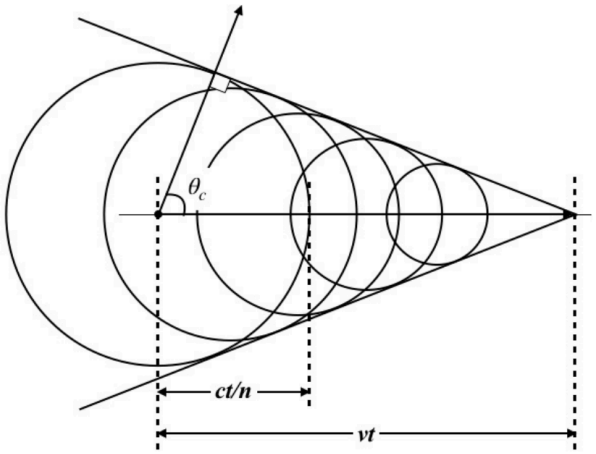

FIGURE 2.2: Schematic diagram of Cherenkov radiation [9]. The circles indicate the spherical wavefronts emitted by a charged particle moving through a medium, and their envelope forms a conical wavefront. The angle θ_c denotes the Cherenkov angle between the particle direction and the cone surface. The quantities ct/n and vt indicate the distances traveled by the emitted radiation and the particle, respectively.

The minimum kinetic energy E required for a charged particle of rest mass m to emit Cherenkov radiation (Cherenkov threshold) is expressed as

$$E = \frac{mc^2}{\sqrt{1-\beta^2}} = \frac{mc^2}{\sqrt{1-(1/n)^2}} = \frac{nmc^2}{\sqrt{n^2-1}}. \tag{2.2}$$

The energy threshold depends on the particle species. Table 2.1 summarizes the Cherenkov thresholds in water ($n \sim 1.34$) for representative charged particles.

TABLE 2.1: Cherenkov thresholds for representative charged particles in water [45]

Particle	Rest mass [MeV/c^2]	Cherenkov threshold [MeV]
$e^{\pm}$	0.511	0.768
$\mu^{\pm}$	105.7	158.8
$\pi^{\pm}$	139.6	209.7
$K^{\pm}$	493.7	741.7
$p^{\pm}$	938.3	1410

2.1.2 Detector components

Water tank

The water tank is a stainless-steel structure with a diameter of 39.3 m and a height of 41.4 m, divided into the ID and OD. PMTs are installed on both ID and OD surfaces. The ID, with a diameter of 33.8 m and height of 36.2 m, contains 32.5 kton of water and is instrumented with 11,129 20-inch PMTs. The photocathode coverage is approximately 40%, while the uncovered areas are shielded with black sheets to suppress reflections (Figure 2.3). The OD consists of a $\sim$ 2 m water layer surrounding

the ID, equipped with 1,885 outward-facing 8-inch PMTs. The OD surfaces, excluding the photocathodes and wavelength shifter plates, are covered with reflective Tyvek sheets to enhance photon collection.

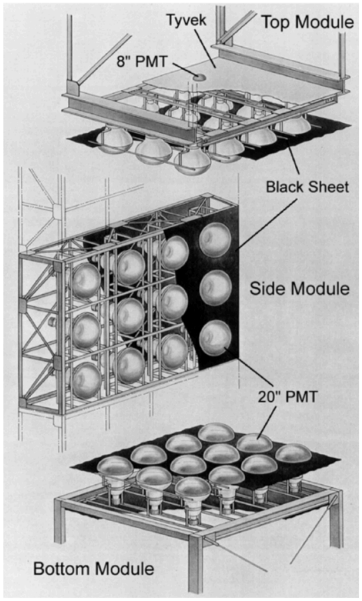

FIGURE 2.3: Schematic illustration of the detector tank [10]

Photomultiplier Tubes (PMTs)

The PMTs installed in the ID are 20-inch R3600 models manufactured by Hamamatsu Photonics, optimized for the SK experiment. As shown in Figure 2.4, 11,129 PMTs are deployed in the ID: 7,650 on the barrel, 1,740 on the top, and 1,739 on the bottom. PMTs convert photons into photoelectrons at the photocathode, amplify them by a factor of $\sim 10^6$ via dynodes, and output them as electrical signals. The "20-inch" refers to the diameter of the photocathode. In SK, a single photoelectron is amplified by a factor of approximately 6.0×10^6, corresponding to a total charge of 1 pC, which ensures single-photon detectability.

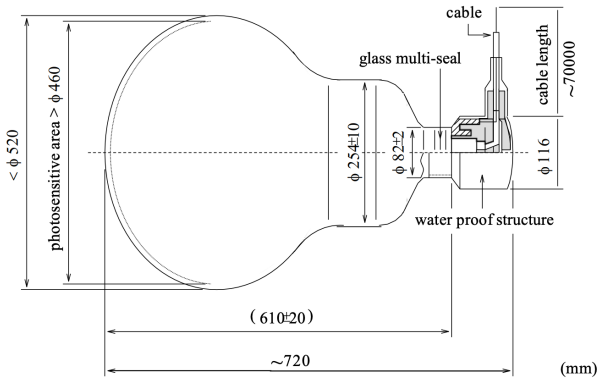

FIGURE 2.4: Schematic illustration of a 20-inch PMT [10]

The OD is instrumented with 1,885 8-inch PMTs (1,275 on the barrel, 302 on the top, and 308 on the bottom). To compensate for the smaller photocathode area, each OD PMT is equipped with a wavelength shifter (WS) plate of size 60 cm × 60 cm × 1.3 cm. The WS is an acrylic plate doped with 50 mg L^{-1} bis-MSB ($C_{24}H_{22}$), which absorbs ultraviolet light and re-emits photons in the blue-green region. With WS plates, the photon collection efficiency in the OD is enhanced by up to 60%, although the time resolution for single photoelectron signals decreases from 13 ns to 15 ns.

Gadolinium sulfate water circulation system

The 50 kton of ultrapure water in SK is produced from abundant groundwater in the Kamioka mine. Groundwater contains microscopic impurities, bacteria, trace metals such as iron, nickel, and cobalt, as well as radioactive elements such as radon and radium. These impurities degrade water transparency and increase background levels. The gadolinium sulfate ($Gd_2(SO_4)_3$) water circulation system is employed to purify the water and maintain its quality. A schematic diagram of the circulation system is shown in Figure 2.5.

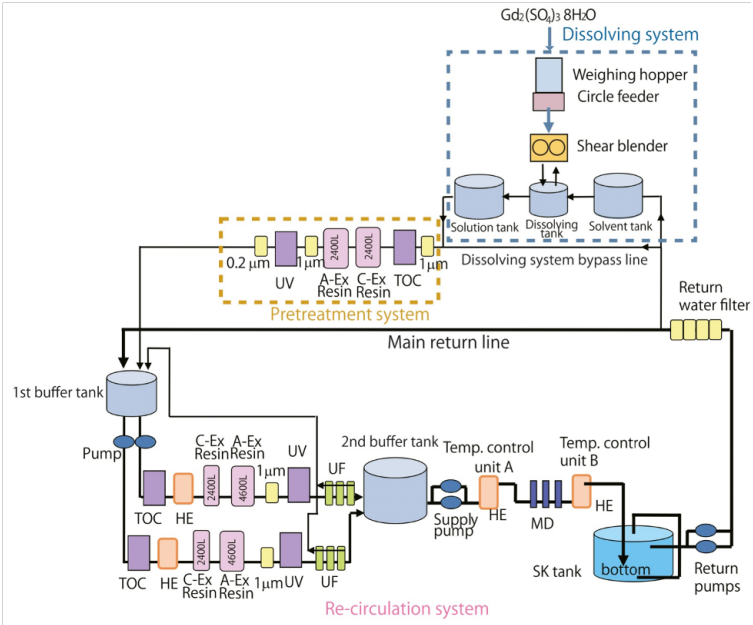

FIGURE 2.5: Schematic diagram of the gadolinium sulfate water circulation system [11]

The main components of the system are:

1. UV sterilizer: eliminates bacteria by ultraviolet irradiation.
2. Heat exchanger (HE): maintains the water temperature at ∼ 13 °C with a precision of 0.01 °C. This suppresses PMT dark noise, prevents bacterial growth, and preserves transparency.
3. Ultra filter (UF): removes impurities larger than 10 μm.

Purified water is supplied from the bottom of the tank and collected at the top through a circulation pipeline.

Software Trigger

The electronics for data acquisition were updated from SK-IV to a new system named QBEE [80]. The QBEE front-end electronics enable high-speed waveform digitization, allowing all PMT hits to be provisionally transferred to the Merger PC. The collected hit information is subsequently processed by a software-based trigger system, which constructs physical events from the time-correlated PMT signals.

The trigger algorithm evaluates the number of PMT hits within a 200 ns sliding time window, corresponding approximately to the light propagation time across the detector tank. A trigger is generated when the hit multiplicity exceeds a predefined threshold. In the ID, four trigger categories are defined: Super High Energy (SHE), High Energy (HE), Low Energy (LE), and Super Low Energy (SLE). In addition, an independent trigger is implemented for the OD. Once an SHE, HE, or LE trigger is issued, PMT hits in a time window from -5 μsto $+35$ μs relative to the trigger time are recorded. The extended readout window improves the efficiency for identifying delayed secondary signals, such as Michel electrons originating from muon decays. PMT hits only within a narrower time window of approximately 1.5 μs around the trigger time in order to limit the data volume. To enhance sensitivity to delayed neutron capture signals, a dedicated trigger referred to as the After Trigger (AFT) was introduced starting from the SK-IV. Following the issuance of an SHE trigger, an additional 500 μs acquisition window is opened during which all PMT hits are recorded. In order to limit the data rate and storage requirements, the AFT trigger condition without a coincident OD trigger rate was initially limited to 50 Hz, reflecting its primary purpose of detecting IBD interactions of electron antineutrinos. Beginning with SK-V, the requirement of no coincident OD trigger was removed to allow the recording of neutron signals associated with muon-induced processes, such as spallation. Furthermore, from the middle of the SK-IV period, improvements to the online data acquisition system enabled a relaxation of the AFT rate limitation, thereby expanding the accessible parameter space for neutron-related studies.

2.1.3 SK-Gd experiment

The SK experiment started the "SK-Gd experiment" in July 2020 by dissolving gadolinium (Gd) sulfate octahydrate in ultra-pure water in the detector tank. Compared to the pure-water phase, the neutron tagging efficiency has been significantly improved by detecting the total energy of approximately 8 MeV gamma rays emitted following thermal neutron capture on Gd.

Gadolinium loading

Between July 14 and August 17, 2020, 13 ton of Gd sulfate octahydrate ($Gd_2(SO_4)_3 \cdot 8H_2O$) was dissolved in the detector, initiating the SK-Gd phase with a Gd concentration of 0.01% by mass [11]. Gd has the largest thermal neutron capture cross section among naturally occurring elements and releases a total energy of approximately 8 MeV in γ-rays following neutron capture. This higher energy, compared with 2.2 MeV γ ray emitted from neutron capture on hydrogen during the pure-water phase, enables more efficient identification of neutron capture events. Figure 2.6 shows the basic idea of the delayed coincidence method, which uses the correlation between a prompt positron signal and a delayed neutron capture signal [81]. By dissolving about 0.01% of the Gd in mass concentration, roughly 50% of neutrons are captured on Gd nuclei.

From May 31 to July 5, 2022, an additional 27 ton of gadolinium sulfate octahydrate was introduced into SK. With this improvement, the mass concentration of Gd

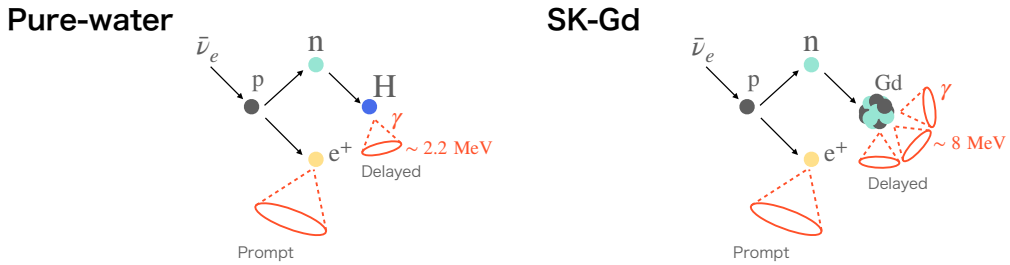

FIGURE 2.6: Idea of the delayed coincidence method for identification of inverse beta decay in pure-water phase (left) and SK-Gd (right).

increased to about 0.03%, and roughly 75% of neutrons will be captured on Gd nuclei as shown in Figure 2.7.

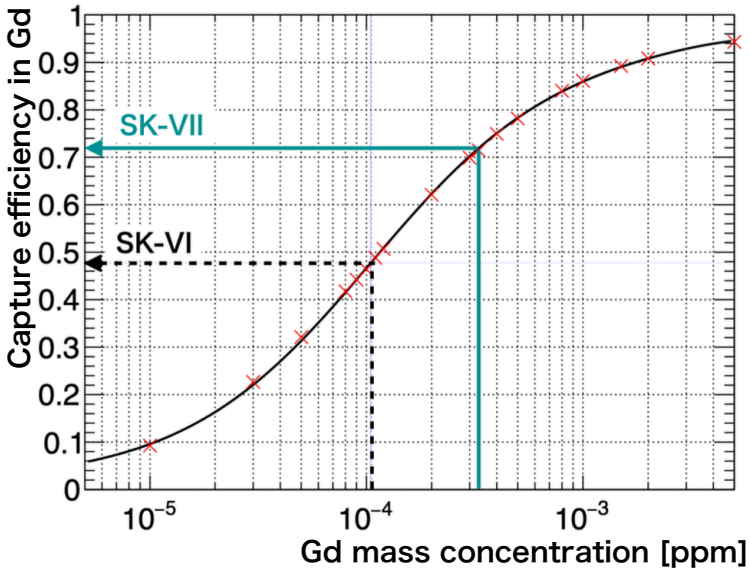

FIGURE 2.7: The relationship between Gd mass concentration and capture efficiency in Gd. The capture efficiency increases 1.5 times from SK-VI to SK-VII. The curves are obtained by fitting the data points (red points) measured by the AmBe MC simulation based on the Geant4.10.5 using an inverse polynomial function.

2.2 Evaluation of neutron tagging efficiency

The enhancement of neutron tagging efficiency enables improved sensitivity to various physics targets, such as the DSNB, and more accurate reconstruction of the supernova direction. For these physics targets, an accurate evaluation of the neutron identification efficiency is essential. In a previous study [41], the neutron tagging efficiency was measured during the 0.01% Gd mass concentration phase using an Am/Be source. The resulting tagging efficiency was evaluated to be $40.5 \pm 0.1(\text{stat.})^{+1.0}_{-2.1}(\text{sys.})\%$. In this work, the neutron tagging efficiency is evaluated using an Am/Be neutron source

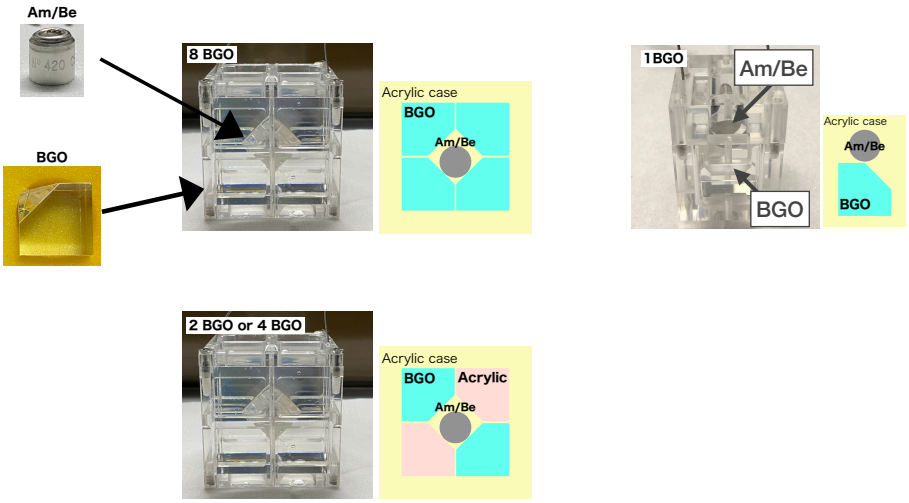

FIGURE 2.8: Appearance of the source set up for 8 BGO, 1 BGO(upper), and 2 or 4 BGO structure (lower).

during the SK-Gd phase with a Gd mass concentration of 0.03%, which has been in operation since June 2022.

2.2.1 Am/Be source measurement

Accurate evaluation of the neutron tagging efficiency is essential for estimating the physics sensitivity in SK-Gd. To achieve this, I performed dedicated neutron calibration measurements using a ^{241}Am/^{9}Be (Am/Be) radioactive neutron source. The Am/Be source is widely used for this purpose because it emits neutrons in coincidence with a characteristic gamma ray. Its production mechanism can be summarized as follows:

$$^{241}\mathrm{Am} \rightarrow {}^{237}\mathrm{Np} + \alpha, \qquad {}^{9}\mathrm{Be} + \alpha \rightarrow {}^{12}\mathrm{C} + n + \gamma\ (4.4\ \mathrm{MeV}). \tag{2.3}$$

Thus, each neutron emission is accompanied by a prompt 4.4 MeV gamma ray from the de-excitation of ^{12}C. In this calibration, the delayed-coincidence pair consisting of a prompt 4.4 MeV gamma ray and a subsequent thermal neutron capture on Gd is used to evaluate the neutron tagging performance.

To distinguish the 4.4 MeV gamma ray from other low-energy background events, the Am/Be source was coupled to a BGO scintillator crystal, which enhances the light yield of the prompt gamma signal. In the previous SK-IV study [28], two source configurations—referred to as "1 BGO" and "8 BGO"—were employed to evaluate the potential impact of the BGO crystal on the neutron tagging efficiency. In the 8 BGO configuration, the source was fully enclosed by eight BGO crystals, whereas in the 1 BGO configuration, the source was mounted with a single crystal. In the present study, two new intermediate configurations, denoted as "2 BGO" and "4 BGO", are introduced. These configurations are based on the 8 BGO geometry but with part of the BGO coverage replaced by acrylic, such that the source is only partially surrounded by BGO crystals. Photographs of the Am/Be source and the associated BGO crystal assemblies are shown in Figure 2.8.

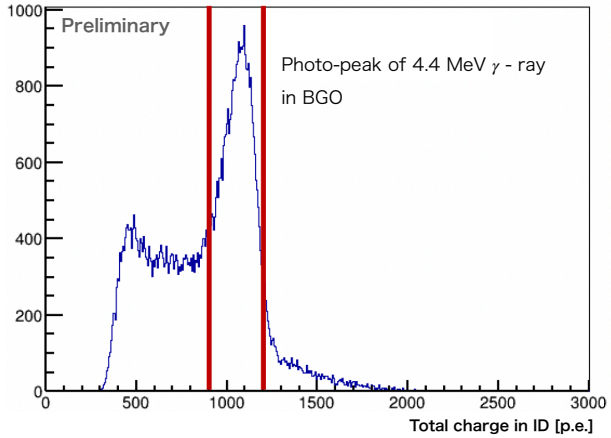

FIGURE 2.9: Distribution of the total photo-electrons recorded by the inner detector PMTs. The peak around 1000 p.e. corresponds to the 4.4 MeV gamma ray deposited in the BGO scintillator.

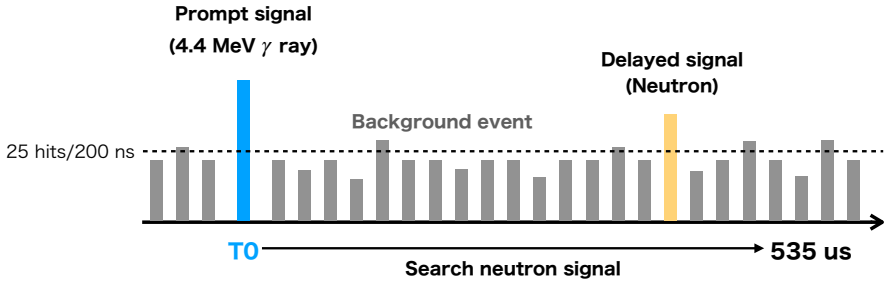

FIGURE 2.10: Schematic diagram of the data acquisition structure.

2.2.2 Analysis method

The neutron tagging efficiency, ϵ_n, is defined as

$$\epsilon_n = \frac{(\text{Number of tagged neutrons}) - (\text{Estimated background})}{\text{Number of prompt events}}. \tag{2.4}$$

To identify prompt events produced by the Am/Be + BGO source, I use the total number of photo-electrons (p.e.) recorded by the ID PMTs. Figure 2.9 shows the distribution of the total observed p.e. for all triggered events.

Events with a total charge around 1000 p.e. are selected as prompt candidates for the subsequent analyses. All PMT hits within a time window of 535 μs following each prompt event are recorded and used to search for delayed neutron signals. The delayed neutron candidates are required to occur between 4 μs and 535 μs after the prompt signal. Figure 2.10 illustrates the data acquisition structure used for this analysis. Delayed neutron candidates are identified by scanning the hit pattern with a 200 ns sliding time window and selecting clusters containing more than 25 hits. Each neutron candidate is then subjected to five selection criteria based on event reconstruction variables. Figure 2.11 shows examples of two of these variables, along with the corresponding selection thresholds. Filled histograms indicate the neutron signal predicted by the MC simulation. A FV cut that removes events within 2 m of the tank wall has already been applied. In this study, background data from the 0.01%

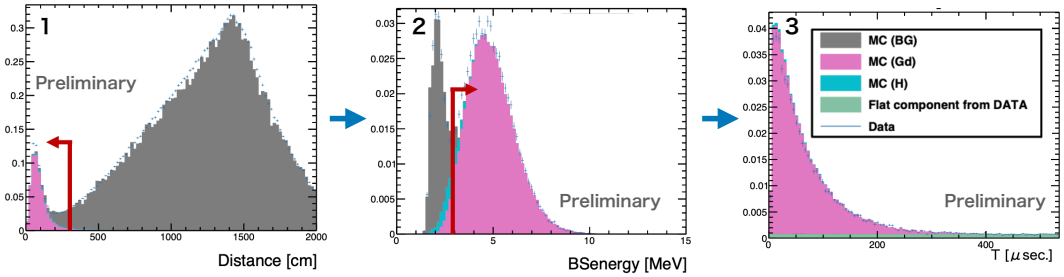

FIGURE 2.11: Distributions of selected reconstruction variables used in the neutron candidate selection: (1) distance from the source, (2) reconstructed energy, and (3) time difference between the prompt and delayed signals. The red arrows indicate the applied selection thresholds. Each panel includes all preceding cuts.

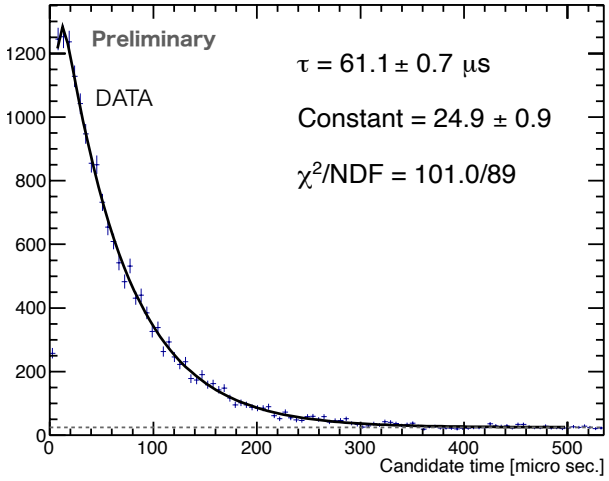

FIGURE 2.12: Time difference distribution between the prompt event and neutron event of the detector center (8 BGO).

Gd mass-concentration phase in the MC simulation were used, as the background estimation for the 0.03% Gd phase had not yet been completed at that time. After subsequent improvements to the MC simulation, the discrepancy between the two phases has been resolved [82], and no significant difference is now observed.

2.2.3 Analysis result

The distribution of the time difference between the prompt event and the delayed event of the tagged neutron is shown in Figure 2.12. The time constant τ was extracted by fitting this distribution, yielding a value of $\tau \simeq 61$ μs, which is in good agreement with the expected value (~ 60 μs). The number of background candidates is evaluated from the same fit of the timing distribution.

The correlation between the tagging efficiency and the number of surrounding BGO is evaluated by data at the detector center, as shown in Figure 2.13. The error bars for the data correspond to statistical uncertainties only, while those for the MC account for both statistical and systematic uncertainties. The systematic uncertainties are evaluated by comparing the data obtained with the 8 BGO source at the detector center and the corresponding MC sample. These uncertainties are classified into four

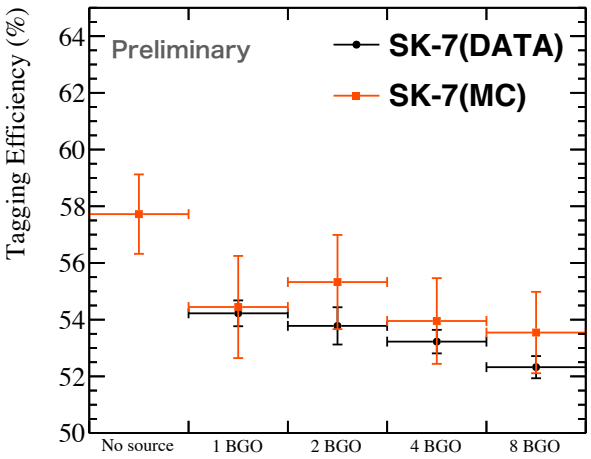

FIGURE 2.13: The tagging efficiency for each BGO. The black circles and red squares represent data and MC, respectively. The error of MC includes statistical and systematic errors.

categories: uncertainties related to the prompt event selection, those arising from the delayed event selection, effects due to the MC modeling and input parameters, and position-dependent variations within the detector. Each component is evaluated by comparing the data taken with the 8 BGO source at the detector center and the corresponding MC sample. A detailed description of the evaluation procedure is provided in [41]. The relative difference between data and MC is 0.4% (2.2%) in the case of 1 BGO (8 BGO). Tagging efficiency without any BGO is estimated to be 59.7 ± 1.2 (stat. + sys.)% by MC simulation. This evaluation is incorporated into the sensitivity estimation for failed SN in the SK-Gd phase, as presented in Section 6.4.1. The probability of a misidentification caused by a noise event is 0.31 $\pm$ 0.06%, which is higher than the 0.01% Gd concentration phase (0.18 $\pm$ 0.06%), primarily due to increasing dark noise.

In order to investigate the position uniformity of tagging efficiency, I measured at 15 positions. Figure 2.14 shows the position uniformity of tagging efficiency and time difference from the prompt event of the neutron event, respectively. The values at each position are consistent within statistical uncertainties for both the tagging efficiency and the time difference, and the weighted averages are estimated to be 51.68 ± 0.13% and $61.56 \pm 0.18 \mu$s, respectively.

2.3 Supernova Neutrino Observation in SK

As illustrated in Figure 1.10, the observational strategy and scientific objectives for supernova neutrinos are influenced by the distance to explosion. In this section, the analyses conducted in SK for different distance range–neaby Galactic supernovae, supernovae in the Mpc region.

As mentioned in Section 1.2.3, the detection of neutrinos from SN 1987A provided the first confirmation of neutrino emission from a CCSN. This milestone established the foundation of neutrino astronomy and demonstrated the effectiveness of water-Cherenkov detectors for such studies. Following this success, the SK detector has been continuously operating to search for neutrino signals from future galactic supernovae.

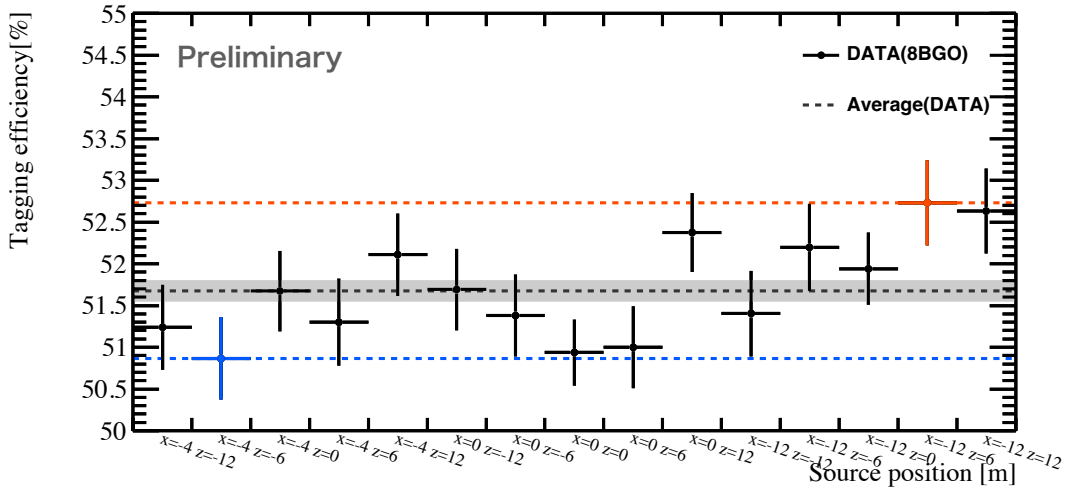

(a)

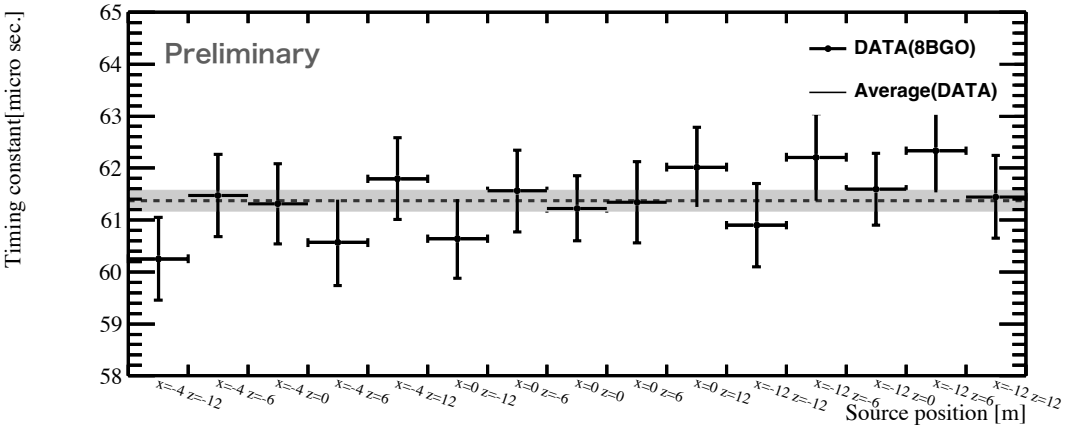

(b)

FIGURE 2.14: (a) shows the position uniformity of the tagging efficiency. The maximum value is 52.73% shown as red, and the minimum value is 50.87% shown as blue. Position dependence of the time difference between the prompt event and the associated neutron event is illustrated in (b).

SK is highly sensitive to neutrinos from CCSNe occurring within the Milky Way. For a CCSN at a distance of 10 kpc, about $\mathcal{O}(1000)$ IBD ($\bar{\nu}_e + p \rightarrow e^+ + n$) events are expected to be observed. In the pure water phase relevant for the SK-IV, which includes the dataset used for the neutrino search from a failed SN candidate in this study, the neutron is captured mainly on hydrogen as described in Section 2.1.3. This signal is challenging to identify because its energy region overlaps with background-dominated regions, making delayed coincidence tagging difficult without gadolinium loading.

For CCSNe occurring in nearby galaxies (e.g., within 1 Mpc), the expected number of neutrino events decreases dramatically to $\mathcal{O}(1)$. Since supernova neutrinos are emitted over several to tens of seconds, the signal would be observed as only a few detected events within a short time window. Therefore, by taking advantage of their characteristic timing clustering, it becomes possible to search for burst-like events.

2.3.1 Supernova neutrino burst search

SK has conducted several searches for SN burst neutrinos [83, 22]. These analyses scanned the full dataset with multiple cluster definitions reflecting theoretically motivated timescales, including the initial collapse and bounce, shock revival, and PNS cooling. The searches are not directed at known astrophysical objects, but rather aimed to identify SNe in a blind manner, including those that might have occurred but remained undetected in optical observations due to dust obscuration. To efficiently identify genuine burst signals while suppressing background clusters from spallation and accidental coincidences, the analyses used recent and realistic supernova models to optimize the event selection criteria. A key component of the method is a multidimensional fit-based categorization, which evaluates the spatial topology of each cluster—using reconstructed event vertices—to determine whether it is volume-like (as expected for a supernova), or instead point-like or line-like, as typically seen for backgrounds. This technique is particularly effective for identifying low multiplicity clusters that would be produced by nearby supernovae. In addition, the analysis utilizes the entire ID, extending beyond the conventional fiducial volume. If a candidate cluster is initially found within the FV, the search is expanded to the full ID to examine additional correlated events and obtain more information about the candidate.

In the case of ordinary SN neutrino search in SK-IV, multiple time windows–0.5, 2.0, and 10.0 s–were employed as summarized in Table 2.2. The time window of 0.5

TABLE 2.2: Time window settings used in the cluster search [22].

Time Window	Condition	Duration [s]
1	≥ 2 events	0.5
2	≥ 2 events	2.0
3	≥ 4 events	10.0

sec corresponds to the duration of the initial core collapse and subsequent bounce. The 2.0-sec window reflects the typical timescale for shock revival, while the 10.0-sec window represents the cooling phase of the PNS. After performing the cluster search over the entire SK-IV dataset, no clusters associated with a supernova burst were identified. Based on this null result, the upper limit on the supernova rate within a distance of 100 kpc was calculated as

$$R_{\mathrm{SN}} = \frac{\lambda_{\mathrm{lim}}}{T_{\mathrm{live}} \times P_{\mathrm{detect}}}, \tag{2.5}$$

where P_{detect} is the detection probability at 100 kpc, T_{live} is the total detector livetime, and λ_{lim} represents the 90% C.L. upper limit on the number of supernova-induced clusters, derived from the non-observation of any such clusters. The 90% C.L. upper limit of supernova rate out to 100 kpc is 0.29 /year. This limit applies to all models and neutrino mass hierarchies, except for the case of failed supernovae [22].

While the analysis uses the same SK-IV dataset as in the blind SN burst searches as described above, the search strategy in this study is specifically optimized for the failed SN candidate M31-2014-DS1, as described in Section 5. This approach allows for a focused investigation under similar observational conditions but optimized for the characteristics of a failed SN.

2.3.2 Supernova monitor

SK is equipped with a real-time supernova monitoring system known as "SN Watch" [12]. This system is optimized for the detection of CCSNe within nearby galaxies and continuously monitors the detector data to identify potential neutrino bursts from core-collapse supernovae. Once a supernova burst is detected, the SNWatch searches for "event clusters" and determines their occurrence time and direction within approximately 30 minutes. The results are automatically reported to optical observatories worldwide to enable rapid multi-messenger follow-up observations.

Data processing

The data processing flow of the SNWatch is illustrated in Figure 2.15. Unlike the standard data stream used for offline analyses, the SNWatch employs a dedicated and simplified data processing system to enable rapid analysis. Event selection is performed according to the criteria listed in Table 2.3. In this framework, the reconstructed energy of each event, E, is used as the primary cut. The PMT timing quality g_t^2 and spatial hit-pattern quality, g_p^2, are employed to characterize the event reconstruction. To further assess event quality, the N/S ratio is defined as the fraction of PMT hits with charges below the single photoelectron level divided by the total number of PMT hits [84]. Event selection is based on software triggers: the LE and HE triggers correspond to ID PMT hit thresholds of 49 and 52 within 200 ns, respectively, while the OD trigger is activated when at least 22 OD PMTs register a hit. Finally, d_{wall} denotes the distance from the reconstructed vertex to the nearest ID wall, which is used to reduce background near the detector boundaries.

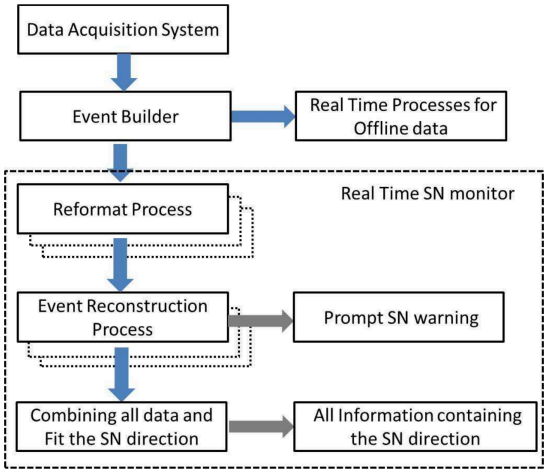

FIGURE 2.15: Flowchart of the data processing in the SNWatch [12]. Arrows indicate the data flow, and rectangles represent each processing step.

Identification of event clusters

The event cluster search procedure of the SNWatch is illustrated in Figure 2.16. In this process, the number of events within a given time window is counted, and when this number exceeds the corresponding threshold, the set of events is identified as an "event cluster." There are three types of event clusters. A "silent alarm" is issued when an event cluster is detected within a 20 s time window, but the number of

TABLE 2.3: Event cluster selection criteria in the SNWatch [46]. The "Prompt" and "Delayed" candidates shown in Figure 2.6. Here. E denotes the reconstructed energy of the event. The quantities g_t^2 and g_p^2 correspond to the PMT timing quality and the spatial hit-pattern quality, respectively.

Conditions for "Prompt" Candidates	**Conditions for "Delayed" Candidates**
$E > 7$ MeV	$E < 10$ MeV
$g_t^2 \geq 0.4$	$g_t^2 - g_p^2 > 0$
Number of PMT hits < 500	Within the fiducial volume
N/S ≤ 0.4	Not a "prompt" candidate
$d_{\text{wall}} > 200$ cm	...
LE- or HE-triggered event	...
Not an OD triggered event	...

events is below 25. Such characteristics are typical of background activity, including spallation products as described in detail in Section 5.4. Silent alarms are therefore confirmed to internal monitoring and are not communicated outside the collaboration. A "normal alarm" is generated when a cluster containing 25 or more events within 20

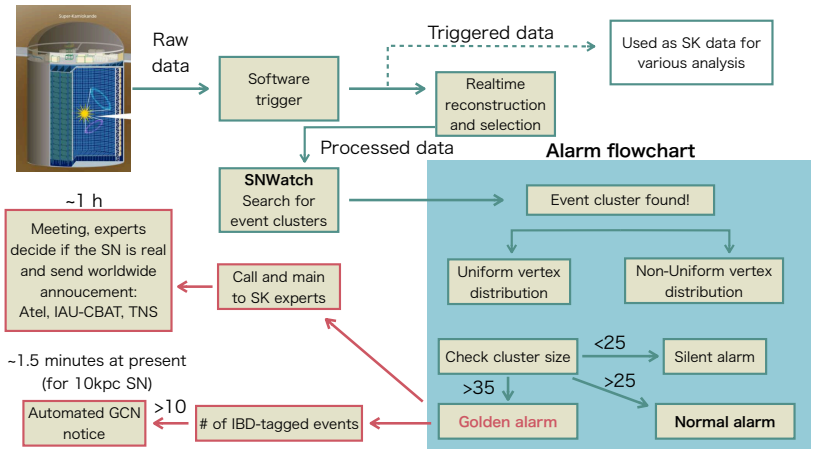

FIGURE 2.16: Flowchart of the process from event selection to alert notification.

s is observed.

A "golden alarm" represents the highest-confidence alert in the SNWatch. This alarm is issued when the following conditions are satisfied:

- A highly significant event cluster, containing 25 or more events, is detected within a 20 s time window.
- The reconstructed vertices exhibit a uniform spatial distribution.

Where these strict conditions are satisfied, the probability that the burst originates from Galactic CCSN becomes extremely high. After the confirmation process, which typically takes about one hour, a global announcement is disseminated via channels such as ATel, IAU CBAT, TNS, and GCN. The golden alarm thus ensures both a negligibly low false-alarm rate and swift worldwide notification of a highly reliable supernova detection.

Figure 2.17 represents the pointing accuracy of SNWatch as a function of supernova distance. The estimate is based on the $20M_{\odot}$ progenitor model presented in Ref. [3].

For this model, the angular resolution at a distance of 10 kpc is evaluated to be 3.96 ± 0.13 deg.. Depending on the assumed supernova model, the expected angular resolution at 10 kpc typically falls within the range of $3 - 7$ deg., as reported in Ref. [46]. In Figure 2.18, the probability of issuing an alarm as a function of distance

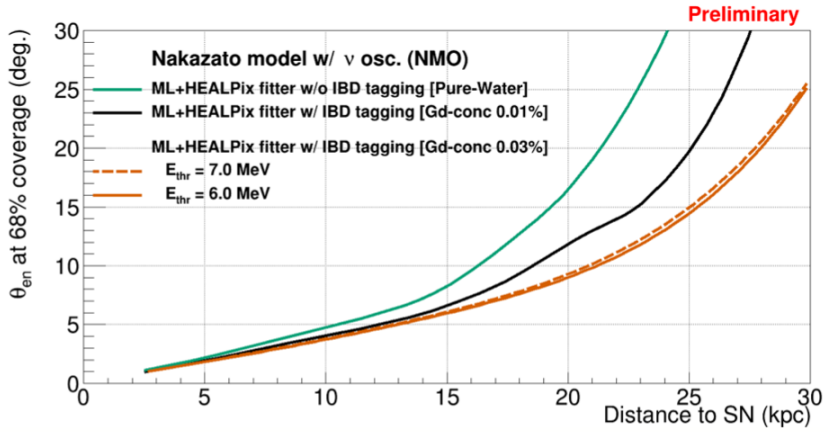

FIGURE 2.17: The pointing accuracy as a function of distance. In this estimation, I use $20M_{\odot}$ of progenitor in [3].

is shown. For a supernova in the Large Magellanic Cloud (LMC) at approximately 50 kpc, the probability of issuing a golden alarm is essentially 100%. Even for the Small Magellanic Cloud (SMC), located at a distance of about 60 kpc, the golden alarm can be issued with a probability exceeding 90%.

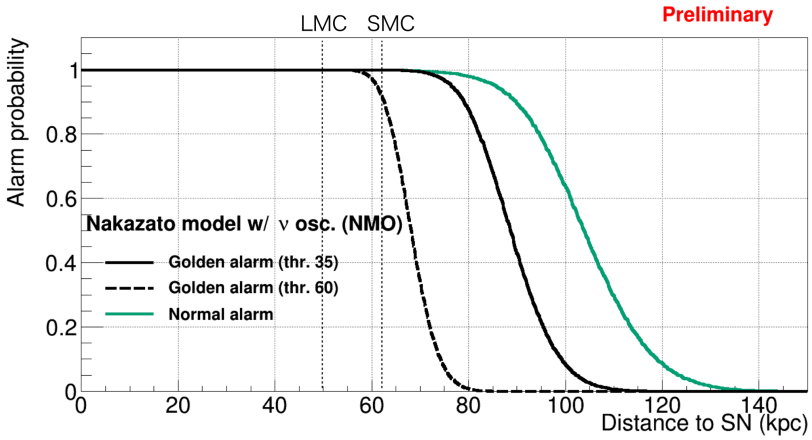

FIGURE 2.18: The alarm probability in SNWatch as a function of distance. In this estimation, I use $20M_{\odot}$ of progenitor in [3].

2.3.3 Detection sensitivity of supernova neutrino

In Section 4, I demonstrate the capability of our analysis method to extract physical information from the late-phase neutrino signal. The expected neutrino event in SK and the supernova rate as a function of distance are shown in Table 2.4. Compared to ordinary SN, failed SN are expected to produce approximately an order of magnitude more neutrino events. As discussed in Section 1.2, this enhancement arises from the

TABLE 2.4: Relationship between the expected neutrino events in SK and the supernova rate as a function of distance. For this estimate, I assume an ordinary SN model with a 20-$M_\odot$ progenitor and metallicity $Z = 0.02$ [3], and a failed SN model with a 30-$M_\odot$ progenitor and metallicity $Z = 0.04$ [24].

	10 kpc	1 Mpc	10 Mpc	$\langle E_\nu \rangle$
SN rate (/year)	~ 0.01	~ 0.1	~ 0.8	—
Expected ν event in SK (event / ordinary SN)	$\mathcal{O}(10^3)$	$\mathcal{O}(10^{-1})$	$\mathcal{O}(10^{-3})$	17.5
Expected ν event in SK (event / Failed SN)	$\mathcal{O}(10^4)$	$\mathcal{O}(1)$	$\mathcal{O}(10^{-2})$	35.1

long accretion phase before black hole formation, during which a larger number of high-energy neutrinos is emitted.

Figure 2.19 shows the expected observed neutrino event in SK as a function of distance using the supernova neutrino event generator as described in Section 3. SN Watch, as described in Section 2.3.2, covers out to the LMC and can make an alert for other observations. Because regions beyond approximately 100 kpc are not fully covered by the SNWatch online monitor, it is necessary to perform an offline search for neutrino clusters originating from supernovae. Section 5 describes the cluster search conducted for a supernova candidate.

2.3.4 Search for neutrinos from SN2023ixf in SK

SN2023ixf was discovored in 2023 in the galazy M101, located at a distance of 6.9 ± 0.1 Mpc [85]. Because of its closeness, it attracted significant attention as one of the nearest supernova explosions observed in recent years. Given this distance, the expected number of neutrino events in SK is of the order 10^{-3}.

A search for neutrinos associated with SN2023ixf was performed using SK data. Before performing the cluster search, the search period was defined based on the expected timing of neutrino emission from SN2023ixf. The progenitor of SN2023ixf is considered to be a red supergiant (RSG), for which the shock breakout (SBO) is expected to occur several days after the core collapse, as illustrated in Figure 2.20. Since neutrinos are emitted promptly at core collapse and therefore precede the SBO, the search window was set to cover the 10 days prior to the estimated SBO time. Accordingly, the SK data from May 9 to May 19, 2023, were used as the search period. A cluster search was conducted to identify time-correlated events, requiring two or more neutrino events to occur within a 10 s time window. For this analysis, the suppression of background events within the time window is essential in order to identify possible neutrino signals associated with the SN2023ixf. The analysis was performed using energy thresholds of 8 MeV and 15 MeV. At the 8 MeV threshold, background events were suppressed by applying a neutron tagging cut, which is described in Section 5.4.7, while at 15 MeV the background was reduced by raising the energy threshold. In this search, no time-correlated event cluster, defined as two or more events within 10 s time window, was found in the signal region.

An independent search for an excess of events above the expected background was also conducted. For an energy threshold of 8 MeV, 108 events were observed, consistent with the expected background of 99.4 ± 6.2 events, yielding a p-value of 0.82. At an energy threshold of 15 MeV, no events were observed, while the expected background was 0.8 ± 0.3 events, corresponding to a p-value of 0.51.

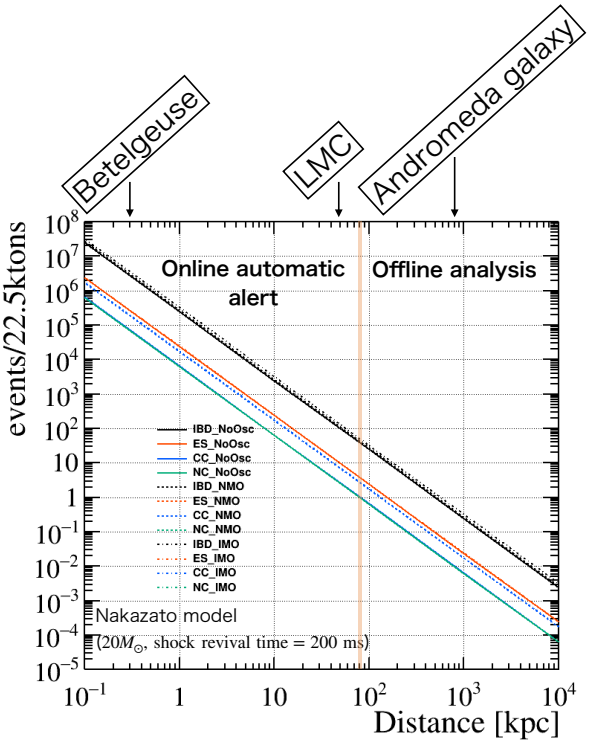

FIGURE 2.19: The relationship between expected neutrino events and distance. In this estimation, I use $20M_\odot$ of progenitor in [3]. The solid, dashed, and dot-dashed lines represent the cases without neutrino oscillation, with normal mass ordering, and with inverted mass ordering, respectively. The area to the right of the orange line defines the cluster-search region, whereas the area to the left marks the sensitivity region of the online SNwatch.

Since no significant excess was observed in any of the analyses, upper limits on the neutrino fluence from SN2023ixf were derived. The fluence limits were calculated assuming the Nakazato model with a progenitor mass of $20M_\odot$, a shock revival time of 200 ms [3], and normal mass ordering. The resulting 90% confidence level upper limits on the fluence are 5.36×10^8 cm^{-2} for an energy threshold of 8 MeV, 5.04×10^7 cm^{-2} for 15 MeV, and 7.42×10^7 cm^{-2} for 8 MeV with neutron tagging.

Based on these results, no neutrino signal associated with SN2023ixf was detected in SK. This result was reported through a GCN Circular [86] and an Astronomer's Telegram [87] on behalf of the SK collaboration. This marked the first time that the results of a neutrino search were associated with a supernova since SK started operation in 1996. The analysis framework and experience obtained through this study also form the basis of the neutrino search for failed SN candidate presented in Section 5.

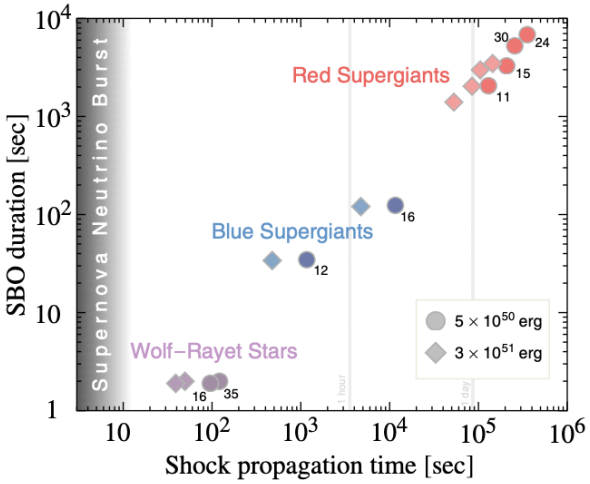

FIGURE 2.20: Predicted shock propagation time through the stellar envelopes and corresponding shock breakout (SBO) durations for supernova progenitor models with initial masses ranging from 11 to 35 $M_{\odot}$ [13]. The calculations are based on progenitor density structures taken from Ref. [14] for RSGs and from Ref. [15] for blue supergiants and Wolf-Rayet stars. Results are shown for explosion energies of 0.5×10^{51} erg and 3×10^{51} erg.

Chapter 3

Development of Supernova Neutrino Event Generator

To investigate the capability of a water Cherenkov detector to observe neutrinos from a nearby CCSN under realistic experimental conditions, I have developed a dedicated supernova neutrino event generator (SKSNSim). In this chapter, I describe the design and implementation of this generator, explaining how it is integrated into the SKSNSim framework. Although a full detector simulation of SK is not employed, the framework incorporates experimentally motivated signal and background models, enabling an analysis that closely reflects actual observation conditions.

Building on this simulation environment, I focus on the late-time neutrino emission from long-duration supernova models and study the corresponding observable signals at SK as described in Section 4. The SKSNSim framework is also employed to analyze failed SNe, which is discussed in Section 5. In that study, SKSNSim is used to estimate the expected number of neutrino events at SK originating from failed SNe.

3.1 Supernova Neutrino Event Generator

If a CCSN occurs in our Galaxy in the future, it will be essential to rapidly alert the astronomical community of its direction using neutrino signals. This early notification enables rapid follow-up observations in optical and other electromagnetic wavelengths. Furthermore, the observation of the diffuse supernova neutrino background (DSNB) is becoming increasingly promising, as current experimental upper limits are approaching theoretical predictions. To support these efforts, I have developed a new event simulator for supernova neutrinos in water Cherenkov neutrino detectors, such as the highly sensitive SK [88]. This simulator, called Super-Kamiokande SuperNova Simulator (SKSNSim)[1], is designed to simulate neutrino interactions in water for both CCSN bursts and the DSNB. SKSNSim is originally developed for SK but is applicable to any water-based Cherenkov detector. It incorporates all relevant neutrino interaction channels, including those with oxygen nuclei, to enable a more realistic generation of supernova neutrino events. The simulation provides a unified framework for modeling both SN bursts and DSNB, allowing us to evaluate the angular resolution for supernova direction determination and estimate the expected DSNB event rate. In this section, I present the structure of SKSNSim and demonstrate its key capabilities.

3.1.1 Flow of the simulation software

The software can be run in two modes: either for the simulation of individual SN bursts or for the simulation of the DSNB. While some parts are common for both

[1] available on GitHub, https://github.com/SKSNSim/SKSNSim

modes, there is a major difference: the SN burst flux is a function of time with sub-second precision, whereas the DSNB flux is constant in time. The details of DSNB simulation are described in Appendix B.2.

The SN burst simulation consists of the following steps: (1) the calculation of the expected number of interacting neutrinos for each neutrino type in the defined time and energy bins from the neutrino flux, cross section, and neutrino oscillation effects, (2) the estimation of the number interacting neutrinos by throwing a random number according to a Poisson Distribution, (3) the determination of the kinematics of particles, such as the interaction vertex and momentum, generated for each event using random numbers, based on the expected number of events obtained in (1) and the cross section. The sequence of steps(1)-(3) is repeated over the burst duration.

3.1.2 Choice of supernova model

There is a variety of models, both for the SN burst and the DSNB, based on different simulation approaches. In dealing with any model, SKSNSim requires the original neutrino flux information for each time and energy in the SN burst simulation. In the case of the DSNB simulation, the neutrino flux information for each energy is necessary.

In the case of SN bursts, many SN burst modelers publish their results with data tables containing time from core-bounce and the mean energy for each neutrino species to express the simulation results. I decide to support only the text format distributed by [3] in the SN burst simulation to handle all models in a unified manner. This format includes differential neutrino number flux and differential neutrino luminosity for every time and energy bin and types of neutrino ν_e, $\bar{\nu}_e$, ν_x, and $\bar{\nu}_x$. Here, ν_x represents ν_μ (ν_τ) because the distributions of ν_μ and ν_τ are equal, and also ν_μ and ν_τ of $\mathcal{O}(10)$ MeV behave the same way in water Cherenkov detectors.

SN burst models listed in Table 3.1 are implemented in SKSNSim. This table also includes failed SN models. The same simulation framework can be applied to both ordinary SNe and failed SNe by changing only the underlying model.

TABLE 3.1: List of currently supported SN burst models. The Sumiyoshi model and Choi model are failed SN models. The Nakazato model also includes failed SN models. The refrences shown from top to bottom are [3, 47, 48, 49, 50, 51, 30, 31, 32].

Model	Supported configuration	Reference
Nakazato	all parameters in the reference	Nakazato et al (2013)
Mori	9.6 $M_\odot$	Mori et al (2021)
Wilson	20 $M_\odot$	Totani et al (1998)
Tamborra	27 $M_\odot$	Tamborra et al (2014)
Fischer	8.8 $M_\odot$	Fischer et al (2010)
Hüdepohl	full neutrino interactions and 8.8 $M_\odot$	Nomoto et al (1987)
Sumiyoshi	$40M_\odot$, $50M_\odot$	Sumiyoshi et al (2007, 2088)
Choi	$23M_\odot$	Choi et al (2025)

3.1.3 Implementation of neutrino interactions

I consider the following four types of neutrino interactions in SKSNSim with a large cross section in the supernova neutrino energy region observed in water. Figure 3.1 shows the cross section for each interaction.

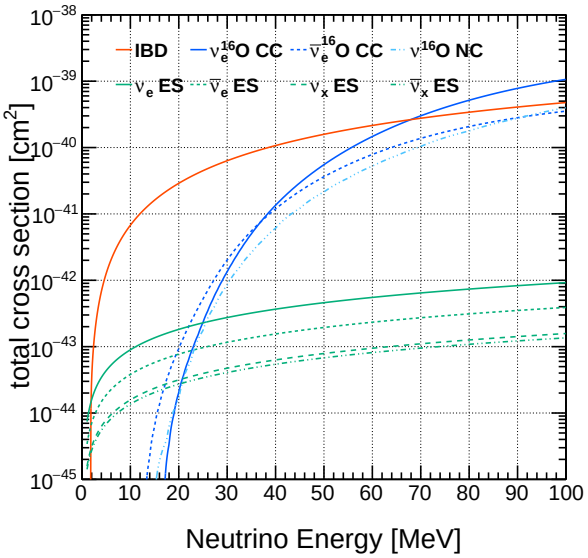

FIGURE 3.1: Total cross section of neutrinos with water as a function of neutrino energy. The solid red line indicates IBD and the green lines represent ES with a neutrino flavor: ν_e (solid) $\bar{\nu}_e$ (dotted), ν_x (dashed), and $\bar{\nu}_x$ (dot-dashed). The solid blue and dashed blue lines represent ^{16}O CC ν_e and $\bar{\nu}_e$, respectively. The dot-dashed light blue line indicates ^{16}O NC interaction. The cross section are calculated according to [16] for IBD, [17] for ES, [3] for ^{16}O CC interactions, and [18], and [19] for ^{16}O NC interaction.

Inverse Beta Decay (IBD):

$$\bar{\nu}_e + p \rightarrow n + e^+, \tag{3.1a}$$

Electron Scattering (ES):

$$\nu_e/\bar{\nu}_e/\nu_x/\bar{\nu}_x + e^- \rightarrow \nu_e/\bar{\nu}_e/\nu_x/\bar{\nu}_x + e^-, \tag{3.1b}$$

Charged-Current reaction with oxygen (^{16}O CC):

$$\nu_e/\bar{\nu}_e + {}^{16}\mathrm{O} \rightarrow e^-/e^+ + {}^{16}\mathrm{F}/{}^{16}\mathrm{N}, \tag{3.1c}$$

Neutral-Current reaction with oxygen (^{16}O NC):

$$\nu_e/\bar{\nu}_e/\nu_x/\bar{\nu}_x + {}^{16}\mathrm{O} \rightarrow p/n + \gamma + {}^{15}\mathrm{N}/{}^{15}\mathrm{O}. \tag{3.1d}$$

IBD reaction has the largest cross section for the neutrinos with water. As a default, the cross section of IBD is calculated as below on [16],

$$\frac{\mathrm{d}\sigma}{\mathrm{d}t} = \frac{{G_F}^2 \cos^2\theta_\mathrm{C}}{2\pi(s - m_p^2)^2}|\mathcal{M}^2|, \tag{3.2}$$

where G_F is the Fermi coupling constant, θ_C is the Cabibbo angle, s and t are the Mandelstam variables which are functions of each particle's momentum, m_p is the proton mass, and $|\mathcal{M}|$ is a matrix element, respectively. The order of the IBD cross section is 10^{-41} cm^2 for the typical supernova neutrino energies. SKSNSim includes the calculation by [89], [16] (default in SKSNSim), and [90]. Users can switch between these calculations.

Electron scattering (ES) is a reaction in which a neutrino elastically scatters off an

electron. All flavors of neutrinos contribute to this interaction. The order of the cross section is about two orders of magnitude smaller than that of the inverse beta decay (IBD) reaction. However, while IBD events have almost no directional sensitivity to the supernova, ES events are characterized by a strong angular correlation between the incoming neutrino and the scattered electron, providing valuable directional information. The basic equation for the reaction cross section is derived from the weak interaction. This generator adopts the formulation that includes radiative corrections as described in [91]:

$$\begin{aligned}\frac{d\sigma}{dT} = \frac{2{G_F}^2 m_e}{\pi} \Big\{ & {g_L}^2(T)\Big[1+\frac{\alpha}{\pi}f_-(z)\Big] \\ & + {g_R}^2(T)(1-z)^2\Big[1+\frac{\alpha}{\pi}f_+(z)\Big] \\ & - g_R(T)g_L(T)\frac{m_e}{q}z\Big[1+\frac{\alpha}{\pi}f_{+-}(z)\Big]\Big\},\end{aligned} \tag{3.3}$$

where m_e denotes the electron mass, $T = E - m_e$ is the kinetic energy of the recoil electron, q is the incoming neutrino energy, and $z = T/q$. g_L and g_R represent the left- and right-handed electron weak couplings, respectively, and $f_{+,-,+-}$ denote the radiative correction factors derived from QED. Equation (3.3) corresponds to neutrino scattering, while the cross section for antineutrinos is obtained by interchanging g_L and g_R.

Alternatively, the differential cross section can be expressed in terms of the scattering angle θ and neutrino energy E_ν:

$$\frac{d\sigma}{d\cos\theta} = 4\frac{m_e}{E_\nu}\frac{\left(1+\frac{m_e}{E_\nu}\right)^2\cos\theta}{\left[\left(1+\frac{m_e}{E_\nu}\right)^2-\cos^2\theta\right]^2}\frac{d\sigma}{dy}, \tag{3.4}$$

where

$$\frac{d\sigma}{dy} = \frac{G_F^2 m_e E_\nu}{2\pi}\left[A + B(1-y)^2 - Cy\frac{m_e}{E_\nu}\right], \tag{3.5}$$

and

$$y = \frac{2\frac{m_e}{E_\nu}\cos^2\theta}{\left(1+\frac{m_e}{E_\nu}\right)^2-\cos^2\theta}. \tag{3.6}$$

Here, the speed of light is taken as $c = 1$, and the Fermi coupling constant is $G_F = 1.166\times10^{-11}$ MeV^{-2}. E_ν is the incident neutrino energy, and θ is the scattering angle between the incoming neutrino and the recoil electron. The coefficients A, B, and C depend on the neutrino flavor and are summarized in Table 3.2. These formulations

TABLE 3.2: Coefficients for electron scattering. Here, $g_V = -0.5 + \sin^2\theta_W$, where θ_W is the Weinberg angle ($\sin^2\theta_W \approx 0.23$), and $g_A = -0.5$.

Neutrino Type	A	B	C
ν_e	$(g_V+g_A+2)^2$	$(g_V-g_A)^2$	$(g_V+1)^2-(g_A+1)^2$
$\bar{\nu}_e$	$(g_V-g_A+2)^2$	$(g_V+g_A+2)^2$	$(g_V+1)^2-(g_A+1)^2$
$\nu_\mu,\ \nu_\tau$	$(g_V+g_A)^2$	$(g_V-g_A)^2$	$g_V^2-g_A^2$
$\bar{\nu}_\mu,\ \bar{\nu}_\tau$	$(g_V-g_A)^2$	$(g_V+g_A)^2$	$g_V^2-g_A^2$

describe the elastic scattering of neutrinos on electrons, which plays an important role in the detection of supernova neutrinos due to its distinct angular correlation despite its relatively small cross section compared to IBD.

The charged-current reaction with oxygen (^{16}O CC) in the supernova neutrino energy region is a process in which oxygen nuclei interact with neutrinos, leading to a giant resonance in which the entire assembly of nucleons resonates. In the case of charged current reactions, an electron or positron is released from the oxygen nucleus for the charged-current reactions, and the nucleus changes to fluorine or nitrogen, respectively. Fluorine or nitrogen may be produced as excited states, of which there are many. When the fluorine or nitrogen exceeds the particle emission threshold, particles such as protons, neutrons, and alpha are emitted according to their respective thresholds. What is emitted from the nucleus is determined by which channel the nucleus branches into during deexcitation. In this simulation, I consider 43 excited states, as listed in Table 3.3, with multiple channels considered for a single excited state. The total of 31 channels considered in SKSNSim is detailed in Table 3.4. The cross section is implemented according to [52, 53] and provided in SKSNSim.

In the case of a neutral-current reaction with oxygen (^{16}O NC), SK is expected to detect electrons produced via Compton scattering of gamma rays emitted during deexcitation, such as from nitrogen or oxygen. In SKSNSim, I only consider states that emit a single gamma-ray during the deexcitation of ^{15}N or ^{15}O, as [18] specifically considers states of ^{15}N or ^{15}O generated when a single proton or neutron is emitted from ^{16}O. The cross section is implemented according to [18] and [19].

Previous studies [18, 19] investigated in detail the NC interactions induced by ν_x and $\bar{\nu}_x$. In particular, Ref. [18] focused on NC reactions on oxygen and evaluated the resulting energy spectra of supernova neutrinos expected in water Cherenkov detectors by considering the excited states listed in Table 3.5. The resulting energy distributions are shown in Figure 3.2. The solid lines represent the combined energy spectrum of γ rays emitted from NC interactions induced by ν_x and $\bar{\nu}_x$ and positrons produced via IBD, while the dashed lines show the energy spectrum of positrons from IBD alone. These spectra were derived assuming Fermi–Dirac distributions for the neutrino energy spectra. Panel (a) corresponds to the case with neutrino temperatures of $T = 8$ MeV for ν_x and $T = 5$ MeV for ν_e, with a chemical potential $\mu = 0$. Panel (b) shows the case with $T = 6.26$ MeV for ν_x, $T = 4$ MeV for ν_e, and a chemical potential of $\mu = 3T$. The horizontal axis, E, denotes the energy of the emitted positrons or γ rays. However, this figure does not take into account the detector energy resolution. More realistic simulations, including detector response effects, are discussed in Section 3.2.2.

3.1.4 Implementation of neutrino oscillation

As for the neutrino oscillations, there are oscillations during propagation in matter and a vacuum, and collective oscillation [92]. In SKSNSim, I only take into account the MSW effect [93, 94] inside the star as described in Section 1.3.2.

In the MSW effect, as neutrinos propagate outward, they are sensitive only to the electron number density at each position, which defines the effective matter potential. The resonance occurs where this matter potential matches the neutrino oscillation scale, and is independent of global stellar properties such as the progenitor mass or radius. Therefore, neutrino flavor conversion is governed primarily by the local electron density profile.

The neutrino flux at the stellar surface is evaluated using Equation 1.32 for the normal mass ordering and Equation 1.33 for the inverted mass ordering.

TABLE 3.3: List of excited states included in SKSNSim.

$^{16}O(\nu_e, e^- N'')N'$	0^- (MeV)	1^- (MeV)	2^- (MeV)	3^- (MeV)	1^+ (MeV)
$^{16}O(\nu_e, e^- N'')N'$	0^- (MeV)	1^- (MeV)	2^- (MeV)	3^- (MeV)	1^+ (MeV)
	14.906	15.157	15.205	15.250	18.664
	27.580	20.567	19.413		19.431
	27.990	23.271	21.617		20.684
		25.514	22.473		21.937
		25.718	27.255		22.968
		26.728	27.823		24.431
		27.218	28.103		24.858
		28.141	28.922		25.772
		28.515			26.593
		29.200			27.412
		29.353			27.802
		29.975			28.082
		30.250			29.967
		30.803			31.084
		31.754			31.693
					32.981
$^{16}O(\bar{\nu}_e, e^+ N'')N'$	0^- (MeV)	1^- (MeV)	2^- (MeV)	3^- (MeV)	1^+ (MeV)
	10.932	11.183	11.231	11.276	14.285
	23.606	16.593	15.439		15.052
	24.016	19.297	17.643		16.305
		21.540	18.499		17.558
		21.744	23.281		18.589
		22.754	23.849		20.052
		23.244	24.129		20.479
		24.167	24.948		21.393
		24.541			22.214
		25.226			23.033
		25.379			23.423
		26.001			23.703
		26.276			25.588
		26.829			26.705
		27.780			27.314
					28.602

Note. This table shows excited states for $^{16}O(\nu_e, e^- N'')N'$ and $^{16}O(\bar{\nu}_e, e^+ N'')N'$. Here, N' denotes the nucleus after deexcitation (^{16}F or ^{16}N), and N'' the emitted nucleus. $J^\pi = 0^-, 1^-, 2^-, 3^-, 1^+$ correspond to ^{16}O states. References: [52, 53].

TABLE 3.4: List of channels included in SKSNSim. This table lists channels for $^{16}\mathrm{O}(\nu_e, e^- N'')N'$ and $^{16}\mathrm{O}(\bar{\nu}_e, e^+ N'')N'$. Here, N' is the nucleus after deexcitation (^{16}F or ^{16}N), and N'' denotes the emitted nucleus [52, 53].

Reaction: $^{16}\mathrm{O}(\nu_e, e^- N'')N'$				
$^{16}\mathrm{O}(\nu_\mathrm{e}, \mathrm{e}^-\gamma)^{16}\mathrm{F}$	$^{16}\mathrm{O}(\nu_\mathrm{e}, \mathrm{e}^-\mathrm{n})^{15}\mathrm{F}$			
$^{16}\mathrm{O}(\nu_\mathrm{e}, \mathrm{e}^-\mathrm{p})^{15}\mathrm{O}$	$^{16}\mathrm{O}(\nu_\mathrm{e}, \mathrm{e}^-\mathrm{pn})^{14}\mathrm{O}$			
$^{16}\mathrm{O}(\nu_\mathrm{e}, \mathrm{e}^-2\mathrm{p})^{14}\mathrm{N}$	$^{16}\mathrm{O}(\nu_\mathrm{e}, \mathrm{e}^-{}^3\mathrm{He})^{13}\mathrm{N}$	$^{16}\mathrm{O}(\nu_\mathrm{e}, \mathrm{e}^-\alpha)^{12}\mathrm{N}$		
$^{16}\mathrm{O}(\nu_\mathrm{e}, \mathrm{e}^- N'')^{13}\mathrm{C}$	$^{16}\mathrm{O}(\nu_\mathrm{e}, \mathrm{e}^- N'')^{12}\mathrm{C}$	$^{16}\mathrm{O}(\nu_\mathrm{e}, \mathrm{e}^-\mathrm{p}\alpha)^{11}\mathrm{C}$	$^{16}\mathrm{O}(\nu_\mathrm{e}, \mathrm{e}^- N'')^{10}\mathrm{C}$	
$^{16}\mathrm{O}(\nu_\mathrm{e}, \mathrm{e}^- N'')^{12}\mathrm{B}$	$^{16}\mathrm{O}(\nu_\mathrm{e}, \mathrm{e}^- N'')^{11}\mathrm{B}$	$^{16}\mathrm{O}(\nu_\mathrm{e}, \mathrm{e}^- N'')^{10}\mathrm{B}$	$^{16}\mathrm{O}(\nu_\mathrm{e}, \mathrm{e}^- N'')^{9}\mathrm{B}$	
$^{16}\mathrm{O}(\nu_\mathrm{e}, \mathrm{e}^- N'')^{11}\mathrm{Be}$	$^{16}\mathrm{O}(\nu_\mathrm{e}, \mathrm{e}^- N'')^{10}\mathrm{Be}$	$^{16}\mathrm{O}(\nu_\mathrm{e}, \mathrm{e}^- N'')^{9}\mathrm{Be}$	$^{16}\mathrm{O}(\nu_\mathrm{e}, \mathrm{e}^- N'')^{8}\mathrm{Be}$	$^{16}\mathrm{O}(\nu_\mathrm{e}, \mathrm{e}^- N'')^{7}\mathrm{Be}$
$^{16}\mathrm{O}(\nu_\mathrm{e}, \mathrm{e}^- N'')^{10}\mathrm{Li}$	$^{16}\mathrm{O}(\nu_\mathrm{e}, \mathrm{e}^- N'')^{9}\mathrm{Li}$	$^{16}\mathrm{O}(\nu_\mathrm{e}, \mathrm{e}^- N'')^{8}\mathrm{Li}$	$^{16}\mathrm{O}(\nu_\mathrm{e}, \mathrm{e}^- N'')^{7}\mathrm{Li}$	$^{16}\mathrm{O}(\nu_\mathrm{e}, \mathrm{e}^- N'')^{6}\mathrm{Li}$
$^{16}\mathrm{O}(\nu_\mathrm{e}, \mathrm{e}^- N'')^{6}\mathrm{He}$	$^{16}\mathrm{O}(\nu_\mathrm{e}, \mathrm{e}^- N'')^{5}\mathrm{He}$	$^{16}\mathrm{O}(\nu_\mathrm{e}, \mathrm{e}^- N'')^{4}\mathrm{He}$	$^{16}\mathrm{O}(\nu_\mathrm{e}, \mathrm{e}^- N'')^{3}\mathrm{He}$	
$^{16}\mathrm{O}(\nu_\mathrm{e}, \mathrm{e}^- N'')^{3}\mathrm{H}$	$^{16}\mathrm{O}(\nu_\mathrm{e}, \mathrm{e}^- N'')^{2}\mathrm{H}$			
Reaction: $^{16}\mathrm{O}(\bar{\nu}_e, e^+ N'')N'$				
$^{16}\mathrm{O}(\bar{\nu}_\mathrm{e}, \mathrm{e}^+\gamma)^{16}\mathrm{N}$	$^{16}\mathrm{O}(\bar{\nu}_\mathrm{e}, \mathrm{e}^+\mathrm{n})^{15}\mathrm{N}$	$^{16}\mathrm{O}(\bar{\nu}_\mathrm{e}, \mathrm{e}^+2\mathrm{n})^{14}\mathrm{N}$	$^{16}\mathrm{O}(\bar{\nu}_\mathrm{e}, \mathrm{e}^+ N'')^{13}\mathrm{N}$	
$^{16}\mathrm{O}(\bar{\nu}_\mathrm{e}, \mathrm{e}^+\mathrm{pn})^{14}\mathrm{C}$	$^{16}\mathrm{O}(\bar{\nu}_\mathrm{e}, \mathrm{e}^+{}^3\mathrm{H})^{13}\mathrm{C}$	$^{16}\mathrm{O}(\bar{\nu}_\mathrm{e}, \mathrm{e}^+ N'')^{12}\mathrm{C}$	$^{16}\mathrm{O}(\bar{\nu}_\mathrm{e}, \mathrm{e}^+ N'')^{11}\mathrm{C}$	$^{16}\mathrm{O}(\bar{\nu}_\mathrm{e}, \mathrm{e}^+ N'')^{10}\mathrm{C}$
$^{16}\mathrm{O}(\bar{\nu}_\mathrm{e}, \mathrm{e}^+ N'')^{14}\mathrm{B}$	$^{16}\mathrm{O}(\bar{\nu}_\mathrm{e}, \mathrm{e}^+ N'')^{13}\mathrm{B}$	$^{16}\mathrm{O}(\bar{\nu}_\mathrm{e}, \mathrm{e}^+\alpha)^{12}\mathrm{B}$	$^{16}\mathrm{O}(\bar{\nu}_\mathrm{e}, \mathrm{e}^+ N'')^{11}\mathrm{B}$	$^{16}\mathrm{O}(\bar{\nu}_\mathrm{e}, \mathrm{e}^+ N'')^{10}\mathrm{B}$
$^{16}\mathrm{O}(\bar{\nu}_\mathrm{e}, \mathrm{e}^+ N'')^{9}\mathrm{B}$	$^{16}\mathrm{O}(\bar{\nu}_\mathrm{e}, \mathrm{e}^+ N'')^{8}\mathrm{B}$			
$^{16}\mathrm{O}(\bar{\nu}_\mathrm{e}, \mathrm{e}^+ N'')^{12}\mathrm{Be}$	$^{16}\mathrm{O}(\bar{\nu}_\mathrm{e}, \mathrm{e}^+ N'')^{11}\mathrm{Be}$	$^{16}\mathrm{O}(\bar{\nu}_\mathrm{e}, \mathrm{e}^+ N'')^{10}\mathrm{Be}$	$^{16}\mathrm{O}(\bar{\nu}_\mathrm{e}, \mathrm{e}^+ N'')^{9}\mathrm{Be}$	$^{16}\mathrm{O}(\bar{\nu}_\mathrm{e}, \mathrm{e}^+ N'')^{8}\mathrm{Be}$
$^{16}\mathrm{O}(\bar{\nu}_\mathrm{e}, \mathrm{e}^+ N'')^{7}\mathrm{Be}$				
$^{16}\mathrm{O}(\bar{\nu}_\mathrm{e}, \mathrm{e}^+ N'')^{9}\mathrm{Li}$	$^{16}\mathrm{O}(\bar{\nu}_\mathrm{e}, \mathrm{e}^+ N'')^{8}\mathrm{Li}$	$^{16}\mathrm{O}(\bar{\nu}_\mathrm{e}, \mathrm{e}^+ N'')^{7}\mathrm{Li}$	$^{16}\mathrm{O}(\bar{\nu}_\mathrm{e}, \mathrm{e}^+ N'')^{6}\mathrm{Li}$	
$^{16}\mathrm{O}(\bar{\nu}_\mathrm{e}, \mathrm{e}^+ N'')^{6}\mathrm{He}$	$^{16}\mathrm{O}(\bar{\nu}_\mathrm{e}, \mathrm{e}^+ N'')^{4}\mathrm{He}$	$^{16}\mathrm{O}(\bar{\nu}_\mathrm{e}, \mathrm{e}^+ N'')^{3}\mathrm{He}$		
$^{16}\mathrm{O}(\bar{\nu}_\mathrm{e}, \mathrm{e}^+ N'')^{3}\mathrm{H}$	$^{16}\mathrm{O}(\bar{\nu}_\mathrm{e}, \mathrm{e}^+ N'')^{2}\mathrm{H}$			

TABLE 3.5: Excitation energies of ^{15}N and ^{15}O considered in Ref. [18].

	(MeV)		(MeV)
^{15}N	5.27	^{15}O	5.18
	6.33		6.18
	7.16		6.69
	7.56		7.28
	8.32		
	8.57		
	9.05		
	9.76		

3.2 Demonstration

In this section, I describe the demonstration of SKSNSim in its SN burst mode. It generates observable particles in water Cherenkov detectors and can pass information about these particles to detector simulators in two modes: the SN burst and the DSNB mode. Section 3.2.1 provides examples of events generated by neutrino interactions in the SN burst mode.

3.2.1 Generated neutrino events

This section shows the simulation result of an SN burst using SKSNSim. The process begins by calculating the number of events for each interaction, followed by defining the kinematics for each event. Users have the flexibility to change the direction of the supernova object in each event and the distance from a supernova to a detector. In this mode, the neutrino energy is determined by a random number that follows the energy distribution defined by the model, and the interaction vertex is generated

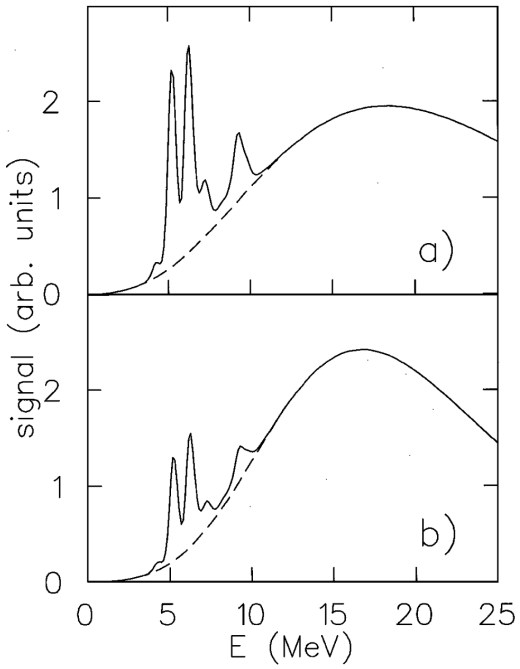

FIGURE 3.2: Energy spectra of supernova neutrino events expected in a water Cherenkov detector [18]. The solid lines show the combined energy spectra of γ rays from NC interactions induced by ν_x and $\bar{\nu}_x$ and positrons from IBD, while the dashed lines represent the energy spectra of positrons from IBD alone. The spectra are calculated assuming Fermi–Dirac distributions for neutrino energies. Panel (a) assumes $T = 8$ MeV for ν_x, $T = 5$ MeV for ν_e, and $\mu = 0$, while panel (b) assumes $T = 6.26$ MeV for ν_x, $T = 4$ MeV for ν_e, and $\mu = 3T$. The horizontal axis represents the energy of positrons or γ rays.

uniformly inside the detector. Furthermore, using the previously determined energy and direction of the neutrino, the kinematics of outgoing particles, such as positrons in the IBD interaction, are determined based on their respective differential cross section.

SKSNSim does not include detector response, such as energy resolution or detection efficiencies. These effects are taken into account by applying the detector simulation [95] to the output of SKSNSim. Figure 3.3 shows the time, energy, and angular distributions of neutrino events interacting with water. In the SN burst mode, the type of neutrino interaction, its time and vertex, as well as the type of generated particle, its direction, and energy, are stored as event information for a single supernova explosion. θ_{SN} represents the angle between neutrinos and a generated particle for each interaction. This case assumes the Nakazato model [3].

TABLE 3.6: Summary of progenitor masses and revival times T_{rev} considered in this study.

Progenitor mass ($M_{\odot}$)	T_{rev} (ms)
13	100
13	200
13	300
20	100
20	200
20	300
30	100
30	200
30	300
50	100
50	200
50	300

3.2.2 Neutrino interaction simulation with oxygen nuclei in SK

CC interaction

As described in Section 3.1.3, there are CC and NC reactions in the interaction with neutrinos and oxygen nuclei. As shown in Figure 3.1, CC and NC interactions become dominant in the neutrino energy region above 20 MeV and therefore play a crucial role in observations at these energies.

As summarized in Table 3.6, twelve supernova models were employed to compare the expected number of CC interaction events. These models differ in the progenitor mass and the shock revival time T_{rev}. Using these supernova models, the expected number of CC interaction events was estimated and is shown in Figure 3.4. This figure assume observations with SK FV and a supernova distance of 10 kpc. In this simulation, the effects of neutrino oscillations on the expected event numbers are not taken into account. Table 3.7 summarizes the variation in the expected event numbers due to differences in the shock revival time for models with a progenitor mass of 20 $M_{\odot}$.

TABLE 3.7: Expected numbers of events for each interaction channel for different shock revival times.

	$20M_{\odot}$, $T_{\mathrm{rev}} = 100$ ms	$20M_{\odot}$, $T_{\mathrm{rev}} = 300$ ms
IBD	2993	3821
CC(ν_e, e^-)	32	64
CC($\bar{\nu}_e, e^+$)	30	59

While the expected number of IBD events increases by approximately a factor of 1.3 from the model of $20M_{\odot}$, $T_{\mathrm{rev}} = 100$ ms, to model of $20M_{\odot}$, $T_{\mathrm{rev}} = 300$ ms, the expected number of CC events increases by nearly a factor of two, indicating a stronger model dependence for CC interactions. The masses listed in parentheses represent the neutron star masses resulting from the explosion. The relationship between the expected event numbers and the progenitor mass, as well as the resulting neutron star mass, is summarized in Table 3.8. The neutron star mass increases

TABLE 3.8: Expected numbers of events for each interaction channel for different progenitor masses. The masses shown in parentheses correspond to the masses of the neutron stars formed after the explosion. All models in this table are $T_{\mathrm{rev}} = 300$ ms.

	$13M_\odot$ (1.64 $M_\odot$)	$20M_\odot$ (1.57 $M_\odot$)	$50M_\odot$ (1.87 $M_\odot$)
IBD	4446	3821	6295
CC(ν_e, e^-)	1009	64	248
CC($\bar{\nu}_e, e^+$)	89	59	178

with decreasing mass loss during the explosion [3]. Consequently, both IBD and CC event rates increase with neutron star mass. However, the variation among models is significantly larger for CC interactions than for IBD interactions.

Next, the effects of neutrino flavor oscillations on the expected event numbers were examined. Figure 3.5 shows the neutrino energy spectra for the model of $20M_\odot$, $T_{\mathrm{rev}} = 100$ ms. The red curve corresponds to the case without neutrino oscillations, the black curve to the normal mass ordering, and the blue curve to the inverted mass ordering. In both oscillation scenarios, the neutrino flux is enhanced in the energy region around 20 MeV because ν_x neutrinos, which are characterized by higher average energies than electron-type neutinos, are mixed. Table 3.9 summarizes the expected event numbers for each oscillation scenario.

TABLE 3.9: Expected numbers of events for each interaction channel under different neutrino oscillation assumptions.

Model of $20M_\odot$, $T_{\mathrm{rev}} = 100$ ms	without oscillation	normal ordering	inverted ordering
IBD	2993	3367	4217
CC(ν_e, e^-)	32	153	116
CC($\bar{\nu}_e, e^+$)	30	51	98

Table 3.10 summarizes the expected numbers of neutron-emitting events for the model with a progenitor mass of $20M_\odot$ and a revival time of $T_{\mathrm{rev}} = 200$ ms. In this table, the expected number of events is evaluated without including the effects of neutrino oscillations, and the distance between SK and the supernova is assumed to be 10 kpc. For CC interactions induced by ν_e, events accompanied by neutron emission are almost negligible. In contrast, for CC interactions induced by $\bar{\nu}_e$, it is found that approximately 60% of the events are accompanied by neutron emission. However, neutron-emitting events are also produced by IBD and NC interactions, which will be discussed in the next section. Therefore, it is difficult to discriminate CC interactions from other reaction channels based on neutron emission. On the other hand, some CC interactions are accompanied by gamma-ray emission in addition to neutron emission. If both gamma-ray and neutron information can be utilized simultaneously, it may be possible to distinguish CC interactions from other reaction channels. A detailed investigation of this discrimination method is planned for future work.

NC interaction

In SK, CC interactions are observable only for ν_e and $\bar{\nu}_e$, whereas NC interactions can also be induced by ν_x and $\bar{\nu}_x$. In addition, since NC interactions occur for all neutrino flavors, the total number of NC events is not affected by neutrino flavor oscillations. Consequently, NC interactions provide a direct probe of the total neutrino flux emitted during a supernova explosion.

TABLE 3.10: Expected numbers of CC interaction events with and without neutron emission for the 20 $M_\odot$ model with $T_{\rm rev}$ = 200 ms. Neutrino oscillations are not considered, and a supernova distance of 10 kpc is assumed.

Model of 20 $M_\odot$, $T_{\rm rev}$ = 200 ms	without neutron	with neutron
CC(ν_e, e^-)	43	4
CC($\bar{\nu}_e, e^+$)	19	26

In this study, the NC interaction cross sections as functions of neutrino energy, shown in Figure 3.6, are implemented in a neutrino interaction simulation to estimate more realistic NC event rates and the expected energy spectra in SK.

Two supernova models, $30M_\odot$, $T_{\rm rev}$ = 200 ms (ordinary SN model) and $30M_\odot$ (failed SN model), are used in this analysis. Using an SKSNSim, the expected numbers of NC events are calculated, and the reconstructed energy distributions are estimated with the SK detector simulation. Figure 3.7 shows the neutrino energy spectra for the two models. As shown in Figure 3.1, the NC interaction cross section becomes dominant for neutrino energies above 20 MeV. From Figure 3.7, the failed SN model predicts a larger neutrino flux in this energy region than the ordinary SN model. Table 3.11 summarizes the expected numbers of IBD and NC events for the two models, assuming observations with the 32.5 kton FV of SK, and energy threshold of 5 MeV, and a supernova distance of 10 kpc. Neutrino oscillation effects are not included. Figure 3.8 shows the reconstructed energy distributions estimated using

TABLE 3.11: Expected numbers of events for each interaction channel. The event rates are calculated assuming observations with the 32.5 kton fiducial volume of SK and a supernova distance of 10 kpc. Neutrino oscillation effects are not taken into account.

Interaction	30 $M_\odot$ ordinary SN model	30 $M_\odot$ failed SN model
IBD	5936	18357
NC (^{15}N)	177	1124
NC (^{15}O)	48	304

the detector simulation under the same observational conditions. In the ordinary SN model, no clear gamma-ray peak originating from NC interactions is observed. In contrast, in the failed SN model, where higher-energy neutrinos are more abundant, a pronounced gamma-ray peak from NC interactions appears in the reconstructed energy range of E = 3–10 MeV. Therefore, focusing on NC interactions enhances the ability to discriminate between different supernova models based on the observed energy distributions of supernova neutrino events. However, with the start of the SK-Gd phase, gamma rays from neutron capture on gadolinium are also expected to contribute in the same energy region as the NC signal. The impact of these neutron-capture gamma rays on the reconstructed energy distribution must be evaluated in future studies.

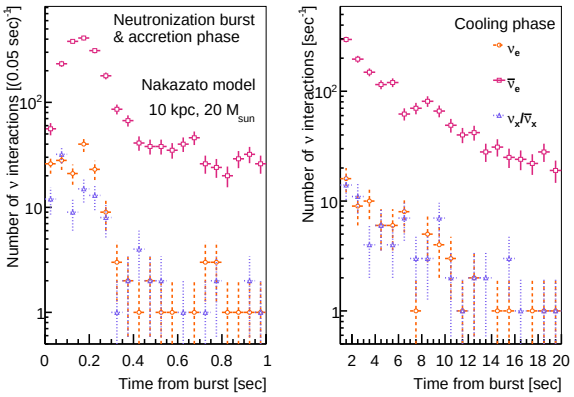

(a)

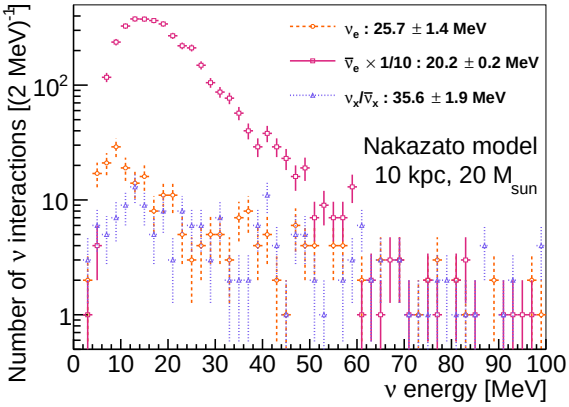

(b)

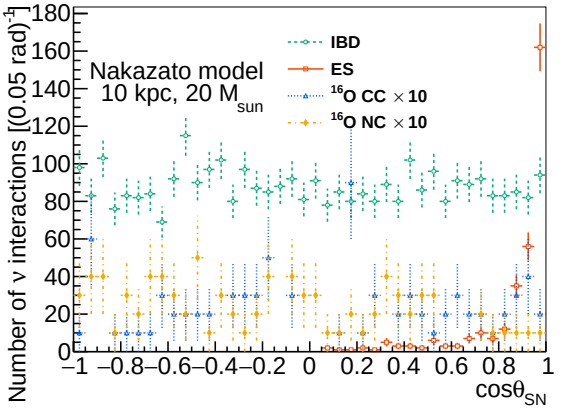

(c)

FIGURE 3.3: Distributions of neutrino events generated by a typical supernova burst. These distributions show true kinematics without detector response. (a) Timing distributions of generated neutrino events. The left focuses on the neutronization burst and accretion phases, while the right corresponds to the cooling phase. (b) Time-integrated energy distribution of generated neutrino events over all phases. The numbers in the legend indicate the mean energy for each neutrino species. (c) θ_{SN} distributions between neutrinos and secondary particles for the IBD, ES, ^{16}O CC, and ^{16}O NC channels. The underlying model is taken from [3], assuming a progenitor mass of $M = 20\ M_{\odot}$, a shock revival time of 200 ms, a metallicity of $Z = 0.02$, and a distance of $d = 10$ kpc. Neutrino oscillations are not included.

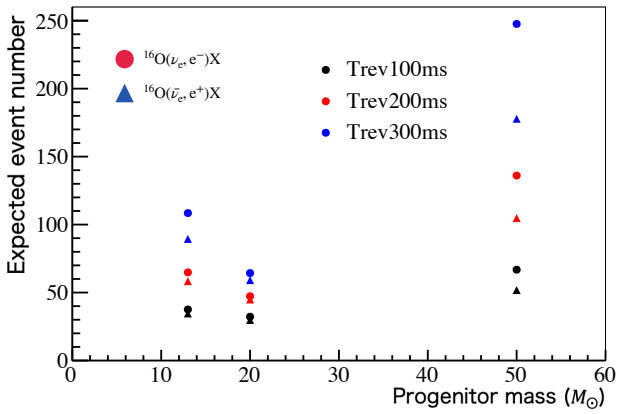

FIGURE 3.4: Expected numbers of CC interaction events. Black points correspond to $T_{\rm rev} = 100$ ms, red points to $T_{\rm rev} = 200$ ms, and blue points to $T_{\rm rev} = 300$ s. Circular markers represent CC interactions induced by electron neutrinos, while triangular markers represent CC interactions induced by electron antineutrinos.

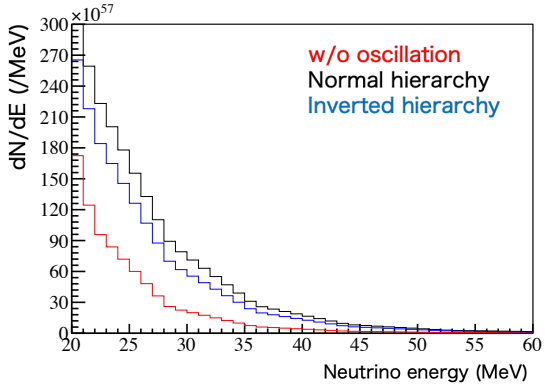

FIGURE 3.5: Neutrino energy spectra for the model of $20M_\odot$, $T_{\rm rev} = 100$ ms.

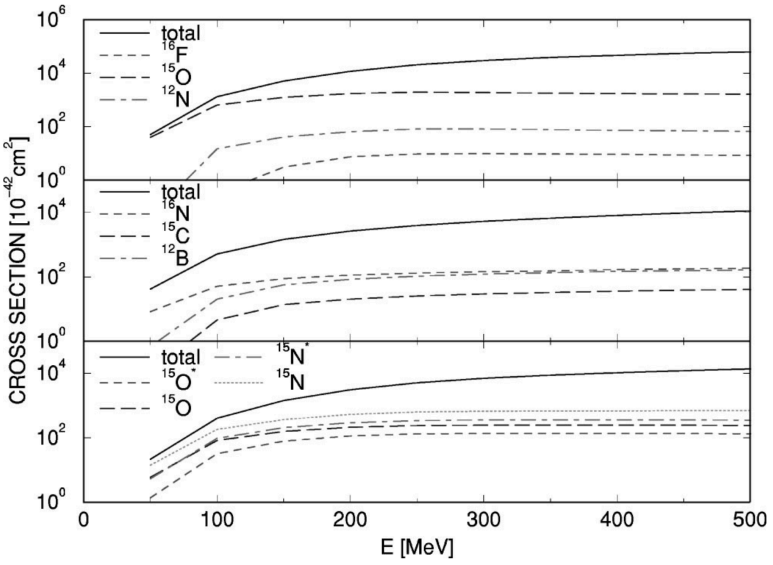

FIGURE 3.6: Neutrino interaction cross sections on ^{16}O as functions of neutrino energy [19]. The top panel shows the CC interaction (ν_e, e^-), the middle panel shows $(\bar{\nu}_e, e^+)$, and the bottom panel shows the NC interaction (ν, ν'). In the bottom panel, cross sections for reactions exceeding the particle emission threshold, such as those producing ^{15}N and ^{15}O, are also shown.

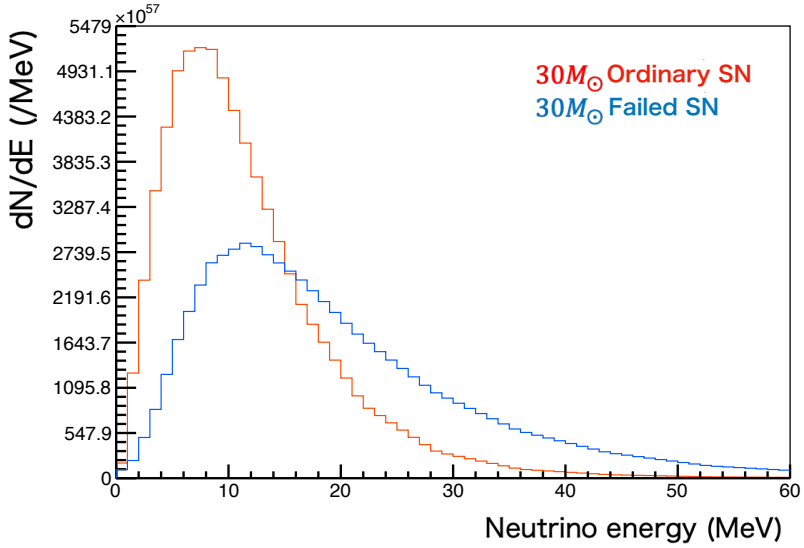

FIGURE 3.7: Neutrino energy spectra for the $30M_\odot$ ordinary SN model (red) and the $30M_\odot$ failed SN model (blue).

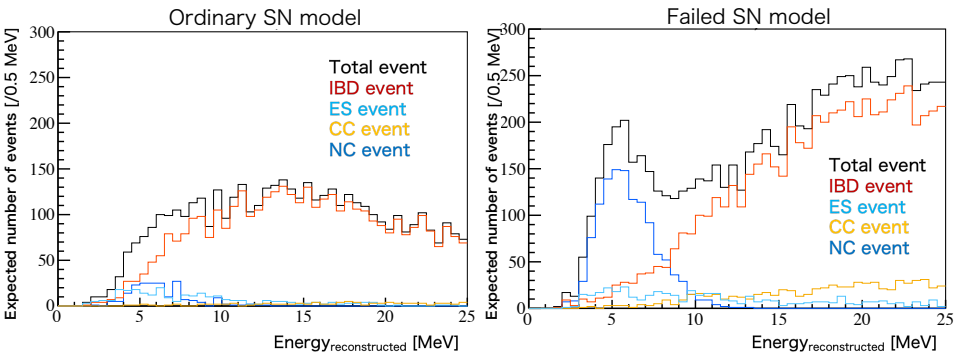

FIGURE 3.8: Reconstructed energy distributions for the ordinary SN model (left) and the failed SN model (right). The black histogram represents all events, while the red, light blue, yellow, and blue histograms correspond to IBD, ES, CC, and NC events, respectively.

Chapter 4

Study of Neutrinos Associated with Stellar Core Collapse

Building on SKSNSim as described in Section 3, I focus on the late-time neutrino emission from long-duration supernova models and study the corresponding observable signals at SK. In particular, I investigate methods to identify the last neutrino event detected in the burst and assess the potential to discriminate between different supernova models based on the timing characteristics of this final event [96].

4.1 Analysis of Neutrino Light Curves

4.1.1 Discriminating the Nuclear EOS

Determining the nuclear EOS enables us to infer the composition of nuclear matter inside neutron stars. Consequently, identifying the EOS from neutrino observations constitutes one of the major scientific goals. The EOS is most directly reflected in the mass–radius relation of neutron stars. Figure 4.1 shows the mass–radius relation of neutron stars formed in four supernova models: the Shen EOS, the Lattimer & Swesty EOS, and the Togashi EOS, all of which were introduced in Section 1.4, together with the hybrid T+S EOS [74], in which the high-density region with baryon number density $\rho_B \geq 10^{14.3}\ \mathrm{g\,cm^{-3}}$ follows the Togashi EOS while the low-density region with $\rho_B \leq 10^{14}\ \mathrm{g\,cm^{-3}}$ follows the Shen EOS.

The curves indicate the radii at which a star with a given mass can be supported in hydrostatic equilibrium by its internal pressure. Each EOS provides a different maximum mass that can be sustained. For example, in the Shen EOS model, the maximum mass corresponds to a radius of approximately $r = 13$ km. The T+S EOS was constructed to investigate how non-uniform nuclear matter near the surface of the PNS affects neutrino emission. The difference between the Togashi and T+S EOS models lies in the fraction of non-uniform nuclear matter in the outer layers of the PNS. By comparing their neutrino emission properties, one can assess the impact of non-uniform matter on the neutrino signal.

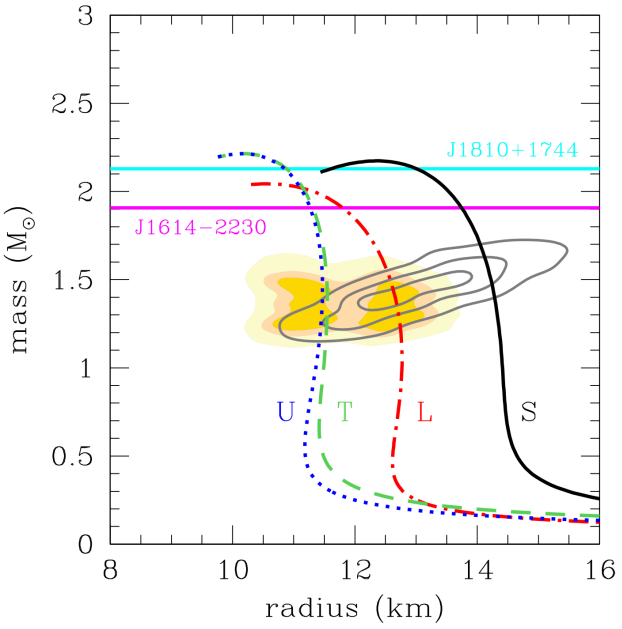

FIGURE 4.1: Mass–radius relation of neutron stars [20]. Black: Shen EOS; red: LS220 EOS; blue: T+S EOS; green: Togashi EOS. The shaded and enclosed regions represent observational constraints on neutron star masses and radii obtained from gravitational-wave and gamma-ray observations. The two horizontal lines indicate the masses of the most massive neutron stars observed so far.

For a neutron star of mass $1.5M_\odot$ in Figure 4.1, the predicted radius differs among the EOS models, increasing in the order of T+S EOS, Togashi EOS, LS220 EOS, and Shen EOS. Thus, once the EOS is identified, the neutron star radius can be constrained accordingly. This information is crucial for determining the density of matter composing neutron stars.

4.1.2 Differences in the Time Evolution of Neutrino Emission among EOS Models

Previous studies [21, 29] have carried out long-term simulations extending beyond 10 s in order to deepen our understanding of neutrinos emitted during the PNS cooling phase, focusing on the emission behavior and the expected event rates in SK. In Ref. [21], models based on the Shen EOS were constructed by varying the initial entropy and PNS mass to examine differences in the time evolution of neutrino emission. Figure 4.2 shows the initial entropy $s(m_b)$ and electron fraction $Y_e(m_b)$ used in that study. Since the entropy and electron fraction vary with the position inside the PNS, they are defined as

$$s(m_b) = \begin{cases} s_1 & (0 \le m_b \le 0.4\,M_\odot) \\ \dfrac{s_1(0.7\,M_\odot - m_b) + s_2(m_b - 0.4\,M_\odot)}{0.3\,M_\odot} & (0.4\,M_\odot \le m_b \le 0.7\,M_\odot) \\ s_2 & (0.7\,M_\odot \le m_b \le M_b) \end{cases} \tag{4.1}$$

$$Y_e(m_b) = \frac{0.3(M_b - m_b) + 0.5 m_b}{M_b}, \tag{4.2}$$

where M_b is the PNS baryon mass, defined as the total number of protons and neutrons multiplied by the atomic mass unit (931.494 MeV), and m_b denotes the baryon mass coordinate. Although the gravitational mass of a PNS changes over time due to energy loss by neutrino emission, the total baryon number remains conserved except for processes such as electron capture that convert protons into neutrons. Thus, the baryon mass is commonly used as a conserved mass descriptor, even though it does not account for the neutron–proton mass difference. Models with high and low initial entropies were constructed using $(s_1, s_2) = (2k_B, 6k_B)$ and $(1k_B, 4k_B)$, respectively. In addition to the fiducial PNS mass of $M_b = 1.47M_\odot$ [74], models with $M_b = 1.29M_\odot$ and $M_b = 2.35M_\odot$ were examined, corresponding to the lowest and highest neutron star masses observed in binary systems.

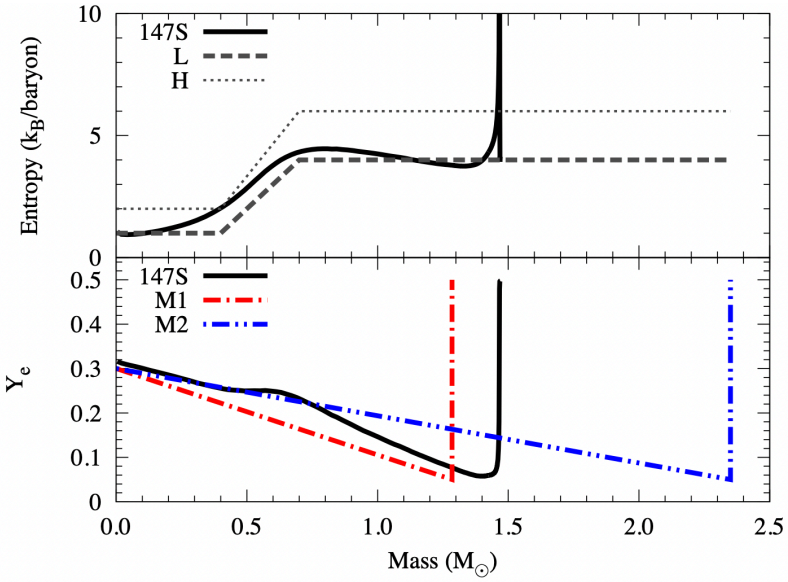

FIGURE 4.2: Initial entropy (upper panel) and electron fraction (lower panel) [21]. The horizontal axis shows the baryon mass coordinate defined in Eq. (1.35). In the upper panel, the thin dashed line represents the high-entropy model (H), and the thick dashed line represents the low-entropy model (L). In the lower panel, the red line corresponds to the low-mass model M1 ($M_b = 1.29M_\odot$), the blue line to the high-mass model M2 ($M_b = 2.35M_\odot$), and the black line shows the reference model with $M_b = 1.47M_\odot$.

The horizontal axis in Figure 4.2 represents the baryon mass coordinate defined in Eq. (1.35), where the origin corresponds to the stellar center and larger values correspond to positions closer to the stellar surface. The vertical axes show the entropy per baryon and the electron fraction. The behavior of the initial entropy and electron fraction is described as follows. The entropy profile exhibits a plateau around $m_b \simeq 0.7M_\odot$, which corresponds to the location of shock formation. In this mass coordinate region, the entropy increases as a result of shock heating. A second rise in entropy appears around $m_b = 1.47M_\odot$, which marks the position where infalling material collides with the shock front and kinetic energy is converted into thermal energy. Inside the shock radius, the entropy remains approximately $1\,k_B$ per baryon, reflecting the thermodynamic conditions of the inner core during collapse. The electron fraction decreases from the center outward to the shock position. When the shock encounters infalling iron-group nuclei, photodisintegration breaks them into free neutrons and

protons. These free protons undergo rapid electron capture,

$$\mathrm{p} + \mathrm{e}^- \rightarrow \mathrm{n} + \nu_e, \tag{4.3}$$

which proceeds much more efficiently than for bound nuclei, resulting in a decrease in Y_e in the region affected by the shock.

Ref. [29] discussed differences in the time evolution of neutrino emission among EOS models. In that study, PNS baryon masses of 1.40, 1.47, 1.54, and $1.62 M_\odot$, which represent the total baryonic rest mass of the PNS, are considered. For a PNS baryon mass of $1.47 M_\odot$, the PNS radius at $t = 50$ s measured from core bounce is 14.1 km for the Shen EOS and 11.8 km for the Togashi EOS [74]. As a consequence, the central density becomes higher in the Togashi EOS, reaching $\rho = 7.73 \times 10^{14}$ g cm^{-3}, compared to $\rho = 4.87 \times 10^{14}$ g cm^{-3} for the Shen EOS. A higher density leads to stronger neutrino–matter interactions inside the PNS and therefore a shorter neutrino mean free path. As a result, neutrino diffusion takes longer and produces a slower temporal decline in the luminosity. Figure 4.3 shows the time evolution of the neutrino light curves (upper panels) and average energies (lower panels) for the four EOS models introduced above. From the neutrino light curves, it is evident that the luminosity of the Shen EOS decreases more rapidly, whereas the Togashi EOS exhibits a more gradual decline. This behavior is primarily attributed to the differences in the PNS radius determined by the EOS, as shown in Figure 4.1. Comparing the light curves of the Togashi EOS and T+S EOS, their behavior remains similar up to $t \simeq 70$ s. This similarity indicates that the PNS evolution is largely determined by the high-density region of the EOS, which is shared between the two models.

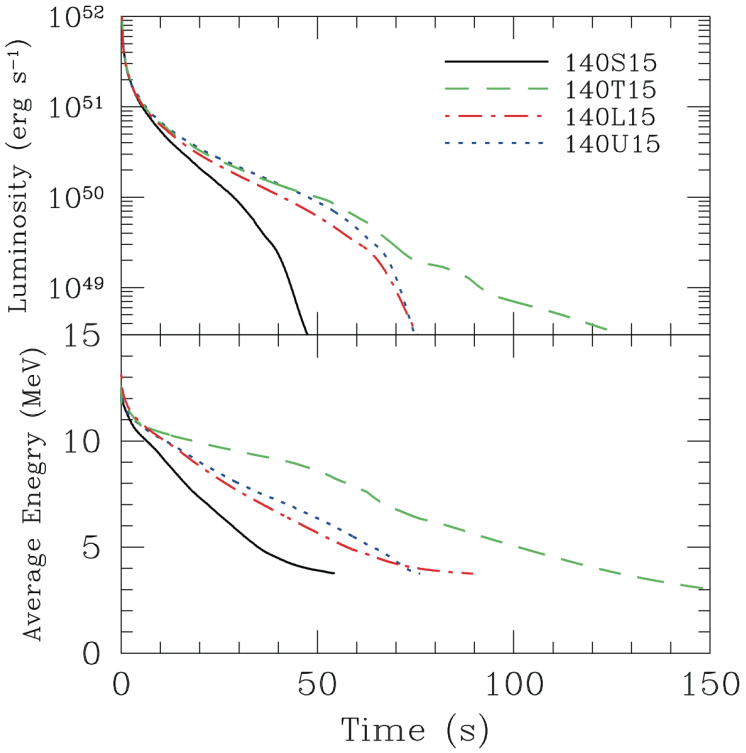

FIGURE 4.3: Time evolution of the electron antineutrino luminosity (upper panels) and average energy (lower panels) [20]. The PNS baryon mass used in these models is $1.40M_{\odot}$. Black, red, blue, and green lines correspond to the Shen, LS220, T+S, and Togashi EOS models, respectively. The progenitor mass of these models is $15M_{\odot}$.

4.1.3 Backward-Time Analysis

The time evolution of neutrino emission exhibits EOS dependence, particularly during the cooling phase of the PNS. Extracting this information can therefore contribute to discriminating among different EOS models. Figure 4.4 shows the cumulative number of expected supernova neutrino events in SK, where the time origin is defined by the first detected event.

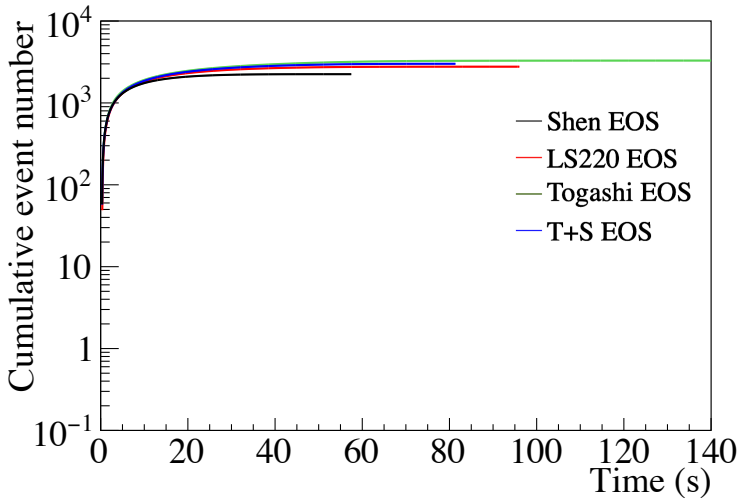

FIGURE 4.4: Time evolution of cumulative supernova neutrino events for different EOS models. Black, red, blue, and green lines represent the Shen, LS220, T+S, and Togashi EOS models, respectively. A PNS baryonic mass of $M_b = 1.40\,M_\odot$ is assumed.

As seen in Figure 4.4, the cumulative time evolution from the first event shows only minor differences among the EOS models, making discrimination difficult. To address this, Suwa et al. [21] proposed a "Backward-Time Analysis", which uses neutrinos emitted during the PNS cooling phase to distinguish differences in mass and initial entropy. The result of their analysis is shown in Figure 4.5. In this method, the time origin is defined by the *last* detected neutrino event, and the cumulative number of events is plotted as a function of time counted backward (e.g., 10 s or 20 s before the last event).

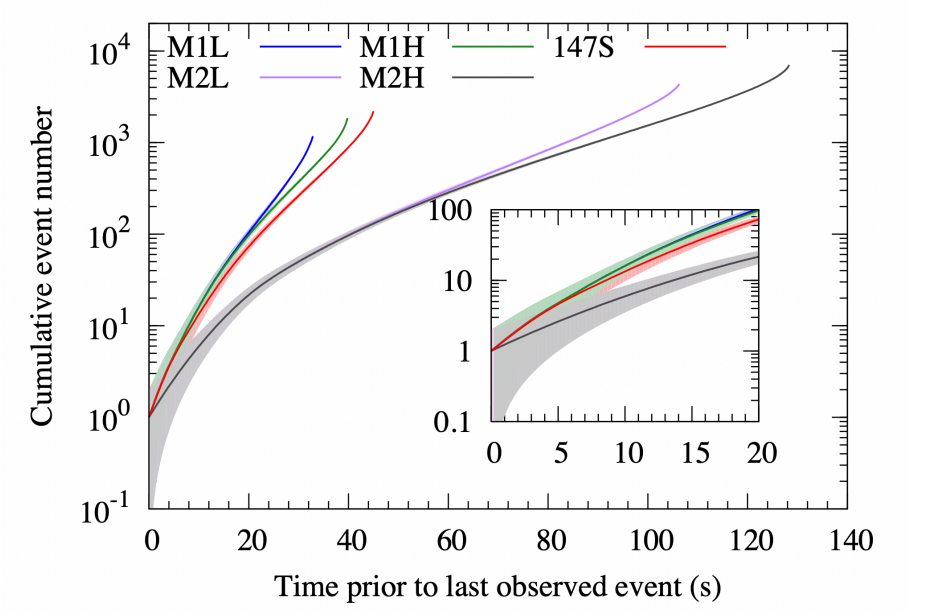

FIGURE 4.5: Comparison of PNS mass and initial entropy using the Backward-Time Analysis [21]. The labels follow the same notation as in Figure 4.2.

As shown in Figure 4.5, in contrast to the forward-time evolution in Figure 4.4, the dependence on PNS mass becomes pronounced. Furthermore, extending the backward integration time makes it possible to distinguish differences in the initial entropy, such as those between the M1L and M1H models at integration times of around 20 s. A subsequent study [20] investigated the effects of EOS and PNS mass on neutrino emission by applying the Backward-Time Analysis to a set of 32 supernova models. The models include the four EOS models presented in Section 4.1.1. The assumed PNS baryonic masses are 1.40, 1.47, 1.54, and 1.62 $M_\odot$ for progenitors of 15 $M_\odot$, and 1.62, 1.70, 1.78, and 1.86 $M_\odot$ for progenitors of 40 $M_\odot$. Figure 4.6 shows the EOS dependence of the backward-time evolution. Unlike the mass dependence seen in Figure 4.5, the EOS dependence is much more significant. In all mass cases, the Shen EOS exhibits the shortest backward-time evolution due to its steep luminosity decay, whereas the Togashi EOS shows the longest evolution corresponding to its slower luminosity decline.

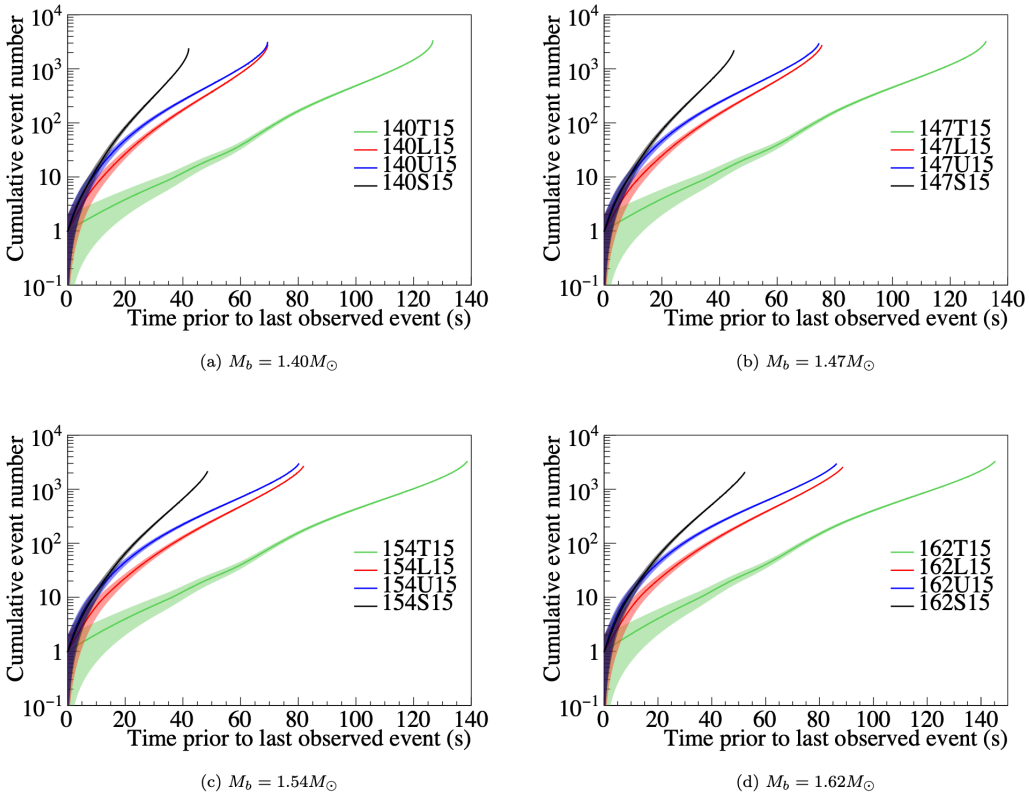

(a) $M_b = 1.40 M_\odot$ (b) $M_b = 1.47 M_\odot$

(c) $M_b = 1.54 M_\odot$ (d) $M_b = 1.62 M_\odot$

FIGURE 4.6: Differences in backward-time evolution for various EOS models [20]. Black, red, blue, and green correspond to Shen, LS220, T+S, and Togashi EOS, respectively. The panels show baryonic masses of 1.40 $M_\odot$ (upper left), 1.47 $M_\odot$ (upper right), 1.54 $M_\odot$ (lower left), and 1.62 $M_\odot$ (lower right).

Figure 4.7 shows the dependence on PNS baryonic mass. Although the differences are smaller than those between EOS models, the separation becomes more pronounced as the backward-time window increases, regardless of the EOS.

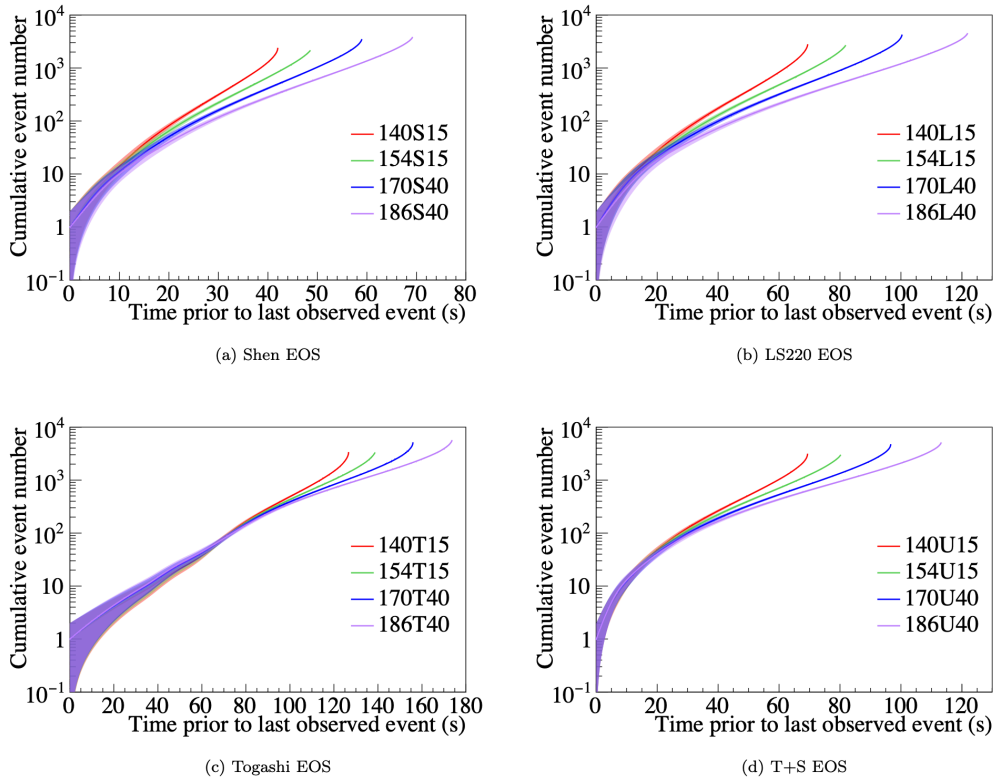

(a) Shen EOS

(b) LS220 EOS

(c) Togashi EOS

(d) T+S EOS

FIGURE 4.7: Backward-time evolution for different PNS baryonic masses [20]. Colors indicate PNS mass: red ($1.40\,M_{\odot}$), green ($1.54\,M_{\odot}$), blue ($1.70\,M_{\odot}$), and purple ($1.86\,M_{\odot}$). The panels correspond to Shen (upper left), LS220 (upper right), Togashi (lower left), and T+S EOS (lower right).

These studies demonstrate that, if the time of the final neutrino event can be identified in an actual observation, the Backward-Time Analysis can be used to constrain both the EOS and the PNS mass. However, both previous works considered only IBD events in SK and did not include other interaction channels, such as ES and interaction with oxygen nuclei. Moreover, they did not address quantitative background estimation or how the last observed event should be identified in the presence of background. In this study, I perform a realistic estimation of the expected number of detected events in SK using all neutrino interaction channels described in Section 3, rather than IBD alone.

4.2 Framework for Mock Data Construction

4.2.1 Supernova signal

I simulate the supernova neutrino signal using SKSNSim as presented in Section 3. In this study, I demonstrate the four neutrino interaction channels observed in SK for neutrino energies below 100 MeV—IBD, ES, CC interactions on oxygen, and NC interactions on oxygen—as described in Section 3.1.3.

4.2.2 Background sources and reduction strategies

In this study, to reflect realistic observational conditions, I adopt the background estimation from [22]. This step is an essential component for developing a realistic method to determine the last observed event.

In searches for supernova neutrinos, several types of background must be considered, including radioimpurities, spallation products, decay electrons from muons, and atmospheric neutrinos. Among these, spallation backgrounds originate from cosmic-ray muons traversing the detector, which interact with oxygen nuclei in the water and induce nuclear breakup. These interactions produce radioactive isotopes that subsequently decay and generate low-energy events that can appear similar to supernova neutrino signals. The detailed properties of spallation backgrounds and the corresponding reduction techniques are described in Section 5.4.4. In particular, the suppression of spallation backgrounds is essential for analyses of late-phase CCSN neutrinos, which are characterized by low event rates. Spallation events are spatially and temporally correlated with the trajectories of cosmic-ray muons, and are largely suppressed by the "spallation cut," which removes about 90% of such events [97], though at the cost of ∼20% loss of genuine supernova neutrino signals [98]. The methods used to suppress these radioactive and spallation backgrounds are described in detail in Section 5.4.

Figure 4.8 shows the expected background rates in SK as estimated by [22] for three cases: within the FV, within FV after applying a spallation cut, and outside FV. It shows that the FV cut removes 96.1% of background events in the ID and that 64.7% of the remaining background is eliminated by the spallation cut, which applies the 80% criterion described above. Consequently, the final background rate after spallation cut in FV for events with reconstructed energies above 5 MeV is 8.2×10^{-3} (s^{-1}).

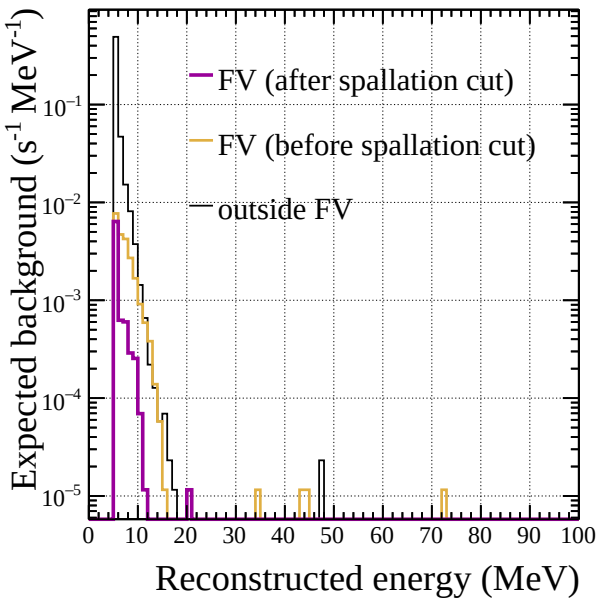

FIGURE 4.8: Background rate for the FV (orange), FV with spallation cut (violet), and outside FV (black) samples in SK. Background rates are generated according to [22]. In the present analysis, I use the background rate above 5 MeV following that study.

In Figure 4.9, an example scatter plot showing the true neutrino energy of MC as a function of time for a single MC simulation is presented. These signal events correspond to the model featuring the Shen EOS and a $1.40M_{\odot}$ PNS mass. Figure 4.9 (a) and (b) respectively represent the event distribution in the entire ID case and that with both the FV and spallation cuts applied. In this analysis, both the FV cut and the spallation cut are applied to ensure a low-background environment.

Averaged over all models, approximately 69% of the signal events remain after applying the FV cut, and about 55% remain after the additional spallation cut. The specific interaction channel does not affect the signal efficiency.

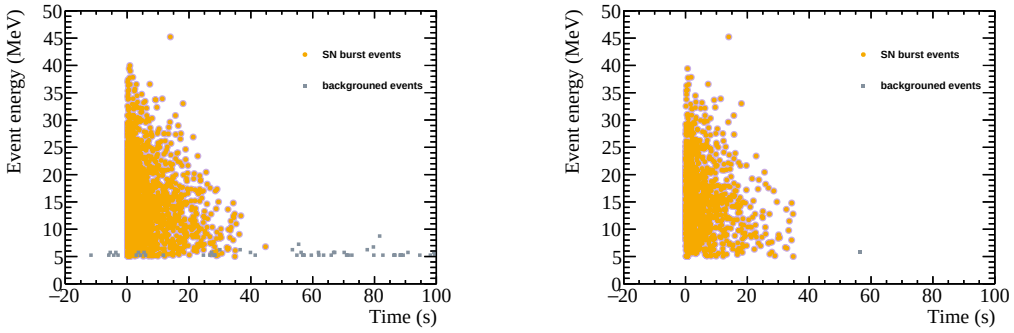

(A) Entire inner detector (ID) (B) After reduction

FIGURE 4.9: An example scatter plot showing the visible energy of the observed events in SK as a function of time from the supernova explosion based on a single simulation. Signal events, represented by the orange points, and background events, represented by the gray points, are shown for the case with an energy threshold of 5 MeV. For signal events, I use the Shen EOS with a $1.40M_{\odot}$ PNS mass. Panel (a) is assumed to be the full volume observation, while panel (b) applies a spallation cut within the fiducial volume.

4.2.3 Technique to determine the last observed event

In this section, I describe how to determine the last observed event. The CCSN models used in this study are Shen EOS, LS220 EOS, Togashi EOS, and Furusawa-Togashi EOS, whose details are provided in Section 1.4. The summary of expected neutrino events in SK for each of the progenitor mass and baryonic mass of the neutron star is shown in Table 4.1. In this table, full volume observation in SK is assumed. To begin with, by performing 1000 SN event generations using SKSNSim, I investigate the distribution of the last observed event under the assumption of no background and no cuts. The detection time of the last observed event, generated without any cuts or background, is denoted as $T_{\rm last}^{\rm true}$ and its resulting distribution is shown in Figure 4.10. Some of the $T_{\rm last}^{\rm true}$ distributions are terminated at the right-edge, because the numerical simulation covers a finite time range. The Shen EOS exhibits the shortest $T_{\rm last}^{\rm true}$, while the Togashi EOS features the longest. Additionally, the Togashi EOS has a broader distribution. The $T_{\rm last}^{\rm true}$ behavior is attributed to the luminosity evolution; $T_{\rm last}^{\rm true}$ tends to be shorter for a rapid decline in luminosity, whereas a slower luminosity decline results in a longer $T_{\rm last}^{\rm true}$, as shown in Figure 1.18.

In a realistic analysis, the time of the last observed signal needs to be determined in the presence of possible background contamination. Therefore, I develop a method for determining the last observed event based on two key parameters: the time width ($T_{\rm wid}$), which defines a time window for event selection, and an energy threshold

TABLE 4.1: Expected number of events for each interaction channel for the PNS cooling models. These event numbers are calculated under the assumption that the full volume of SK is used. The total number of events includes all neutrinos with energies above 0 MeV.

Model	$M_{\mathrm{ZAMS}}(M_\odot)$	EOS	$M_b(M_\odot)$	Total	IBD	ES	CC(ν_e, e^-)	CC($\bar{\nu}_e, e^+$)	NC(ν, p)	NC(ν, n)
140S15	15	Shen	1.40	2836.8	2538.2	264.8	2.0	11.0	16.5	4.4
147S15	15	Shen	1.47	2549.9	2274.8	246.5	1.7	9.9	13.3	3.6
154S15	15	Shen	1.54	2486.3	2217.6	243.2	1.7	9.5	11.2	3.0
162S15	15	Shen	1.62	2413.4	2151.4	238.7	2.1	9.2	9.5	2.6
162S40	40	Shen	1.62	4048.6	3634.0	367.1	2.8	15.6	22.9	6.2
170S40	40	Shen	1.70	4179.7	3748.1	382.0	3.2	16.6	23.4	6.3
178S40	40	Shen	1.78	4289.1	3842.6	396.1	3.4	17.2	23.3	6.3
186S40	40	Shen	1.86	4421.5	3958.8	412.0	3.7	17.8	23.0	6.2
140L15	15	LS220	1.40	3413.2	3059.7	307.9	3.5	15.9	20.6	5.6
147L15	15	LS220	1.47	3185.4	2846.9	298.4	3.3	14.6	17.4	4.7
154L15	15	LS220	1.54	3070.8	2740.7	295.0	3.4	13.5	14.4	3.9
162L15	15	LS220	1.62	2919.1	2600.8	288.3	3.3	12.2	11.4	3.1
162L40	40	LS220	1.62	4855.6	4359.8	430.3	5.4	23.0	29.2	7.9
170L40	40	LS220	1.70	5001.0	4483.1	449.2	6.3	24.3	29.9	8.1
178L40	40	LS220	1.78	5124.7	4586.9	467.9	7.3	25.2	29.5	8.0
186L40	40	LS220	1.86	5256.6	4698.4	487.7	8.2	25.8	28.7	7.8
140F15	15	Furusawa-Togashi	1.40	3958.9	3551.7	358.4	4.2	18.1	20.8	5.6
147F15	15	Furusawa-Togashi	1.47	3692.8	3303.2	345.6	4.2	17.4	17.6	4.8
154F15	15	Furusawa-Togashi	1.54	3709.7	3314.5	352.7	4.5	17.4	16.3	4.4
162F15	15	Furusawa-Togashi	1.62	3645.3	3249.8	355.1	4.7	16.6	15.0	4.1
162F40	40	Furusawa-Togashi	1.62	5648.0	5071.0	506.2	6.4	25.8	30.3	8.2
170F40	40	Furusawa-Togashi	1.70	6012.1	5395.1	540.3	7.4	28.4	32.2	8.7
178F40	40	Furusawa-Togashi	1.78	6240.1	5593.2	566.3	8.3	30.3	33.0	8.9
186F40	40	Furusawa-Togashi	1.86	6442.9	5767.8	592.1	9.2	31.8	33.1	8.9
140T15	15	Togashi	1.40	3936.7	3535.7	350.7	3.4	16.8	23.6	6.4
147T15	15	Togashi	1.47	3716.1	3330.5	338.8	3.5	16.3	21.3	5.8
154T15	15	Togashi	1.54	3777.6	3385.1	346.1	3.8	16.6	20.5	5.5
162T15	15	Togashi	1.62	3761.2	3367.4	348.5	4.0	16.4	19.6	5.3
162T40	40	Togashi	1.62	5634.4	5065.5	495.7	5.3	24.1	34.5	9.3
170T40	40	Togashi	1.70	6016.3	5407.3	529.1	6.2	26.5	37.1	10.0
178T40	40	Togashi	1.78	6277.2	5637.0	555.4	7.1	28.5	38.8	10.5
186T40	40	Togashi	1.86	6514.7	5845.3	581.0	7.9	30.1	39.6	10.7

(E_{th}) which is applied to individual events to reject low-energy background events. The detection time of the last observed event selected using the method is denoted as T_{last}. Figure 4.11 shows a schematic diagram of how T_{last} is determined. The time T is measured relative to the first supernova neutrino event observed in SK ($T = 0$). In order to determine T_{last}, events with $T \geq 0$ and with energies a given threshold E_{th} are counted within a sliding interval with a given width T_{wid}. The interval slides forward in time until events are no longer detected. The time of the latest event in last interval with events is then defined as T_{last}.

In the following analysis, T_{wid} and E_{th} are chosen to ensure that the event defining T_{last} is inconsistent with the expected background at a significance level greater than 5σ. To achieve this condition, I use the background rate in the FV after applying the spallation cut described above (Figure 4.8). A suitable combination of T_{wid} and an E_{th} is determined based on Poisson statistics, assuming only the measured background rate to establish the required detection significance. I note that the background is more easily rejected with smaller values of T_{wid} and larger values of E_{th}. In contrast, most signal events are likely to survive even under these conditions due to their concentration within tens of seconds and relatively high energies. Some combinations of T_{wid} and E_{th} satisfying the detection requirements above are summarized in Table 4.2.

Figure 4.12 shows the T_{last} distributions selected based on T_{wid} and E_{th} for four models. For $T_{\mathrm{wid}} \geq 5$ s, the distributions are largely consistent except for the Togashi EOS, where more variation is seen. Note that lowering E_{th} in general increases the total number of detected events, improving the statistical reliability. In particular, since the average neutrino energy decreases in the late emission phase, lowering E_{th}

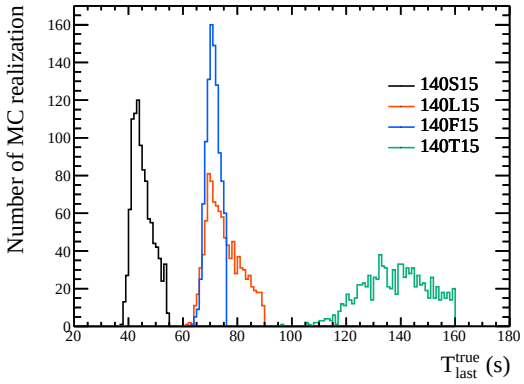

FIGURE 4.10: T^{true}_{last} distribution for PNS models with a baryon mass of $M_b = 1.40 M_\odot$, represented as follows: black for the Shen EOS, red for the LS220 EOS, blue for the Furusawa-Togashi EOS, and green for the Togashi EOS case. This plot is made from 1000 MC realizations; the vertical axis shows the number of MC realizations per second. I assume observations from a supernova at a distance of 10 kpc.

TABLE 4.2: Pairs of time width and energy threshold that provide no background events at greater than 5σ for FV events.

Time width (T_{wid}) [s]	Energy threshold (E_{th}) [MeV]
1	6.0
5	8.0
10	9.5
20	10.0

allows for the detection of more events from that phase. Therefore, I select $T_{wid} = 5$ s and $E_{th} = 8.0$ MeV for the analysis presented below. As a result of this energy cut, the signal efficiency remains approximately 47% for all supernova models, while about 98% of background events are rejected.

4.2.4 Backward Time Analysis Results and Their Implications

In this section, I show the T_{last} distribution determined from mock samples and the cumulative event distribution starting from T_{last} as time origin. The results presented here are all produced under the proper background consideration from the previous section. Model discrimination using the T_{last} information is also discussed.

Analysis based on the T_{last} distribution

The T_{last} distributions for several models and for different PNS baryonic masses as determined by the method described in Section 4.2.3 are shown in Figure 4.13. Summary information from those distributions is additionally presented in Table 4.3. Comparing Figure 4.10 and Figure 4.13 (a) shows that the value of T_{last} tends to be smaller than T^{true}_{last}. This is because the method using $T_{wid} = 5$ s is more likely to select events earlier than T^{true}_{last} in the final stage of PNS cooling, where the interval between signal events is expected to be only a few seconds, and also because some events are lost due to the energy threshold cut. Figure 4.14 shows the time evolution of signal intervals, which increase beyond 5 seconds as the final stage of PNS cooling. T^{true}_{last} in the final

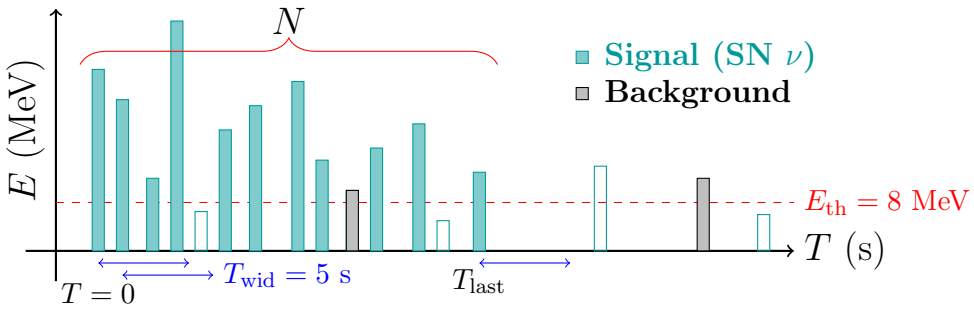

FIGURE 4.11: Schematic diagram of $T_{\rm last}$ determination method. It represents supernova neutrino and background events plotted over time, with their corresponding energy values represented on the vertical axis. Green box shows supernova neutrino events whose energy is more than $E_{\rm th}$ and the black boxes indicate background events. White boxes with green outlines show supernova neutrino events that are excluded because their energy is below a $E_{\rm th}$ or their time difference from $T_{\rm last}$ exceeds $T_{\rm wid}$.

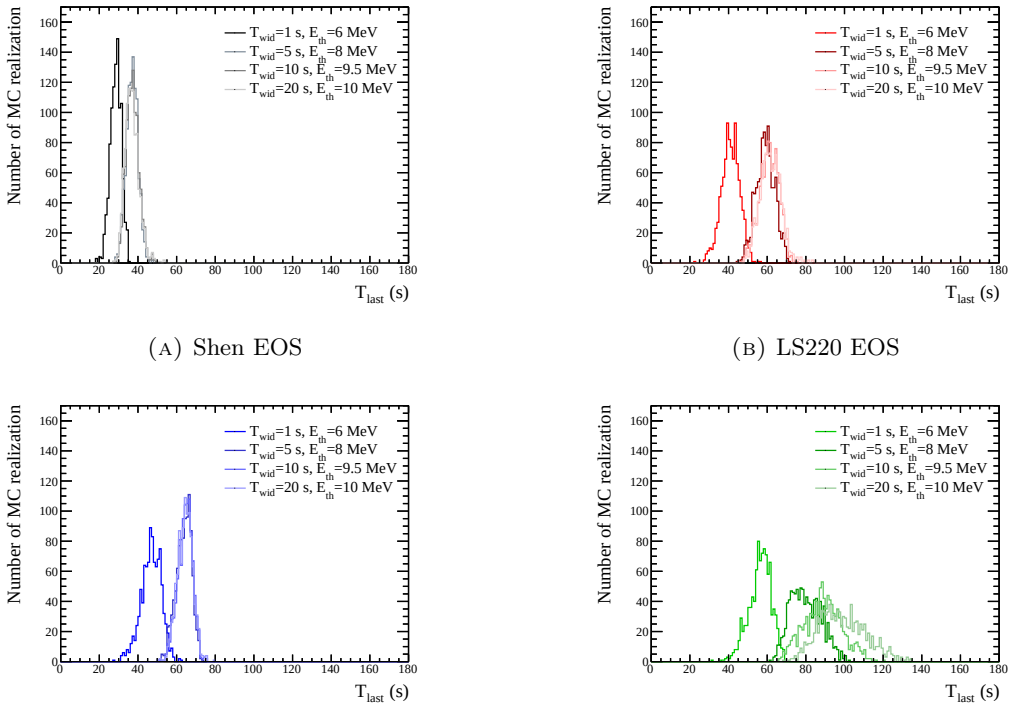

(A) Shen EOS

(B) LS220 EOS

(C) Furusawa–Togashi EOS

(D) Togashi EOS

FIGURE 4.12: The $T_{\rm last}$ distribution for each combination of $T_{\rm wid}$ and $E_{\rm th}$. Panel (a), (b), (c), and (d) correspond to Shen EOS, LS220 EOS, Furusawa–Togashi EOS, and Togashi EOS, respectively. Here, the PNS models with mass of $M_b = 1.40 M_\odot$ and $M_{\rm ZAMS} = 15 M_\odot$ are shown.

stage of PNS cooling, where the interval between signal events is expected to be only a few seconds. In this analysis, the last observed event is required to be identified as

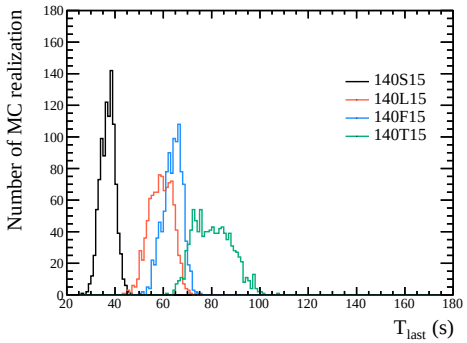

(a) $M_b = 1.40M_\odot$, $M_{\rm ZAMS} = 15M_\odot$

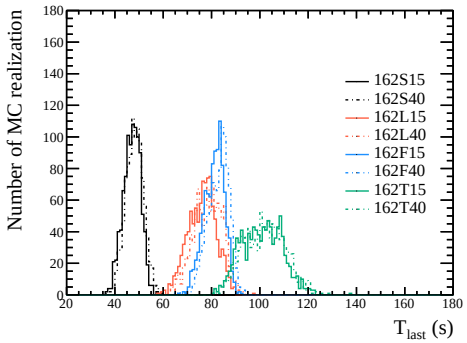

(b) $M_b = 1.62M_\odot$, $M_{\rm ZAMS} = 15M_\odot$, $40M_\odot$

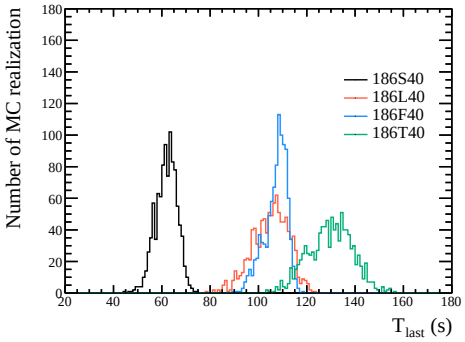

(c) $M_b = 1.86M_\odot$, $M_{\rm ZAMS} = 40M_\odot$

FIGURE 4.13: $T_{\rm last}$ distribution. The black, red, blue, and green lines represent Shen EOS, LS220 EOS, Furusawa–Togashi EOS, and Togashi EOS, respectively. The horizontal axis shows $T_{\rm last}$ for each MC realization, and the vertical axis shows the number of MC realizations in 1-second bins. The solid and dashed lines in panel (b) correspond to $M_{\rm ZAMS} = 15M_\odot$ and $M_{\rm ZAMS} = 40M_\odot$, respectively.

a signal with a significance exceeding 5σ, which leads to $T_{\rm last}$ rarely coinciding with $T_{\rm last}^{\rm true}$. Nevertheless, as shown in Figure 4.13, the expected differences among models can be seen. Consistent with the trend shown in Figure 4.10, the Shen EOS results in the shortest $T_{\rm last}$, while the Togashi EOS shows the longest. Furthermore, $T_{\rm last}$ tends to become longer with the PNS baryonic mass.

I use the cumulative event number to estimate how long neutrinos are detectable. Figure 4.15 (a) shows the backward time distribution for the model in Figure 4.13 (a). The curves show the expected cumulative event distributions, plotted backward in time from $T_{\rm last}$, which is taken as the time origin. Horizontal error bars indicate the range of times falling within 1σ around the mean estimated from 1000 MC simulations. The backward cumulative distribution exhibits a different time profile depending on the EOS model and PNS mass. In particular, the Shen EOS and the Togashi EOS distributions show a relatively large separation, while LS220 and Furusawa-Togashi EOS overlap somewhat. These features reflect the differences in luminosity evolution as described in Section 4.2.3.

When the event times are measured relative to $T_{\rm last}$, the horizontal error bars increase as events accumulate, giving the appearance of overlap among the models. Figure 4.15 (b) shows the distribution when the time baseline is set to that of the

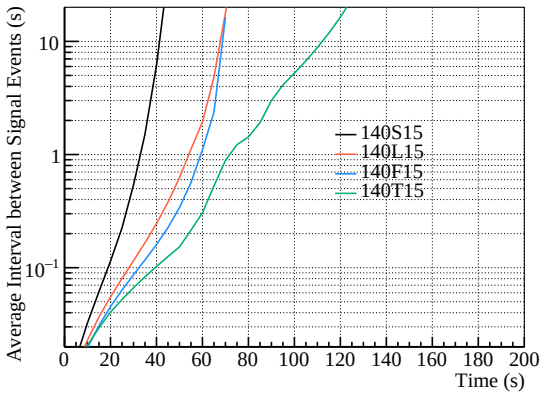

FIGURE 4.14: Average interval between signal events as a function of time after the bounce. The black, red, blue, and green represent Shen EOS, LS220 EOS, Furusawa-Togashi EOS, and Togashi EOS, respectively.

500-th-to-last event, while still plotting the event accumulation starting from T_{last}. The curves are the same as those in Figure 4.15 (a), but the error bars indicate the magnitude of the time uncertainty, measured from the updated reference event. This shift in the reference clearly reduces the width of the error bars and better indicates the differences between models.

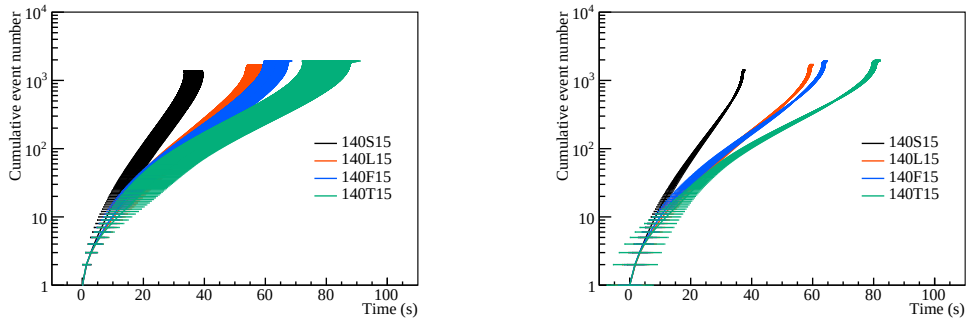

(a) Error bars evaluated from T_{last}.

(b) Error bars evaluated from T_{500}.

FIGURE 4.15: Backward time analysis comparing different EOSs. The horizontal axis represents backward time, which sets the last observed event as the time origin, and the vertical axis represents the cumulative event number from that event. The black, red, blue, and green represent Shen EOS, LS220 EOS, Furusawa–Togashi EOS, and Togashi EOS, respectively. In both panels, the curves show the expected time evolution of the cumulative event number starting from T_{last}. In panel (a), the timing uncertainties are evaluated with the time origin set at T_{last} and are indicated by the error bars. In panel (b), the time origin is shifted to the 500-th-to-last event (T_{500}), and the error bars reflect the reduced timing uncertainties achieved by referencing this earlier event.

The same backward analysis applied to models with differing PNS baryonic masses is shown in Figure 4.16. Both panels use the same time origins as the corresponding panel in Figure 4.15. Compared to the differences between EOS models, the variations

in the baryonic mass are smaller because the behavior of the backward cumulative distribution is mainly characterized by the time evolution of the luminosity. As shown in Figure 1.18, the evolution of the luminosities is similar for different PNS masses when they have a common EOS.

Analyzing intermediate events rather than only the final event improves the statistics and makes the differences between models more visible. Focusing on the time evolution beyond the 500-th-to-last event counting from the last observed event, I summarize the time difference between the 500-th-to-last and 1000-th-to-last events in Figure 4.17 and Table 4.3. Panel (b) of the Figure 4.17 compares distributes for 15 and $40 M_{\rm ZAMS}$ for models with the same EOS and PNS mass ($M_b = 1.62 M_\odot$). The differences are small and within errors as shown in the table. Here, the differing $M_{\rm ZAMS}$ values imply differences in the initial entropy. While analysis results using all events throughout the entire neutrino emission period do depend on the initial entropy, as discussed in [21], this time analysis using the late-phase does not depend on the physics during the early phase of collapse, such as initial entropy. Furthermore, some models with different combinations of PNS mass and EOS exhibit similar time differences, such as the models with 147L15 (6.93 ± 0.40 s) and 178S40 (6.91 ± 0.35 s) as listed in the table. The combination of $T_{\rm last}$ distribution shown in Figure 4.13 and the backward time analysis presented in Figure 4.15 and 4.16 improves the ability to distinguish between such models.

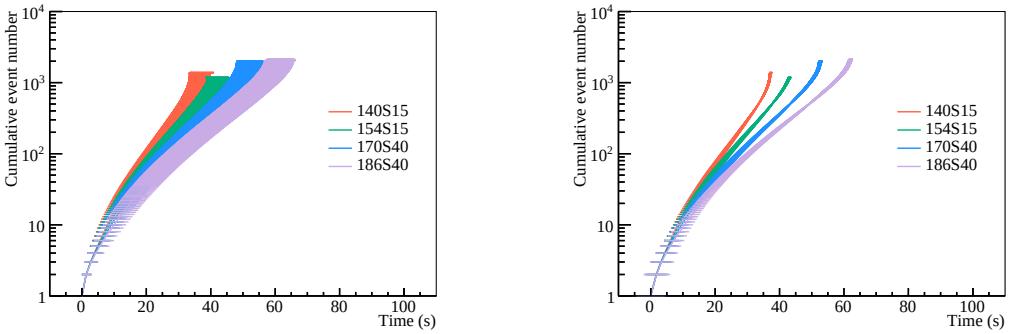

(a) Error bars evaluated from $T_{\rm last}$. (b) Error bars evaluated from T_{500}.

FIGURE 4.16: Same as Figure 4.15, but showing the comparison of different PNS baryonic masses in Shen EOS. The red, green, blue, and light purple represent $M_b = 1.40\,M_\odot$, $M_b = 1.54\,M_\odot$, $M_b = 1.70\,M_\odot$, and $M_b = 1.86\,M_\odot$, respectively.

4.3 Discussion and Conclusion

4.3.1 Demonstration of model discrimination

Here, I investigate the potential of using $T_{\rm last}$ for supernova model discrimination in the presence of experimental background. I adopt a Bayesian framework, where the posterior probability of a certain model is given by Bayes' theorem:

$$P(\text{model}|T_{\rm last}) = \frac{\text{PDF}(T_{\rm last}|\text{model}) \times P(\text{model})}{\sum_{\text{model}} [\text{PDF}(T_{\rm last}|\text{model}) \times P(\text{model})]} \tag{4.4}$$

where "model" denotes those in Table 4.3, each characterized by a different EOS, M_b and $M_{\rm ZAMS}$. Meanwhile, $\text{PDF}(T_{\rm last}, \text{model})$ represents the probability density

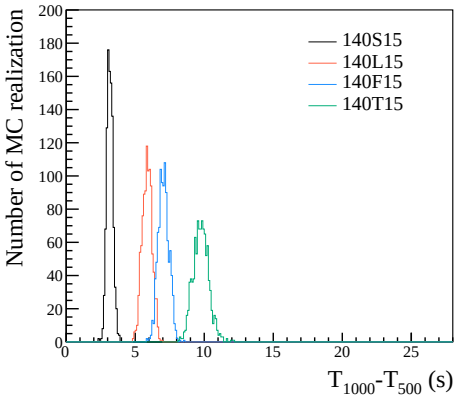

(a) $M_b = 1.40M_\odot,\ M_{\rm ZAMS} = 15M_\odot$

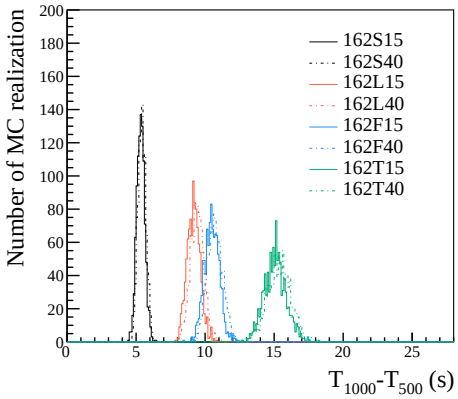

(b) $M_b = 1.62M_\odot,\ M_{\rm ZAMS} = 15M_\odot,\ 40M_\odot$

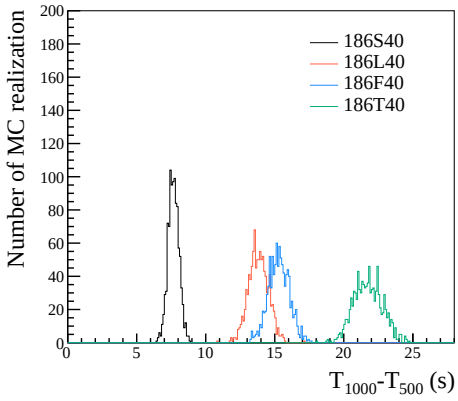

(c) $M_b = 1.86M_\odot,\ M_{\rm ZAMS} = 40M_\odot$

FIGURE 4.17: The time difference distribution between the 500-th-to-last event and the 1000-th-to-last event. The black, red, blue, and green lines represent Shen, LS220, Furusawa–Togashi, and Togashi EOS, respectively. The horizontal axis shows the difference between the time of the 500-th-to-last event (T_{500}) and that of the 1000-th-to-last event (T_{1000}). In panel (b), the solid and dashed lines correspond to $M_{\rm ZAMS} = 15M_\odot$ and $M_{\rm ZAMS} = 40M_\odot$, respectively.

function (PDF) obtained from Figure 4.13 and $P(\text{model})$ is the prior probability. In this analysis, I assume a uniform prior, assigning an equal probability to all 32 models, i.e., $P(\text{model}) = 1/32$. Here, models of $M_b = 1.62 M_\odot$ with different M_{ZAMS} are treated separately. I evaluate $P(\text{model}|T_{\text{last}})$ every 4 sec for $0 < T_{\text{last}} < 160$ s and present the results in Figure 4.18. While identifying both the PNS baryonic mass and the EOS is difficult, this analysis demonstrates that it is possible to distinguish between the Shen and Togashi EOS. As shown in Figure 1 of [20], the mass-radius relations of cold neutron stars differ between EOS models. For a given neutron star mass, the Shen EOS corresponds to an EOS with a large radius, and EOS models with a larger radius tend to be associated with a shorter T_{last}. On the other hand, the distinctive feature of the Togashi EOS is its high abundance of heavy nuclei within the PNS. The nuclear composition influences T_{last}, leading to longer times when more nuclei with higher mass numbers are present. In summary, based on this probability calculation, a shorter T_{last} suggests a lower central density in the neutron star, whereas a longer T_{last} suggests the presence of heavy nuclei near the surface region.

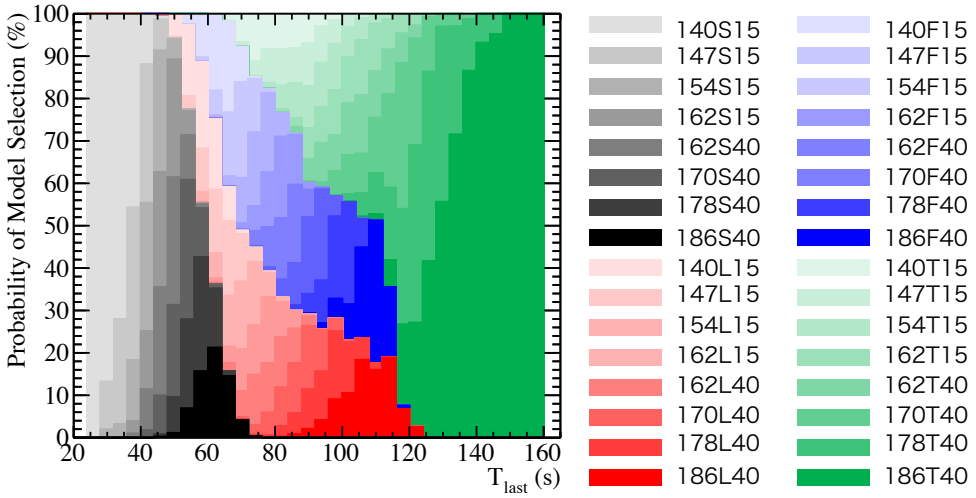

FIGURE 4.18: The probability of model selection for each model (vertical axis) given a certain T_{last} (horizontal axis), with a bin width of 4 sec. The color gradients represent different models: Shen (gray to black), LS220 (light red to red), Furusawa-Togashi (light blue to blue), and Togashi (light green to green). The differences in color intensity represent variations in the baryonic mass of the PNS, with darker colors indicating higher mass.

Figure 4.19 shows the model selection probability calculated using Equation 4.4, but with T_{last} changed to the time difference between the 500-th-to-last and 1000-th-to-last events. As in Figure 4.18, calculations using the time difference can also narrow down possible EOS candidates. The impact of background contamination in both Figures 4.18 and 4.19 is negligible, as confirmed by mock samples without background that produce consistent results. This negligible impact is due to the background suppression to the 5σ significance level, as discussed in Section 4.2.3.

4.3.2 Conclusion

I simulated late-phase supernova neutrino events in the SK detector and developed a new analytical framework to identify the last observed event and its time, T_{last},

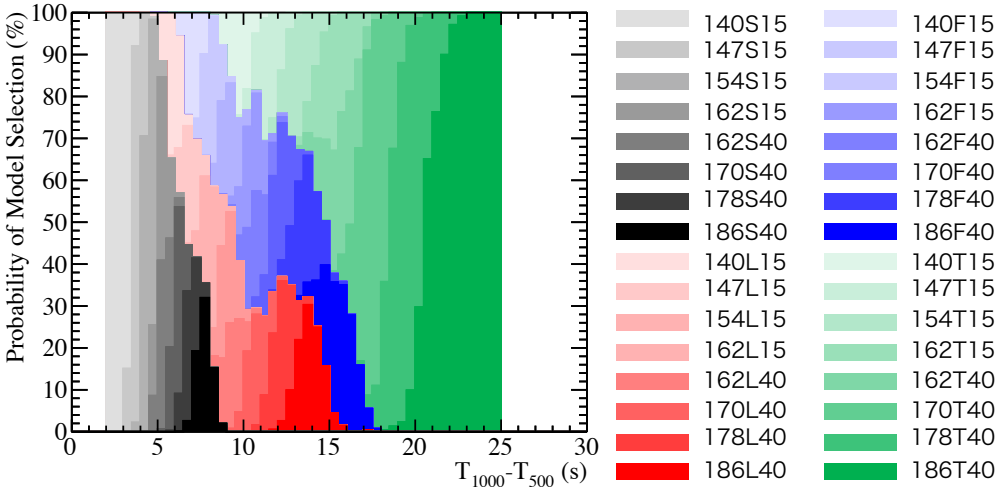

FIGURE 4.19: The probability of model selection (vertical axis) given a certain time difference (horizontal axis), with a bin width of 0.5 s. The color gradients are the same as Figure 4.18.

while explicitly accounting for realistic background contamination. I demonstrated that $T_{\rm last}$ can be used to differentiate between CCSNe models with different PNS masses and EOS. Furthermore, by performing a backward time analysis with $T_{\rm last}$ as the time origin, I have shown, in particular, that the Shen EOS and Togashi EOS can be effectively distinguished. In addition, I found that timing information from earlier events, such as T_{500}, can reduce statistical fluctuations and improve discrimination between models with similar time evolution, like those with the LS220 EOS and Furusawa-Togashi EOS. However, I also found that changing $M_{\rm ZAMS}$ in models with the same EOS did not appreciably change the available information from the late phase neutrino emission. This suggests that, unlike the early phase neutrino emission, late-phase neutrino emission does not depend on complicated physics, but depends more on simple parameters such as the radius and mass of the PNS governed by EOS (c.f. [21]). Finally, using a simple Bayesian calculation, I demonstrated that $T_{\rm last}$ can be used to constrain EOS models, though it is challenging to also simultaneously constrain the PNS baryonic mass. Specifically, a shorter $T_{\rm last}$ suggests a lower central density in the neutron star, whereas a longer $T_{\rm last}$ indicates the presence of heavy nuclei near the surface region. In future studies, this framework can be extended by adopting more advanced inference frameworks, such as machine learning-assisted analysis.

When the next supernova neutrino is observed, our analysis method, which utilizes a $E_{\rm th}$ and $T_{\rm wid}$, will enable us to extract characteristics of the PNS and the properties of nuclear matter in the core. Moreover, it will be a useful addition to more detailed analyses incorporating more than event timing information. Though this paper has presented our method in the context of the SK detector, it can be similarly applied to any other neutrino detector with event-by-event timing information.

TABLE 4.3: The average of $T_{\rm last}$, and the time difference between the 500-th-to-last and 1000-th-to-last event ($T_{1000} - T_{500}$) for each model. The error shows the 1σ range of the distribution.

Model	$T_{\rm last}$ (s)	$T_{1000} - T_{500}$ (s)
140S15	37.0 ± 3.0	3.16 ± 0.22
147S15	39.9 ± 3.2	3.78 ± 0.24
154S15	43.4 ± 3.3	4.55 ± 0.27
162S15	47.1 ± 3.6	5.34 ± 0.29
162S40	48.1 ± 3.6	5.43 ± 0.29
170S40	52.4 ± 3.9	6.19 ± 0.32
178S40	57.1 ± 3.9	6.91 ± 0.35
186S40	61.8 ± 4.4	7.67 ± 0.39
140L15	59.0 ± 4.8	5.86 ± 0.35
147L15	64.7 ± 5.0	6.93 ± 0.40
154L15	70.0 ± 5.4	8.04 ± 0.43
162L15	76.2 ± 5.8	9.17 ± 0.47
162L40	78.4 ± 5.9	9.41 ± 0.48
170L40	86.7 ± 6.1	10.74 ± 0.56
178L40	95.2 ± 6.9	12.24 ± 0.61
186L40	105.0 ± 7.5	13.82 ± 0.72
140F15	63.9 ± 4.0	7.06 ± 0.38
147F15	64.7 ± 4.0	8.08 ± 0.44
154F15	75.1 ± 4.2	9.25 ± 0.49
162F15	81.0 ± 4.2	10.49 ± 0.54
162F40	83.0 ± 4.4	10.72 ± 0.56
170F40	90.3 ± 4.6	12.13 ± 0.61
178F40	98.5 ± 4.7	13.64 ± 0.69
186F40	107.2 ± 4.8	15.30 ± 0.76
140T15	80.5 ± 7.7	9.76 ± 0.57
147T15	86.7 ± 8.2	11.40 ± 0.62
154T15	93.1 ± 8.0	13.25 ± 0.71
162T15	100.9 ± 8.4	15.08 ± 0.79
162T40	102.2 ± 8.3	15.35 ± 0.83
170T40	111.3 ± 8.6	17.47 ± 0.87
178T40	120.2 ± 8.8	19.59 ± 0.94
186T40	129.8 ± 9.1	21.76 ± 1.03

Chapter 5

Search for Neutrinos from Failed SN Candidate in M31

While the previous chapter focused on exploring the potential of neutrino observations from Galactic CCSNe to probe the nuclear EOS, this chapter shifts the focus to an observational search for neutrinos from a failed SN candidate located beyond the Milky Way. Specifically, I investigate a possible failed SN event in the nearby Andromeda galaxy (M31), designated M31-2014-DS1. In such events, the collapse of a massive star leads directly to black hole formation without producing a bright optical signature, making neutrinos the primary observable messengers of the core-collapse process. This chapter presents the dedicated search for neutrino signals from this candidate event. In the case of failed SN observation, most of the gravitational binding energy is released as neutrinos within a short timescale, making neutrino observations a powerful probe of these otherwise optically invisible events.

Motivated by the discovery of the M31-2014-DS1 neutrino event, reported as a possible failed SN at a distance of approximately 770 kpc, this analysis utilizes SK data to search for coincident neutrino bursts from the M31 during the period of interest. By examining temporal clusters of low-energy events, the study aims to constrain the neutrino emission properties and assess the detectability of such events in current and future water Cherenkov detectors.

5.1 Overview of failed SN candidate

In 2024, M31-2014-DS1, a candidate failed SN was reported in M31 at a distance of about 770 kpc [23]. The object exhibited a 50% increase in mid-infrared (MIR) flux over a two-year period starting in 2014 [99, 100], while remaining undetected in optical and near-infrared (NIR) imaging observations as of 2023 as shown in Figure 5.1. The progenitor is estimated to have been a massive hydrogen-depleted supergiant, with an estimated mass of around $20M_{\odot}$, for which models indicate that the explosion may fail [2]. In addition, the radius of the inner shell was found to decrease more than 1000 days after the initial MIR brightening. These observations suggest that a black hole was likely to be formed sometime between 2014 and 2017. The optical counterpart of the progenitor candidate for M31-2014-DS1 was identified as an irregular variable star showing optical brightness variations between 2010 and 2014. Based on its luminosity and colors, it has been suggested to be a red supergiant (RSG) in M31. Using archival Hubble Space Telescope (HST) and Spitzer Space Telescope (SST) data taken between 2008 and 2012, the complete spectral energy distribution was modeled by including a warm circumstellar dust shell to reproduce the flat mid-infrared spectrum. The best-fit model indicates a luminous ($\log(L/L_{\odot}) \approx 5$), cool supergiant ($T_{\rm eff} \approx 4500$ K) surrounded by dust at ~ 110 AU with a temperature of ~ 870 K. Comparison with stellar evolution models suggests that the progenitor was initially a $\sim 20M_{\odot}$ star

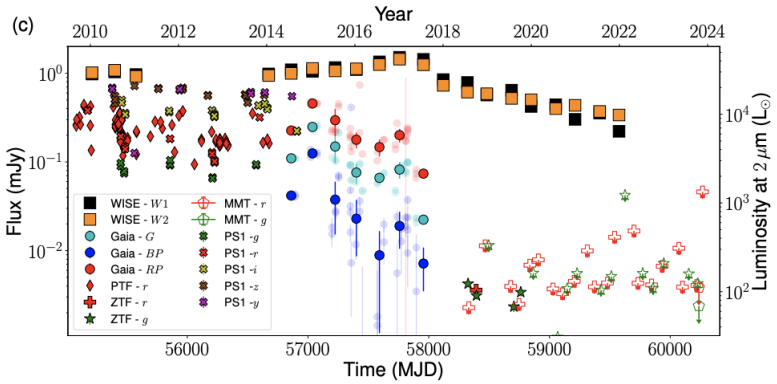

FIGURE 5.1: The temporal evolution of the optical and IR sources [23].

that evolved to a final mass of $\sim 6.7 M_{\odot}$ with a thin hydrogen envelope of $\sim 0.55 M_{\odot}$, consistent with a star that experienced enhanced mass loss prior to collapse. Figure 5.2

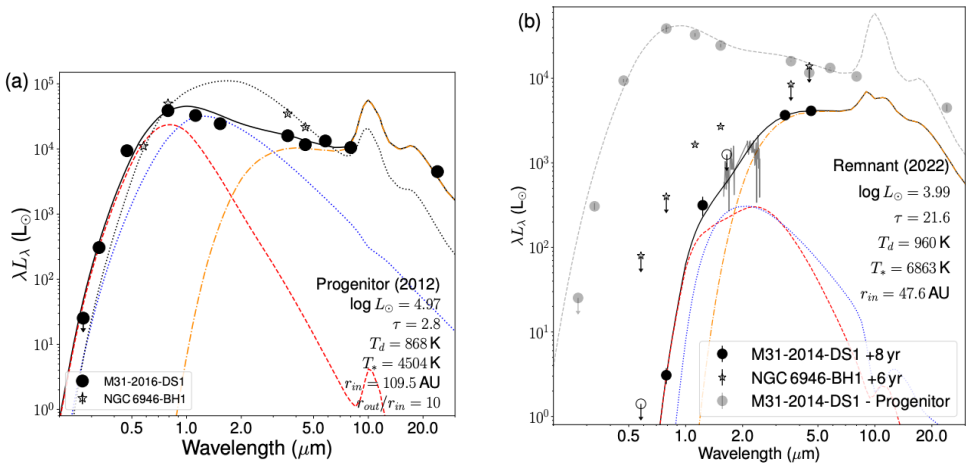

(a) 2012 year (b) 2022 year

FIGURE 5.2: The spectral energy distribution of the progenitor of M31-2014-DS1 [23]. The black solid line, orange dot-dashed line, and blue dotted line represent total flux, dust emission, and attenuated stellar emission, respectively.

presents the spectral energy distributions (SEDs) of the progenitor candidate of M31-2014-DS1 obtained in 2012 and 2022. Panel (a) shows the SED of the progenitor before the disappearance, while panel (b) corresponds to the remnant phase observed about eight years later. The black solid, orange dot-dashed, red dashed, and blue dotted lines represent the total flux, dust emission, scattered stellar emission, and attenuated stellar emission, respectively. For comparison, open star symbols indicate the SED of the progenitor of NGC 6946-BH1, and the black dotted line shows its reported best-fit model. In 2012, the progenitor was well reproduced by a luminous red supergiant model ($\log(L/L_{\odot}) \simeq 4.97$, $T_{\rm eff} \simeq 4500$ K) surrounded by warm dust at ~ 110 AU with a temperature of ~ 870 K. By contrast, the 2022 SED shows a significant decline in luminosity ($\log(L/L_{\odot}) \simeq 3.99$) and an increase in optical depth, indicating that the progenitor has vanished and that the remaining emission originates primarily from circumstellar dust.

In the case of observations with SK, the expected energy spectrum of neutrinos

from M31 is shown in Figure 5.3. The gray histogram represents the expected background in SK. In this figure, four failed supernova models are considered [29, 30]. Because the distance to M31 is relatively close, the expected number of neutrino events within 10 s is higher than that of the background.

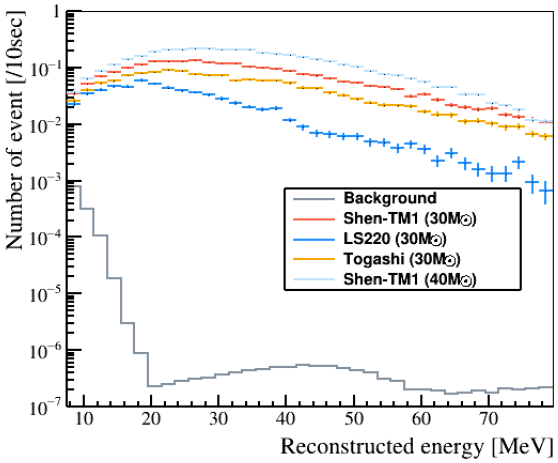

FIGURE 5.3: Expected energy spectrum of black hole models assuming 770 kpc in SK. Shen, LS220, Togashi, and Shen-TM1 correspod to [29, 30], respetively.

In IBD interactions, the prompt positron emits Cherenkov light, while the delayed neutron is captured on a proton, producing a 2.2 MeV gamma ray as described in Section 2. However, this delayed signal is often undetectable in the pure-water phase due to the low detection efficiency. Figure 5.4 shows the expected number of neutrino events as a function of the positron energy threshold, both with and without applying the neutron tagging cut. This also indicates that the expected background for a 10-second time window is sufficiently suppressed above 8 MeV by the spallation cut. Taking into account the detection efficiency, the expected number of detected neutrino events from CCSNe occurring in nearby galaxies (e.g., within 1 Mpc) is significantly reduced to $\mathcal{O}(0.1)$. Although the expected number of events generally decreases as the energy threshold increases, the signal efficiency increases with energy. As a result, the expected number of events becomes slightly larger for higher thresholds; for example, the expected signal for a 14 MeV threshold is somewhat higher than that for an 8 MeV threshold, especially when using the neutron-tagging cut, for which the signal efficiency differs between the low and high energy regions. Since supernova neutrinos are emitted over a timescale of several to tens of seconds, the few events expected from such distances would appear as a small cluster of events in the SK data. Therefore, I adopt a time-clustering analysis to search for such event grouping.

5.2 Theoretical Model of Black Hole Formation

Models in which a black hole forms following core collapse have been extensively simulated. In general, for massive progenitor stars, the large mass of the iron core causes the initially generated shock wave to stall rapidly, preventing a successful supernova explosion. As a result, the iron core and overlying material continue to accrete onto the newly formed PNS, leading to a rapid increase in its mass on a short timescale. When the PNS mass eventually exceeds its maximum mass, a second core collapse

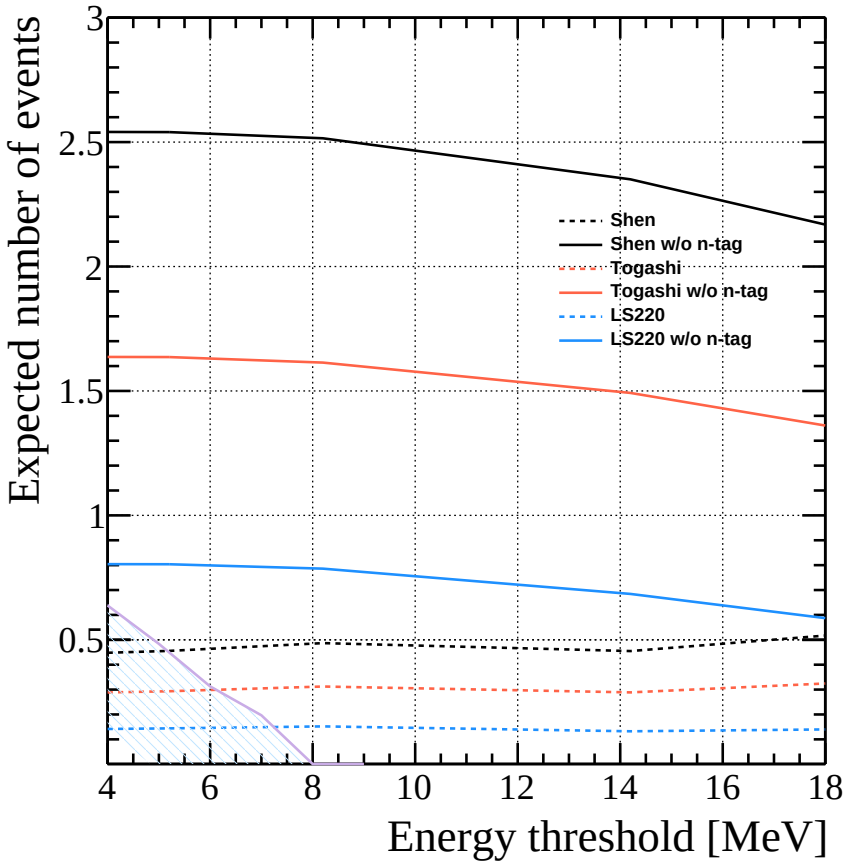

FIGURE 5.4: Expected neutrino event for three failed SN models [24] as a function of energy threshold. The black, red, and blue lines represent Shen EOS, Togashi EOS, and LS220 EOS, respectively. The dashed lines show the case of applying the neutron tagging cut. The purple line represents the expected background rate estimated for a 10-second time window. Background events above 8 MeV are effectively suppressed by the spallation cut.

occurs, leading to black hole formation in what is referred to as a failed SN. The maximum mass of the PNS depends on the nuclear EOS. Table 5.1 provides a summary of the models that result in black hole formation. Most of the models listed in this table are failed SN, while the SFHo models with progenitor masses of 19.56, 23, 40, and 100 $M_\odot$ correspond to the fallback SN models discussed in Section 1.1.5. This table is based on the work of [25]. The $t_{\rm BH}$ denotes the time elapsed from core bounce to black hole formation. This quantity characterizes the duration of neutrino emission prior to black hole formation and therefore differs among supernova models. In failed SN models, black holes typically form within about 1 s or a few seconds. In contrast, in fallback supernovae, accretion can continue over a longer period, which may result in a longer $t_{\rm BH}$ compared to standard failed supernova models. Because the maximum mass of the PNS is determined by the nuclear EOS, the choice of EOS plays a crucial role in shaping the neutrino emission and black hole formation timescales. As described in Section 1.4, the Shen EOS [30] is constructed within the framework of relativistic mean-field theory, while the Togashi EOS [101] incorporates advanced nuclear many-body calculations, providing detailed predictions of nuclear composition and structural properties at supra-nuclear densities. In this study, I employ two parameterizations of the Shen EOS: the original Shen-TM1 and the revised Shen-TM1e. The Shen-TM1e features a reduced symmetry-energy slope compared to Shen-TM1, which affects both the neutrino luminosities and energy spectra. The SFHo EOS [102], derived from relativistic mean-field models constrained by experimental nuclear data, is widely used because it offers a realistic description of nuclear-matter properties relevant to PNS formation and neutrino emission.

Dependence of EOS

In the model comparison between Shen EOS, LS220 EOS, and Togashi EOS, as described in Section 1.4, are conducted in the failed SN case [24]. Figure 5.5 presents the central core profiles of density, temperature, and electron fraction at a post-bounce time of $t_{\rm pb} = 300$ ms. At this moment, the central core has reached a baryonic mass of approximately 2.3, $M_\odot$ for all EOS models. From those profile, the Togashi EOS

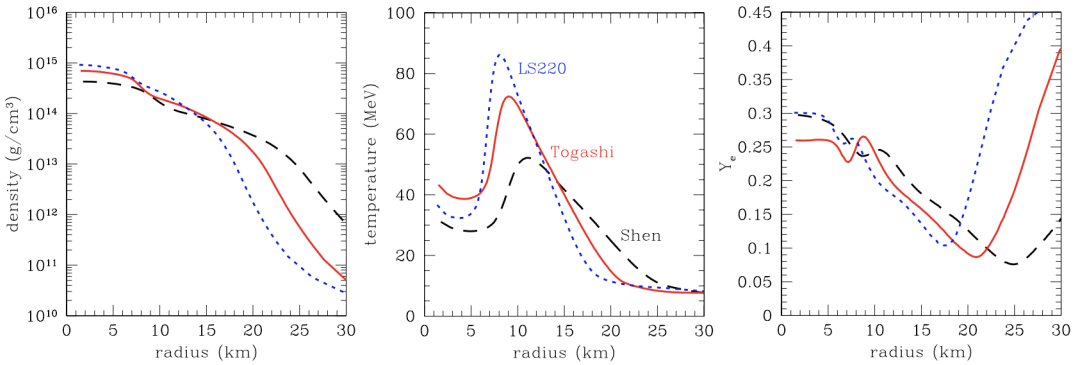

FIGURE 5.5: Profile of the density (left), temperature (middle), and electron fraction (right) at $t_{\rm pb} = 300$ ms [24]. Details of the $30M_\odot$ progenitor model with metallicity $Z = 0.004$ are provided in [3]. The black dashed, blue dotted, and red solid lines indicate the models using the Shen EOS, LS220 EOS, and Togashi EOS, respectively.

model has a larger core radius, which is defined as the radius where the density is 10^{12} g cm^{-3}, than the LS220 EOS, but smaller than Shen EOS. In the case of the

temperature profile, Togashi EOS is higher than LS220 EOS. The reason why Togashi EOS yields a higher central temperature than LS220 EOS originates from the treatment of the nucleon effective mass (M^*) and its connection to the thermal pressure. As discussed in [103], the thermal pressure ($P_{\rm b}^{\rm th}$) of baryons follows the relation

$$P_{\rm b}^{\rm th} \propto M^* T^2, \tag{5.1}$$

where T is the temperature. This expression indicates that, for a given T, a larger M^* leads to higher thermal pressure. Conversely, if M^* is smaller, the temperature must increase in order to achieve the same level of thermal pressure.

In LS220 EOS, M^* is assumed to be equal to the nucleon rest mass. Because M^* remains relatively large, sufficient thermal pressure can be supplied without requiring a particularly high temperature. In contrast, Togashi EOS incorporates both density and temperature dependencies of M^*. As a result, M^* becomes smaller than the rest mass at high densities. To offset this reduction and to provide the required $P_{\rm b}^{\rm th}$, the temperature must increase. This mechanism explains why the central temperature tends to be higher in simulations using Togashi EOS.

In Figure 5.6, the time evolution of the luminosity and average neutrino energy is represented for three models. The endpoint of each line corresponds to the time of

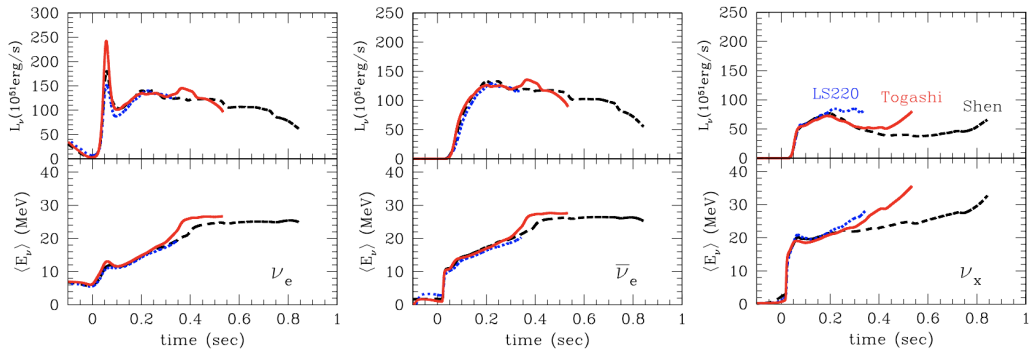

FIGURE 5.6: Time evolution of the luminosity, average energy of nu_e (left), $\bar{\nu}_e$ (middle), and ν_x (right) [24]. The notation of the EOS model is the same as Figure 5.5.

black hole formation, and its point is different for each model. In the case of average neutrino energy, ν_x has a larger average neutrino energy than ν_e or $\bar{\nu}_e$, and ν_x has a large difference between EOS models. Because the interaction strength of ν_x is weak and its mean free path is long, the ν_x signal is sensitive to the hotter and denser regions near the center core. If the EOS is more compressible, core collapse proceeds further, leading to a center core that becomes denser and hotter. Consequently, the average energy of ν_x increases. In addition, the differences among EOS models become most pronounced in the center core. However, the neutrinosphere is located outside this center core, and therefore, the structural differences in the inner region do not strongly affect neutrino emission. As a result, the influence of the EOS primarily appears in the duration of neutrino emission. In particular, a stiffer EOS tends to collapse more readily and form a black hole at an earlier time.

The expected time of black hole formation from core bounce is different between failed SN models. Figure 5.7 shows the relationship between the averaged neutrino energy and the duration time of neutrino emission. The expected duration time of neutrino emission is within a few second in many failed SN models.

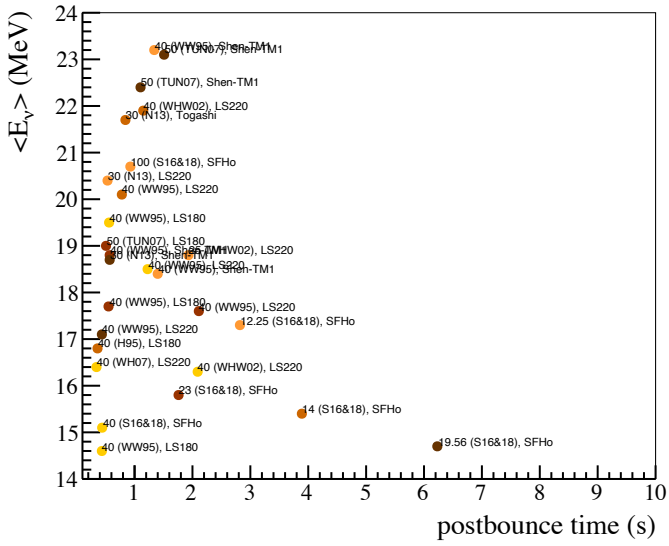

FIGURE 5.7: The relationship between averaged neutrino energy and duration time of neutrino emission. The postbounce time represents the time from the core bounce. Points show different failed SN models as summarized in Table 1 in Ref. [25].

5.3 Data Analysis in SK

5.3.1 Definition of time window for cluster search

I first defined a 10-second time window as the basis of the cluster search. This choice is motivated by numerical simulations of failed SNe, which show the termination of neutrino emission within a few seconds after core bounce as discussed in Section 1.2. Using this 10-second window, a time clustering analysis of the SK data to search for neutrino signals associated with the failed SN candidate M31-2014-DS1 is performed. In this analysis, a cluster is defined as a group of at least two events occurring within a 10-second interval, which serves as the fundamental criterion of the search. Since the expected number of detected neutrinos from the distance of M31 is only order of one, a careful definition of the cluster criteria is required. Therefore, I defined the cluster criteria and evaluated the expected background to determine the optimal energy threshold. The event selection applied in this search is described in Section 5.5.

5.3.2 Data set

In this analysis, SHE-triggered events collected during the normal physics operation of SK-IV are analyzed. Hereafter, this is called as SHE event. In the present analysis, I use data from the pure-water phase, prior to the addition of gadolinium sulfate [i.e., before the SK-Gd phase 104, 105]. This represents the most stable operation period. The energy threshold is 3.49 MeV of electron kinetic energy [106]. After excluding runs and periods with potential data quality concerns, the resulting dataset corresponds to an effective livetime of 2970.1 days. The analysis energy range, expressed in terms of reconstructed kinetic energy (E_{rec}), is defined according to the SHE trigger condition, which was revised once during SK-IV from 70 hits to 58 hits. These thresholds correspond to $E_{\mathrm{rec}} = 9.49$ MeV and 7.49 MeV, respectively. For the period relevant to the black hole search, the trigger and corresponding energy thresholds were 58 hits and 7.49 MeV, respectively.

TABLE 5.1: Summary of the model of black hole formation. *indicate fallback SN model.

Progenitor mass ($M_\odot$)	EOS	$t_{\rm BH}$ (s)	E_{ν_e} (10^{53} erg)	$E_{\bar{\nu}_e}$ (10^{53} erg)	E_{ν_X} (10^{53} erg)	$\langle\varepsilon_{\nu_e}\rangle$ (MeV)	$\langle\varepsilon_{\bar{\nu}_e}\rangle$ (MeV)	$\langle\varepsilon_{\nu_X}\rangle$ (MeV)
40	LS180	0.56	0.554	0.467	0.228	16.3	19.5	21.5
40	Shen-TM1	1.34	1.46	1.35	0.526	20.3	23.2	23.9
40	LS180	0.36	0.334	0.271	0.160	13.5	16.8	21.9
50	Shen-TM1	1.51	1.35	1.27	0.526	20.0	23.1	24.2
50	LS180	0.507	0.450	0.372	0.191	15.7	19.0	21.2
40	LS180	0.435	0.507	0.376	0.231	14.1	14.6	19.7
40	Shen-TM1	1.40	1.73	1.53	0.715	16.0	18.4	21.0
40	LS220	0.780	0.729	0.627	0.382	17.3	20.1	24.1
40	LS180	0.435	0.422	0.337	0.209	13.8	17.1	18.3
40	LS220	0.55	0.525	0.436	0.279	14.4	17.7	19.2
25	LS220	1.225	0.696	0.632	0.331	15.3	18.5	17.7
40	LS220	1.93	0.852	0.796	0.402	15.8	18.8	17.4
50	Shen-TM1e	1.15	0.941	0.850	0.330	18.7	21.9	21.6
40	Shen-TM1e	1.103	1.15	1.05	0.422	19.3	22.4	23.1
40	LS220	0.57	0.572	0.539	0.375	16.2	18.8	20.2
30	LS220	0.342	0.403	0.287	0.211	12.5	16.4	22.3
30	Togashi	0.533	0.685	0.533	0.289	16.1	20.4	23.4
30	Shen-TM1	0.842	0.949	0.81	0.400	17.5	21.7	23.4
40	LS220	0.57	0.938	0.862	0.483	15.7	18.7	17.6
40	LS220	2.11	0.544	0.449	0.281	14.4	17.6	18.8
40	D2D2 RDF-1.7	1.03	0.368	0.384	0.132	13.3	15.6	14.2
12.25	SFHo	> 2.09	0.563	0.511	0.297	13.9	16.3	15.5
14	SFHo	> 2.82	0.768	0.711	0.393	15.0	17.3	15.9
19.56	SFHo*	3.89	0.906	0.889	0.694	12.9	15.4	16.0
23	SFHo*	6.23	0.776	0.736	0.609	12.4	14.7	14.8
40	SFHo*	1.76	0.798	0.766	0.499	12.4	15.8	16.0
100	SFHo*	0.44	0.529	0.462	0.246	12.9	15.1	17.1
40	Togashi	0.927	0.824	0.705	0.471	18.1	20.7	25.7

5.4 Background Event Reduction for Supernova Neutrino Observation in SK

In the search for supernova neutrinos, there are several types of background in SK, such as radioimpurities, spallation background, decay electrons from muons, and atmospheric neutrinos. In particular, background reduction from radioimpurities and spallation products is important for searches focusing on low-rate neutrino signals, including those from supernovae occurring outside the Milky Way. In this section, I present an overview of the background event and its reduction process in SK.

5.4.1 Overview of Background Events

For searches targeting extragalactic supernovae in the Mpc range, the expected number of signal events is only a few. In such cases, cluster searches are performed using a time-window method to identify potential signals from among the continuously present background events. Therefore, particular attention should be paid to background events that exhibit temporal correlations. The detailed procedure of this cluster search is described in Section 5.5. In this section, I introduce the main background sources relevant to both types of searches described above.

TABLE 5.2: Summary of isotopes, their half-lives, decay modes, yields, and primary production processes. This information is referred from [54].

Isotope	Half-life [s]	Decay mode	Yield [$\times 10^{-7}$ μ^{-1}g^{-1}cm^2]	Primary process
n	2030	–	–	–
^{18}N	0.624	β^-	0.02	^{18}O(n,p)
^{17}N	4.173	$\beta^- + n$	0.59	^{18}O$(n,n+p)$
^{16}N	7.13	$\beta^- + \gamma(66\%)$, $\beta^-(28\%)$	18	^{18}O(n,p)
^{16}C	0.747	$\beta^- + n$	0.02	$(\pi^-, n+p)$
^{15}C	2.449	$\beta^- + \gamma(63\%)$, $\beta^-(37\%)$	0.82	$(n,2p)$
^{14}B	0.0138	$\beta^- + \gamma$	0.02	$(n,3p)$
^{13}O	0.0086	β^+	0.26	$(\mu^-, p+2n+\mu^-+\pi^-)$
^{13}B	0.0174	β^-	1.9	$(\pi^-, 2p+n)$
^{12}N	0.0110	β^-	1.3	$(\pi^+, 2p+2n)$
^{12}B	0.0202	β^+	0.02	$(n,\alpha+p)$
^{12}Be	0.0236	β^-	12	$(n,\alpha+p+n)$
^{11}Be	13.8	$\beta^-(55\%)$, $\beta^-(31\%)$	0.10	$(n,\alpha+2p)$
^{11}Li	0.0085	$\beta^- + n$	0.01	$(\pi^+, 5p+\pi^++\pi^0)$
^{9}C	0.127	β^+	0.89	$(n,\alpha+4n)$
^{9}Li	0.178	$\beta^- + n(51\%)$, $\beta^-(49\%)$	1.9	$(\pi^-, \alpha+2p+n)$
^{8}B	0.77	β^+	5.8	$(\pi^-, \alpha+2p+2n)$
^{8}Li	0.838	β^-	13	$(\pi^-, \alpha+{}^2\text{H}+p+n)$
^{8}He	0.119	$\beta^- + \gamma(84\%)$, $\beta^- + n(16\%)$	0.23	$(\pi^-, {}^3\text{H}+4p+n)$
^{15}O	–	–	351	(γ, n)
^{15}N	–	–	773	(γ, p)
^{14}O	–	–	13	$(n,3n)$
^{14}N	–	–	295	$(\gamma, n+p)$
^{14}C	–	–	64	$(n,n+2p)$
^{13}N	–	–	19	$(\gamma, {}^3\text{H})$
^{13}C	–	–	225	$(n, {}^2\text{H}+p+n)$
^{12}C	–	–	792	(γ,α)
^{11}C	–	–	105	$(n,\alpha+2n)$
^{11}B	–	–	174	$(n,\alpha+p+n)$
^{10}C	–	–	7.6	$(n,\alpha+3n)$
^{10}B	–	–	77	$(n,\alpha+p+2n)$
^{9}Be	–	–	24	$(n,\alpha+2p+n)$
^{9}Be	–	–	38	$(n,2\alpha)$
Sum	–	–	3015	–

Spallation event

Although the SK detector is located at 2700 m.w.e., cosmic-ray muons arrive at a rate of approximately 2 Hz and can interact with the water to produce a variety of secondary particles through muon-induced spallation. When a high-energy muon passes through the detector, it can break the oxygen nuclei in water, generating cascades of hadrons, such as neutrons and pions, as well as photons. These hadrons may trigger further secondary nuclear reactions, creating a wide range of radioactive isotopes.

The radioactive isotopes produced by muon spallation decay by emitting β and γ rays, and in some cases neutrons. The visible energy of these decay products typically lies below 20 MeV, placing them squarely within the signal region relevant for supernova neutrinos.

For each isotope generated in water, Li et al. [107, 108, 109] characterized the half-life, decay models, production yields, and primary spallation mechanisms with FLUKA simulations, as summarized in Table 5.2. The end-point energies of the electron-like particles and their yields above 3.5 MeV are illustrated in Figure 5.8. Because several isotopes produce decay electrons up to about 20 MeV (notably ^{14}B and ^{11}Li), understanding the production and decay characteristics of spallation isotopes and developing efficient rejection methods below 24 MeV are essential components of the background reduction strategy in this study.

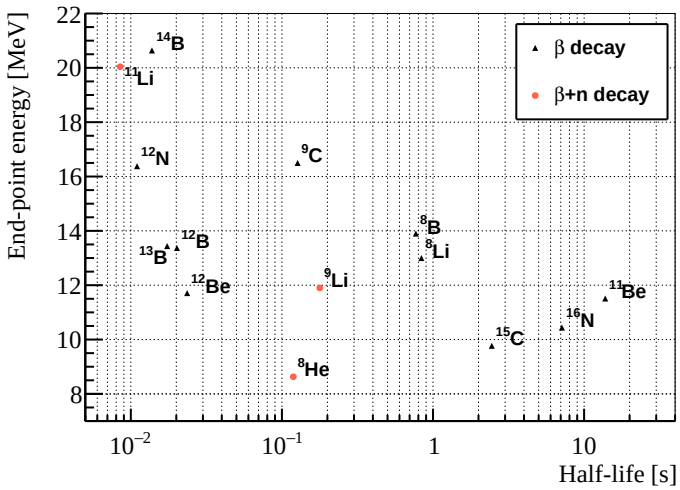

FIGURE 5.8: Scatterplot of spallation products expected to occur in SK, showing their half-life and energy.

Atmospheric neutrino events

In the energy region of several tens of MeV, atmospheric neutrinos constitute a significant source of background. The dominant background components originate from charged-current and neutral-current interactions of atmospheric neutrinos with oxygen nuclei in the detector. These interactions can produce secondary particles, such as electrons, positrons, or gamma rays, that mimic true low-energy neutrino signals. A detailed understanding and accurate modeling of these atmospheric neutrino-induced backgrounds are therefore essential for reliable signal extraction in this energy range.

- Decay electron from muons
  Some atmospheric neutrino interactions produce muons with energies below the Cherenkov threshold. Such muons, referred to as *invisible* muons, do not emit Cherenkov light and therefore cannot be directly detected in the detector. These muons subsequently decay into electrons or positrons with a mean lifetime of 2.2 μs. Figure 5.9 illustrates the characteristic features of decay electron background events. Such events can originate not only from the decay of invisible muons but also from pion decay chains in which both the pion and the resulting muon are below the Cherenkov threshold.

- Visible pions and muons
  For pions and muons whose energies exceed their Cherenkov threholds, the characteristic Cherenkov light pattern recorded in SK allows for reliable particle identification. When such particles decay within the ID, the resulting prompt and delayed signal pair can be utilized as a characteristic pattern. Figure 5.10 presents an example of a visible muon event followed by its associated decay electron signal.

- Electrons from CC ν_e interactions
  Electrons produced via ν_e CC interactions with neutrons cannot be separated from signals in SK. Because the interaction cross section rises with neutrino

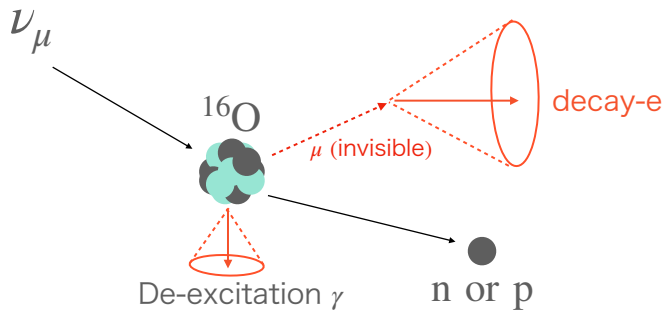

FIGURE 5.9: Schematic diagram of a decay electron background event. A decay electron originating form an undetected muon, which created in a charged-current quasi-elastic (CCQE) interaction of an atmospheric neutrino, is illustrated.

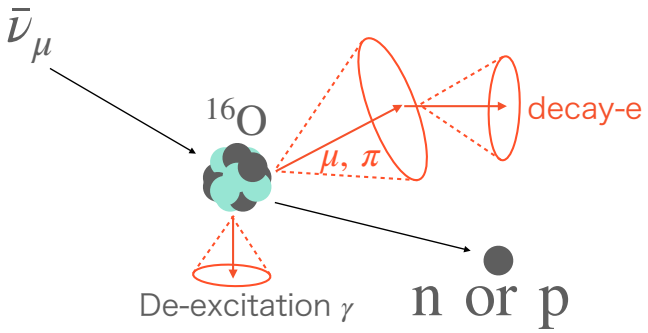

FIGURE 5.10: Illustration of visible muon and pion backgrounds. The figure shows a visible muon and a decay electron produced through a CCQE interaction of an atmospheric neutrino.

energy, these delectrons typically carry an energy similarly correlated with that of the incident ν_e. Figure 5.11 shows an example of an electron event originating from a ν_e CC interaction.

5.4.2 First reduction: Pre-cut

From this section, I describe the event reduction used to remove the background events discussed in the previous section. The reduction procedure follows the event selection framework established for the DSNB search [28].

5.4.3 Non-SHE-triggered event and noise event cut

In the first reduction, non-physical events are removed using cut criteria at run and event levels, as shown in Table 5.3.

Cosmic ray muon-induced event cut

Cosmic-ray muons enter SK at a rate of about 2 Hz, typically producing an OD trigger. Some of these muons are followed by decay electrons (decay-e) with a mean lifetime of 2.2 μs. If the time difference between the muon and the decay-e is sufficiently long

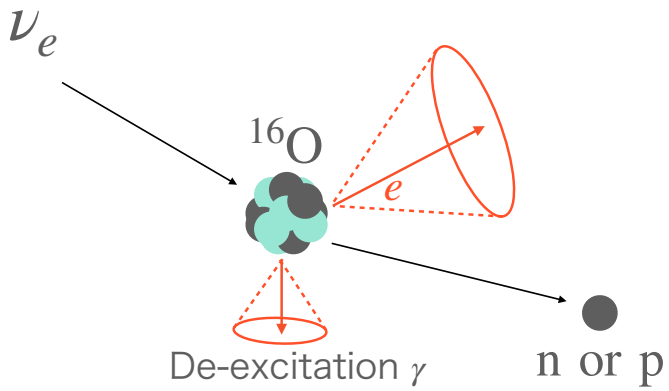

FIGURE 5.11: Diagram showing an electron background event generated by a CCQE interaction of an atmospheric electron neutrino.

TABLE 5.3: Summary of run- and event-level removal criteria applied in the analysis.

Category	Condition
Run-level removal	
	• Run time shorter than 5 minutes
	• Run started less than 15 minutes after the high-voltage recovery
	• Any hardware problem reported
	• Unusual event distribution due to detector problems
Event-level removal	
	• Calibration trigger events
	• Periodic trigger events
	• T2K beam trigger events
	• Pedestal events

that they are reconstructed as separate events, the decay-e is not associated with the OD trigger. To avoid contamination from such cases, all events occurring within 50 μs after a muon event are removed. This cut also helps to eliminate short-lived isotopes produced by muon spallation, as described in Section 5.4.4.

Fiducial volume cut

In the case of radioimpurities, such backgrounds mainly originate from the detector materials and the surrounding rock of the SK tank. In order to reduce radioactive backgrounds, an FV cut is applied, which excludes events occurring within 2 m of the tank wall. As a result, the tank volume is reduced from the entire ID volume of 32.5 kton to 22.5 kton. Analysis in SK typically focuses on events within this FV.

Fit quality cut

Low-energy background events, including detector noise and other non-neutrino sources, tend to show poor reconstruction quality. To address this issue, a selection based on the vertex reconstruction goodness parameter (g_{vtx}) is applied. Events with g_{vtx} values below 0.5 are relected. This criterion efficiency removes events with poor fit quality, which are primarily associated with radioactive backgrounds near the detector

wall that remain after the FV cut. The g_{vtx} requirement suppresses such background events while retaining more than 99.9% of the signal MC events above 8 MeV.

Trigger requirement

In this analysis, both the SHE and AFT triggers are required. In addition, candidate events must not trigger on OD, ensuring that the selected events correspond to genuine neutrino signals rather than external backgrounds. Events that satisfy this condition–triggered by the SHE but not by OD–are hereafter referred to as SHE events. However, until the middle of the SK-IV period, the AFT trigger rate was limited to once every 21 ms, resulting in instances where a SHE trigger occurred without a corresponding AFT trigger. This discrepancy must be carefully evaluated using real data and properly accounted for in the normalization of the MC simulation. The AFT trigger efficiency, denotet as ϵ_{AFT}, is calculated for each reconstructed energy bin of 2 MeV according to the following definition:

$$\varepsilon_{\mathrm{AFT}} = \frac{N_{\mathrm{AFT}}}{N_{\mathrm{SHE}}}, \tag{5.2}$$

where N_{AFT} represents the number of AFT-triggered events and N_{SHE} denotes the number of SHE-triggered events in each 2 MeV energy bin. The resulting values of $\varepsilon_{\mathrm{AFT}}$ for all bins are summarized in Table 5.4.

TABLE 5.4: After-trigger (AFT) efficiency $\varepsilon_{\mathrm{AFT}}$ as a function of reconstructed energy in SK-IV.

Energy bin [MeV]	**AFT efficiency [%]**
8–10	85.3
10–12	80.4
12–14	74.3
14–16	70.0
16–18	67.9
18–20	63.4
20–22	89.7
22–24	90.0
24–26	90.0
26–28	100.0
28–30	90.5
>30	93.7

5.4.4 Second reduction: Spallation cut

The "spallation background" arises from the beta-decays of the radioisotopes generated by the spallation of oxygen nuclei in the tank by cosmic-ray muons. Such spallation creates hadronic showers that result in secondary hadrons undergoing hadronic interactions with detector nuclei to produce various radioisotopes. The observable particles appearing in the final, such as beta and gamma rays, have energies ranging from a few MeV to $\sim$ 20 MeV, which overlaps with the energy range for supernova neutrinos. Consequently, these events can contribute to the background during supernova neutrino observation. The idea of the spallation cut is to use the relationship between the SHE events and muons detected close in time to the SHE events.

1 ms cut

Gamma rays and neutrons are produced through hadronic interactions induced by secondary nucleons and mesons with energies of several hundred MeV, which are generated by cosmic ray muon spallation. In certain cases, such gamma rays can trigger the SHE, while the accompanying neutrons may appear as delayed signals. To suppress these spallation-induced backgrounds, events occurring within 1 ms of a preceding cosmic ray muon are excluded from the analysis.

Multiple spallation cut

Energetic cosmic ray muons occasionally generate multiple radioactive isotopes through the spallation process. When one of these decays produces an SHE event, another low-energy event originating from the same muon may appear in close temporal and spatial proximity to it. To identify such correlated low-energy events associated with an SHE event, the selection criteria established in the solar neutrino analysis [110] are applied to all low-energy events within a ± 60 s time window, and are then examined. These selection cuts make use of event position, reconstruction quality, and related variables to remove non-physical background events. To suppress these correlated backgrounds, SHE events with a minimum distance of less than 4.0 m from a low-energy event are rejected. The selection efficiency for uncorrelated (random) events, estimated using randomized vertices, is evaluated to be 98%.

Neutron cloud cut

In addition to suppressing multiple spallation events, muon-induced hadronic showers are identified by detecting neutron captures occurring within 500 μs after cosmic-ray muons. These clusters of neutron captures, referred to as "neutron clouds," are typically produced in muon-induced hadronic showers, which serve as the production sites of spallation isotopes. Neutron capture events following muons are collected independently from the SHE event using a dedicated trigger, the Wideband Intelligent Trigger (WIT) [111, 112, 113]. This trigger applies both a threshold on the number of PMT hits and additional cuts on event quality and the reconstructed vertex distance from the ID wall. Events triggered by WIT within 500 μs of a preceding muon are identified as neutron captures if their reconstructed vertices lie within 5 m of the reconstructed muon track.

If multiple neutron captures are detected after a single muon, they are grouped into a "neutron cloud" following the definition in [114]. SHE events that occur close in time and space to these neutron clouds are subsequently rejected, following the same procedure.

To evaluate the efficiency of this neutron cloud cut for both signal and background, muons are paired with SHE events in the data to form two samples: a "presample," consisting of muons occurring up to 60 s before each candidate, and a "postsample," consisting of muons within 30 s after the candidate. The presample includes both correlated and accidental pairs, while the postsample contains only accidental ones. The postsample is thus used to estimate the signal efficiency and to characterize the spatial and temporal correlations between spallation isotopes and their parent muons in the presample.

An example of the distance distribution between spallation events and the neutron clouds of their parent muons is shown in Figure 5.12. The neutron cloud cut is optimized by modeling the neutron cloud shape from data and maximizing the statistical significance of the signal relative to the spallation background. The overall

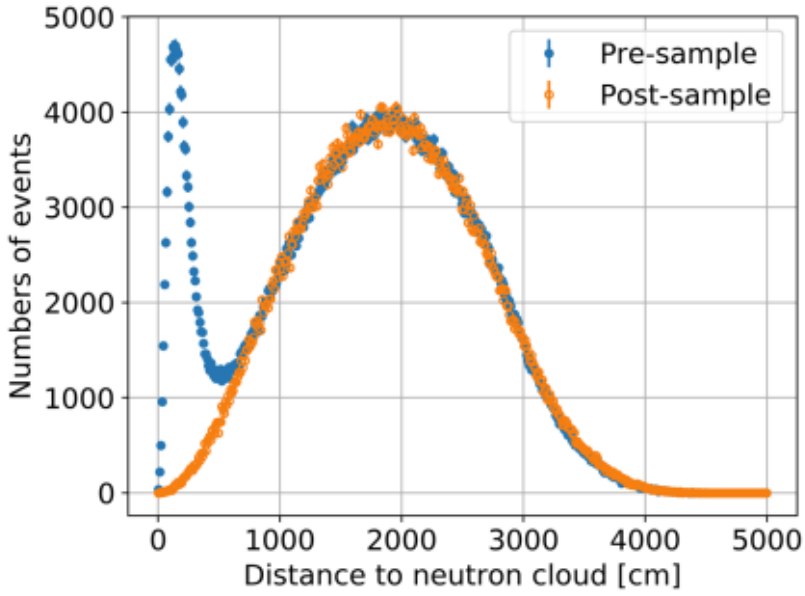

FIGURE 5.12: Distribution of the distance between spallation events and the neutron clouds associated with their parent muons [26]. The shaded histogram represents the randomized (uncorrelated) sample, while the solid histogram shows the data. The excess at short distances indicates a clear spatial correlation between spallation decays and muon-induced neutron clouds. This distribution is used to optimize the neutron cloud cut applied in the analysis.

performance of this cut is currently limited by the weak neutron-capture signal and by the restricted WIT live time of 388 days during SK-IV. While the signal efficiency exceeds 99%, this cut removes approximately 10% of the total spallation background in the full data set, and about 40% during the WIT live period.

Spallation likelihood cut

To further suppress the spallation events, I explore a statistical method based on the log-likelihood. In this approach, muons surrounding the SHE event are separated into 'pre-' and 'post-' regions, which are defined relative to the timing of the SHE. Muon events occurring within 30 s before the SHE event are assigned to the pre-region, while those occurring within 30 s after the SHE event are assigned to the post-region. The definitions of the pre- and post-regions are illustrated in Figure 5.13. The pre-region contains muon events that may have induced spallation before the rise of the SHE event, whereas the post-region contains muon events that are uncorrelated with the SHE event. All muon events are labeled for both the pre- and post-samoles for each SHE event.

Using the pre- and post-samples defined above, Probability Density Functions (PDFs) of the spallation-related variables are created. Here, the spallation sample refers to muon events that are likely to have produced spallation, while the random sample represents uncorrelated spallation events. In this procedure, the post-sample is treated as the random sample, and the spallation sample is obtained by subtracting the post-sample distribution from that of the pre-sample. The spallation variables used for constructing the PDFs are listed below.

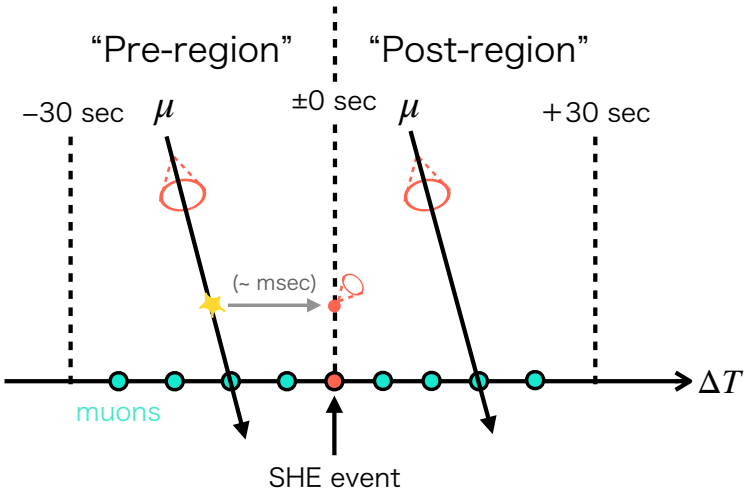

FIGURE 5.13: Definition of the muon spallation sample and the random sample.

dt: Time difference between the SHE and the muon event. For spallation events, this variable should represent the decay time characteristic of the produced radioactive isotopes.

L_t: Transverse distance from the muon track to the SHE event. For spallation events, this variable is expected to be within a few meters.

L_l: Longitudinal distance from the point of maximum energy deposition along the muon track to the SHE event. The point of maximum energy deposition is correlated with the spallation point, and this variable should be within a few meters for spallation events.

Q_μ: Total charge deposited by the muon in the inner detector (ID). The Q_μ value for spallation events tends to be larger than that expected from a minimum-ionizing muon.

$Q_{\rm res}$: Difference between Q_μ and the charge expected from the minimum ionization, defined as

$$Q_{\rm res} = Q_\mu - Q_{\rm MI} \times L, \tag{5.3}$$

where $Q_{\rm MI}$ is the number of photoelectrons per centimeter expected from the minimum ionization, and L is the muon track length. For multiple muons, L represents the sum of all track lengths. The value of $Q_{\rm res}$ indicates the likelihood that a muon induces nuclear spallation.

Each PDF of spallation variables are shown in Figure 5.14, 5.15, and 5.16.

The spallation likelihood, which is calculated by spallation and random sample PDFs is defined as

$$L_{\rm spall} = \log \prod_i \left(\frac{{\rm PDF}_i^{\rm spall}(x)}{{\rm PDF}_i^{\rm random}(x)} \right), \tag{5.4}$$

where the ${\rm PDF}_i^{\rm spall}(x)$ represents PDF of the spallation sample, and ${\rm PDF}_i^{\rm random}(x)$ denotes the PDF of the random sample. The subscript i refers to the i-th variable involved in the calculation, and x denotes the value of the i-th variable.

TABLE 5.5: Summary of cut criteria of spallation box cuts for each reconstructed-energy region.

Energy region	**Muon type**	**Cut criteria**
$E < 24$ MeV	–	$dt < 0.1$ s and $\ell_t < 400$ cm
$16 < E < 20$ MeV	misfit	$dt < 1.5$ s
$16 < E < 18$ MeV	single	$g_\mu \geq 0.4$ and $dt < 7$ s and $\ell_t < 150$ cm
$16 < E < 18$ MeV	stopping	$g_\mu < 0.3$ and $dt < 6$ s
$16 < E < 20$ MeV	stopping	$dt < 0.05$ s
$16 < E < 20$ MeV	multiple	$dt < 0.1$ s and $\ell_t < 400$ cm

For misfit and poorly reconstructed muons, only the dt is used to compute the spallation likelihood, as the other variables are not considered reliable. In the case of multiple-muon events, only the fit results from the first reconstructed track are utilized, while the total number of tracks is also taken into account. Figure 5.17 presents the spallation likelihood distributions for the different muon categories in the same energy range of SHE event. In all cases, a clear excess at high spallation-likelihood values is observed in the pre-sample, corresponding to contributions from spallation events. The cut criteria are defined separately for each muon category and are indicated by the dashed green lines in the Figure 5.17. SHE events that have at least one associated muon in the pre region with a spallation likelihood exceeding the threshold as represented by the green lines are removed from the sample.

Spallation box cut

At reconstructed energies above 15.49 MeV, the optimization of the spallation likelihood cut becomes challenging due to the limited statistics of the muon-induced spallation sample. Consequently, the selection criteria summarized in Table 5.5 are adopted for SHE events with $E_{\mathrm{vis}} > 15.49$ MeV. Here, g_μ denotes the goodness of the muon track reconstruction, which is described in detail in [41].

Spallation remaining rate

The efficiencies for spallation and random events in the spallation cut are evaluated as follows. The random event efficiency is obtained by calculating the spallation likelihood for the events in the toy MC sample and applying the cut criteria determined above. Since the data sample at this stage is dominated by spallation and solar neutrino events, the spallation efficiency is evaluated using data by separating the solar component. This separation is performed using the $\cos\theta_{\mathrm{sun}}$ distribution, where θ_{sun} is defined as the angle between the reconstructed event direction and the direction of the Sun at the event time, as schematically illustrated in Figure 5.18. In this distribution, events are classified into two categories: solar and non-solar. The numbers of solar and non-solar events are denoted as N_{sol} and N_{nonsol}, respectively. Solar events are concentrated near $\cos\theta_{\mathrm{sun}} = 1$, while non-solar events are uniformly distributed. The number of non-solar events, N_{nonsol}, is obtained by fitting the $\cos\theta_{\mathrm{sun}} < 0$ region with a constant. The non-solar component consists primarily of spallation and atmospheric neutrino events. The contribution from atmospheric neutrinos is negligible for $E_{\mathrm{rec}} <$ 11.49 MeV, but becomes visible at higher energies. Finally, the spallation efficiency,

TABLE 5.6: Random and spallation cut efficiencies in each E_{rec} region.

E_{rec} region (MeV)	$\varepsilon_{\mathrm{random}}$	$\varepsilon_{\mathrm{spall}}$
7.49–9.49	0.478 ± 0.014	0.077 ± 0.001
9.49–11.49	0.549 ± 0.016	0.098 ± 0.001
11.49–19.49	0.827 ± 0.010	0.101 ± 0.001

$\varepsilon_{\mathrm{spall}}$, is calculated as:

$$\varepsilon_{\mathrm{spall}} = \frac{N_{\mathrm{nonsol}}^{\mathrm{after}} - N_{\mathrm{atm}}^{\mathrm{after}}}{N_{\mathrm{nonsol}}^{\mathrm{before}} - N_{\mathrm{atm}}^{\mathrm{before}}}\,, \tag{5.5}$$

$$N_{\mathrm{atm}}^{\mathrm{after}} = N_{\mathrm{atm}}^{\mathrm{before}} \times \varepsilon_{\mathrm{random}}\,. \tag{5.6}$$

The quantities $N_{\mathrm{nonsol}}^{\mathrm{before}}$ ($N_{\mathrm{atm}}^{\mathrm{before}}$) and $N_{\mathrm{nonsol}}^{\mathrm{after}}$ ($N_{\mathrm{atm}}^{\mathrm{after}}$) denote the numbers of non-solar (atmospheric neutrino) events before and after applying the spallation cut, respectively. The atmospheric neutrino events are evaluated using MC simulations. Because atmospheric neutrino events occur independently of muons, $N_{\mathrm{atm}}^{\mathrm{after}}$ is obtained by multiplying $N_{\mathrm{atm}}^{\mathrm{before}}$ by the random event efficiency. The resulting efficiencies are summarized in Table 5.6. The random event efficiency exceeds 80% above 11.49 MeV, while it decreases to approximately half of that value at lower energies.

Determination of spallation cut criteria

To determine the spallation cut thresholds below 16 MeV, the Receiver Operating Characteristic (ROC) curve, which provides a quantitative measure of the trade-off between signal efficiency and reduction, is employed. The ROC curve is constructed by scanning the likelihood threshold and evaluating, for each point, the corresponding signal efficiency and the reduction power for spallation-induced events. The details are shown in Appendix A.4.

Above 16 MeV, because atmospheric neutrino interactions dominate in this energy region, the spallation component cannot be robustly characterized, preventing a meaningful optimization based on ROC performance. Therefore, for reconstructed energies exceeding 16 MeV, the likelihood threshold is instead determined by selecting the value that maximizes the random efficiency after the box cut has been applied.

5.4.5 Positron Event Selection

Effective wall distance cut

To further suppress backgrounds originating near the detector wall, a cut based on the variable *effwall* is applied. The effwall distributions for the $\bar{\nu}_e$ signal MC and data after the spallation cut are shown in Figure 5.19. As the signal-to-background ratio becomes lower for events with effwall below 500 cm, these events are excluded from the analysis. The signal efficiency after this cut is approximately 92% across all reconstructed energy regions.

Pre-PMT activity and post-PMT activity cut

When a visible muon decays into an electron, or when de-excitation gamma rays or an invisible muon are produced, the resulting event can contain multiple hit peaks within the time interval of [-5, 25] μs. Such events are rejected by examining the hit structure immediately before and after the primary peak. To eliminate events

exhibiting an early secondary peak, the TOF-subtracted interval from -5 μs to -12 ns relative to the main peak is scanned using a sliding 15 ns TOF-subtracted window. If any window contains more than 11 hits, the event is discarded. To suppress events with a late peak, the number of decay electrons occurring within 35 μs of the main peak($N_{\mathrm{decay-e}}$) is evaluated using the decay electron identification algorithm employed in previous SK studies [115].

Charge over hit cut

In order to suppress background events with fuzzy or multiple Cherenkov ring patterns, a parameter based on the charge distribution within a short time window is introduced. The total charge collected by all PMTs within 50 ns, denoted as Q_{50}, and the corresponding number of hit PMTs, N_{50}, are used to quantify this feature. The ratio Q_{50}/N_{50} reflects how concentrated the detected light is, and therefore serves as an indicator of the sharpness of the reconstructed Cherenkov ring. Figure 5.20 shows the Q_{50}/N_{50} distributions for the $\bar{\nu}_e$ signal and atmospheric neutrino Monte Carlo samples after all preceding selection criteria. Events with $Q_{50}/N_{50} > 2$ tend to originate from mis-reconstructed or multi-ring backgrounds, and are therefore rejected. The efficiency of this cut for genuine IBD signal events is approximately 99%.

5.4.6 Cherenkov angle cut

Electron-like events are typically reconstructed with a Cherenkov opening angle of approximately 42°, whereas NC events tend to apper at larger angles. Figure 5.21 shows the reconstructed Cherenkov angle (θ_{C}) distributions for the $\bar{\nu}_e$ signal and atmospheric neutrino MC samples after all preceding reduction steps. To further suppress background, events are required to satisfy $38^\circ < \theta_{\mathrm{C}} < 50^\circ$. The signal efficiency of this selection depends on the reconstructed energy, as lower-energy events exhibit a broader θ_{C} distribution due to increased multiple scattering, leading to a higher probability of being rejected. After applying this third reduction, the atmospheric neutrino background is suppressed to below 15% of its original level, while retaining 80-90% of the $\bar{\nu}_e$ signal, depending on the reconstructed energy region.

5.4.7 Neutron tagging cut

The neutron tagging cut became available in SK-IV owing to the introduction of the AFT trigger, which allows the delayed signal from neutron capture to be recorded. Tagging a neutron produced in the $\bar{\nu}_e$ IBD interaction serves as an effective means of enhancing signal identification. In the method of pure water phase, neutron captures on hydrogen are targeted through the detection of the accompanying 2.2 MeV gamma ray, which typically appears with a delay of approximately 200 μs relative to the prompt positron signal. However, at energies below 3.5 MeV, the rate of background events–primarily PMT dark noise and low-energy radioactive contamination–is sufficiently high that conventional selection variables are unable to discriminate the 2.2 MeV signal. To overcome this limitation, SK employs a machine-learning-based neutron tagging algorithm that utilizes boosted decision trees (BDT) to separate signal-like and background-like events with high efficiency [116]. Using this neutron tagging technique, an analysis aimed at searching DSNB events has been conducted [28]. More detailed descriptions of the method and its development in SK can be found in [117, 118, 119].

In the pure water phase, the neutron tagging algorithm proceeds in two stages: a pre-selection followed by a BDT classification. In the pre-selection step, a sliding 10 ns

window scans the late-hit region [+2, +535]μs, searching for localized hit clusters. A window with more than seven PMT hits ($N_{10} > 7$) is retained as a candidate 2.2 MeV gamma signal. To prevent multiple counting of the same capture gamma, an additional 20 ns window is checked, and any clusters found there are merged with the original one.

The performance of the neutron tagging technique is evaluated using MC samples that include neutron-capture signals as well as samples without such signals. The resulting misidentification rate is on the order of 10^{-4}. However, as discussed in Section 5.4.8, the signal efficiency after applying the neutron tagging cut is relatively low, at approximately 20%.

5.4.8 Reduction Summary

The signal efficiency for each reduction cut was estimated using MC. The signal efficiency in the supernova neutrino energy region is summarized in Table 5.7 and shown in Figure 5.23. The multiplication is performed beginning at the FV cut. Because neutrons are captured with low efficiency in the pure-water phase, applying the neutron tagging cut substantially decreases the overall signal efficiency. After this cut, efficiency can drop to less than 30%, indicating a significant loss relative to the case without applying the neutron tagging cut. In addition, because the neutron tagging cut severely suppresses the detectable signal in the few-event regime relevant for cluster searches, this cut is not employed in the present analysis, as detailed in the following section.

TABLE 5.7: Summary of selection efficiencies in each energy region [28].

Energy region [MeV]	7.49–9.49	9.49–11.49	11.49–19.49	19.49–29.49
Fit quality cut	> 0.999	> 0.999	> 0.999	> 0.999
Spallation cut	0.478	0.549	0.827	1.000
Effwall cut	0.924	0.921	0.920	0.918
Pre-activity cut	> 0.999	> 0.999	> 0.999	> 0.999
Post-activity cut	> 0.999	> 0.999	> 0.999	> 0.999
Pi-like cut	0.974	0.978	0.982	0.980
Charge/hit cut	0.999	0.998	0.995	0.989
Cherenkov angle cut	0.793	0.852	0.909	0.952
Neutron tagging	0.129	0.151	0.146	0.241

5.5 Cluster Search

5.5.1 Determination of the search region

The exact determination of black hole formation time is difficult with optical telescope observations, because the stellar core where the black hole forms is not directly visible due to the surrounding stellar envelope. Therefore, I define the "signal time range" as the period from June 1, 2013, to December 31, 2017 (1416.3 days), which fully encompasses the expected timeframe for black hole formation. If a signal-like cluster were to be identified at any point within this signal time range, it would indicate that some astrophysical phenomenon capable of producing a neutrino burst occurred during this period. In such a case, the most likely candidate would be M31-2014-DS1, for which an observational report has already been published. On the other hand, if

TABLE 5.8: Definition of the signal and background time ranges.

Time range	Period	Duration (days)
Signal time range	2013 Jun. 1 – 2017 Dec. 31	1416.3
Background time range (before)	2012 Mar. 15 – 2013 Jun. 1	390.5
Background time range (after)	2018 Jan. 1 – 2018 May 31	118.1

no signal-like cluster is found, this result itself provides meaningful information: the absence of neutrino activity throughout the signal window served as a useful constraint for future estimates of the black hole formation time associated with M31-2014-DS1.

To estimate the background rate, I define the "background time range" as the periods immediately before and after the signal time range: from March 15, 2012, to June 1, 2013 (390.5 days), and from January 1, 2018, to May 31, 2018 (118.1 days), respectively. The pre-signal background time range is defined as the interval following a known supernova candidate observed in March 2012, and extending up to the beginning of the signal time range. The post-signal background time range is defined until the end of the pure-water phase after the signal time range. The details are summarized in Table 5.8.

The effective livetime fraction during the signal time range was evaluated. Although it cannot be completely excluded that the SK data were unavailable at the time of the M31-2014-DS1 event (e.g., due to calibration or maintenance periods), the yearly averaged live-time efficiencies were evaluated as shown in Figure 5.24. The efficiencies were $89.1 \pm 2.4\%$, $84.9 \pm 4.6\%$, $91.5 \pm 1.6\%$, $82.2 \pm 6.4\%$, and $76.8 \pm 6.0\%$ for 2013, 2014, 2015, 2016, and 2017, respectively, indicating that the detector was generally operational during this period.

5.5.2 Estimation method of atmospheric neutrino background

To determine the optimal energy threshold for the cluster search, I estimate the background event rate and the probability of background-induced clusters. However, the event rate above 20 MeV is very low due to limited statistics. Therefore, the total background estimate is constructed from two components: (1) a data-driven estimate based on the background in SK below 20 MeV, and (2) an MC-based atmospheric neutrino background above 20 MeV.

To reliably estimate the background rate above 20 MeV, I use a 500-year atmospheric neutrino Monte Carlo (MC) sample based on the HKKM 2011 flux [120, 121] and the NEUT 5.3.6 interaction generator [122]. The flux of atmospheric neutrino CCQE events in the MC is normalized by fitting the reconstructed energy spectrum in the range ($30 < E_{\mathrm{rec}} < 60$ MeV) to the data. This fit uses the full 10-year data set, including the signal-time range, to ensure sufficient statistics. Although the signal-time range is included, this energy region is above the typical expected neutrino energies from failed SNe, and even if a few signal events were present, their impact on the spectrum would be negligible.

5.5.3 Evaluation of background cluster

To determine the proper energy threshold for the cluster search, I evaluate the probability of background-induced clusters using a toy MC approach. For each candidate energy threshold, I perform 10^7 trials in which background events are randomly generated according to the estimated background rate. The corresponding energy distribution of the background rate derived from the atmospheric neutrino MC is shown in

Figure 5.25. To account for residual differences between the MC prediction and the data above 20 MeV, a scale factor is applied. The scale factor S is determined by evaluating the Chi-square calculation as shown:

$$\chi^2 = \Sigma(\frac{N_i^{\rm obs} - S \times N_i^{\rm bkg}}{\sigma_i}). \tag{5.7}$$

$N_i^{\rm obs}$, $N_i^{\rm bkg}$, and σ_i represent the number of events in data, the number of events in MC, and the statistical error of each bin of data, respectively. The scale factor is $s = 0.758 \pm 0.059$ from the chi square calculation in Figure 5.26. This uncertainty is shown as an error of the scale factor. As a result, the estimated background rate obtained with the $S = 0.758$ is 10.58 day^{-1} for 8 MeV $< E_{\rm rec} \leq$ 80 MeV and 0.09 day^{-1} for 18 MeV $< E_{\rm rec} \leq$ 80 MeV.

In the estimation of the background cluster probability, two sources of systematic uncertainty are considered. The first is the scaling uncertainty between data and MC, which is treated using Gaussian sampling. The second is the statistical uncertainty in the data, for which the statistical error of each energy bin below 20 MeV is taken into account. For each toy MC trial, the scale factor is randomly varied within its uncertainty. The background rate for a given energy threshold is then recalculated, incorporating both the data-driven and MC-based components. For energy bins below 20 MeV, the background rate consists of a data-driven component obtained through random sampling and an MC-based component scaled by the factor S. The total background rate (Bkg._Rate) is the sum of these two components.

Once the background rate is determined, the time differences between consecutive background events are generated by sampling from an exponential distribution with a mean of 1/Bkg._Rate. The sampled time intervals are cumulatively summed until their total exceeds the duration of the signal-time window (4.58 years), at which point the trial is terminated.

In each trial, I search for clusters defined as ≥ 2 events within a 10-second window, and count the number of such occurrences. The cluster probability is defined as the fraction of trials with more than one cluster:

$$P = \frac{N_{\geq 1\,\rm cluster}}{N_{\rm trials}}, \tag{5.8}$$

where $N_{\geq 1\,\rm cluster}$ is the number of trials with one or more clusters, and $N_{\rm trials}$ is the total number of trials. I require the probability to be below the 3σ level ($P < 0.003$), ensuring that any observed cluster is not likely to be due to statistical fluctuations of the background. As shown in Figure 5.27, the cluster probability decreases with increasing energy threshold. Based on this evaluation, I set the energy threshold to 18 MeV, which satisfies the 3σ criterion. At this threshold, the observation of two or more events within 10 s would constitute a detection.

5.5.4 Detection probability in SK

I evaluate the detection probability of neutrino signals from M31-2014-DS1 in SK, assuming an analysis threshold of 18 MeV in positron energy. In this study, a detection is defined as the observation of two or more neutrino events. The detection probability is calculated using a Poisson distribution for the expected number of signal and background events within the 10-second window. I denote the expected number of signal events by $N_{\rm sig}$ and the expected number of background events by $N_{\rm bkg}$. The

probability of detecting at least two events is then given by

$$P(N_{\bar{\nu}_e} \geq 2) = P(N_{\bar{\nu}_e} \geq 1) - (N_{\rm sig} + N_{\rm bkg}) \times e^{-(N_{\rm sig}+N_{\rm bkg})}, \tag{5.9}$$

where the second term represents the probability of observing exactly one event. The $N_{\rm sig}$ is computed using SKSNSim for a failed SN model at a reference distance of 770 kpc with an 18 MeV positron energy threshold, and is scaled by distance when evaluating the detection probability shown in Table 5.7. For the background expectation, I use 0.09 day^{-1}. Figure 5.28 shows the resulting detection probability as a function of distance under the analysis conditions adopted here. For the optimistic failed supernova model based on the Shen-TM1 relativistic mean-field EOS [30], which is relatively stiff and yields a maximum cold neutron star mass of $2.2M_{\odot}$, the detection probability at 770 kpc is approximately 72%. Figure 5.29 further presents the results when both normal and inverted neutrino mass orderings are taken into account. When neutrino oscillations are included, the mixing of $\bar{\nu}_x$ shifts the average $\bar{\nu}_e$ energy to higher values, as illustrated in Figure 5.31. In particular, the SFHo ($23M\odot$) model [32] predicts a relatively large flux of $\bar{\nu}_x$. Under the inverted mass ordering, the near-complete conversion of $\bar{\nu}_x$ to $\bar{\nu}_e$ leads to a substantial enhancement in the expected event rate at SK. Consequently, the detection probability increases from roughly 14% in the no-oscillation case to nearly 70% when oscillation effects are included. Across several failed SN models, the expected detection probability spans approximately 5–75% depending on the oscillation scenario. Therefore, under optimistic emission conditions, our results indicate that SK retains sufficient sensitivity to detect neutrinos from M31-2014-DS1.

5.6 Search Result

5.6.1 Evaluation of excess events in the signal time range

Figure 5.33 shows a comparison of the energy distributions in the signal and background time ranges. As shown in Figure 5.33, no significant excess is found in the energy region above 18 MeV, which is the range expected for neutrinos from black hole formation. To evaluate the significance of the excess between the observed number of events ($N_{\rm obs}$) and the expected background ($N_{\rm bkg}$) above a positron energy of 18 MeV, I use the p-value. In this estimation, I use the entire pre-signal time range region in SK-IV to improve statistics. The p-value represents the probability of obtaining the observed number of events under the assumption that the pre-signal time range in SK-IV consists of background. Assuming that the background follows a Poisson distribution with mean $N_{\rm bkg}$, the p-value is given by

$$p = \sum_{k=N_{\rm obs}}^{\infty} \frac{N_{\rm bkg}^{k}}{k!}\, e^{-N_{\rm bkg}}, \tag{5.10}$$

which corresponds to the upper-tail probability of the Poisson distribution under the background-only hypothesis. Using this formula, the resulting p-value is evaluated to be $p = 0.225$. This value indicates that the observed events are fully compatible with statistical fluctuations of the expected background, and therefore, no evidence for an excess is obtained.

5.6.2 Results of the cluster search

Following the cluster search procedure, no clusters consisting of two or more events within a 10-second window were found in the signal time range. Based on this result, I evaluate the upper limit on the time-integrated electron antineutrino luminosity ($L_{\bar{\nu}_e}$) using two complementary methods. In both methods, the expected number of signal events in SK is estimated by taking into account the detector response and signal efficiency.

In the first approach, I derive the upper limit on the $L_{\bar{\nu}_e}$ by first calculating the 90% confidence level upper limit on the neutrino fluence at SK, based on the assumption of specific failed SN models. The fluence upper limit is calculated as:

$$\Phi = \frac{N_{90}}{N_T \int dE_{\bar{\nu}_e} \lambda(E_{\bar{\nu}_e}) \sigma(E_{\bar{\nu}_e}) R(E_e, E_{\rm vis}) \epsilon(E_{\rm vis})} \tag{5.11}$$

Here, Φ is the upper limit on the low-energy neutrino flux. N_{90}, E_e, $E_{\rm vis}$ represent the 90% confidence level upper limit on the number of neutrino events, the true electron energy, and the reconstructed visible energy, respectively. Since no clusters are observed within a 10-second time window, I set $N_{90} = 3.89$, based on Poisson statistics. N_T is the number of target particles in the detector. $\lambda(E_{\bar{\nu}_e})$ denotes the normalized neutrino energy spectrum, $\sigma(E_{\bar{\nu}_e})$ is the neutrino interaction cross section from Strumia-Vissani model for IBD [123], $R(E_e, E_{\rm vis})$ is the energy response function that connects E_e to $E_{\rm vis}$, and $\epsilon(E_{\rm vis})$ is the detection efficiency as a function of visible energy. The effect of $R(E_e, E_{\rm vis})$ is expected to be small in the energy range relevant to this analysis, and is therefore not taken into account in this analysis. Using the fluence upper limit Φ, I derive the corresponding upper limit on the total emitted energy under the assumption of isotropic emission. The relation is given by:

$$L_{\bar{\nu}_e} = 4\pi D^2 \langle E_{\bar{\nu}_e} \rangle \cdot \Phi, \tag{5.12}$$

where D is the distance to the source and $\langle E_{\bar{\nu}_e} \rangle = \int_0^\infty \lambda(E) dE$ is the mean energy of the emitted electron antineutrinos based on the failed SN model spectrum. Although neutrinos of all flavors are emitted in a CCSN, only the detectable electron antineutrinos are considered here, as the IBD interaction is the dominant detection channel in SK. In Figure 5.34, the $L_{\bar{\nu}_e}$ upper limit for each failed SN model is shown.

In another approach, I estimate the number of expected events for IBD using a Fermi-Dirac neutrino spectrum characterized by a temperature T and a $L_{\bar{\nu}_e}$. The expected number of events is calculated as:

$$N_{\rm event} = \int_{E_{\rm th}}^{\infty} N_T \cdot \phi(E_{\bar{\nu}_e}) \cdot \sigma(E_{\bar{\nu}_e}) \cdot \epsilon(E_{\bar{\nu}_e}) \cdot dE_{\bar{\nu}_e}. \tag{5.13}$$

Here, $\phi(E_{\bar{\nu}_e})$ is the neutrino flux at Earth, and other variables are the same as Equation 5.11. The flux $\phi(E_{\bar{\nu}_e})$ is derived from a Fermi-Dirac distribution assuming a T and $L_{\bar{\nu}_e}$, with zero chemical potential. $N_{\rm event}$ for each mean energy and $L_{\bar{\nu}_e}$ is illustrated in Figure 5.35. The distribution is normalized to satisfy the condition:

$$L_{\bar{\nu}_e} = \int_0^\infty E_{\bar{\nu}_e} \cdot \frac{dN}{dE_{\bar{\nu}_e}} dE_{\bar{\nu}_e}. \tag{5.14}$$

The distance to the source, D, is assumed to be 770 kpc, and the flux is given by

$\phi(E_{\bar{\nu}_e}) = 1/4\pi D^2 \cdot dN/dE_{\bar{\nu}_e}$. Figure 5.36 shows the excluded region from the no cluster result, along with model predictions in the total emitted energy of electron antineutrinos, $E_{\bar{\nu}_e}$, and the mean neutrino energy, $\langle E_{\bar{\nu}_e} \rangle$ plane. The shaded regions represent the excluded parameter space derived from the nondetection of time-clustered events in SK, assuming Poisson statistics. Each contour represents a confidence level of 50%, 68%, 90%, 95%, and 99%, respectively, which translates to a Poisson upper limit of 1.68, 2.35, 3.89, 4.74, and 6.64 events. Contours indicate combinations of emission parameters ($L_{\bar{\nu}_e}$, $\langle E_{\bar{\nu}_e} \rangle$) for which the probability of detecting two or more events would have exceeded the given confidence level. While the 18 MeV threshold in the cluster search is chosen to ensure a background-free condition for the analysis, the sensitivity remains sufficient to constrain the Shen-TM1 model at a confidence level exceeding 68%, demonstrating that this method can effectively constrain optimistic black hole formation scenarios.

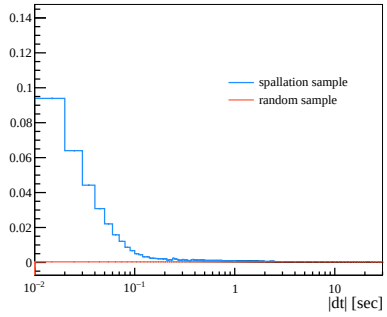

(A) dt

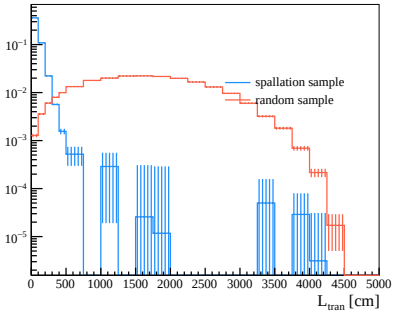

(B) L_{t}

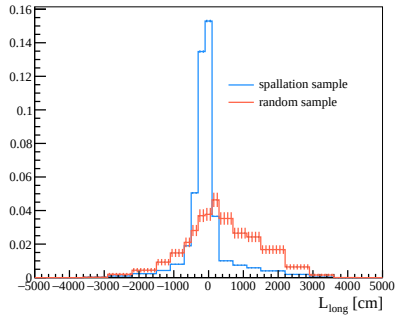

(C) L_{l}

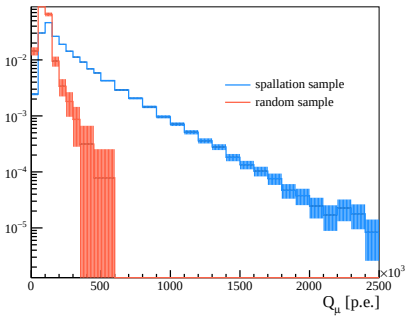

(D) Q_{μ}

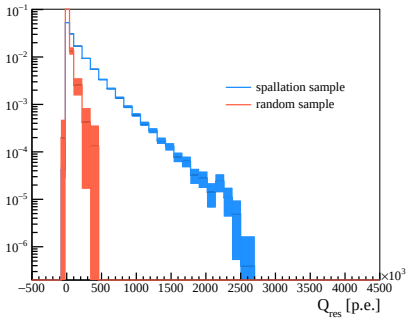

(E) Q_{res}

FIGURE 5.14: PDFs of the muon spallation sample (blue) and the random sample (red) for single-through going muons. dt and L_{t} bin are $0-0.05$ s and $0-300$ cm, respectively.

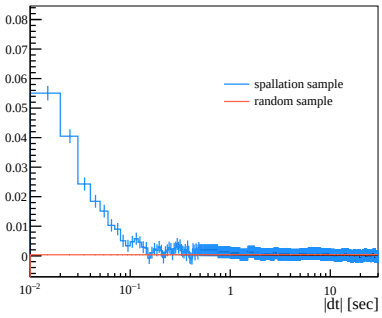

(A) dt

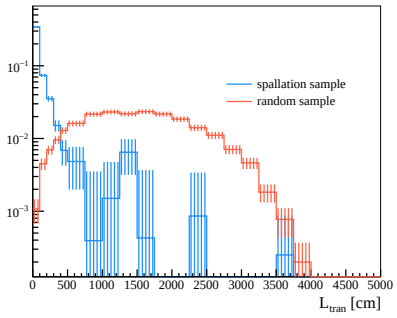

(B) L_{t}

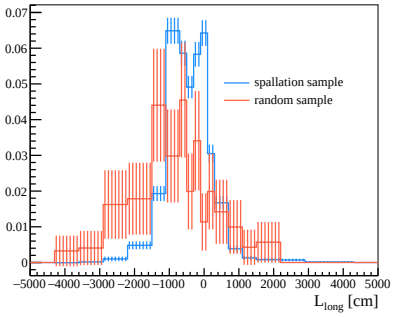

(C) L_{l}

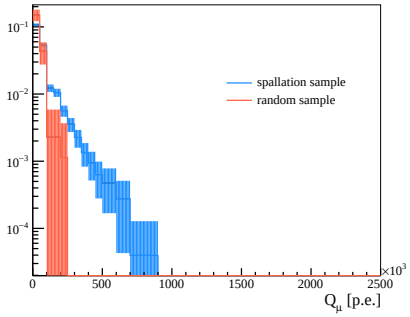

(D) Q_{μ}

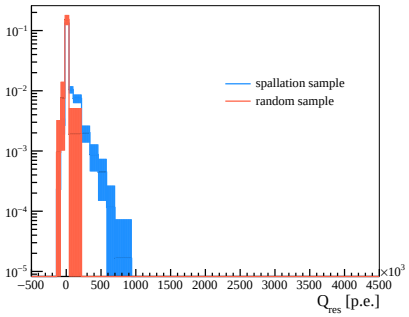

(E) Q_{res}

FIGURE 5.15: PDFs of the muon spallation sample (blue) and the random sample (red) for stopping muons. dt and L_{t} bin are $0-0.05$ s and $0-300$ cm, respectively.

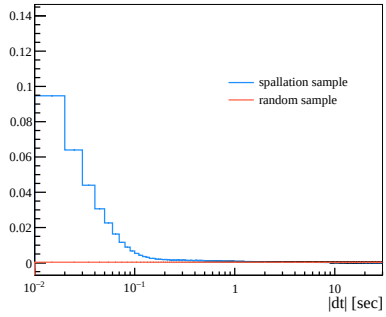

(A) dt

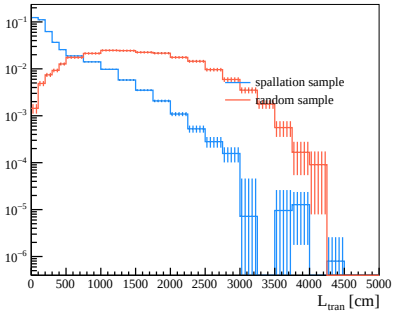

(B) L_{t}

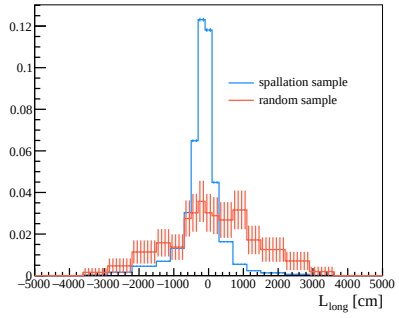

(C) L_{l}

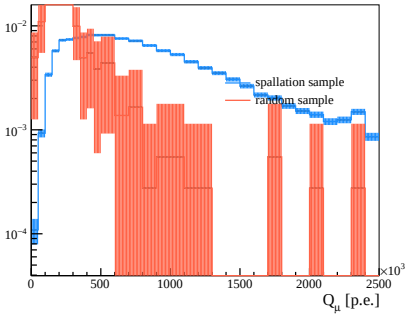

(D) Q_{μ}

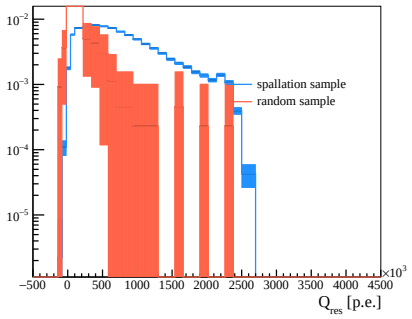

(E) Q_{res}

FIGURE 5.16: PDFs of the muon spallation sample (blue) and the random sample (red) for multiple muons. dt and L_{t} bin are $0-0.05$ s and $0-300$ cm, respectively.

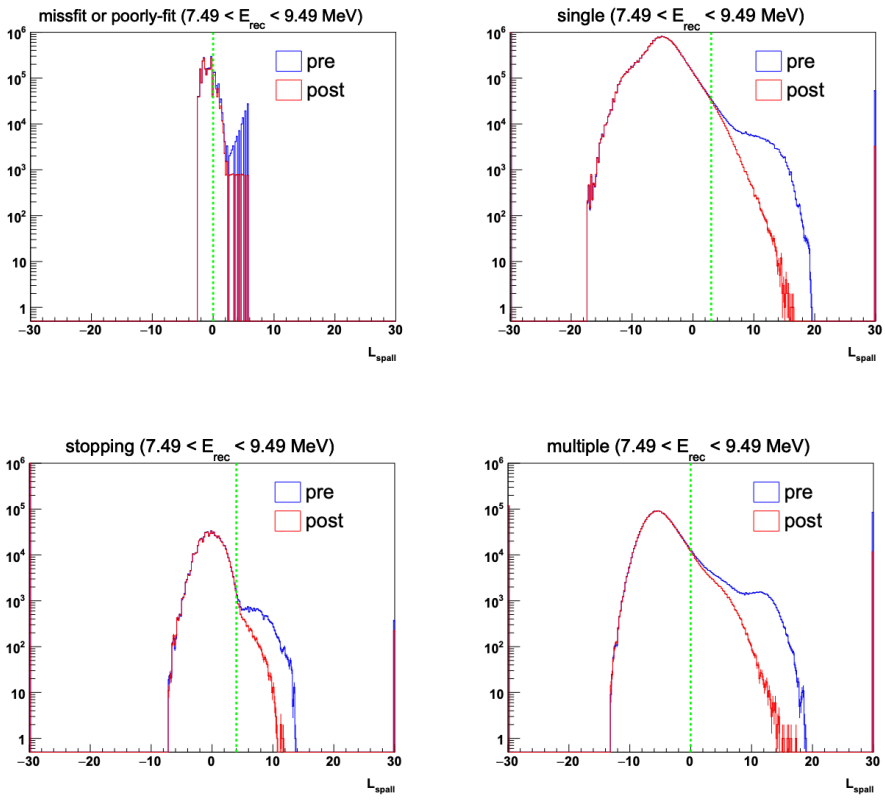

FIGURE 5.17: Spallation likelihood distributions for each muon type in the 7.49 – 9.49 MeV energy range [27]. The dashed green lines indicate the cut positions, and events on the right side are rejected.

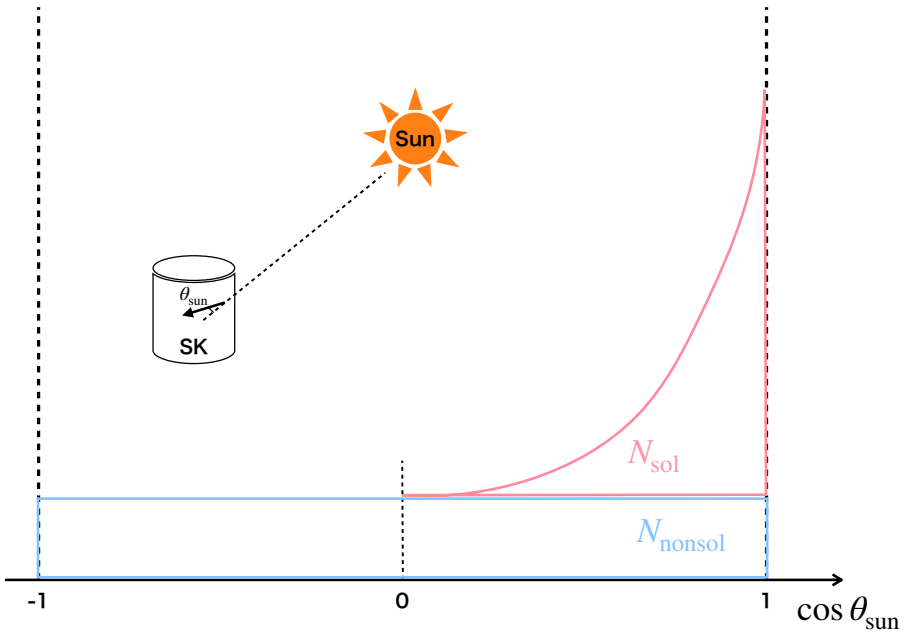

FIGURE 5.18: Shcematic diagram of the definition of $\theta_{\rm sun}$ and the $\cos\theta_{\rm sun}$ distribution,

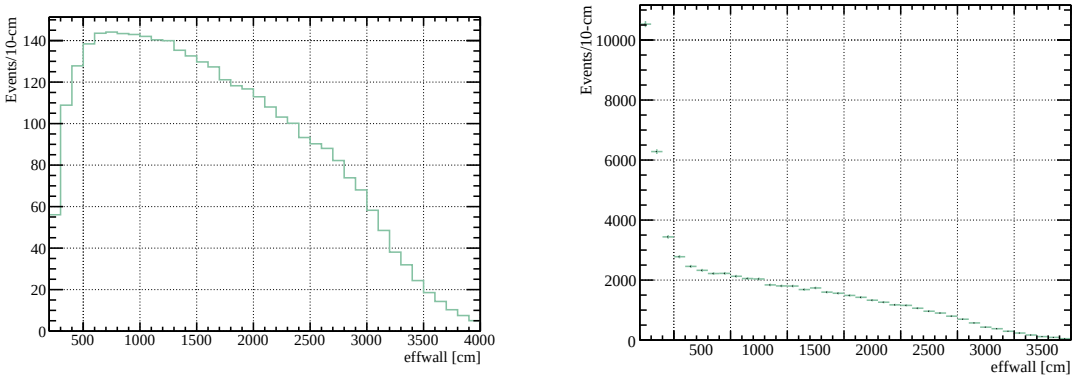

(a) $\bar{\nu}_e$ MC (b) data (SK-IV 2970.1 days)

FIGURE 5.19: The distribution of *effwall* for the $\bar{\nu}_e$ signal MC and data after the spallation cut.

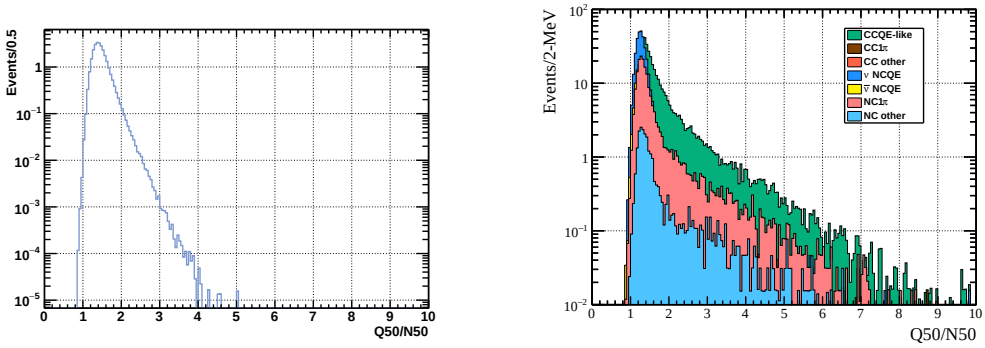

(A) $\bar{\nu}_e$ MC (B) Atmospheric neutrino MC

FIGURE 5.20: Distributions of Q_{50}/N_{50} for the $\bar{\nu}_e$ signal (left) and atmospheric neutrino (right) Monte Carlo samples after the application of the pilike cut.

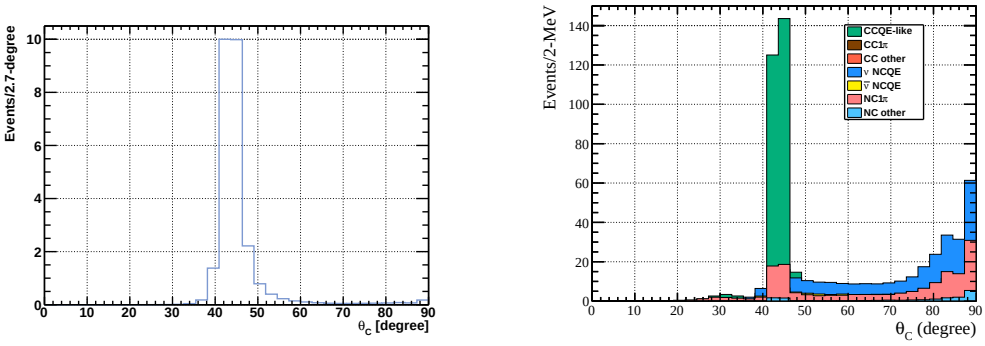

(A) $\bar{\nu}_e$ MC (B) Atmospheric neutrino MC

FIGURE 5.21: Distributions of θ_C for the $\bar{\nu}_e$ signal (left) and atmospheric neutrino (right) MC samples after Q_{50}/N_{50} cut.

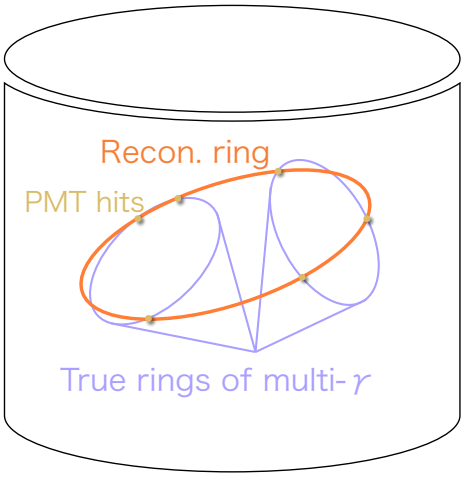

FIGURE 5.22

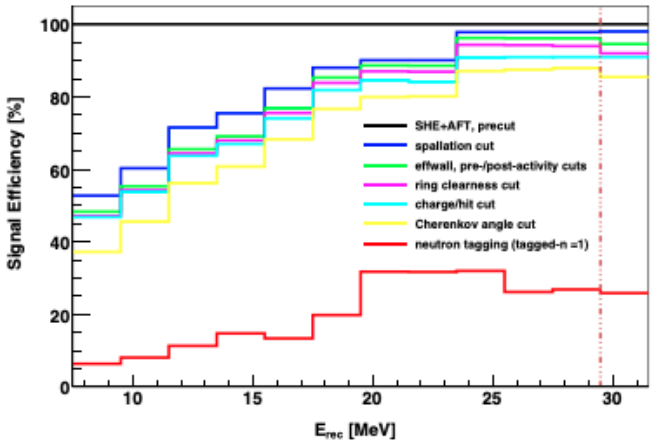

FIGURE 5.23: Efficiency of signal detection as a function of reconstructed kinetic energy E_{rec} [28].

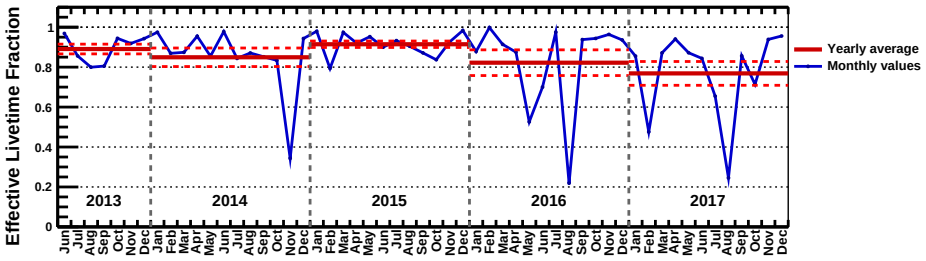

FIGURE 5.24: Livetime fraction of SK used in this analysis. The blue points indicate the effective livetime fraction for each month, while the red solid lines show the yearly averaged effective livetime fraction. The red dashed lines represent the standard deviation of the yearly mean. The loss of livetime is mainly attributed to detector calibrations and maintenance periods.

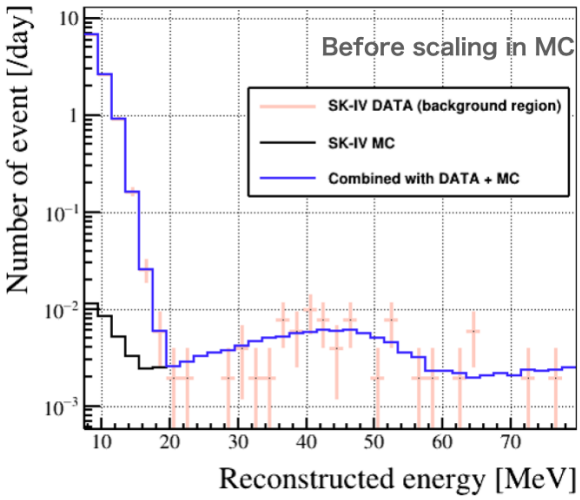

FIGURE 5.25: The energy distribution of the background event. The blue histogram is the energy distribution of the atmospheric neutrino MC.

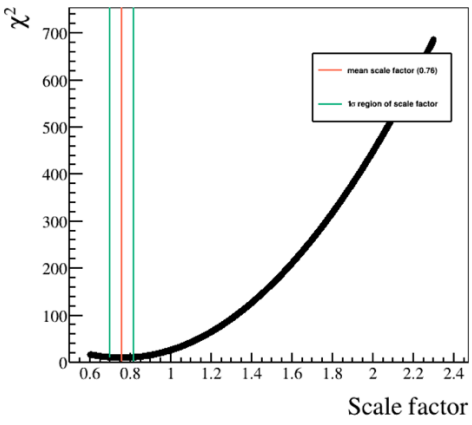

FIGURE 5.26: The best fit of chai square

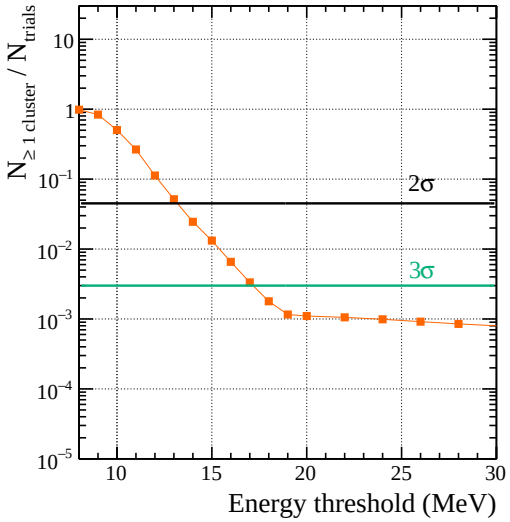

FIGURE 5.27: The expected probability of observing clusters due to background events at each energy threshold. The red points indicate the probability of observing one or more clusters within the signal time range.

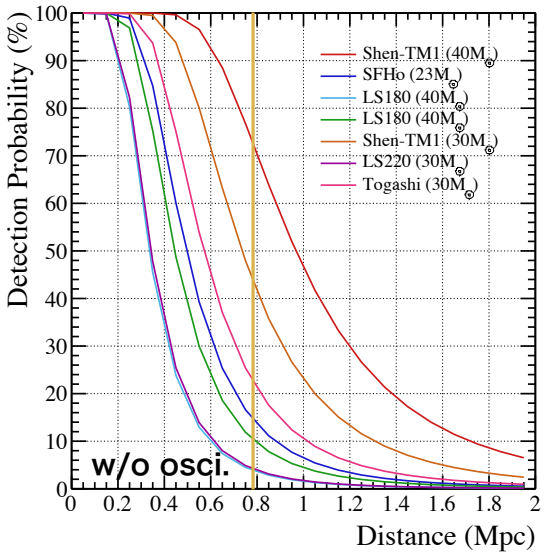

FIGURE 5.28: Detection probability in SK as a function of distance. The orange line shows the distance to M31. In this estimation, the same analysis conditions, such as 18 MeV positron energy threshold, are used. The models correspond to [29, 30, 31, 32]. In this plot, the neutrino oscillation of the MSW effect is not included.

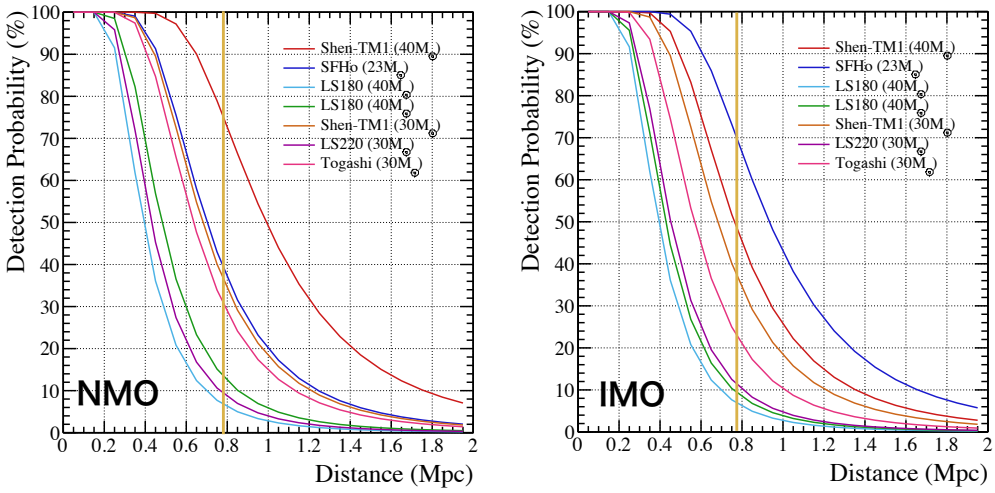

(a) Normal mass ordering (b) Inverted mass ordering

FIGURE 5.29: The same plot of Figure 5.28, but these are considered neutrino oscillation of the MSW effect.

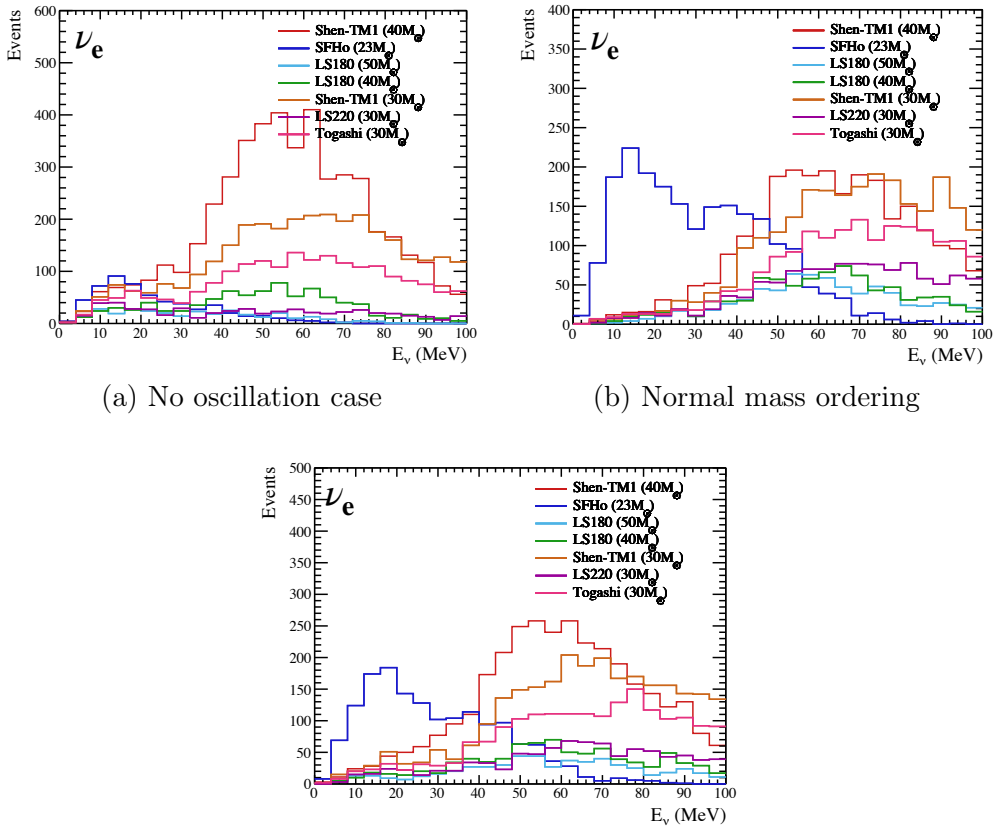

(a) No oscillation case (b) Normal mass ordering

(c) Inverted mass ordering

FIGURE 5.30: Neutrino energy spectra for three oscillation scenarios.

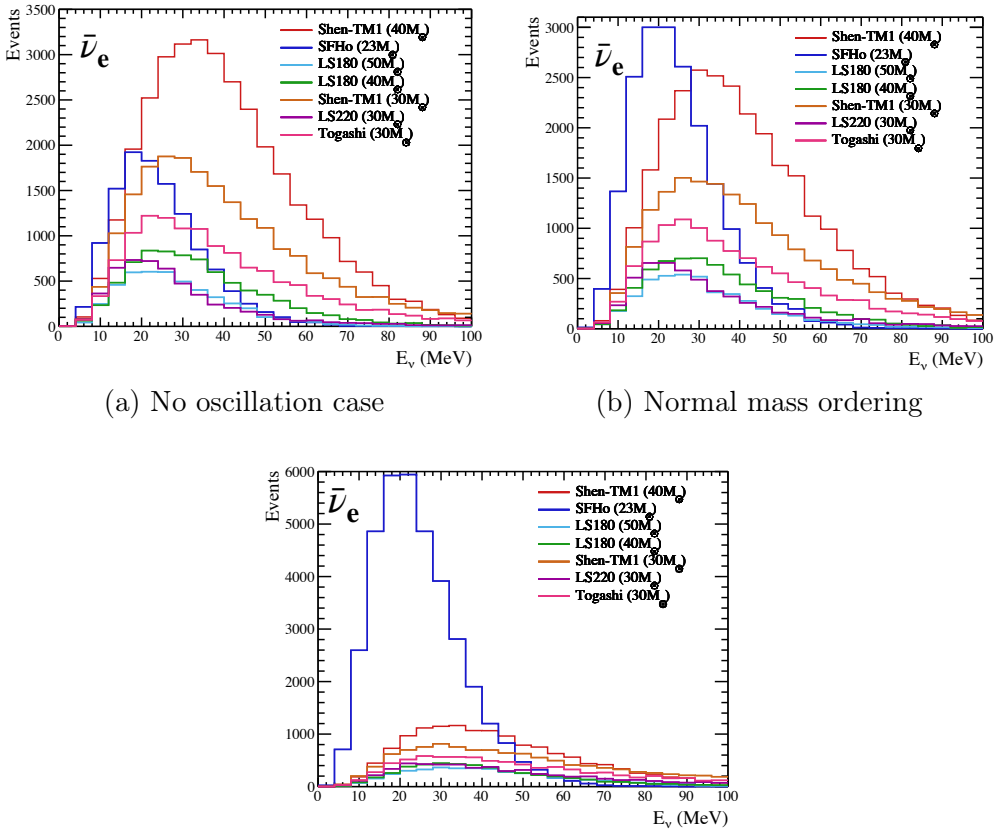

(a) No oscillation case

(b) Normal mass ordering

(c) Inverted mass ordering

FIGURE 5.31: Neutrino energy spectra for three oscillation scenarios.

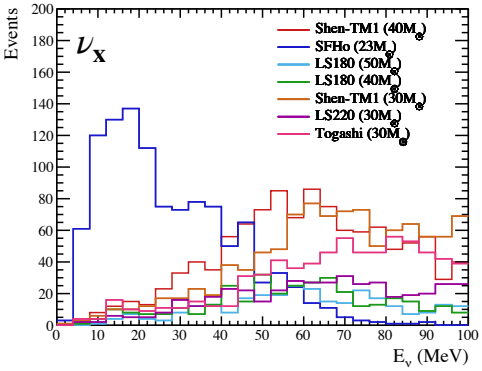

(a) No oscillation case

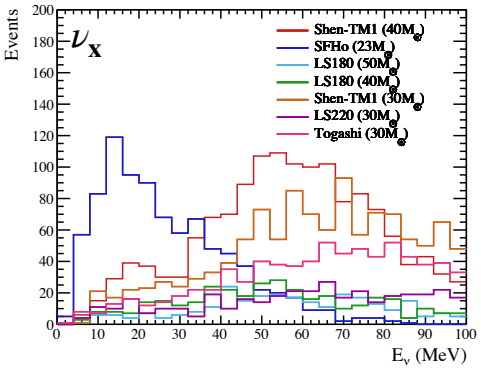

(b) Normal mass ordering

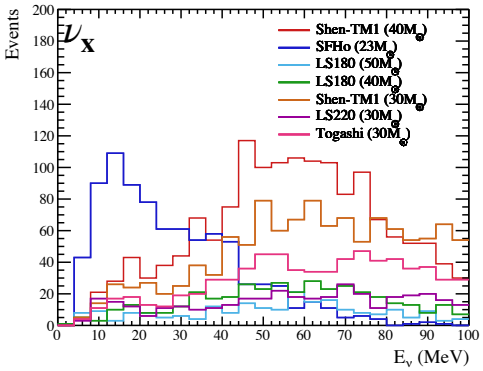

(c) Inverted mass ordering

FIGURE 5.32: Neutrino energy spectra for three oscillation scenarios.

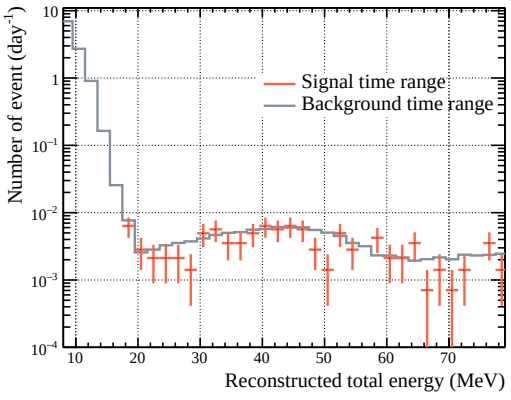

FIGURE 5.33: The energy spectrum of events. The gray and red histograms represent the energy distribution in the background and signal time ranges, respectively. The signal time range spans from June 1, 2013, to December 31, 2017, while the background time range includes all periods before the signal time range in SK-IV. The background also includes MC events above 20 MeV.

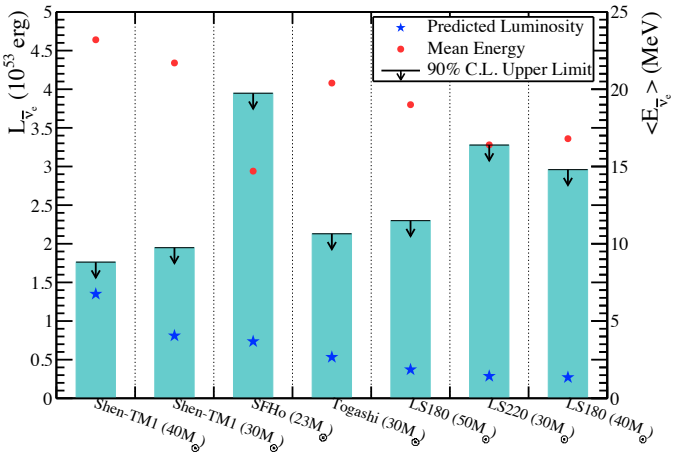

FIGURE 5.34: Upper limits on the time-integrated electron antineutrino luminosity ($L_{\bar{\nu}_e}$) for each failed SN model. The star marks the predicted $L_{\bar{\nu}_e}$ of the model, whereas the solid black line indicates the 90% confidence-level upper limit obtained in the present work. From left to right, the models correspond to [29, 30, 31, 32]. The circle points show the average energy for each model.

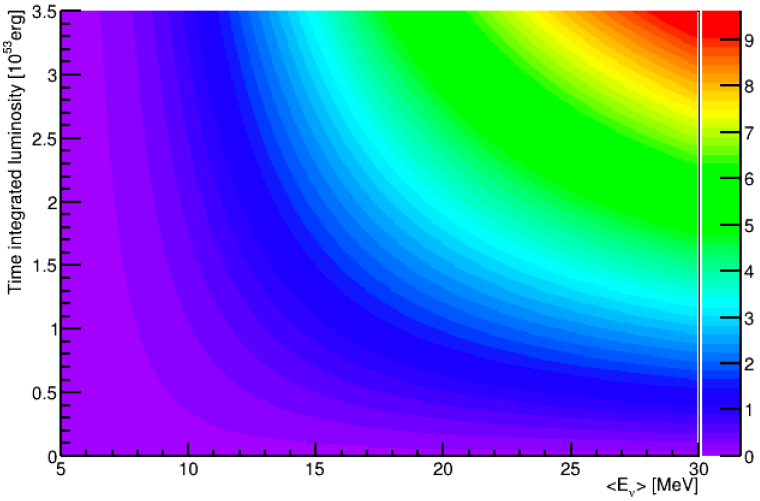

FIGURE 5.35: The relationship of time-integrated electron antineutrino luminosity and reconstructed mean energy. Color shows the expected neutrino event in SK for each luminosity and mean energy point.

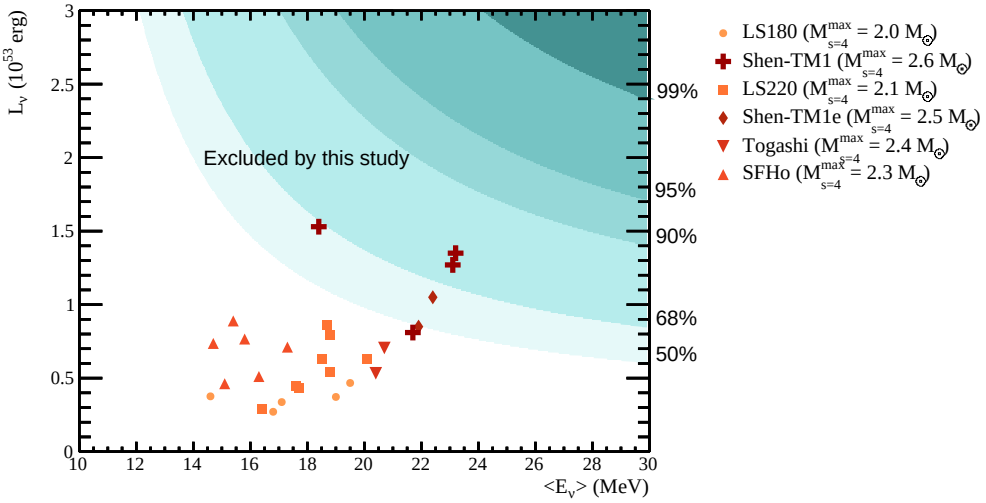

FIGURE 5.36: Total emitted electron antineutrino energy L_ν versus mean energy $\langle E_{\bar{\nu}_e} \rangle$. The shaded bands indicate regions that would have produced ≥ 2 correlated events in SK with probabilities of 50%, 68%, 90%, 95%, and 99% (light to dark cyan), assuming Poisson statistics for a source at the distance of 770 kpc. Filled circles show individual simulation results for six nuclear equations of state (EOS): LS180, LS220, SFHo, Togashi, Shen-TM1e, and Shen-TM1. Each model corresponds to Figure 1 and Table 1 in [25].

Chapter 6

Discussion in Failed SN Candidate in M31

6.1 Consideration for Discriminating Failed SN Models with Different EOS

In Section 5.6, I derived the 90% C.L. upper limits on the time-integrated electron antineutrino luminosity. As shown in Figure 5.34, for models such as Shen-TM1($40M_{\odot}$), which predict both high $L_{\bar{\nu}_e}$ and higher mean neutrino energy, the upper limit derived from our analysis approaches the predicted total emitted neutrino energy. In contrast, for models like SFHo ($23M_{\odot}$), which have lower mean neutrino energy, the fluence upper limit is more affected by the analysis energy threshold, resulting in upper limits that tend to be further from the model predictions.

In addition, stiffer EOSs generally allow for large maximum PNS gravitational masses. To interpret these differences among models, I discuss the maximum mass, as indicated in the Figure 5.36 legend. Larger maximum mass leads to a longer accretion phase before black hole formation, thereby resulting in a large total neutrino emission. Among the EOSs considered in this analysis, the Shen EOS yields the largest maximum mass. Consequently, models based on the Shen EOS, which predict the highest neutrino emission, are subject to relatively strong constraints in the present study.

Because of the lack of sensitivity in SK, a detailed discussion of failed SN model discrimination remains challenging at this time. However, this is the first search for an associated failed SN candidate, and future discoveries of similar events—or a more precise determination of the black hole formation time of M31-2014-DS1—may enable a more comprehensive examination of model discrimination.

6.2 Consideration of Neutrino Oscillation in 90% Upper Limit

In this section, the impact of neutrino oscillations due to the MSW effect on the time-integrated electron antineutrino luminosity is examined. The MSW effect is evaluated using Equations 1.32 and 1.33. To estimate the effect of neutrino oscillations, the time-integrated electron antineutrino luminosity and the mean electron antineutrino energy for failed SN models are calculated as follows.

$$L_{\bar{\nu}_e}^{\mathrm{obs}} = \begin{cases} \cos^2\theta_{12}\, L_{\bar{\nu}_e}^{\mathrm{src}} + \sin^2\theta_{12}\, L_{\bar{\nu}_x}^{\mathrm{src}}, & \text{normal mass ordering,} \\ L_{\bar{\nu}_x}^{\mathrm{src}}, & \text{inverted mass ordering.} \end{cases} \tag{6.1}$$

$$\langle E\rangle_{\bar{\nu}_e}^{\mathrm{obs}} = \begin{cases} \dfrac{\cos^2\theta_{12}\, L^0_{\bar{\nu}_e}\, \langle E\rangle^0_{\bar{\nu}_e} + \sin^2\theta_{12}\, L^0_{\nu_x}\, \langle E\rangle^0_{\nu_x}}{\cos^2\theta_{12}\, L^0_{\bar{\nu}_e} + \sin^2\theta_{12}\, L^0_{\nu_x}}, & \text{normal mass ordering,} \\ \langle E\rangle^0_{\bar{\nu}_x}, & \text{inverted mass ordering.} \end{cases} \tag{6.2}$$

In the inverted mass ordering case, all $\bar{\nu}_x$ are converted into $\bar{\nu}_e$ through flavor transformation, whereas in the normal mass ordering case, $\bar{\nu}_x$ and $\bar{\nu}_e$ are partially mixed. Figure 6.1 shows the resulting Fermi–Dirac distributions when the corresponding neutrino oscillation effects are taken into account. In typical supernova neutrino emission,

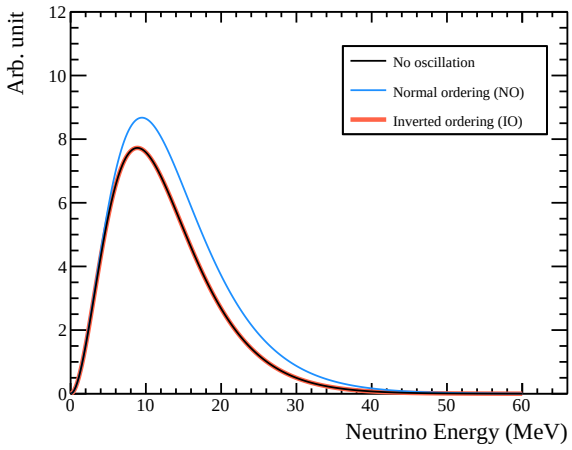

FIGURE 6.1: Fermi-Dirac distribution. Black, blue, and red lines represent the no oscillation case, normal mass ordering case, and inverted mass ordering case, respectively.

the mean energy of $\bar{\nu}_x$ is higher than that of $\bar{\nu}_e$. Therefore, in the Fermi-Dirac calculations, the temperature of $\bar{\nu}_x$ is set to be 1.2 times that of ν_e and $\bar{\nu}_e$, reflecting the approximate difference in their mean energies.

Figure 6.2 shows the excluded region in the plane of the time-integrated electron antineutrino luminosity and the mean electron antineutrino energy. In the case of normal mass ordering, the expected number of neutrino events increases, which shifts the excluded region toward lower luminosities. On the other hand, the excluded region in the inverted mass ordering case remains unchanged compared with the non-oscillation case. As a result, the Shen-TM1e EOS model additionally enters the 68% excluded region. In addition, for failed SN models, the emitted number of $\bar{\nu}_x$ is smaller than that of $\bar{\nu}_e$, so the model points shift downward once neutrino oscillations are included. Consequently, the constraints on the failed SN models become weaker in the inverted mass ordering case.

6.3 Proper Signal Time Range for Cluster Search in SK

In this study, I searched for neutrinos associated with M31-2014-DS1 by defining a signal time range of 3.88 years. However, with such a long time range, the positron energy threshold is set to 18 MeV, which is slightly higher than the mean energies predicted by failed SN models, as required to suppress backgrounds. One possible way to lower the energy threshold is to narrow the signal time range. Figure 6.3 shows the relationship between the expected probability of observing clusters and the positron energy threshold for several assumed signal time ranges. By restricting the

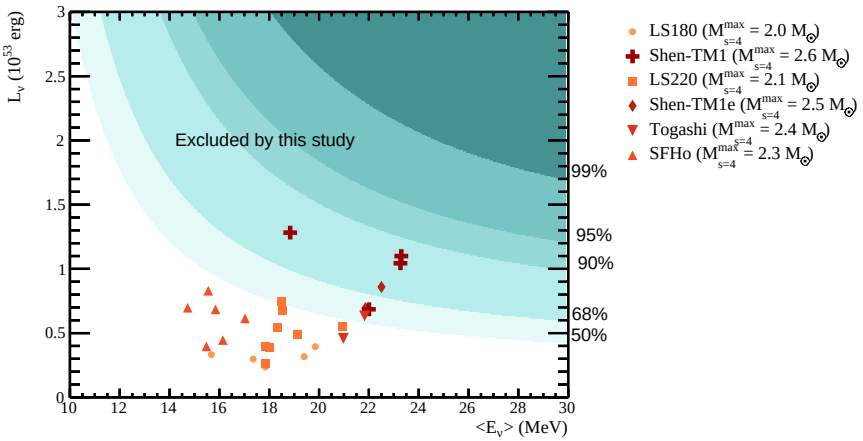

(a) Normal mass ordering

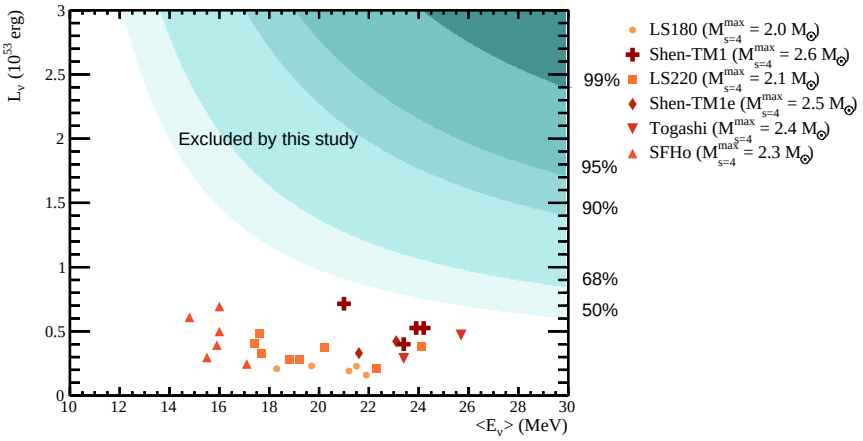

(b) Inverted mass ordering

FIGURE 6.2: Same plot with Figure 6.12. In these plots, the neutrino oscillation of the MSW effect is considered.

signal time range to within 10 days, the positron energy threshold can be lowered to 11 MeV, thus covering nearly the entire energy range predicted by failed SN models. Moreover, most failed SN models undergo black hole formation within approximately 1 second. If black hole formation is expected to occur within 10 seconds, the analysis can be performed with a sufficiently low energy threshold, starting from 8 MeV.

6.4 Future Prospect

6.4.1 Neutrino sensitivity of M31-2014-DS1 in SK-Gd

In the current SK-Gd experiment, the increased Gd mass concentration, together with the enhanced selection of neutron-induced events achieved through machine learning techniques, has led to an improvement in the neutron detection efficiency [33]. This efficient neutron tagging capability enables a progressive reduction of background events without accompanying neutrons. In this section, I discuss the sensitivity of SK-Gd to neutrino signals from a failed supernova candidate, such as M31-2014-DS1.

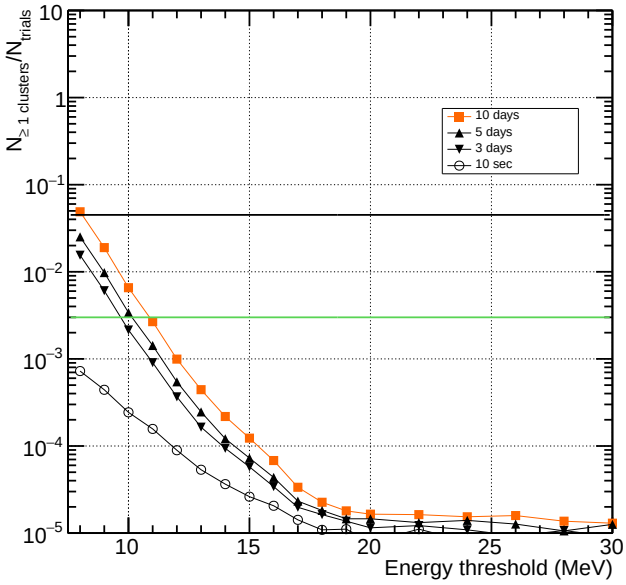

FIGURE 6.3: The expected probability of observing clusters due to background events at each positron energy threshold. The square, upward triangle, downward triangle, and circle points represent signal time ranges for 10 days, 5 days, 3 days, and 10 seconds, respectively.

Figure 6.4 shows the energy spectrum of background events in SK-VII after using the neutron tagging cut. The detail of the neutron tagging cut is described in Section 5.4.7. Thanks to the improvement in neutron tagging performance, the back-

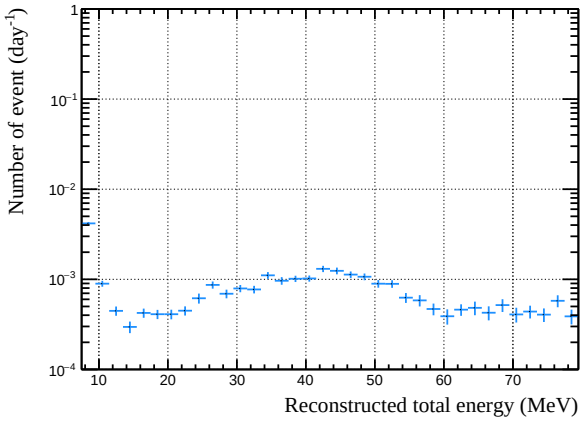

FIGURE 6.4: The energy spectrum of background events after using the neutron tagging cut in SK-VII.

ground rate is significantly reduced, compared with Figure 5.33. In SK-IV, the background rate before applying the neutron tagging cut was 10.59 day^{-1}. In contrast, in the current SK-VII period, the application of the neutron tagging cut reduces the background rate to 0.09 day^{-1}. Considering this signal efficiency as shown in Figure 6.5, the expected neutrino event at 770 kpc is estimated in Figure 6.6. Here, the Neural Net is used as neutron tagging cut. The purple and green lines represent the expected background events during a 3.88-year signal time range, with and without

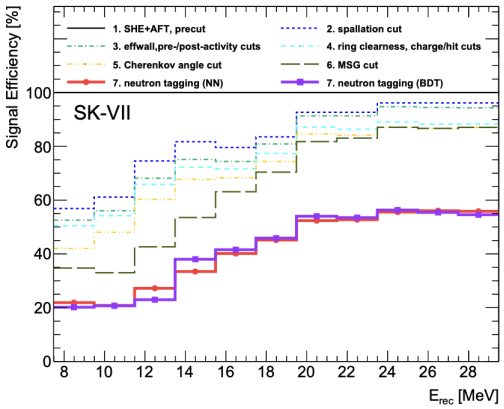

FIGURE 6.5: Signal efficiency as a function of reconstructed positron energy [33].

the neutron-tagging cut, respectively. In the SK-VII period, where the signal efficiency is improved, the expected signal sufficiently exceeds the background level.

Figure 6.7 shows the cluster probability in the SK-Gd phase estimated from the same method as described in Section 5.5. Because the background rate can be reduced to a very low level, it becomes possible to achieve an effectively background-free condition even when the energy threshold is lowered to 8 MeV, while retaining the same signal time range of 3.88 years as adopted in this study.

6.4.2 Neutrino sensitivity of M31-2014-DS1 in Hyper-Kamiokande

As a future extension of this study, I consider the sensitivity of the next-generation water Cherenkov detector, Hyper-Kamiokande (HK) [124], which is currently under construction in Japan.

Overview of Hyper-Kamiokande

HK is a next-generation water Cherenkov detector currently under construction in the Kamioka mine, Gifu, Japan. A schematic view of the detector is shown in Figure 6.8. The detector will consist of a cylindrical water tank with a diameter of approximately 68 m and a height of 71 m, located about 600 m underground to provide shielding from cosmic rays. The inner detector will be instrumented with about 40,000 newly developed 50 cm high-sensitivity photomultiplier tubes (PMTs), while the outer detector will be equipped with smaller PMTs for tagging entering particles.

With a fiducial volume about 8.4 times larger than that of SK and equipped with these new photosensors, HK will achieve significantly higher detection efficiency by newly developed PMT, as well as improved energy and directional resolution. The construction of HK is underway, and the start of operation is expected around 2028.

Expected supernova detection rate

Given its much larger target mass and improved photon detection capability, HK is expected to significantly enhance sensitivity to various neutrino sources. In particular, for CCSNe, HK will be capable of detecting tens of thousands of neutrino events from a Galactic explosion and will extend the detectable range to nearby galaxies. In the following, I estimate the expected supernova detection rate for HK based on the same framework used for SK, assuming identical analysis conditions. Figure 6.9 shows the

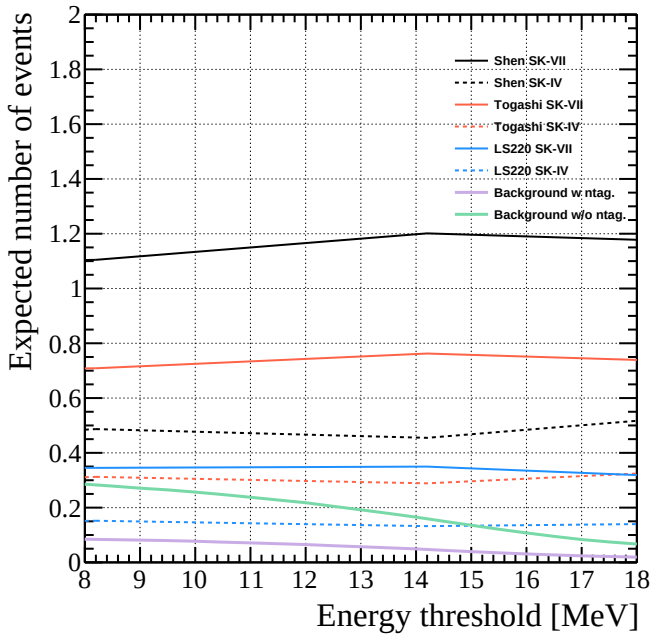

FIGURE 6.6: Expected neutrino events for the three failed supernova models are shown as a function of the energy threshold. The black, red, and blue lines correspond to the Shen EOS, Togashi EOS, and LS220 EOS, respectively. The solid and dashed lines indicate the expected neutrino events when applying neutron tagging in SK-VII and SK-IV. The purple and green lines show the expected background events for 3.88 years with and without neutron tagging in SK-VII.

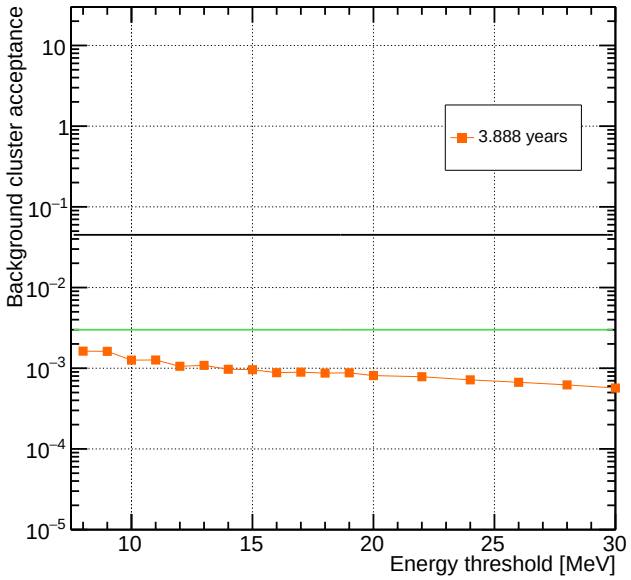

FIGURE 6.7: The expected probability of observing clusters due to background events at each energy threshold. The red points indicate the probability of observing one or more clusters within the signal time range.

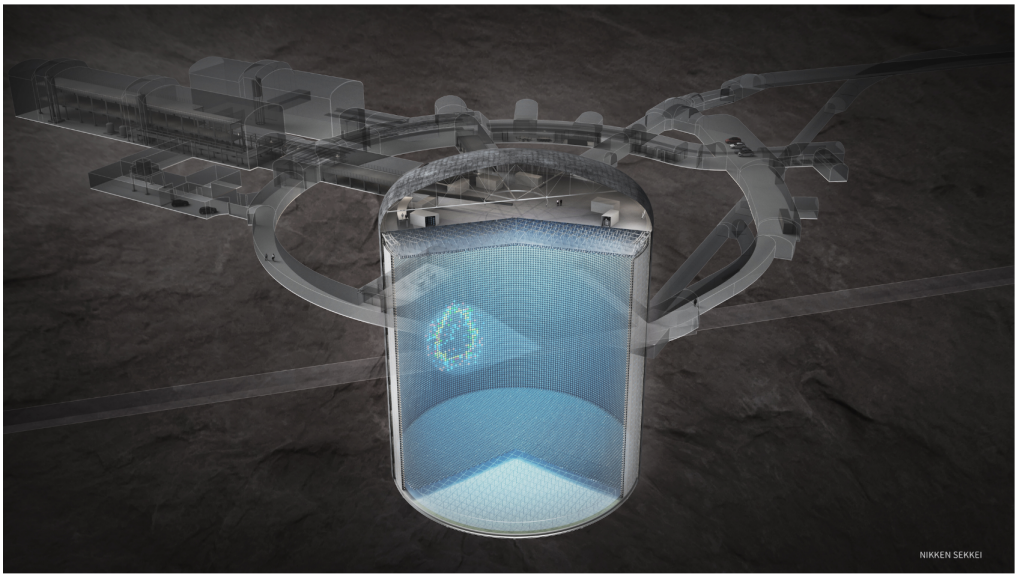

FIGURE 6.8: Schematic view of the Hyper-Kamiokande detector [34].

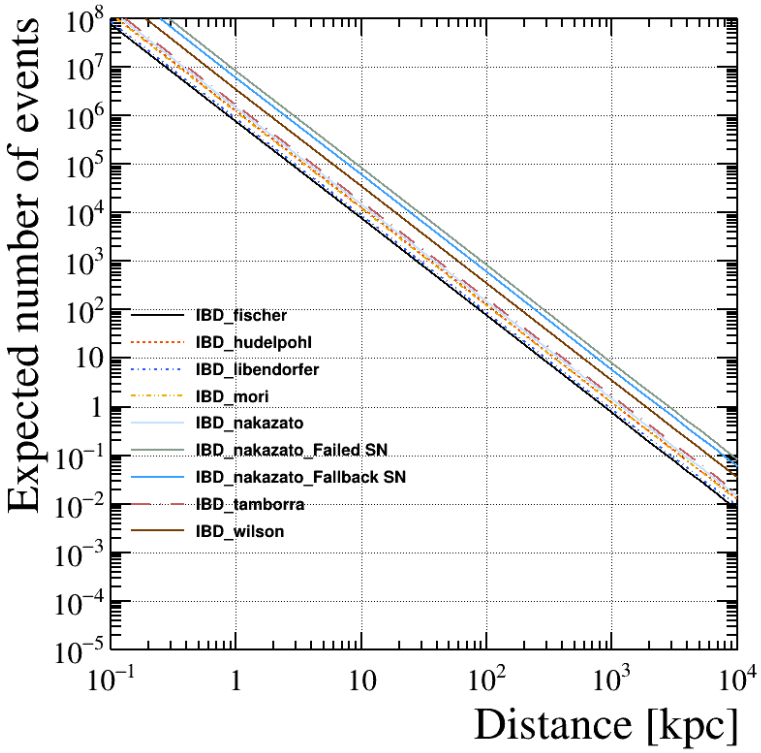

FIGURE 6.9: Expected number of events of IBD interaction as a function of the distance to a SN. The band of each line shows different SN models.

TABLE 6.1: Expected number of detected events for various CCSN models (Normal mas ordering case) at 10 kpc. The tank volume of HK assumes 8 times of SK FV.

Model	Total	IBD	ES	CC	NC
Fischer	8346.49	7627.61	564.011	87.5982	67.2661
Hüdépohl	13721	12561.8	883.24	187.42	88.6156
Libendorfer	10241.6	8969.15	500.382	487.636	284.395
Mori	13479	12200.2	922.663	162.023	194.189
Nakazato	16838.1	14611.4	705.247	1109.26	412.103
Tamborra	18725.7	16848.7	912.358	684.587	280.027
Wilson	45492.1	35418	2054.13	5889.79	2130.23

expected number of IBD events in FV as a function of the distance to an SN. Each line represents a different SN model, and the range of predicted event numbers is given by the spread among the model predictions. At a distance of 10 kpc, corresponding to a typical Galactic center, the number of IBD events is expected to be on the order $10^4 - 10^5$, depending on the SN model assumptions. Even at distances beyond the Large Magellanic Cloud (LMC, $\sim$ 50 kpc), several thousand events are expected, ensuring a robust detection. The expected number of detected events for various CCSN models is summarized in Table 6.1.

Using the expected number of events as a function of distance, the detection probability is estimated in Figure 6.10. In this figure, the probabilities of detecting more than one, two, and three events are shown separately. Within 500 kpc, the detection probability reaches nearly 100% for all cases, and remains above 50% for the detection of two or more events even at 1 Mpc.

To estimate the cumulative number of observable neutrino events in HK from CCSNe within the nearby galaxy, I calculate the expected "stacked" event rate as a function of time. The total number of expected neutrino events up to a distance of 10 Mpc can be expressed as

$$N_{\text{stacked}} = \sum_{D=1\ \text{Mpc}}^{10\ \text{Mpc}} R_{\text{SN}}(D) \cdot N_{\text{exp}}(D), \tag{6.3}$$

where D is the distance in Mpc, $R_{\text{SN}}(D)$ is the CCSN rate at distance D estimated from the observed nearby galaxy, and $N_{\text{exp}}(D)$ is the expected number of neutrino events in HK from a single CCSN at distance D. Here, only IBD events are considered, and background events are neglected. For the fallback SN model by [125], I assume that all CCSNe in the sample result in black hole formation (100% black hole formation fraction) to obtain the most optimistic estimate of the detectable flux. Figure 6.11 shows the expected cumulative number of stacked neutrino events as a function of the HK operation time for various CCSN models. The calculation assumes a supernova rate distribution consistent with the observed sample of CCSNe within 10 Mpc. Even within a decade of operation, HK is expected to observe several stacked neutrino events depending on the assumed neutrino emission model. In particular, for energetic or black-hole forming models, the total number of observable neutrino events can exceed $\sim$10 events over ten years.

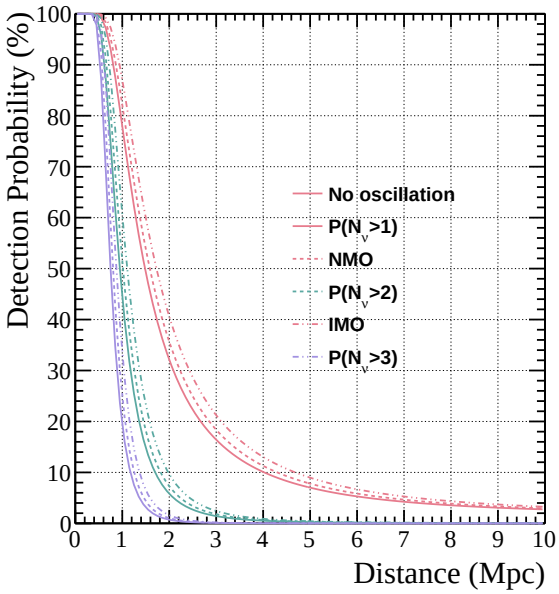

FIGURE 6.10: Detection probability of supernova neutrinos versus distance at HK assuming 8 times of SK volume. Supernove model is Shen EOS in progenitor mass of $20M_{\odot}$ [3]. Solid, dotted, and dot-dashed lines represent the case of no oscillation, normal mass ordering, and inverted mass ordering, respectively. Colors of red, green, and purple show detection probability detecting one or more, two or more, and three or more events.

Sensitivity to Neutrinos from failed SN in HK

In the estimation, I do not change any analysis conditions. In Figure 5.36, the blue dashed line shows the 90% C.L. upper limit in the case that clusters cannot be observed. Under this assumption, many failed SN models can be constrained, highlighting the significant discovery potential of future large-scale detectors. I note that more detailed and dedicated studies are being carried out for HK, which will provide a more realistic assessment of its sensitivity.

In addition, I estimate the expected number of failed SN candidates occurring within 1 Mpc that would be observable during a five-year observation with HK. Figure 6.13 shows the CCSN rate as a function of redshift. A smaller redshift corresponds to a shorter distance, and multiple observational studies indicate that the local CCSN rate ($R_{\rm SN}$), including approximately 1 Mpc, is about 1.5×10^{-4} yr^{-1} Mpc^{-3}. The fraction of CCSNe that result in failed supernovae has also been estimated observationally. Adams et al. [126] monitored RSG stars in galaxies within 10 Mpc over a period of seven years and searched for stars that disappeared from optical observations, corresponding to failed SN candidates. Based on the detection of one such candidate during this period, the fraction of failed supernovae ($f_{\rm BH}$) was estimated to lie in the range $0.046 < f_{\rm BH} < 0.471$. These observational constraints on $R_{\rm SN}$ and $f_{\rm BH}$ provide the basis for estimating the expected number of nearby failed supernovae. The failed supernova rate is given by $R_{\rm SN} \times f_{\rm BH}$. For HK, the detection probability for cluster events consisting of two or more neutrino events from failed SNe is shown in Figure 6.14. Owing to its much larger detector volume compared to SK, HK achieves a detection probability of nearly 100% within 1 Mpc for the Shen-TM1 ($40M_{\odot}$) model. Using the estimated failed SN rate and corresponding detection probability, I define

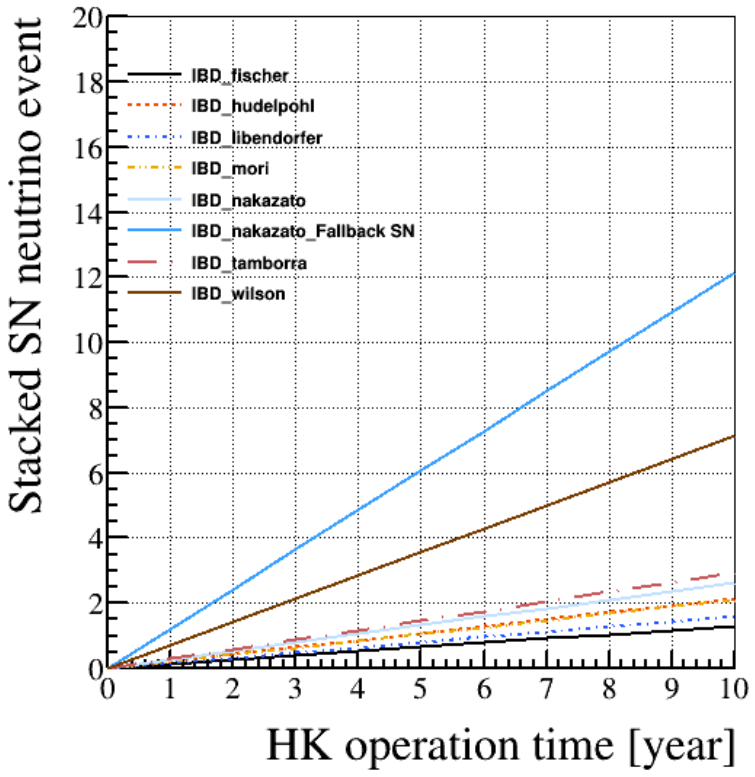

FIGURE 6.11: Expected cumulative number of stacked supernova neutrino events in HK as a function of the detector operation time. The calculation integrates CCSNe from 1 to 10 Mpc using the observed nearby galaxy sample. Only IBD events are included, and background events are not considered. The line labeled "Nakazato_Fallback SN" corresponds to the case where all CCSNe form black holes (100% black hole fraction).

the expected number of observable failed SNe within 1 Mpc per year during the HK observation, defined as

$$N_{\rm exp}^{\rm BH} = 4\pi \int_0^{D_{\rm max}} P(N_{\bar{\nu}_e} \geq 2)\, f_{\rm BH}\, R_{\rm SN}\, D^2\, dD, \tag{6.4}$$

where I set $D_{\rm max} = 1$ Mpc and $P(N_{\bar{\nu}_e} \geq 2)$ is the detection probability of observing two or more events, evaluated using the same formalism as described in Section 5.5.4. The expected number of observable failed SNe during an observation period T is then given by

$$N_{\rm exp} = N_{\rm exp}^{\rm BH} \times T. \tag{6.5}$$

Here, I assume an observation time of five years. Figure 6.15 shows the expected number of observable failed SN candidates for a five-year HK observation for several theoretical models. Overall, these results indicate that approximately one failed SN is expected to be observable, although the exact number may vary due to the uncertainty in $f_{\rm BH}$, demonstrating that HK will have sufficient sensitivity to test and constrain failed SN models. For failed SN models with higher detection probabilities, the impact of the uncertainty in $f_{\rm BH}$ becomes more pronounced, leading to a broader range of expected values.

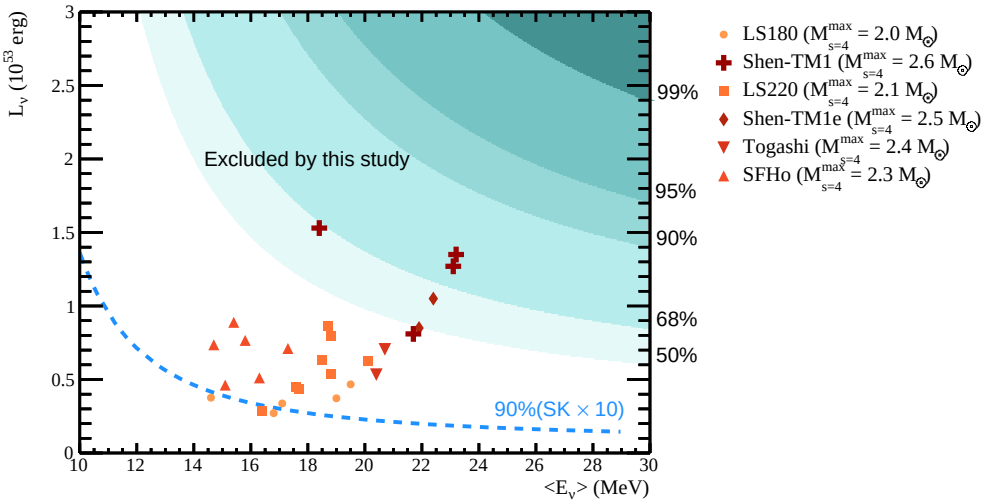

FIGURE 6.12: Same plot of Figure 5.36. The blue dashed line indicates the case of a detector with 10 times the volume of SK. Filled circles show individual simulation results for six nuclear equations of state (EOS): LS180, LS220, SFHo, Togashi, Shen-TM1e, and Shen-TM1. Each model corresponds to Figure 1 and Table 1 in [25].

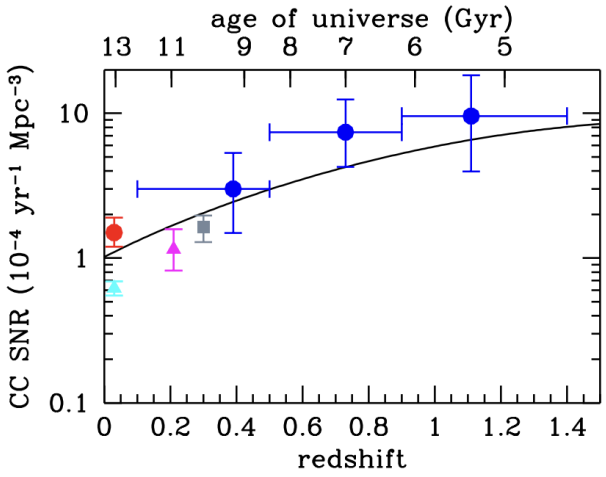

FIGURE 6.13: CCSNe rate as a function of redshift [35]. The cyan triangle, red dot, magenta triangle, gray square, and blue dots represent data points as taken [36, 37, 38, 39]. The solid line shows the CCSN rates predicted from the cosmic star-formation history.

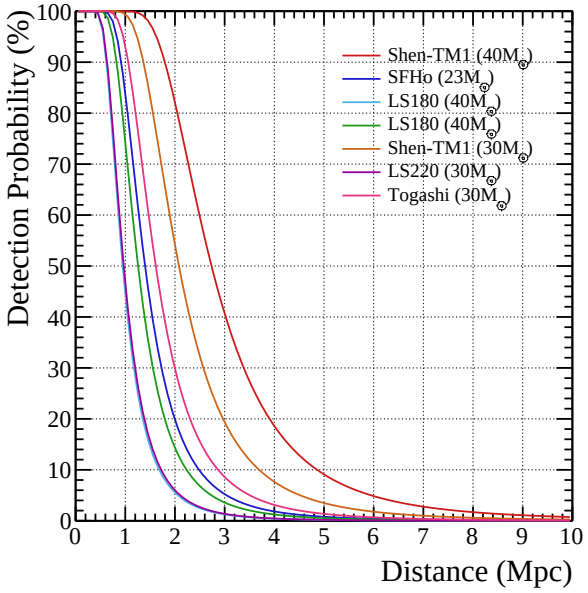

FIGURE 6.14: Detection probability of neutrino events from failed SN candidate in HK.

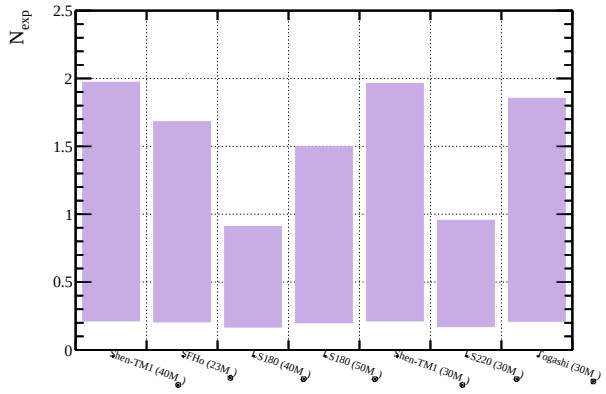

FIGURE 6.15: Expected number of failed SN candidates observed in HK for 5-year observation. Failed SN models are same with Figure 5.34.

Chapter 7

Summary and Conclusion

CCSNe represent the final evolutionary stage of massive stars. Stars above approximately $8M_{\odot}$ undergo gravitational collapse accompanied by intense neutrino emission, while those exceeding roughly $18M_{\odot}$ may fail to explode and instead collapse directly into black holes. Because more than 99% of the energy emitted during a supernova is carried away by neutrinos, supernova neutrino observations provide essential information on the explosion mechanism, the nuclear EOS, and the formation of compact remnants. Recent theoretical developments covering a wide range of progenitor masses and EOSs motivate improved approaches for extracting late-phase neutrino signals under realistic detector backgrounds.

In this study, we constructed a supernova neutrino event generator developed for use in the water Cherenkov detector and developed an analysis framework that incorporates realistic background conditions. This framework enables a stable determination of the last observed neutrino event and its timing, T_{last}, even when backgrounds dominate the data. Using this method, we demonstrated that T_{last} exhibits strong discriminatory power among CCSN models with different PNS masses and EOSs. Clear distinctions emerge especially between the Shen and Togashi EOS when the event sequence is analyzed backward in time from T_{last}. We also investigated earlier timing observables such as T_{500} and found that they help reduce statistical fluctuations and improve model separation for EOS combinations with similar temporal evolution, such as LS220 and Furusawa–Togashi EOS. In contrast, varying the progenitor mass while fixing the EOS yields only minor differences in late-phase signals, indicating that this phase is governed primarily by basic PNS properties—such as radius and mass—rather than by the detailed structure of the progenitor. A Bayesian analysis further confirmed that T_{last} provides meaningful EOS constraints, although simultaneously determining both the EOS and the PNS baryonic mass remains difficult.

Motivated by the discovery of the failed supernova candidate M31-2014-DS1 in the Andromeda galaxy, we performed a dedicated neutrino search using SK data. Because the black hole formation time is not observable in optical wavelengths, the search window was defined from June 1, 2013, to December 31, 2017. We developed a cluster-based search method optimized for the short neutrino burst expected from a failed supernova at the distance of M31. A cluster was defined as two or more events within 10 s, and a positron energy threshold of 18 MeV was applied to suppress backgrounds. This framework can be generalized to future failed supernova searches by re-optimizing the threshold according to the observational period and the expected number of signal events at a given distance. For M31-2014-DS1, no cluster satisfying the criteria was found during the signal window.

Upper limits on the time-integrated electron antineutrino luminosity, $L_{\bar{\nu}_e}$, were obtained using two assumptions: predictions from failed supernova models and spectra based on a Fermi–Dirac distribution. For failed supernova models, the limits depend on the spectral properties. Models with high $L_{\bar{\nu}_e}$ and high average energy—such as

Shen–TM1 ($40M_{\odot}$)—yield limits close to their predicted energies, while models with lower average energies (e.g., SFHo, $23M_{\odot}$) are more strongly affected by the 18 MeV threshold, producing larger deviations. In the Fermi–Dirac analysis, models with lower average energy require larger $L_{\bar{\nu}_e}$ to reproduce the same expected event rate, shifting the exclusion contours toward higher luminosities. These behaviors appear in the contour plots of Figure 5.36, while Figure 5.34 provides the corresponding numerical limits. Under the Shen–TM1 EOS assumption, the 90% C.L. upper limit of 1.76×10^{53} erg lies moderately above the expected value of 1.35×10^{53} erg, demonstrating that SK already possesses meaningful sensitivity to extragalactic failed supernovae.

Improving the determination of the black hole formation time would allow a narrower signal window and a reduced analysis threshold, thereby enhancing sensitivity to a wider range of models. Progress in optical transient surveys—including observations from LBT and Subaru/HSC, and future observations by LSST—may provide improved constraints. Next-generation neutrino detectors, such as Hyper-Kamiokande, JUNO, and DUNE, will significantly increase sensitivity to extragalactic failed supernovae, allowing for systematic studies of their population.

In summary, the methods developed in this study integrate theoretical modeling, numerical simulation, and detector data analysis to advance the study of late-phase supernova neutrinos. The framework constructed here applies to any neutrino detector with event-by-event timing capabilities and enables the extraction of physically meaningful timing observables, especially T_{last}. These techniques will play an important role in the multi-messenger era of supernova physics, contributing to constraints on PNS properties, the nuclear EOS, and the astrophysics of stellar collapse. The dedicated search for M31-2014-DS1 further demonstrates that SK already provides significant sensitivity to failed SN in nearby galaxies, and future developments in both observations and detector technology are expected to enhance this capability greatly.

Appendix A

Search for Neutrinos from Supernovae out to 10 Mpc

A.1 Supernova candidates

In this search, we look for neutrinos from supernovae out to a distance of 10 Mpc. Optical telescopes worldwide regularly report discoeries of supernovae, and several catalogs compile this information. For this analysis, we use 3 catalogs to identify potential supernova candidates. The first is the Transient Name Server (TNS)[1], established in 2016 by the IAU Working Group. TNS contains the largest number of supernovae entries, providing informations such as discovery date, equatorial coordinates, redshift, and host galaxy. However, the information on redshift and host galaxy is sparse for events before 2016. To supplement this, we also use the ASAS-SN supernova catalog[2] and the Open Supernova Catalog (OSC)[3]. In this catalog, the supernovae are summarized well before 2010. These tables contain two pieces of information about the supernova ID and redshift. After selecting supernovae with small redshifts, such as those smaller than 0.001, I checked the published paper about their supernova and the accurate distance.

In this analysis, we focus on both CCSN and failed SNe. In total, 24 CCSNe and 1 failed SN candidate are found, as shown in Table A.1. In particular, M31-2014-DS1 was reported in 2024 as a candidate failed SN in M31 (at a distance of about 770 kpc) [23]. Failed supernovae are stellar deaths in which the explosion is unsuccessful and the star collapses into a black hole without a bright optical display. M31-2014-DS1 showed a ∼50% increase in mid-infrared (MIR) flux over a two-year period beginning in 2014 [99, 100], while remaining undetected in optical and near-infrared (NIR) imaging observations as of 2023. The progenitor is estimated to have been a massive, hydrogen-depleted supergiant with an initial mass of about $20M_{\odot}$. Furthermore, the radius of the inner shell was observed to decrease more than 1000 days after the onset of MIR brightening. These observations suggest that black hole formation likely occurred sometime between 2014 and 2017.

A.2 Explosion date and Operational Status in SK

The information about the explosion time is needed to determine the duration of the analysis and to analyze the data. For example, the explosion time is calculated by fitting a luminosity curve obtained from observations with an optical scope. Table A.2 summarizes the explosion date and paper.

[1] Transient name server https://www.wis-tns.org/
[2] ASAS-SN catalog https://www.astronomy.ohio-state.edu/asassn/sn_list.html
[3] Open supernova catalog https://github.com/astrocatalogs/supernovae

TABLE A.1: Mini-burst candidates

Supernova ID	Discovery date	Distance (Mpc)	Host galaxy	SN type	SK phase
SN2024ggi	Apr 11, 2024	6.6	NGC3621	II	SK-VII
SN2023ixf	May 19, 2023	6.9 ± 0.1	M101	II	SK-VII
SN2017eaw	May 14, 2017	6.9	NGC6946	IIP	SK-IV
SN2016adj	Feb 08, 2016	4.0	NGC5128	Ib	SK-IV
SN2016bau	Mar 13, 2016	9.4 ± 1.8	NGC3631	Ib	SK-IV
SN2012fh	Oct 18, 2012	6.9	NGC3344	Ib/c	SK-IV
SN2012aw	Mar 16, 2012	9.9 ± 0.1	NGC3351	II	SK-IV
SN2012A	Jan 07, 2012	9.7 ± 0.5	NGC3239	II	SK-IV
SN2011dh	May 31, 2011	7.1 ± 1.2	M51	IIb	SK-IV
SN2011ja	Dec 18, 2011	3.4 ± 0.1	NGC4945	IIP	SK-IV
SN2009hd	Jul 02, 2009	8.3	NGC3627 (M66)	IIP	SK-IV
SN2008ax	Mar 03, 2008	9.6	NGC4490	IIb	No data
SN2008iz	Apr 2008	3.5	NGC3034 (M82)	II?	No data
SN2008bk	Mar 25, 2008	4.1	NGC7793	IIP	SK-III
SN2008S	Feb 01, 2008	3.9	NGC6946	IIn	SK-III
SN2007gr	Aug 15, 2007	9.3	NGC1058	Ic	SK-III
SN2005af	Feb 08, 2005	3.6	NGC4945	II-P	No data
SN2005cs	Jun 27, 2005	7.3 ± 0.3	NGC5194	IIP	No data
SN2004et	Sep 27, 2004	5.6	NGC6946	II-P	SK-II
SN2004dj	Jul 31, 2004	3.3	NGC2403	II-P	SK-II
SN2004am	Mar 05, 2004	3.5	NGC3034 (M82)	II-P	SK-II
SN2002hh	Oct 31, 2002	5.9 ± 0.4	NGC6946	IIP	No data
SN2002ap	Jan 29, 2002	7.3	M74	Ib/c or hypernova	No data
SN1999em	Oct 29, 1999	7.8	NGC1637	IIn	SK-I

TABLE A.2: Explosion date for each mini-burst candidate

Supernova ID	Discovery date	non-detection date	SBO date
SN2024ggi	Apr. 11, 2024	Apr. 10, 2024	
SN2023ixf	May 19, 2023	May 17, 2023	May 18, 2023
SN2017eaw	May 14, 2017	May 6, 2017	May 4 or 10, 2017
SN2016adj	Feb. 08, 2016	Jul. 12, 2015	
SN2012fh	Oct. 18, 2012		$\sim$130 days before
SN2012aw	Mar. 16, 2012	Mar. 15, 2012	Mar. 16, 2012
SN2012A	Jan. 7, 2012		Jan. 4–8, 2012
SN2011dh	May 31, 2011		May 31, 2011
SN2011ja	Dec. 18, 2011		Dec. 12 ($\pm$1 day), 2011
SN2009hd	Jul. 02, 2009		Jun. 19 ($\pm$3 day), 2009
SN2008iz	Apr., 2009		Feb. 18 ($\pm$6 day), 2008

If mini-burst candidates are found, I need to check the operational status in SK when the supernova occurred.

A.3 spallation likelihood cut in SK-III

In SK-III, the spallation likelihood cut is introduced. The spallation background remains one of the most challenging sources of contamination to remove. High-energy spallation products, such as ^{11}Li and ^{14}B have maximum beta-decay endpoint energies of 20.6 MeV. Due to the finite energy resolution of the detector, these events can be reconstructed with energies up to 23–24 MeV. Fortunately, their short half-lives of approximately 0.01 s facilitate straightforward association with the parent muon.

At lower energies, however, the number of relevant isotopes increases rapidly, and their half-lives become longer, making the background increasingly difficult to suppress. In the 2003 SK analysis, the total positron energy threshold was set to 18 MeV, and the shotgun cut exhibited an inefficiency of 37%. In the SK-III DSNB analysis, the introduction of a likelihood-based method significantly improved the performance of this cut. Using the same SK-I dataset as in the published analysis, lowering the energy threshold to 16 MeV reduced the inefficiency above 18 MeV from 37% to approximately 9%.

To eliminate spallation products, the correlation between signal candidates and preceding muons is used.

A.4 ROC curve

The Receiver Operating Characteristic (ROC) curve is employed to quantitatively assess the effectiveness of the reduction process and to optimize the spallation cut parameters. For reconstructed energies above 16 MeV, the estimation of $\varepsilon_{\mathrm{Li9}}$ is omitted because it exceeds the ^{9}Li decay end-point. In this regime, the residual spallation rate is not considered reliable, as atmospheric neutrinos dominate the event sample and the statistical uncertainty associated with spallation events becomes substantial. The ROC curve for 8-10, 10-12, 12-14, 14-16 MeV energy regions is shown in Figure A.2. These curves illustrate the trade-off between signal efficiency and background rejection for each energy interval, allowing the optimal operating point of the classifier to be evaluated. In particular, the separation performance improves with increasing energy, reflecting the reduced contribution of spallation backgrounds at higher energies.

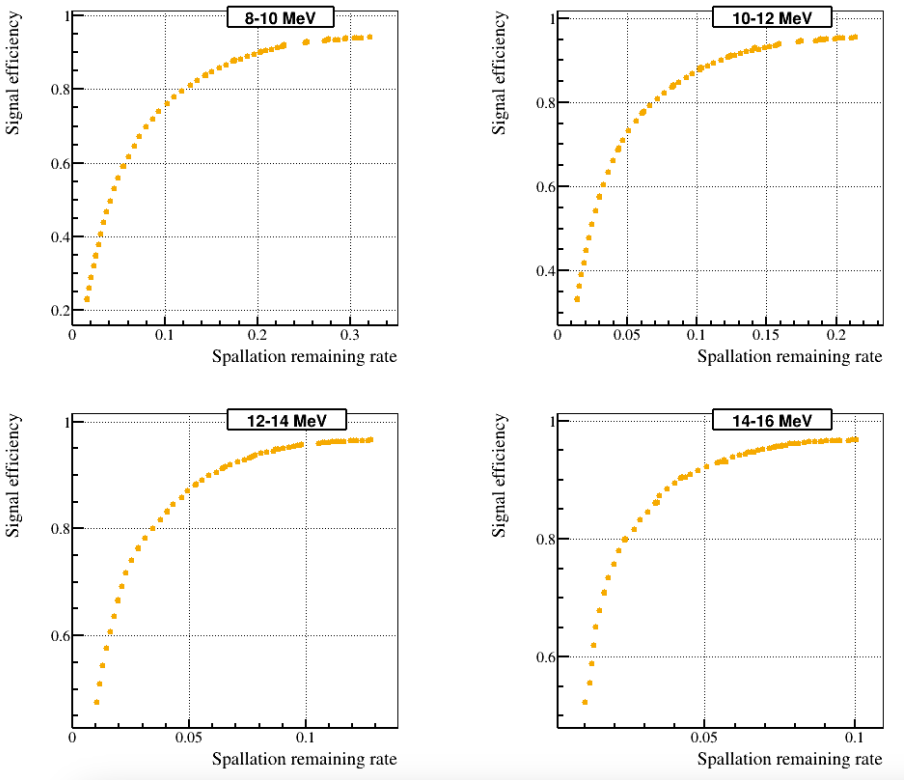

FIGURE A.1: ROC curve between spallation remaining rate and signal efficiency. Top left, top right, bottom left, and bottom right represent 8-10 MeV, 10-12 MeV, 12-14 MeV, and 14-16 MeV, respectively.

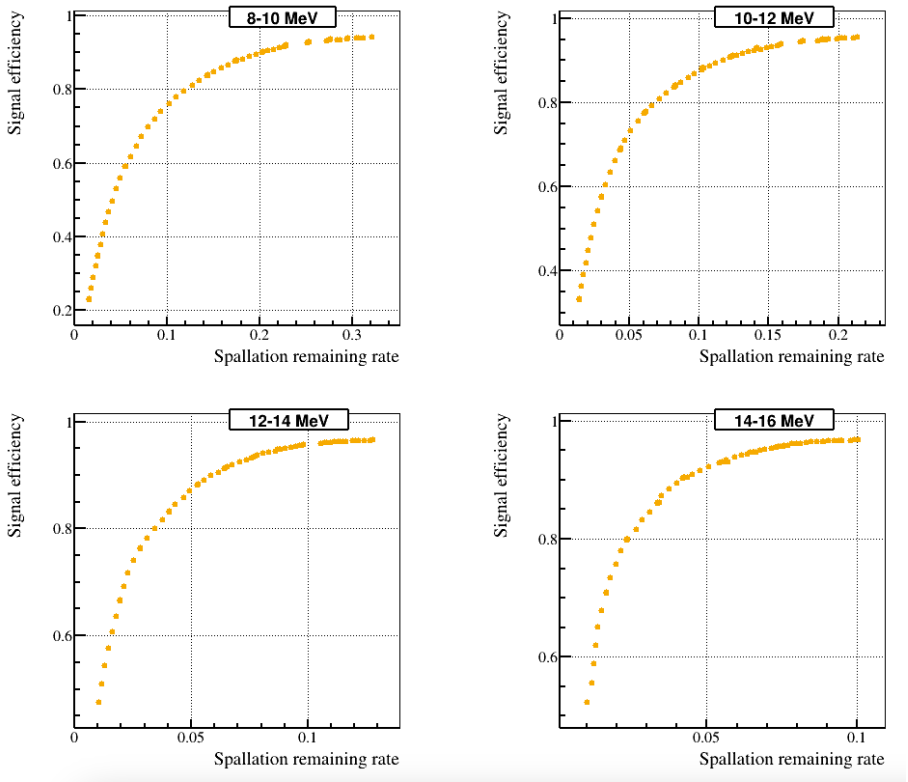

FIGURE A.2: ROC curve between spallation remaining rate and signal efficiency. Top left, top right, bottom left, and bottom right represent 8-10 MeV, 10-12 MeV, 12-14 MeV, and 14-16 MeV, respectively.

Appendix B

Search for Diffuse Supernova Neutrino Background

B.1 Search for diffuse supernova neutrino background

In addition to bursts from individual nearby CCSNe, a continuous flux of neutrinos is expected from all past supernova explosions throughout the universe. This integrated flux is known as the DSNB, or supernova relic neutrinos. The detection of the DSNB would provide important information on the cosmic history of stellar core collapse and star formation.

SK has conducted a series of DSNB searches since its operation began, providing the world's most stringent limits on the DSNB flux. In these analyses, $\bar{\nu}_e$ are detected via IBD interactions, with the prompt Cherenkov light from the positron serving as the observable signal. The main backgrounds in this energy region are reactor neutrinos, spallation products induced by cosmic-ray muons, and atmospheric neutrino interactions. A series of analysis [127, 128, 28] have progressively improved the sensitivity by refining event selection, background modeling, and statistical methods.

The SK-IV analysis [28] achieved a 90% C.L. upper limit on the DSNB $\bar{\nu}_e$ flux of < 2.7 cm^{-2} s^{-1} for $E_\nu > 17.3$ MeV. In the phase of SK-Gd [33], improvements in neutron-tagging and background suppression have enabled further sensitivity gains, bringing the first detection of the DSNB increasingly within reach. Figure B.1 represents the reconstructed energy spectra obtained after applying all event selection criteria, using either the Neural Net and Boosted Decision Tree method for neutron tagging [33].

Figure B.2 presents the results of the latest DSNB search. The achieved sensitivity above 17.3 MeV is now comparable to several theoretical predictions, while the sensitivity in the 13.3 $\sim$ 17.3 MeV range approaches models with the largest predicted fluxes within a factor of two. Compared to the SK-IV analysis [28], the current SK-Gd result demonstrates a clear improvement below 15.5 MeV, primarily due to the enhanced neutron tagging efficiency and reduced accidental coincidence rate. At higher energies, however, the pure-water phase still provides the most stringent sensitivity worldwide, owing to its smaller systematic uncertainties for background events estimation and the larger available dataset.

B.2 DSNB simulation using SKSNSim

B.2.1 Flow of the simulation

The following steps are used for the DSNB simulation: (1) randomization of the neutrino energy according to the chosen energy spectrum and (2) the determination of the kinematics of the particle randomly produced according to the cross section.

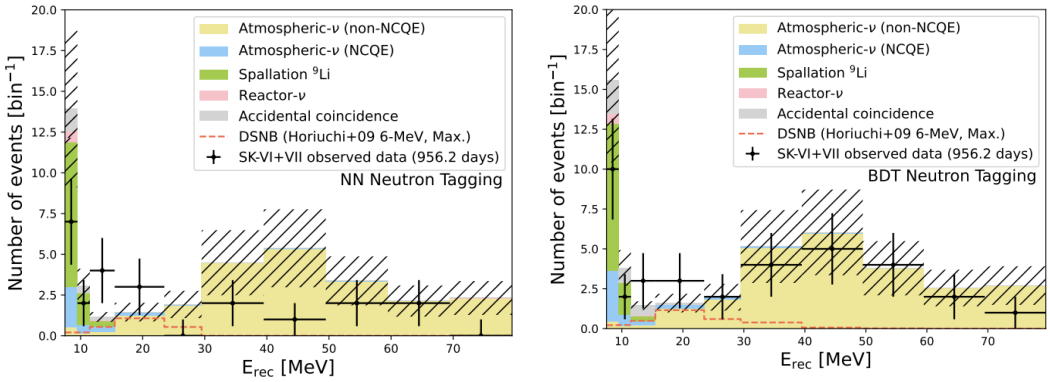

(a) Neural Net (b) Boosted Decision Tree

FIGURE B.1: Reconstructed spectra of the positron kinetic energy for data and expected backgrounds after all selection criteria are shown for the Neural Net-based (left) and Boosted Decision Tree (right) neutron tagging methods [33].

The steps (1)-(2)are repeated as specified by the user. In this case, the final number of events must be normalized by the observation time. In contrast to the SN burst steps, the DSNB steps do not include the neutrino oscillation effect in SKSNSim because most DSNB models include it already.

In the case of DSNB, the time dependence of the DSNB flux is negligible for a typical observation period of $\sim$ 10 years, such as for SK. Therefore, SKSNSim simulates DSNB events using tabulated energy spectra without any time dependence. In addition, the DSNB simulation processes only the $\bar{\nu}_e$ flux since the inverse beta decay (IBD) is the dominant interaction in the typical energy range of DSNB neutrinos of a few tens of MeV. Users can specify any binned $\bar{\nu}_e$ spectrum to simulate the IBD interaction via a text file. This feature allows one to simulate the flux of other $\bar{\nu}_e$ sources, such as nuclear reactors, can be simulated with this tool. By default, it supports the $\bar{\nu}_e$ flux model provided by [129]. Another characteristic of SKSNSim is that it is implemented to simulate events according to a flat energy spectrum in a positron energy space as well as a neutrino energy space. This implementation is useful in a "re-weighting" method. We explain in detail the use of the re-weighting method for the SK DSNB analysis in Section 3.2.

B.3 Demonstration

This section shows the simulation result of a DSNB using SKSNSim. Figure B.3 shows an example of positron energy distribution from 100,000 IBD events generated by DSNB under the assumptions made in [40]. The direction of neutrinos is determined isotropically.

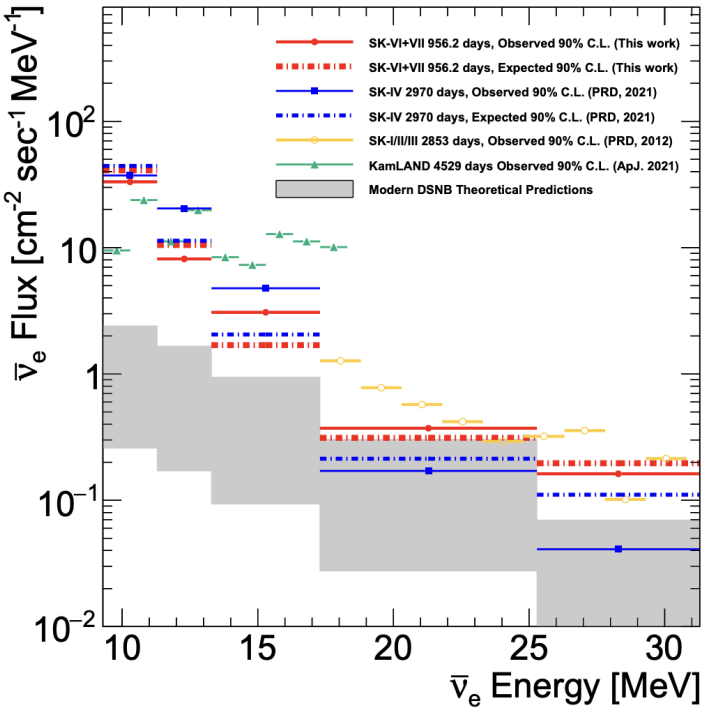

FIGURE B.2: 90% C.L. upper limits on the astrophysical $\bar{\nu}_e$ flux are shown as a function of neutrino energy for each energy bin. [33]. The solid red circles represent the observed upper limits, while the red dot-dashed line indicates the expected sensitivity obtained from the SK-VI+VII dataset.

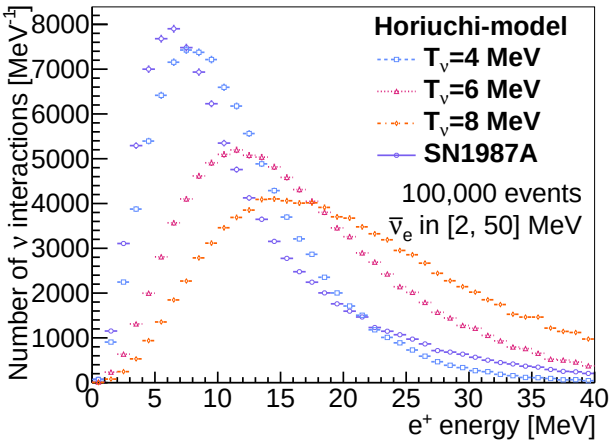

FIGURE B.3: Energy spectra of positrons generated by DSNB with water via the IBD channel. Here, the calculation of [40] is used for the DSNB model, and [16] for the IBD cross section. The Horiuchi model provides several cases with different effective temperatures (T_ν) in the SN core: 4, 6, and 8 MeV in this plot.

Appendix C

Event Reconstruction

C.1 Vertex reconstruction

A charged particle with an energy of order $\mathcal{O}(10)$ MeV propagates only several centimeters in water. This propagation length is sufficiently short compared with the detector scale and is smaller than the effective vertex resolution determined by the PMT timing and spatial resolution. Therefore, the charged-particle trajectory can be approximated as a point-like energy deposition. The interaction vertex is reconstructed using a maximum-likelihood approach. The likelihood function is defined as

$$\mathcal{L}(\mathbf{x}, t_0) = \sum_{i=1}^{N_{\text{hit}}} \log P(t_{\text{res,i}}), \tag{C.1}$$

$$t_{\text{res,i}} = t_i - t_0 - \frac{|\mathbf{x} - \mathbf{h}_i|}{c}. \tag{C.2}$$

where the candidate interaction vertex is denoted by $\mathbf{x} = (x, y, z)$, and t_0 represents the emission time of the charged particle. The total number of PMTs that record a hit is given by N_{hit}. For the i-th hit PMT, the time residual $t_{\text{res,i}}$ is defined as the difference between the observed hit time t_i and the expected photon arrival time calculated from the candidate vertex $\mathbf{x}$ and emission time t_0. The probability density function describing the distribution of timing residual is denoted by $P(t_{\text{res,i}})$. The position of the i-th hit PMT is represented by $\mathbf{h}_i$, and c denotes the group velocity of light in water. The emission time t_0 is treated as a free parameter and is determined by minimizing the overall timing residuals across all hit PMTs. t_0 is fitted to minimize all $t_{\text{res,i}}$. Figure C.1and C.2 present an overview of the SK detector coordinate system [12] and the PDF of the $t_{\text{res,i}}$ [41], respectively. In addition, the vertex reconstruction performance for the SK-I, SK-II, SK-III, and SK-IV is summarized in Figure C.3.

A goodness parameter is introduced to evaluate the performance of the vertex reconstruction, serving as an indicator of how well the vertex position is defined. It is defined as

$$g_{\text{vtx}} = \frac{\sum_{i=1}^{N_{\text{hit}}} \left[\exp\left\{ -\left(\frac{t_{\text{res},i}}{\sqrt{2}\,\omega} \right)^2 \right\} \exp\left\{ -\left(\frac{t_{\text{res},i}}{\sqrt{2}\,\sigma} \right)^2 \right\} \right]}{\sum_{i=1}^{N_{\text{hit}}} \exp\left\{ -\left(\frac{t_{\text{res},i}}{\sqrt{2}\,\omega} \right)^2 \right\}}. \tag{C.3}$$

Here, ω represents the width of the $t_{\text{res,i}}$ distribution, while σ denotes the timing resolution of PMTs. The parameter g_{vtx} takes a value between 0 and 1, with larger

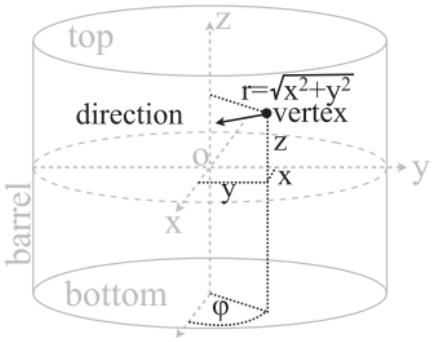

FIGURE C.1: Schematic illustration of the coordinate system used in the SK detector [12].

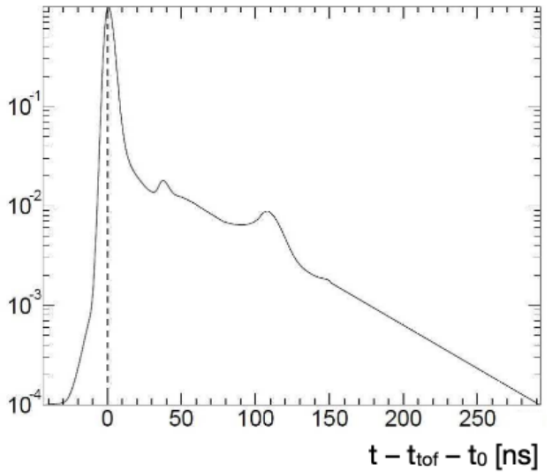

FIGURE C.2: PDF distribution of PMT hit timing residuals [41]. Features around 30 and 100 ns arise from delayed pulses associated with dynode-reflected photoelectrons.

values indicating higher reconstruction quality.

C.2 Direction reconstruction

Following the determination of the interaction of the vertex, the event direction is estimated using a maximum-likelihood technique applied to PMT hits selected within a 20 ns interval. The likelihood function used in this reconstruction is given by

$$\mathcal{L}(d) = \sum_{i=1}^{N_{20}} \left[\log f(\cos\Theta_i,\, E) \times \frac{\cos\theta_i}{a(\theta_i)} \right]. \tag{C.4}$$

Here, d denote the trial particle direction, and N_{20} represents the number of PMT hits within a 20 ns time window. The angle Θ_i is defined as the opeining angle between the candidate direction and the vector pointing from the reconsuructed vertex to the i-th hit PMT. The function $f(\cos\Theta_i, E)$ corresponds to PDF of $\cos\Theta_i$, parametarized by the event energy E. The angle θ_i the angle between the direction from

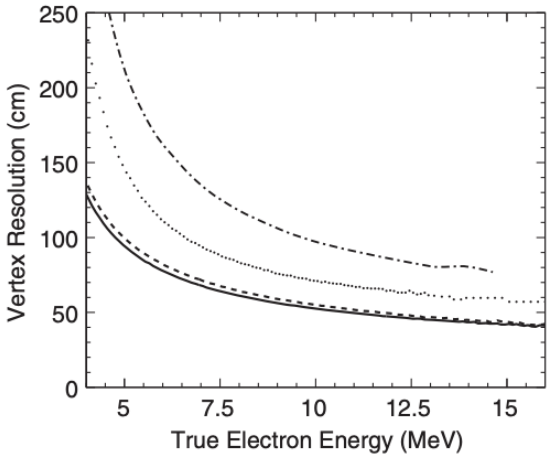

FIGURE C.3: Comparison of vertex resolution across SK-I–IV [12]. The line styles distinguish the detector phases, with dotted, dash–dot, dashed, and solid curves corresponding to SK-I, SK-II, SK-III, and SK-IV, respectively.

the reconstructed vertex to the hit PMT and the orientation axis of that PMT. The function $a(\theta_i)$ denotes the angular dependence of the PMT detection efficiency. This acceptance correction is defined as

$$a(\theta_i) = 0.205 + 0.524\cos\theta_i + 0.390\cos^2\theta_i - 0.132\cos^3\theta_i\,. \tag{C.5}$$

Figure C.4 and C.5 show the PDF for $\cos\Theta_i$ as a function of the energy E, and angular resolution of SK-I and SK-III, respectively.

The quality of the direction reconstruction is quantified by a goodness parameter that evaluates the reliability of the reconstructed direction. This quantity is defined as

$$g_{\mathrm{dir}} = \frac{1}{2\pi}\left\{\max\left(\phi_i - \frac{2\pi i}{N_{\mathrm{hit}}}\right) - \min\left(\phi_i - \frac{2\pi i}{N_{\mathrm{hit}}}\right)\right\}. \tag{C.6}$$

Here, ϕ_i denotes the azimuhal angle of the $i-$th hit PMT. The direction goodness parameter g_{dir} is defined on the interval from 0 to 1, with values approaching zero indicating a more accurately reconstructed direction.

C.3 Energy reconstruction

The event energy is estimated using the effective hit count, N_{eff}, which is constructed to be insensitive to the reconstructed vertex and direction, as well as to variations in the number of inactive PMTs, water transparency, and the relative quantum efficiency (QE) of individual PMTs. The definition of N_{eff} is given by

$$N_{\mathrm{eff}} = \sum_{i=1}^{N_{50}}\left[(X_i + \epsilon_{\mathrm{tail}} - \epsilon_{\mathrm{dark}}) \times \frac{N_{\mathrm{all}}}{N_{\mathrm{alive}}} \times \frac{S(0,0)}{S(\theta_i,\phi_i)} \times \exp\left(\frac{r_i}{L^i_{\mathrm{eff}}}\right) \times \frac{1}{QE_i}\right]. \tag{C.7}$$

Here, N_{50} denotes the number of PMTs registering hits within a 50 ns time window. The individual parameters appearing in Equation C.7 are defined in the following.

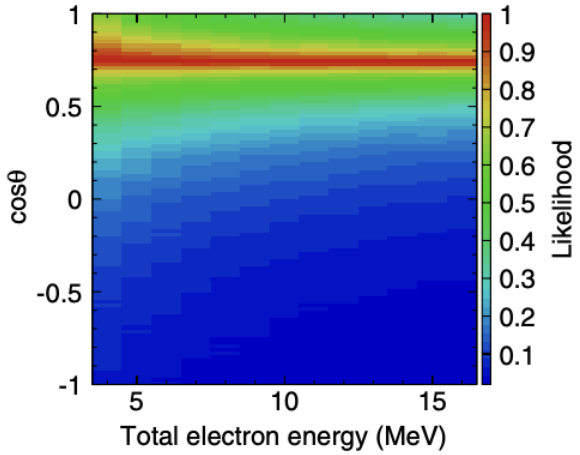

FIGURE C.4: PDF of $\cos\Theta_i$, as function of the total electron energy E [42].

X_i is introduced to account for multiple photoelectron hits on a single PMT. Events occurring near the boundary of the FV, as well as those produced by high-energy charged particles, can generate multiple photons that arrive at the same PMT located close to the reconstructed vertex. This effect is corrected using the factor X_i, which is defined as

$$X_i = \begin{cases} \dfrac{\log\{1/\left(1 - n_i/N_i\right)\}}{n_i/N_i}, & \left(\dfrac{n_i}{N_i} < 1\right), \\ 3.0, & \left(\dfrac{n_i}{N_i} = 1\right). \end{cases} \tag{C.8}$$

Here, N_i denotes the number of PMTs neighboring the hit PMT, while n_i represents the number of hits recorded by those adjacent PMTs. The parameter ϵ_{tail} is introduced to correct for contributions from scattered and reflected Cherenkov photons. Photons that undergo scattering in the water or reflections at the PMT surface or black sheet can arrive at a PMT outside the nominal 50 ns time window. These effects are accounted for through the correction term ϵ_{tail}, which is defined as

$$\epsilon_{\text{tail}} = \frac{N_{100} - N_{50} - N_{\text{alive}} \times R_{\text{dark}} \times 50\ \text{ns}}{N_{50}}. \tag{C.9}$$

Here, N_{100} denotes the number of PMTs with hits recorded within a 100 ns interval, N_{alive} corresponds to the number of operational PMTs, and R_{dark}, expressed in hits per nanosecond, represents the dark-noise rate during the corresponding period. The parameter ϵ_{dark} is introduced to correct for contributions from PMT dark-noise hits. Such noise-induced signals can fall within the 50 ns timing window despite not originating from Cherenkov photons. These spurious contributions are compensated for by the correction term ϵ_{dark}, which is defined as

$$\epsilon_{\text{dark}} = \frac{N_{\text{alive}} \times R_{\text{dark}} \times 50\ \text{ns}}{N_{50}} \times \frac{R^i_{\text{dark}}/N_{50}}{\sum_{i=1}^{N_{50}} R^i_{\text{dark}}/N_{50}}. \tag{C.10}$$

Here, R^i_{dark} represents the dark noise rate of the i-th hit PMT at aperiod.

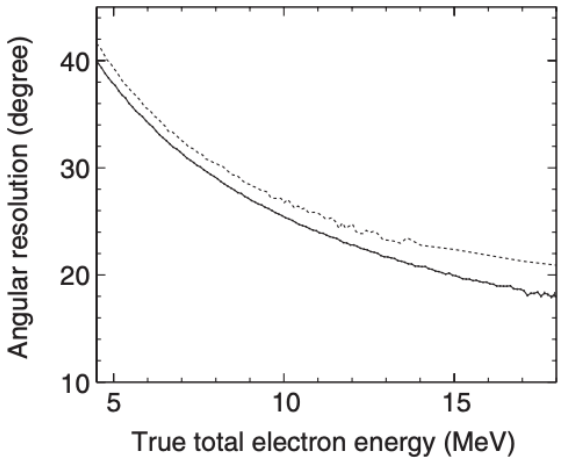

FIGURE C.5: Angular resolution for the SK-I and SK-III phase. [42]. The two detector phases are distinguished by line style, with the dashed and solid curves corresponding to SK-I and SK-III, respectively.

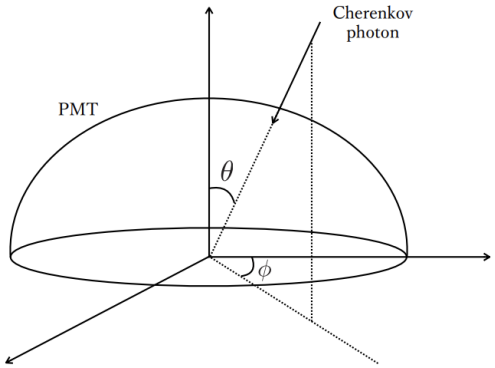

FIGURE C.6: Schematic diagram defining the incident angle [43].

The factor $N_{\mathrm{all}}/N_{\mathrm{alive}}$ is applied to compensate for non-functioning or unstable PMTs. When a fraction of the PMTs is inactive, the recorded hit count is reduced, leading to an underestimation of the reconstructed energy. This effect is corrected by scaling the observed hits by the ratio of the total number of PMTs, $N_{\mathrm{all}}(= 11,\ 129)$, to the number of operational PMTs, N_{alive}. The ratio $S(0,0)/S(\theta_i,\phi_i)$ corrects for variations in effective photocathode coverage arising from the incident angle of Cherenkov photons. Because the detector response depends on the photon incidence angle, this angular dependence is accounted for using the correction function $S(\theta_i,\phi_i)$. The definition of the incident angle and the corresponding distributions of $S(\theta_i,\phi_i)$ for barrel PMTs and for the top and bottom PMTs are shown in Figure C.6and D.5, respectively.

The factor $\exp\left(r_i/L^i_{\mathrm{eff}}\right)$ is introduced to correct for the effects of water transparency. Cherenkov photons may be scattered or absorbed while propagating through the water before reaching a PMT, and the survival probability can be expressed as $\exp\left(r_i/L^i_{\mathrm{eff}}\right)$, where r_i is the distance from the reconstructed vertex to the i-th hit PMT and L^i_{eff} denotes the effective attenuation length. Accordingly, the impact of

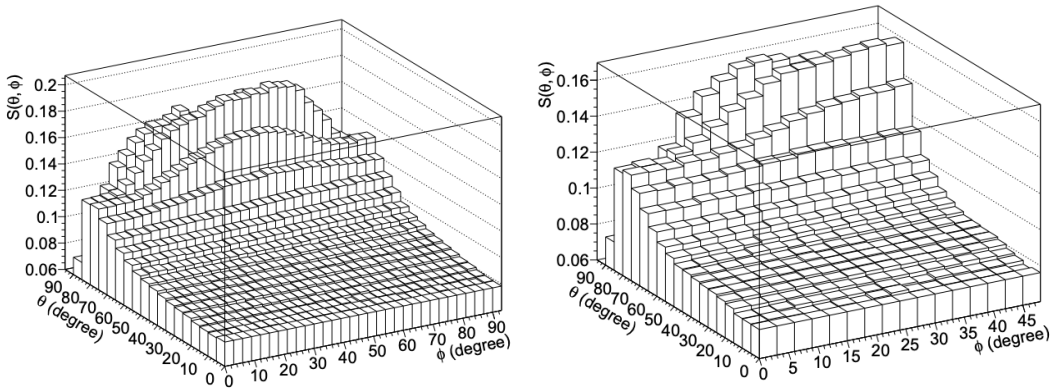

(a) $S(\theta_i, \phi_i)$ for barrel PMTs.

(b) $S(\theta_i, \phi_i)$ for top and bottom PMTs.

FIGURE C.7: Correction function $S(\theta_i, \phi_i)$ accounting for the photocathode coverage [43].

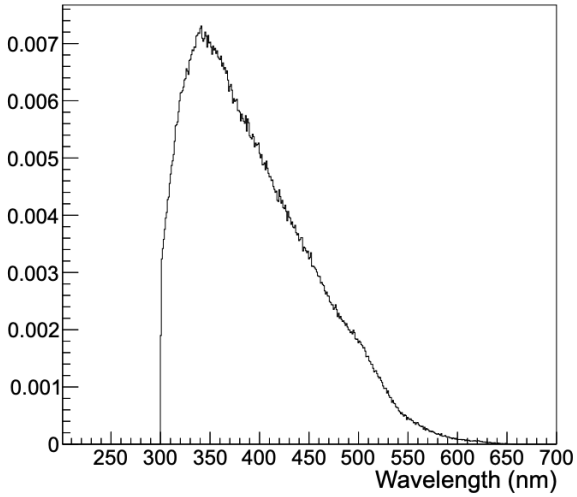

FIGURE C.8: Spectral PDF of Cherenkov photon wavelengths [43].

water transparency is compensated by multiplying the inverse of this factor. The effective attenuation length L^i_{eff} is defined as

$$L^i_{\text{eff}} = -\frac{r_i}{\ln\left[\int_{\lambda_{\min}}^{\lambda_{\max}} w_0(\lambda)\, \exp\{-\sigma_i(\lambda)\, r_i\}\, \mathrm{d}\lambda\right]}\,. \tag{C.11}$$

Here, the integration limits are set to $\lambda_{\min} = 300$ nm and $\lambda_{\max} = 650$ nm. The function $\omega_0\lambda$ represents the wavelength probability density of Cherenkov photons, as illustrated in Figure C.8. The quantity $\sigma_i(\lambda)$ denotes the interaction cross section in water for a Cherenkov photon of wavelength λ propagating over a path length r_i. The functional form of $\sigma_i(\lambda)$ is given by

$$\sigma_i(\lambda) = \alpha_{\text{abs}}(\lambda)\left\{1 + \beta\left(z + \frac{1}{2} r_i \times \mathrm{d}z_i\right)\right\} + C_{\text{sca}}\left\{\alpha_{\text{sym}}(\lambda) + \alpha_{\text{asy}}(\lambda)\right\}\,. \tag{C.12}$$

Here, z denotes the z-coordinate of the reconstructed vertex, and dz_i represents the z-component of the direction vector pointing from the vertex to the i-th hit PMT. The

parameter C_{sca} (approximately 0.44) is a scaling factor that accounts for scattering effects in water. Its value is determined using the SK detector simulation so as to suppress position-dependent variations in N_{eff}. The quantities $\alpha_{\mathrm{abs}}(\lambda)$, $\alpha_{\mathrm{asy}}(\lambda)$ correspond to the wavelength-dependent attenuation coefficients for absorption, symmetric scattering, respectively. The parameter β characterizes the extent of the vertical (z) dependence of the water optical properties. A detailed description of $\alpha_{\mathrm{abs}}(\lambda)$, $\alpha_{\mathrm{asy}}(\lambda)$, and β is provided in Section B.

The quantum efficiency is not uniform across the photomultiplier tubes. To account for this variation, each detected hit is weighted by the inverse of the relative quantum efficiency of the corresponding PMT. The relative quantum efficiency of an individual PMT, denoted by QE_i, is obtained from calibration data. The visible energy of the prompt signal, refreed to as E_{vis}, is reconstructed using the effective number of phhotoelectrons N_{eff}. The relationship between the visible energy and the effective photoelectron conut is expressed by the following equation.

$$E_{\mathrm{vis}} = \begin{cases} \sum_{i=0}^{5} p_i \left(N_{\mathrm{eff}}\right)^i, & (N_{\mathrm{eff}} \leq N_{\mathrm{thr}}), \\ \sum_{i=0}^{5} p_i \left(N_{\mathrm{thr}}\right)^i + \left(N_{\mathrm{eff}} - N_{\mathrm{thr}}\right) \sum_{i=1}^{5} i\, p_i \left(N_{\mathrm{thr}}\right)^{i-1}, & (N_{\mathrm{eff}} > N_{\mathrm{thr}}). \end{cases} \tag{C.13}$$

Table C.1 provides a summary of the coefficients p_i and the corresponding threshold parameter N_{thr}.

TABLE C.1: Coefficients used in the conversion from N_{eff} to E_{vis} and the threshold value N_{thr} [41].

Parameter	Value
p_0	0.702
p_1	0.131
p_2	-2.35×10^{-4}
p_3	2.640×10^{-6}
p_4	-1.188×10^{-8}
p_5	1.930×10^{-11}
N_{thr}	2.202×10^{2}

Appendix D

Detector Calibration

In physics experiments, the reliability of measured data critically depends on the accuracy of detector calibration. Calibration procedures are essential for verifying that the detector operates as intended and that its measurement performance satisfies the required precision. In addition, calibration plays a key role in determining and tuning the parameters used in MC simulations so that they faithfully reproduce experimental observations.

At SK, the calibration program can be broadly divided into several categories: calibration of the ID, photon propagation modeling, calibration of the OD, and calibration of the energy scale. This section focuses on the calibration of the ID, the treatment of photon tracking, and the energy scale calibration performed using a linear accelerator (LINAC). The procedures associated with the OD calibration are documented separately in Ref. [44].

D.1 ID Detector Calibration

Prior to detailing the individual calibration items, an overview of the calibration procedure for the ID is described. The first step involves adjusting the high voltage applied to each ID PMT so that a uniform charge response is obtained across all channels. This equalization reduces non-uniformities in the detector response and leads to an improvement in the energy resolution. The next step is to characterize channel-by-channel variations in the gain and quantum efficiency (QE) of the ID PMTs. The gain is defined as the multiplication factor for a photoelectron that reaches the dynode system of a PMT. The QE is conventionally defined as the probability that an incident photon on the photocathode produces a photoelectron; in SK, this definition is extended to include the probability that the generated photoelectron successfully reaches the first dynode. The relative importance of these parameters depends on the energy scale of the event. For high-energy signals, such as those produced by cosmic-ray muons, the detector response is primarily sensitive to the gain. In contrast, low-energy signals, including those relevant for DSNB and neutral-current quasi-elastic interactions, are typically at the single-photoelectron level and are therefore strongly influenced by the QE. Accurate knowledge of both the gain and QE for each PMT is thus essential, as uncertainties in these parameters directly affect the reconstructed energy. In addition, the timing characteristics of each ID PMT are calibrated to correct for channel-dependent offsets arising from differences in cable lengths, electronic processing delays, and variations in the signal pulse shape.

D.1.1 High-Voltage determination

The high voltage applied to each PMT is adjusted so that all channels yield a uniform charge response. This calibration is performed using an isotropic light source placed at

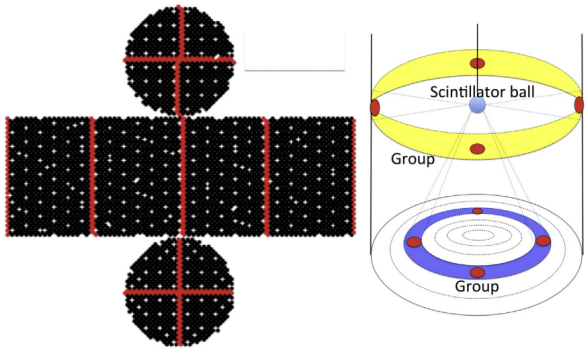

FIGURE D.1: Distribution of standard PMts in the ID (left) and a schematic illustration of the grouping scheme for neighboring PMTs (right) [44]. The standard PMTs are indicated by red markers. The barrel region is divided into 17 groups, while the top and bottom regions are eahc divided into 8 groups.

the geometric center of the SK tank. The light source consists of a Xe lamp, an ultraviolet filter, and a spherical snintillator with a diameter of 5 cm. Light is produced by applying a high voltage across a glass tube filled with Xe gas. The scintillation sphere contains POPOP at concentration of 15 ppm and MgO at concentration of 2000 ppm. The wavelength-shifting function is provided by POPOP, while MgO ensures that the emitted light is diffused uniformly, producing an approximately isotropic emission pattern. The measured charge response of PMT depends not only on its distance from the light source but also on the optical properties of the detector medium, including water transparency and the reflectivity of the PMT surfaces. To control these effects and achieve reliable calibration, 420 pre-calibrated PMTs, referred to as standard tubes, were installed in the ID prior to the measurement. The operating voltages of these standard tubes had been determined independently. Figure D.1 illustrates the spatial distribution of the standard tubes in the ID, as well as a schematic representation of the grouping scheme used for nearby PMTs. For PMTs that were not designated as standard tubes, the high voltage was adjusted such that the measured charge matched the mean charge response of the standard tubes whitin the same group. Once the voltage settings were established, the charge measurement was repeated for all channels using the newly assigned voltages. The resulting channel-to-channel variation in the collected charge was found to have a root-mean-square spread of 1.3%, which is consistent with the dispersion observed in the preliminary calibration of the standard tubes. The Xe light source remains installed in the detector and is subsequently used to track long-term variations is PMT gain after the high-voltage calibration has been completed.

D.1.2 Relative gain measurement

To evaluate the gain of each PMT, both the overall gain scale of the detector and the relative variations among individual PMTs must be quantified. The latter is determined through a two-stage calibration procedure employing an isotropic light source. In the first stage, the light intensity is set sufficiently high so that all PMTs receive ample illumination. The mean collected charge at the i-th PMT obtained in this measurement is denoted as $Q_{\mathrm{obs}}(i)$. In the second stage, the light intensity is reduced such that only a small number of photons reach each PMT. Under this

FIGURE D.2: Ni-Cf source used in the absolute gain collection [44].

condition, the number of recorded hits, defined as instances where the measured charge exceeds a predefined threshold, at the i-th PMT is denoted as $N_{\mathrm{obs}}(i)$. Because both measurements are performed using the same light source at an identical position, the quantities $Q_{\mathrm{obs}}(i)$ and $N_{\mathrm{obs}}(i)$ provide a consistent basis for evaluating the relative again of each PMT, as described below.

$$Q_{\mathrm{obs}}(i) \propto I_{\mathrm{H}} \times a(i) \times \epsilon(i) \times G(i), \tag{D.1}$$

$$N_{\mathrm{obs}}(i) \propto I_{\mathrm{L}} \times a(i) \times \epsilon(i). \tag{D.2}$$

Here, I_{H} and I_{L} represent the mean light intensities for the high and low intensity measurements, respectively. The factor $\alpha(i)$ denotes the geometrical acceptaince of the i-th PMT. Taking the ratio of Equation D.1 and D.2 eliminates the common factors related to light intensity, acceptance, and QE, allowing the gain $G(i)$ to be determined directly.

$$G(i) \propto \frac{Q_{\mathrm{obs}}(i)}{N_{\mathrm{obs}}(i)}. \tag{D.3}$$

The relative gain of each PMT is derived by normalizing Equation D.3 to the mean gain over all PMTs. Through this normalization procedure, the factor $I_{\mathrm{H}}/I_{\mathrm{L}}$ is effectively canceled and therefore does not affect the result. From this calibration, the root-mean-square of the relative gain distribution was determined to be 5.9% [44]. Because the high voltage applied to each PMT is adjusted such that $Q_{\mathrm{obs}}(i)$ is equalized across all PMTs, the observed spread in the relative gain is attributed primarily to variations in the QE among individual PMTs. The resulting relative gain values are subsequently employed as correction factors when converting the measured output charge into the corresponding number of photoelectrons.

D.1.3 Absolute gain measurement

The absolute gain is used to translate the measured output charge, expressed in pC, into the corresponding number of photoelectrons (p.e.). It is evaluated using the charge spectrum of single-photoelectron signals obtained with a Ni-Cf source, which serves as a gamma-ray calibration source. A photograph of the Ni-Cf source is presented in Figure **??**. The source is composed of a spherical assembly made of nickel oxide (NiO) and polyethlene, a brass rod, and a ^{252}Cf source. The ^{252}Cf undergoes spontaneous fission and emits neutrons, which are subsequently moderated through repeated elastic scattering with protons. These thermalized neutrons are captured

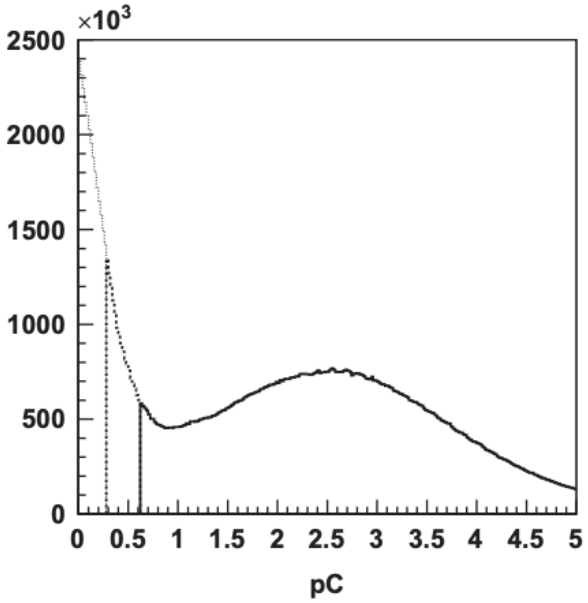

FIGURE D.3: Charge distribution of Ni-Cf source events in SK-III [44]. The dashed curve represents data taken with doubled gain and half the threshold, and the dotted line shows a linear extrapolation.

by nickel nuclei, resulting in the isotropic emission of gamma rays. When the Ni-Cf source is deployed at the center of the SK tank, more than 99% of the detected signals correspond to single photoelectrons. Figure D.3 displays the charge distribution obtained from Ni-Cf source data in the SK-III. This distribution is constructed by first applying the relative gain correction and then summing the charge spectra of all PMTs. To suppress the contribution from PMT noise hits, charge distributions are separately produced for a time window containing signals from the Ni-Cf source (on time) and for a time window excluding such signals (off time), and the off-time distribution is subtracted from the on-time distribution. The absolute gain is defined as the mean value over the entire range of the resulting charge distribution. The absolute gain values determined for SK-I through SK-V are 2.055, 2.297, 2.243, 2.645, and 2.460, respectively. For the SK-VI period, the absolute gain is assumed to be identical to that of SK-V, since the high voltage settings of the PMTs were uncharged from the SK-V configuration.

D.1.4 Relative QE measurement

The relative QE of each PMT is also evaluated using the Ni-Cf source. In this measurement, the Ni–Cf source is first deployed at the center of the SK detector. During data taking, the ultrapure water in the tank is circulated to ensure a uniform water quality throughout the detector volume. The relative QE is then derived from the hit rate of each PMT, denoted as R_i^{Data}, which is calculated from the acquired data. The hit rate R_i^{Data} is defined as

$$R_i^{\mathrm{Data}} = \frac{N_{\mathrm{Hit}}^i \, r_i^2 / a(\theta_i)}{\sum_i \left(N_{\mathrm{Hit}}^i \, r_i^2 / a(\theta_i) \right) / N_{\mathrm{PMT}}}. \tag{D.4}$$

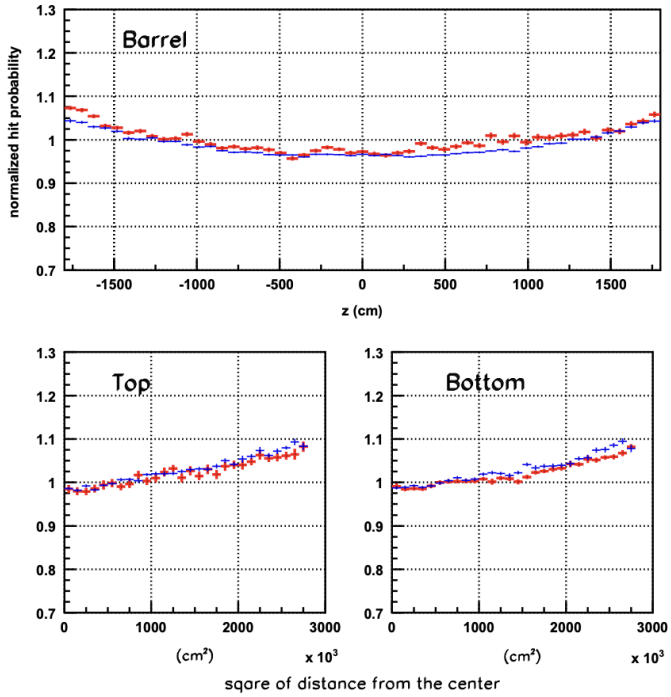

FIGURE D.4: Hit rate distributions for data (red) and MC simulations (blue) [44]. The panels show results for barrel (top), top (bottom left), and bottom (bottom right) PMTs. The horizontal axis represents the z position for barrel PMTs and $x^2 + y^2$ for top and bottom PMTs, while the vertical axis indicates the average hit rate per bin. The Monte Carlo distributions do not account for PMT-to-PMT QE variations.

Here, N^i_{Hit} denotes the total number of hits recorded by the i-th PMT, and r_{i} represents the distance between the Ni–Cf source and the position of the i-th PMT. The function $\alpha(\theta_{\mathrm{i}})$ corresponds to the PMT acceptance correction, defined in the same manner as in Equation C.5. N_{PMT} is the total number of PMTs included in this calculation. The relative QE of each PMT, $\mathrm{QE_i}$, is then evaluated by taking the ratio of R_i^{Data} to R_i^{MC}, where R_i^{MC} is the corresponding hit rate obtained from the MC simulation. This procedure effectively removes systematic effects arising from light reflection and variations in water quality,

$$\mathrm{QE}_i = \frac{R^i_{\mathrm{Data}}}{R^i_{\mathrm{MC}}}. \tag{D.5}$$

Figure D.4 presents the hit rate distributions for data and MC samples. The MC distribution does not include relative QE variations among PMTs, whereas the data distribution shows nonuniform features reflecting PMT-dependent QE differences.

D.1.5 Timing response calibration

The timing characteristics of individual PMTs, which play a crucial role in the reconstruction of charged-particle tracks and interaction vertices, vary due to differences in signal cable lengths and electronic processing delays. In addition, the recorded hit timing depends on the signal amplitude, an effect commonly referred to as time walk. The objective of the timing calibration is to evaluate and correct the time-walk behavior of each PMT, while simultaneously accounting for the total signal processing time

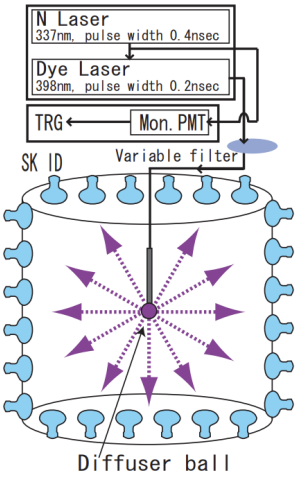

(a) Overview diagram of the experimental setup for the PMT timing calibration.

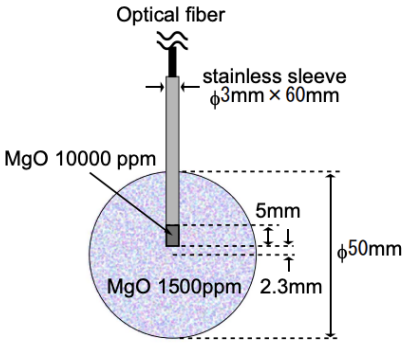

(b) Schematic cross sectional view of the diffuser ball used in the timing calibration system.

FIGURE D.5: Illustration of the timing response calibration apparatus (left) and an internal view of the diffuser sphere (right) [44].

of the detector system. Figure D.5 illustrates the configuration of the timing calibration setup together with a cross sectional view of the diffuser ball. Short light pulses with a wavelength of 337 nm and a full width at half maximum of 0.4 ns are produced using a nitrogen laser. The emission time of each pulse is monitored by a 2-inch PMT with superior timing resolution. The laser light is subsequently wavelength-shifted to 398 nm, corresponding to a region of high PMT quantum efficiency, and transmitted via an optical fiber to the diffuser ball, from which it is emitted uniformly into the detector volume. The light intensity is controlled by optical filters, allowing the timing response to be measured over a range of signal amplitudes. Because the pulse amplitude is directly related to the recorded charge, this procedure is referred to as the TQ (time–charge) calibration.

As illustrated in Figure D.6, this calibration produces a two-dimensional distribution of hit timing versus charge for an individual readout channel, referred to as a TQ map. The timing variable shown on the vertical axis is derived by first computing the time of flight (TOF) from the known geometry between the light source and the PMT, and then evaluating ($T - \mathrm{TOF} - T_{2\mathrm{inch}}$), where (T) denotes the recorded PMT hit time and ($T_{2\mathrm{inch}}$) represents the signal transmission delay measured by the fast 2-inch PMT. The TQ map is divided into discrete charge intervals (Q bins), and the timing peak in each bin is extracted through a fit. By parameterizing the charge dependence of these peak positions with a polynomial function of the Q bin, a set of 15 timing correction coefficients is determined for each channel.

D.2 Photon tracking

D.2.1 Water transparency measurement

In the MC of photon propagation, an accurate description of the optical properties of water, including absorption and scattering, is indispensable. The attenuation of light traveling through water is modeled by an exponential factor of the form $\exp(-l/L(\lambda))$,

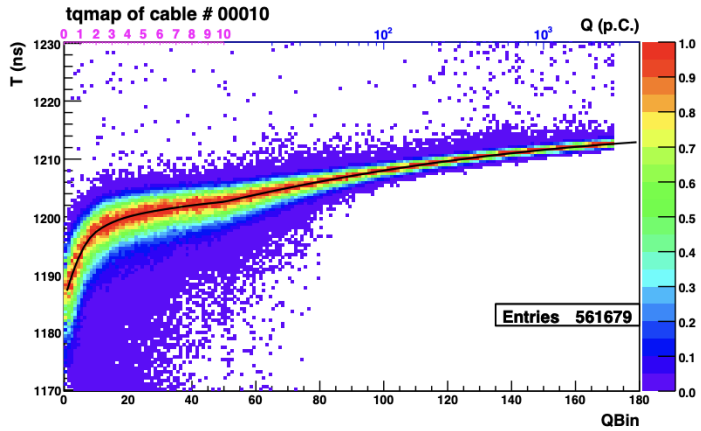

FIGURE D.6: Representative TQ map for a single readout channel [44]. The abscissa shows the hit charge expressed in Q bins, while the ordinate displays the hit timing after correcting for the time of flight. In this representation, increasing (decreasing) values of (T) correspond to earlier (later) signal arrivals.

where l denotes the photon path length and $L(\lambda)$ represents the attenuation length at wavelength λ. In the MC framework, the wavelength-dependent attenuation length $L(\lambda)$ is defined as

$$L(\lambda) = \frac{1}{\alpha_{\mathrm{abs}}(\lambda) + \alpha_{\mathrm{sym}}(\lambda) + \alpha_{\mathrm{asy}}(\lambda)} \,. \tag{D.6}$$

Here, $(\alpha_{\mathrm{abs}}(\lambda))$, $(\alpha_{\mathrm{sym}}(\lambda))$, and $(\alpha_{\mathrm{asy}}(\lambda))$ denote the wavelength-dependent attenuation coefficients for absorption, symmetric scattering, and asymmetric scattering, respectively. The coefficient $(\alpha_{\mathrm{sym}}(\lambda))$ accounts for Rayleigh scattering as well as the symmetric component of Mie scattering, whereas $(\alpha_{\mathrm{asy}}(\lambda))$ represents the forward-peaked component of Mie scattering.

These coefficients are determined using laser calibration data obtained at multiple wavelengths (337, 375, 405, 445, and 473 nm). In this calibration, laser light is injected vertically downward from the top of the SK tank, and the hit timing information recorded by the PMTs is analyzed. Figure D.7 illustrates the configuration of the laser calibration system together with the time-of-flight-subtracted hit timing distributions for both data and MC simulation. The attenuation coefficients are evaluated using PMTs installed on the top of the detector, located 2 m from the laser light injector, with PMTs mounted on the barrel wall. The barrel region is divided into five sections, labeled B1 through B5; section B3 contains PMTs arranged along 11 vertical lines, whereas each of the remaining sections contains PMTs along 10 lines. In the left panel of Figure D.7, the cyan-shaded circular area at the bottom indicates the beam-target position employed in the TOF calculation. In the right panel of Figure D.7, the hits observed between the two blue vertical solid lines originate primarily from scattered photons, and this time window is used to extract the attenuation coefficients. The peaks appearing at later times are attributed to photons reflected from the surfaces of the PMTs or the black sheet. The attenuation coefficients obtained in this manner are implemented in the Monte Carlo simulation using the following experimentally motivated parametrization.

$$\alpha_{\mathrm{abs}}(\lambda) = P_0 \times \frac{P_1}{\lambda^4} + C, \tag{D.7}$$

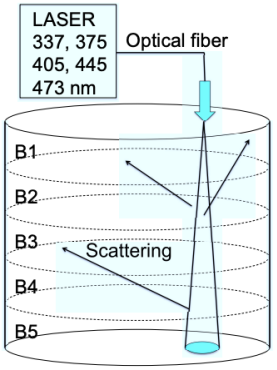

(a) Schematic illustration of the laser calibration system.

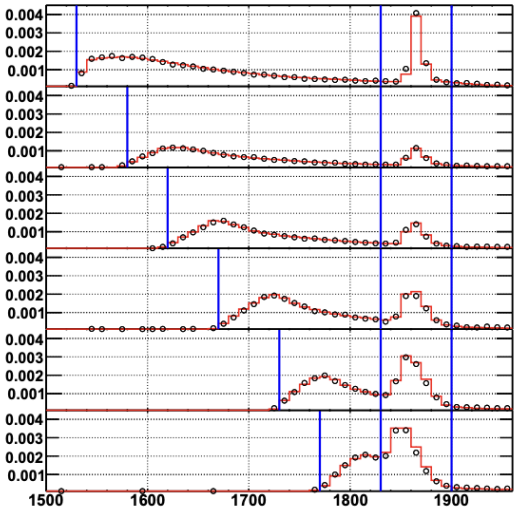

(b) TOF–corrected hit timing distribution.

FIGURE D.7: Schematic illustration of the laser calibration system (a) and the TOF–corrected hit timing distributions obtained from laser calibration data and MC simulation (b) [44]. The tuning of water optical parameters is performed using PMTs located on the top of the detector at a distance of 2 m from the laser light injector, as well as PMTs installed on the barrel wall. The barrel region is divided into five sections, labeled B1 through B5; region B3 contains PMTs along 11 vertical lines, while the remaining regions each include PMTs along 10 lines. In the left panel, the cyan-shaded circular area at the bottom indicates the beam target position used for the TOF calculation. In the right panel, the black markers represent calibration data, and the red histogram shows the corresponding MC results. The total number of observed photoelectrons normalizes both distributions. The time interval between the two leftmost blue vertical solid lines is used for tuning the water parameters, while the later time region is utilized for the measurement of PMT reflectivity.

$$C = P_0 \times P_2 \times \left(\frac{\lambda}{500}\right)^{P_3}, \tag{D.8}$$

$$\alpha_{\mathrm{sym}}(\lambda) = \frac{P_4}{\lambda^4} \times \left(1.0 + \frac{P_5}{\lambda^2}\right), \tag{D.9}$$

$$\alpha_{\mathrm{asy}}(\lambda) = P_6 \times \left\{1.0 + \frac{P_7}{\lambda^4} \times (\lambda - P_8)^2\right\}. \tag{D.10}$$

The attenuation coefficients are obtained by performing a χ^2 minimization between the hit timing distributions observed in data and those predicted by MC simulations. In the simulation, the nine parameters P_0 through P_8 are varied, and the optimal set of parameters is determined by achieving the best agreement with the measured timing distribution. The resulting values of P_0–P_8 are summarized in Table D.1.

TABLE D.1: Values of parameter P_0 to P_8.

Parameter	Value
P_0	0.596600
P_1	5.18888×10^7
P_2	1.06522
P_3	14.1858
P_4	1.13817×10^8
P_5	5.79108×10^4
P_6	2.26159×10^{-4}
P_7	17.1260
P_8	4.48622×10^4

D.3 Energy Scale Calibration

The energy scale for low-energy Monte Carlo simulations is calibrated using the electron linear accelerator (LINAC). A schematic overview of the LINAC system is shown in Figure 5.10 [130]. To minimize contamination from X-rays and gamma rays produced by the accelerator itself, the LINAC facility is installed at a sufficient distance from the SK detector. Electron beams generated by the LINAC are guided into the detector through stainless-steel beam pipes and steering magnets. The kinetic energy of the injected electrons can be tuned between 5 and 18 MeV. In addition, the irradiation point inside the detector is adjustable by extending or retracting the beam pipes. During the SK-VI period, LINAC calibration data were collected at three injection positions, located at $(-1237, -70.7, 1197)$ cm, $(-1237, -70.7, -6)$ cm, and $(-1237, -70.7, -1209)$ cm. At each of these locations, electron beams with kinetic energies of 8, 12, and 15 MeV were used, while an additional run at 6 MeV was performed at the central position $(-1237, -70.7, -6)$ cm. The energy scale parameter is determined by comparing the effective number of photoelectrons, N_{eff}, between the LINAC calibration data and the corresponding LINAC MC samples. For SK-VI, this parameter was found to be approximately 0.88. In the MC simulations, the derived energy scale parameter is applied as a multiplicative correction to the quantum efficiency of the ID PMTs.

Bibliography

[1] K. Sumiyoshi *Genshikaku kara yomitoku chōshinsei bakuhatsu no sekai* Number 21 in Kisohousoku kara yomitoku butsurigaku saizensen. Kyoritsu Shuppan Co., Ltd., 2018.

[2] T. Sukhbold *et al.*, "Core-collapse Supernovae from 9 to 120 Solar Masses Based on Neutrino-powered Explosions," *The Astrophysical Journal*, 821(1):38, April 2016.

[3] K. Nakazato *et al.*, "Supernova Neutrino Light Curves and Spectra for Various Progenitor Stars: From Core Collapse to Proto-neutron Star Cooling," *The Astrophysical Journal Supplement Series*, 205(1):2, March 2013.

[4] M. Liebendörfer *et al.*, "A Finite Difference Representation of Neutrino Radiation Hydrodynamics in Spherically Symmetric General Relativistic Spacetime," *The Astrophysical Journal Supplement Series*, 150(1):263–316, January 2004.

[5] K. S. Hirata *et al.*, "Observation in the kamiokande-ii detector of the neutrino burst from supernova sn1987a," *Physical Review D*, 38:448–458, Jul 1988.

[6] A. S. Dighe and A. Y. Smirnov, "Identifying the neutrino mass spectrum from a supernova neutrino burst," *Physical Review D*, 62:033007, Jul 2000.

[7] K. Sumiyoshi, T. Kojo, and S. Furusawa, "Equation of state in neutron stars and supernovae," *arXiv:2207.00033*, 2022.

[8] Y. Suzuki, "The super-kamiokande experiment," *The European Physical Journal C*, 79(4):298, 2019.

[9] K. Hagiwara *"Search for Astronomical Neutrinos from Blazer TXS0506+056 in Super-Kamiokande"* PhD thesis, Okayama University, 2020.

[10] S. Fukuda *et al.*, "The super-kamiokande detector," *Nuclear Instruments and Methods in Physics Research Section A: Accelerators, Spectrometers, Detectors and Associated Equipment*, 501(2):418–462, 2003.

[11] K. Abe *et al.*, "First gadolinium loading to super-kamiokande," *Nuclear Instruments and Methods in Physics Research Section A: Accelerators, Spectrometers, Detectors and Associated Equipment*, 1027:166248, 2022.

[12] K. Abe *et al.*, "Real-time supernova neutrino burst monitor at super-kamiokande," *Astroparticle Physics*, 81:39–48, aug 2016.

[13] M. D. Kistler, W. C. Haxton, and H. Yüksel, "Tomography of Massive Stars from Core Collapse to Supernova Shock Breakout," *The Astrophysical Journal*, 778(1):81, November 2013.

[14] S. E. Woosley, A. Heger, and T. A. Weaver, "The evolution and explosion of massive stars," *Reviews of Modern Physics*, 74(4):1015–1071, November 2002.

[15] S. E. Woosley and A. Heger, "The Progenitor Stars of Gamma-Ray Bursts," *The Astrophysical Journal*, 637(2):914–921, February 2006.

[16] A. Strumia and F. Vissani, "Precise quasielastic neutrino/nucleon cross-section," *Physics Letters B*, 564(1-2):42–54, July 2003.

[17] J. N. Bahcall, M. Kamionkowski, and A. Sirlin, "Solar neutrinos: Radiative corrections in neutrino-electron scattering experiments," *Physical Review D*, 51:6146–6158, Jun 1995.

[18] K. Langanke, P. Vogel, and E. Kolbe, "Signal for Supernova ν_μ and ν_τ Neutrinos in Water Čerenkov Detectors," *Physical Review Letters*, 76(15):2629–2632, April 1996.

[19] E. Kolbe, K. Langanke, and P. Vogel, "Estimates of weak and electromagnetic nuclear decay signatures for neutrino reactions in Super-Kamiokande," *Physical Review D*, 66(1):013007, July 2002.

[20] K. Nakazato *et al.*, "Observing Supernova Neutrino Light Curves with Super-Kamiokande. II. Impact of the Nuclear Equation of State," *The Astrophysical Journal*, 925(1):98, January 2022.

[21] Y. Suwa *et al.*, "Observing Supernova Neutrino Light Curves with Super-Kamiokande: Expected Event Number over 10 s," *The Astrophysical Journal*, 881(2):139, August 2019.

[22] M. Mori *et al.*, "Searching for supernova bursts in super-kamiokande IV," *The Astophysical Journal*, 938(1):35, oct 2022.

[23] K. De *et al.*, "The disappearance of a massive star marking the birth of a black hole in M31," *arXiv e-prints*, page arXiv:2410.14778, October 2024.

[24] K. Nakazato, K. Sumiyoshi, and H. Togashi, "Numerical study of stellar core collapse and neutrino emission using the nuclear equation of state obtained by the variational method," *Publications of the Astronomical Society of Japan*, 73(3):639–651, may 2021.

[25] Y. Suwa *et al.*, "Neutrino Constraints on Black Hole Formation in M31," *The Open Journal of Astrophysics*, 8, nov 11 2025.

[26] K. Abe *et al.*, "Diffuse supernova neutrino background search at Super-Kamiokande," *Physical Review D*, 104(12):122002, December 2021.

[27] Y. Ashida *"Measurement of Neutrino and Antineutrino Neutral-Current Quasielastic-like Interactions and Applications to Supernova Relic Neutrino Searches"* Phd thesis, Kyoto University, February 2020.

[28] K. Abe *et al.*, "Diffuse supernova neutrino background search at super-kamiokande," *Physical Review D*, 104:122002, Dec 2021.

[29] K. Nakazato, K. Sumiyoshi, and H. Togashi, "Numerical study of stellar core collapse and neutrino emission using the nuclear equation of state obtained by the variational method," *Publications of the Astronomical Society of Japan*, 73(3):639–651, June 2021.

[30] K. Sumiyoshi, S. Yamada, and H. Suzuki, "Dynamics and Neutrino Signal of Black Hole Formation in Nonrotating Failed Supernovae. I. Equation of State Dependence," *The Astrophysical Journal*, 667(1):382–394, September 2007.

[31] K. Sumiyoshi, S. Yamada, and H. Suzuki, "Dynamics and Neutrino Signal of Black Hole Formation in Nonrotating Failed Supernovae. II. Progenitor Dependence," *The Astrophysical Journal*, 688(2):1176–1185, December 2008.

[32] L. Choi, A. Burrows, and D. Vartanyan, "Predicted neutrino signal features of core-collapse supernovae," *Physical Review D*, 111(12):123038, June 2025.

[33] K. Abe *et al.*, "Search for Diffuse Supernova Neutrino Background with 956.2 days of Super-Kamiokande Gadolinium Dataset," *arXiv e-prints*, page arXiv:2511.02222, November 2025.

[34] Hyper-Kamiokande Collaboration Hyper-kamiokande official website https://www-sk.icrr.u-tokyo.ac.jp/hk/en/about/detector.html Accessed: 2025-10-17.

[35] P. Madau Cosmic star formation history In Steven S. Holt and Lee G. Mundy, editors, *The Seventh Astrophysical Conference: Star formation, near and far*, volume 393 of *American Institute of Physics Conference Series*, pages 481–490. AIP, February 1997.

[36] W. Li *et al.*, "Nearby supernova rates from the Lick Observatory Supernova Search - III. The rate-size relation, and the rates as a function of galaxy Hubble type and colour," *Monthly Notices of the Royal Astronomical Society*, 412(3):1473–1507, April 2011.

[37] S. Mattila *et al.*, "Core-collapse Supernovae Missed by Optical Surveys," *The Astrophysical Journal*, 756(2):111, September 2012.

[38] M. T. Botticella *et al.*, "Supernova rates from the Southern inTermediate Redshift ESO Supernova Search (STRESS)," *Astronomy and Astrophysics*, 479(1):49–66, February 2008.

[39] T. Dahlen *et al.*, "The Extended Hubble Space Telescope Supernova Survey: The Rate of Core Collapse Supernovae to z ~1," *The Astrophysical Journal*, 757(1):70, September 2012.

[40] S. Horiuchi, J. F. Beacom, and E. Dwek, "Diffuse supernova neutrino background is detectable in Super-Kamiokande," *Physical Review D*, 79(8):083013, April 2009.

[41] M. Harada *"Development of Neutron Tagging Algorithm and Search for Supernova Relic Neutrino in SK-Gd Experiment"* Ph.d. thesis, Okayama University, 2023.

[42] K. Abe *et al.*, "Solar neutrino results in Super-Kamiokande-III," *Physics Review D*, 83(5):052010, March 2011.

[43] M. Shinoki Super-kamiokande gadolinium jikken ni yoru uchusen myuon kakuhasai hanno ni yurai suru chuseisi seiseiritsu no sokutei Master's thesis, Tokyo University of Science, March 2021.

[44] K. Abe *et al.*, "Calibration of the Super-Kamiokande detector," *Nuclear Instruments and Methods in Physics Research A*, 737:253–272, February 2014.

[45] Y. Hara *Elementary Particle Physics* Shokabo Text Series - Physics. Shokabo, 2016.

[46] Y. Kashiwagi *et al.*, "Performance of SK-Gd's Upgraded Real-time Supernova Monitoring System," *The Astrophysical Journal*, 970(1):93, July 2024.

[47] M. Mori *et al.*, "Developing an end-to-end simulation framework of supernova neutrino detection," *Progress of Theoretical and Experimental Physics*, 2021(2):023E01, February 2021.

[48] T. Totani *et al.*, "Future Detection of Supernova Neutrino Burst and Explosion Mechanism," *The Astrophysical Journal*, 496(1):216–225, March 1998.

[49] I. Tamborra *et al.*, "Neutrino emission characteristics and detection opportunities based on three-dimensional supernova simulations," *Physical Review D*, 90(4):045032, August 2014.

[50] T. Fischer *et al.*, "Protoneutron star evolution and the neutrino-driven wind in general relativistic neutrino radiation hydrodynamics simulations," *Astronomy and Astrophysics*, 517:A80, July 2010.

[51] K. Nomoto, "Evolution of 8–10 M_{sun} Stars toward Electron Capture Supernovae. II. Collapse of an O + NE + MG Core," *The Astrophysical Journal*, 322:206, November 1987.

[52] T. Suzuki *et al.*, "Neutrino-nucleus reactions on ^{16}O based on new shell-model hamiltonians," *Physical Review C*, 98:034613, Sep 2018.

[53] T. Suzuki, "," 2022, "3001private communication".

[54] G. Battistoni *et al.* The fluka code: description and benchmarking In *AIP Conference Proceedings*, volume 896, pages 31–49. American Institute of Physics, mar 2007.

[55] M. Ugliano *et al.*, "Progenitor-explosion Connection and Remnant Birth Masses for Neutrino-driven Supernovae of Iron-core Progenitors," *The Astrophysical Journal*, 757(1):69, September 2012.

[56] S. Horiuchi *et al.*, "The red supergiant and supernova rate problems: implications for core-collapse supernova physics.," *Monthly Notices of the Royal Astronomical Society*, 445:L99–L103, November 2014.

[57] S. J. Smartt *et al.*, "The death of massive stars - I. Observational constraints on the progenitors of Type II-P supernovae," *Monthly Notices of the Royal Astronomical Society*, 395(3):1409–1437, May 2009.

[58] S. Horiuchi *et al.*, "The Cosmic Core-collapse Supernova Rate Does Not Match the Massive-star Formation Rate," *The Astrophysical Journal*, 738(2):154, September 2011.

[59] T. Ertl *et al.*, "A Two-parameter Criterion for Classifying the Explodability of Massive Stars by the Neutrino-driven Mechanism," *The Astrophysical Journal*, 818(2):124, February 2016.

[60] S. A. Colgate, "Neutron-Star Formation, Thermonuclear Supernovae, and Heavy-Element Reimplosion," *The Astrophysical Journal*, 163:221, January 1971.

[61] R. Akaho, H. Nagakura, and T. Foglizzo, "Detectability of late-time supernova neutrinos with fallback accretion onto protoneutron star," *The Astrophysical Journal*, 960:116, 2024.

[62] K. Hirata *et al.*, "Observation of a neutrino burst from the supernova SN1987A," *Physical Review Letters*, 58(14):1490–1493, April 1987.

[63] R. M. Bionta *et al.*, "Observation of a neutrino burst in coincidence with supernova 1987A in the Large Magellanic Cloud," *Physical Review Letters*, 58(14):1494–1496, April 1987.

[64] E. N. Alexeyev *et al.*, "Detection of the neutrino signal from SN 1987A in the LMC using the INR Baksan underground scintillation telescope," *Physics Letters B*, 205(2-3):209–214, April 1988.

[65] D. Griffiths *Introduction to Elementary Particles* Maruzen Publishing, 2019.

[66] Y. Totsuka *Soryushi Butsurigaku* Number 10 in Gendai no Butsurigaku. Iwanami Shoten, 1992.

[67] P. B. Demorest *et al.*, "A two-solar-mass neutron star measured using shapiro delay," *Nature*, 467(7319):1081–1083, 2010.

[68] J. Antoniadis *et al.*, "A massive pulsar in a compact relativistic binary," *Science*, 340(6131), apr 2013.

[69] H. Shen *et al.*, "Relativistic equation of state of nuclear matter for supernova and neutron star," *Nuclear Physics A*, 637(3):435–450, 1998.

[70] H. Shen *et al.*, "RELATIVISTIC EQUATION OF STATE FOR CORE-COLLAPSE SUPERNOVA SIMULATIONS," *The Astrophysical Journal Supplement Series*, 197(2):20, nov 2011.

[71] J. M. Lattimer and F. Douglas Swesty, "A generalized equation of state for hot, dense matter," *Nuclear Physics A*, 535(2):331–376, 1991.

[72] H. Togashi and M. Takano, "Variational study for the equation of state of asymmetric nuclear matter at finite temperatures," *Nuclear Physics A*, 902:53–73, mar 2013.

[73] K. Sumiyoshi *et al.*, "Effects of nuclear matter and composition in core-collapse supernovae and long-term proto-neutron star cooling," *Prog. Theor. Exp. Phys.*, 2023(1):013E02, January 2023.

[74] K. Nakazato, H. Suzuki, and H. Togashi, "Heavy nuclei as thermal insulation for protoneutron stars," *Physical Review C*, 97(3), mar 2018.

[75] K. Nakazato and H. Suzuki, "Cooling Timescale for Protoneutron Stars and Properties of Nuclear Matter: Effective Mass and Symmetry Energy at High Densities," *The Astrophysical Journal*, 878(1):25, June 2019.

[76] K. Nakazato and H. Suzuki, "A New Approach to the Mass and Radius of Neutron Stars with Supernova Neutrinos," *The Astrophysical Journal*, 891(2):156, March 2020.

[77] C. S. Kochanek *et al.*, "The All-Sky Automated Survey for Supernovae (ASAS-SN) Light Curve Server v1.0," *Publications of the Astronomical Society of the Pacific*, 129(980):104502, October 2017.

[78] E. C. Bellm *et al.*, "The Zwicky Transient Facility: System Overview, Performance, and First Results," *Publications of the Astronomical Society of the Pacific*, 131(995):018002, January 2019.

[79] J. L. Tonry *et al.*, "ATLAS: A High-cadence All-sky Survey System," *Publications of the Astronomical Society of the Pacific*, 130(988):064505, June 2018.

[80] S. Yamada *et al.*, "Commissioning of the New Electronics and Online System for the Super-Kamiokande Experiment," *IEEE Transactions on Nuclear Science*, 57(2):428–432, January 2010.

[81] J. F. Beacom and M. R. Vagins, "Antineutrino Spectroscopy with Large Water Čerenkov Detectors," *Physical Review Letters*, 93(17):171101, October 2004.

[82] Y. Hino *et al.*, "Modification on Thermal Motion in Geant4 for Neutron Capture Simulation in Gadolinium Loaded Water," *Progress of Theoretical and Experimental Physics*, 2025(1):013C01, January 2025.

[83] M. Ikeda *et al.*, "Search for Supernova Neutrino Bursts at Super-Kamiokande," *The Astrophysical Journal*, 669(1):519–524, November 2007.

[84] J. Hosaka *et al.*, "Solar neutrino measurements in Super-Kamiokande-I," *Physical Review D*, 73(11):112001, June 2006.

[85] J. Villafane *et al.*, "Optical observations of SN 2023ixf at Teide Observatory," *The Astronomer's Telegram*, 16045:1, May 2023.

[86] M. Nakahata *et al.*, "Super-Kamiokande: Neutrino search for SN2023ixf," *GRB Coordinates Network*, 33916:1, June 2023.

[87] M. Nakahata and the Super-Kamiokande Collaboration Neutrino search for sn2023ixf in super-kamiokande https://www.astronomerstelegram.org/?read=16070, 2023 Astronomer's Telegram #16070, 2 June 2023.

[88] F. Nakanishi *et al.*, "Supernova Burst and Diffuse Supernova Neutrino Background Simulator for Water Cherenkov Detectors," *The Astrophysical Journal*, 965(1):91, April 2024.

[89] P. Vogel and J. F. Beacom, "Angular distribution of neutron inverse beta decay, $\bar{\nu}_e$+p–>e^++n," *Physical Review D*, 60(5):053003, September 1999.

[90] G. Ricciardi, N. Vignaroli, and F. Vissani, "An accurate evaluation of electron (anti-)neutrino scattering on nucleons," *Journal of High Energy Physics*, 2022(8):212, August 2022.

[91] J. N. Bahcall, M. Kamionkowski, and A. Sirlin, "Solar neutrinos: Radiative corrections in neutrino-electron scattering experiments," *Physical Review D*, 51:6146–6158, Jun 1995.

[92] H. Duan, G. M. Fuller, and Y. Qian, "Collective Neutrino Oscillations," *Annual Review of Nuclear and Particle Science*, 60:569–594, November 2010.

[93] L. Wolfenstein, "Neutrino oscillations in matter," *Physical Review D*, 17(9):2369–2374, May 1978.

[94] S. P. Mikheyev and A. Y. Smirnov, "Resonance enhancement of oscillations in matter and solar neutrino spectroscopy," *Yadernaya Fizika*, 42:1441–1448, January 1985.

[95] Masayuki Harada Geant4 based Simulation Study for Super-Kamiokande In *Journal of Physics Conference Series*, volume 1468 of *Journal of Physics Conference Series*, page 012255. IOP, February 2020.

[96] F. Nakanishi *et al.*, "Observing Supernova Neutrino Light Curves with Super-Kamiokande. VI. A Practical Data Analysis Technique Considering Realistic Experimental Backgrounds," *The Astrophysical Journal*, 992(1):27, October 2025.

[97] S. Locke *et al.*, "New methods and simulations for cosmogenic induced spallation removal in Super-Kamiokande-IV," *Physical Review D*, 110(3):032003, August 2024.

[98] K. Abe *et al.*, "Solar neutrino measurements using the full data period of Super-Kamiokande-IV," *Physical Review D*, 109(9):092001, May 2024.

[99] E. L. Wright *et al.*, "The Wide-field Infrared Survey Explorer (WISE): Mission Description and Initial On-orbit Performance," *The Astronomical Journal*, 140(6):1868–1881, December 2010.

[100] A. Mainzer *et al.*, "Initial Performance of the NEOWISE Reactivation Mission," *The Astrophysical Journal*, 792(1):30, September 2014.

[101] H. Togashi *et al.*, "Nuclear equation of state for core-collapse supernova simulations with realistic nuclear forces," *Nuclear Physics A*, 961:78–105, May 2017.

[102] A. W. Steiner, M. Hempel, and T. Fischer, "Core-collapse Supernova Equations of State Based on Neutron Star Observations," *The Astrophysical Journal*, 774(1):17, September 2013.

[103] A. S. Schneider *et al.*, "Equation of state effects in the core collapse of a $20-M_{\odot}$ star," *Physical Review C*, 100:055802, Nov 2019.

[104] J. F. Beacom and M. R. Vagins, "Antineutrino Spectroscopy with Large Water Čerenkov Detectors," *Physical Review Letters*, 93(17):171101, October 2004.

[105] K. Abe *et al.*, "First gadolinium loading to Super-Kamiokande," *Nuclear Instruments and Methods in Physics Research A*, 1027:166248, March 2022.

[106] K. Abe *et al.*, "Solar neutrino measurements in Super-Kamiokande-IV," *Physical Review D*, 94(5):052010, September 2016.

[107] S. W. Li and J. F. Beacom, "First calculation of cosmic-ray muon spallation backgrounds for mev astrophysical neutrino signals in super-kamiokande," *Physical Review C*, 89:045801, Apr 2014.

[108] S. W. Li and J. F. Beacom, "Spallation backgrounds in super-kamiokande are made in muon-induced showers," *Physical Review D*, 91:105005, May 2015.

[109] S. W. Li and J. F. Beacom, "Tagging spallation backgrounds with showers in water cherenkov detectors," *Physical Review D*, 92:105033, Nov 2015.

[110] K. Abe *et al.*, "Solar neutrino measurements in super-kamiokande-iv," *Physical Review D*, 94:052010, Sep 2016.

[111] G. Carminati Proceedings of the 32nd international cosmic ray conference In *Proceedings of the 32nd International Cosmic Ray Conference (ICRC 2011)*, Beijing, China, 2011 Online: http://icrc2011.ihep.ac.cn/paper/proc/v4.pdf.

[112] G. Carminati, "The new Wide-band Solar Neutrino Trigger for Super-Kamiokande," *Physics Procedia*, 61:666–672, January 2015.

[113] M. Elnimr and Super-Kamiokande Collaboration Low Energy ^{8} B Solar Neutrinos with the Wideband Intelligent Trigger at Super-Kamiokande In *Journal of Physics Conference Series*, volume 888 of *Journal of Physics Conference Series*, page 012189. IOP, September 2017.

[114] S. Locke *et al.*, "New methods and simulations for cosmogenic induced spallation removal in Super-Kamiokande-IV," *Physical Review D*, 110(3):032003, August 2024.

[115] K. Abe *et al.*, "Measurement of neutrino and antineutrino oscillations by the T2K experiment including a new additional sample of veinteractions at the far detector," *Physical Review D*, 96(9):1–50, 2017.

[116] A. Hoecker *et al.*, "TMVA - Toolkit for Multivariate Data Analysis," *arXiv e-prints*, page physics/0703039, March 2007.

[117] H. Zhang *Ph.D Thesis* PhD thesis, Tsinghua University, 2012.

[118] H. Watanabe *et al.*, "First study of neutron tagging with a water Cherenkov detector," *Astroparticle Physics*, 31(4):320–328, May 2009.

[119] T. Irvine *Ph.D Thesis* PhD thesis, The University of Tokyo, 2014.

[120] M. Honda *et al.*, "Calculation of atmospheric neutrino flux using the interaction model calibrated with atmospheric muon data," *Physical Review D*, 75(4):043006, February 2007.

[121] M. Honda *et al.*, "Improvement of low energy atmospheric neutrino flux calculation using the JAM nuclear interaction model," *Physical Review D*, 83(12):123001, June 2011.

[122] Y. Hayato, "A Neutrino Interaction Simulation Program Library NEUT," *Acta Physica Polonica B*, 40(9):2477, September 2009.

[123] A. Strumia and F. Vissani, "Precise quasielastic neutrino/nucleon cross-section," *Physics Letters B*, 564(1-2):42–54, July 2003.

[124] K. Abe *et al.*, "Hyper-Kamiokande Design Report," *arXiv e-prints*, page arXiv:1805.04163, May 2018.

[125] K. Nakazato *et al.*, "Impacts of Black-hole-forming Supernova Explosions on the Diffuse Neutrino Background," *The Astrophysical Journal*, 975(1):71, November 2024.

[126] S. M. Adams *et al.*, "The search for failed supernovae with the Large Binocular Telescope: constraints from 7 yr of data," *Monthly Notices of the Royal Astronomical Society*, 469(2):1445–1455, August 2017.

[127] M. Malek *et al.*, "Search for supernova relic neutrinos at super-kamiokande," *Physical Review Letter*, 90:061101, Feb 2003.

[128] K. Bays *et al.*, "Supernova relic neutrino search at super-kamiokande," *Physical Review D*, 85:052007, Mar 2012.

[129] S. Horiuchi, J. F. Beacom, and E. Dwek, "Diffuse supernova neutrino background is detectable in super-kamiokande," *Physical Review D*, 79:083013, Apr 2009.

[130] M. Nakahata *et al.*, "Calibration of Super-Kamiokande using an electron LINAC. The Super-Kamiokande Collaboration," *Nuclear Instruments and Methods in Physics Research A*, 421(1-2):113–129, January 1999.